ION IMPLANTATION EFFECTS IN CdS THIN FILMS

THESIS SUBMITTED TO THE
COCHIN UNIVERSITY OF SCIENCE AND TECHNOLOGY
FOR THE AWARD OF THE DEGREE OF
DOCTOR OF PHILOSOPHY

by

K. LAKSHMI NARAYANAN

DEPARTMENT OF PHYSICS
COCHIN UNIVERSITY OF SCIENCE AND TECHNOLOGY
COCHIN - 682 022
INDIA

November 1997

CERTIFICATE

Certified that the work presented in this thesis entitled " **Ion implantation effects in CdS thin films**" is based on the bonafide research work done by Shri. K. Lakshmi Narayanan under my guidance, at the Department of Physics, Cochin University of Science and Technology, and has not been included in any other thesis submitted for the award of any degree.

Cochin

November 20, 1997

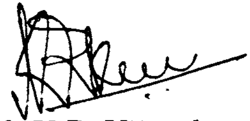

Prof. K.P. Vijayakumar

Contents

1 INTRODUCTION 1

1.1 Cadmium sulphide 2

1.2 Ion implantation 10

1.2.1 Energy loss 11

1.2.2 Range of incident ions 13

1.2.3 Radiation damage 15

1.3 Irradiation effects in semiconductors 17

1.4 Irradiation effects in Cadmium Sulphide 20

1.5 Scope of the thesis 22

1.6 Organization of the thesis 22

2 EXPERIMENTAL TECHNIQUES 30

2.1 Details of ion implantation 30

2.2 Experimental techniques 35

2.2.1 X-ray diffraction 36

2.2.2 Optical absorption spectrometry 36

2.2.3 Variable low energy positron beam 36

2.2.4 Raman scattering 38

2.2.5 Transmission electron microscopy 40

2.2.6 Scanning electron microscopy 40

2.2.7 Resistivity 41

2.2.8 Hot probe method 41

2.2.9 Photoconductivity 41

2.3 Details of heat treatments 43

2.4 Summary 43

3 PREPARATION AND CHARACTERIZATION OF CdS THIN FILMS 45

3.1 Vacuum evaporation technique 46

3.1.1 Preparation of thin films of CdS using vacuum evaporation 46
3.1.2 Substrate cleaning 47
3.1.3 Characterization of the films 47
3.2 Chemical bath deposition technique 53
3.2.1 Optimization of the parameters for synthesis of CdS films 53
3.2.2 Characterization of the films 54
3.3 Effects of annealing on films of CdS prepared by CBD process 58
3.4 Partial conversion of films of CdS to CdO on annealing 67
3.5 Summary 73

4 EFFECT OF ARGON ION IMPLANTATION IN CdS THIN FILMS 79
4.1 Experimental details 80
4.2 Studies of CdS films prepared by CBD technique 82
4.2.1 X-ray diffraction studies 82
4.2.2 As-deposited films 82
4.2.3 Effect of irradiation 84
4.2.4 Effect of post irradiation annealing 84
4.3 Optical absorption studies 87
4.3.1 As-deposited films 87
4.3.2 Effect of Irradiation 87
4.3.3 Effect of post irradiation annealing 96
4.4 Raman scattering studies 101
4.4.1 As deposited films 102
4.4.2 Effect of irradiation 104
4.4.3 Effect of post irradiation annealing 106
4.5 Positron annihilation studies 108
4.5.1 As deposited films 110
4.5.2 Effect of irradiation 112
4.5.3 Effect of post irradiation annealing 114

4.5.4 Effect of annealing the as-deposited films 116
4.6 Studies of CdS films prepared by vacuum evaporation 116
4.6.1 As-deposited thin films 118
4.6.2 Effect of irradiation 118
4.7 Summary 126

5 EFFECT OF NITROGEN AND OXYGEN ION IMPLANTATION IN CdS THIN FILMS 132

5.1 Experimental details 133
5.2 Characterization of structural modifications 134
5.2.1 As deposited films 134
5.2.2 Effect of ion implantation 136
5.2.3 Effect of post implantation annealing 136
5.3 Electrical characterization of N^+ irradiated CdS films 136
5.3.1 Conductivity measurements on N^+ irradiated films 139
5.3.2 Hot Probe measurements 139
5.4 Photoconductivity 143
5.5 Persistent Photoconductivity: 143
5.6 Data Analysis of the Photoconductivity measurements 145
5.7 Optical absorption studies of nitrogen irradiated CdS thin films 159
5.8 Optical bandgap shift in oxygen ion implanted CdS films 163
5.9 Raman scattering studies of O^+ irradiated CdS films 166
5.9.1 X-ray diffraction studies . . . 167
5.9.2 Raman scattering studies 167
5.10 Summary 173
5.11 Appendix A: Causes of Persistent photoconductivity 174
5.11.1 Random local potential fluctuations 174
5.11.2 DX centres 177
5.11.3 Traps and metastable states 178

5.12 Appendix B: Time dependence of the photoconductivity: A Mathematical Approach 180

5.12.1 Donor level excitation without traps 181

5.12.2 Rate equations for electron density with recombination, trapping and detrapping 181

5.12.3 Excitation of intrinsic semiconductor 184

5.12.4 Decay 186

5.12.5 Stretched Exponential Decay 186

5.12.6 Power law decay 188

6 SUMMARY AND CONCLUSION 194

6.1 Future scope of the work 196

PUBLICATIONS 198

CHAPTER 1

1 INTRODUCTION

Ion implantation is being increasingly used in the fabrication of semiconductor devices, as it has several advantages over the more conventional diffusion techniques [1]. During the diffusion process, the depth at which the junction is formed is controlled by the amount of dopants on the surface and temperature and time over which the diffusion occurs. Although such variables can be controlled quite accurately, ion implantation offers a more accurate control over the junction depth. The depth to which the ions penetrate into the substrate is mainly determined by the energy. This means that the junction depth can be accurately specified and easily reproduced by controlling a single variable, ie., the energy of the incident ions. Ion implantation is also being used in many other areas [2, 3] since some of the properties of solids, other than electrical behaviour, can be favourably altered by the addition of the impurities or by radiation damage.

Further the profiles produced by diffusion techniques always have a concentration that decreases slowly towards the point at which the junction is formed, while the implant distribution falls off rapidly on either side of the projected range, resulting in very abrupt junctions.

Another advantage of implantation is the formation of buried layers of by using sufficiently high energy implantation. In fact, buried insulating layers (for device isolation) and conducting links can also be produced by implantation of suitable ions. Yet another advantage of the implantation process is the accuracy with which the dopant concentrations can be monitored during implantation, through the beam current and integrated charge. Unlike diffusion process, the implanted profiles are mostly unaffected by the presence of crystalline imperfections.

Despite several such advantages, it should be remembered that ion implantation is a rather violent process and gives rise to lattice disorder in the substrate. The implantation induced damage can have a strong influence on the electrical and optical properties of the semiconductor material. There have been a large number of investigations [4, 5, 6] in the area of radiation effects on various semiconductors.

The present thesis aims in studying the irradiation effects in a typical II-VI semiconductor namely CdS. Ion implantation effects in CdS thin films are characterized by various techniques such as optical absorption spectroscopy, positron annihilation spectroscopy, Raman scattering, x-ray diffraction (XRD) and photoconductivity measurements.

The organization of this chapter is as follows. In the next section(1.1), the preparation, characterization and properties of cadmium sulphide are reviewed. Section 1.2 gives a brief introduction to the ion implantation technique. The irradiation effects in semiconductors are given briefly in the section 1.3 followed by a brief review of ion implantation studies carried out in CdS in section 1.4. Section 1.5 describes the scope of the thesis.

1.1 Cadmium sulphide

The semiconductors of II-VI family feature direct bandgap from near ultraviolet to the far infrared. This makes them useful in a wide variety of electronic and optoelectronic devices. For direct bandgap semiconductors, the band to band absorption rises steeply, normally being greater than 10^4 cm^{-1} for photon energies above the band gap energy, giving an absorption length of ~ 1 μm. This is in contrast to an indirect band gap semiconductor like silicon, which needs a thickness of 10 μm for absorption of 90 % solar radiation. As a result, the II-VI compounds have played an important role early in the research on photovoltaic effects and in the development of solar cells. Extensive research efforts [7, 8, 9, 10] have been undertaken in the area of solar cells, based on II-VI semiconductors with copper indium selenide, indium phosphide and other semiconductors with the aim of improving the efficiency. The main

thrust of these efforts is to prepare thin films with large area by cost effective techniques and their characterization with regard to optical and electrical properties. Generally, the properties of semiconductors are sensitive to the presence of lattice defects and impurities. Ion implantation forms an ideal technique for the introduction of defects and impurities in a controlled manner. The present thesis aims at investigating the irradiation effects in a typical II-VI semiconductor viz., CdS. A detailed review of the literature available on the preparation and characterization of CdS thin films is given below.

CdS finds extensive applications in the area of photovoltaic devices [8] and laser devices [11] and non-linear integrated optical devices [12]. As prepared, CdS is normally n type with a typical carrier concentration in the range of 10^{15} to 10^{17} ions/cm^2 and has a mobility of 300 cm^2/V-sec. CdS is a direct band gap material having an optical band gap of 2.42 eV. It is frequently used as a window layer in a variety of thin film solar cells, because of its wide bandgap and the ease of fabrication. The basic requirements of the films for these applications are high optical transparency, low electrical resistivity and better crystallinity for the films deposited at room temperature. Thin film photovoltaic solar cells based on CdS have received considerable attention due to economic reasons and ease of fabrication of large-area thin film devices.

CdS thin films have been grown by a variety of techniques such as thermal evaporation [13] , sputtering [14], flash evaporation [15] and chemical bath deposition(CBD) [16]. The chemical bath deposition method was introduced by Mokrushin *et al* [17] and Kiatev *et al* [18]. Among the various techniques mentioned above, the chemical bath deposition is a low cost process and is suitable for preparing large area thin films. It is possible to obtain uniform films with good adherence and reproducibility by this technique. The films can be deposited at low temperatures with uniform stoichiometry. The bath used for the preparation of CdS thin films consists of a suitable cadmium salt such as cadmium sulphate, cadmium chloride, cadmium nitrate or cadmium acetate for providing cadmium ions and thiourea for obtaining sulphur ions. The bath is maintained alkaline, by adding ammonia and bath temperature is

normally maintained at about 333 K. Triethanolamine is used as a complexing agent. The growth of CdS thin films by the chemical bath method occurs either by (i) an ion by ion condensation of Cd^{2+} and S^{2-} ions on the surface of the substrate or by the adsorption of colloidal particles of CdS onto the substrate [19]. The growth process has been discussed in detail by Kaur *et al* [20].

CdS exists in two different structural modifications, namely stable hexagonal wurtzite phase and the metastable cubic sphalerite phase [21, 22]. The CdS thin films prepared by chemical bath deposition are normally found to be either in the metastable cubic phase or as a mixture of cubic and hexagonal phases [23].

Hernandez *et al* [24] reported the thermal annealing studies of CdS thin films prepared by chemical bath deposition, where they studied the optical and electrical properties of the film before and after annealing in different atmospheres. They found that the absorption edge shifts towards the higher wavelengths in CdS films, which was attributed to the structural transformation from cubic to hexagonal phase. They studied the bandgap shift using photoacoustic spectroscopy and the XRD measurements were carried out to confirm the phase transformation.

Jayakrishnan *et al* [25] have reported the study of structural changes and physical properties of CdS thin films after multiple dip coating and rapid thermal annealing using XRD, scanning electron microscopy (SEM) and electrical characterization. Rapid thermal annealing at $5x10^{-2}$ torr resulted in the reduction in the resistivity of films from 10^6 ohm cm to 0.16 ohm cm, where as slow annealing for 30 minutes at the same vacuum resulted in a resistivity of 10^5 ohm cm. The observed reduction in resistivity upon annealing was attributed to the oxygen desorption. Kolhe *et al* [26] investigated air annealing of dip coated CdS films using XPS.

The effect of post-deposition treatments on morphology, structure and opto-electronic properties of chemically deposited films of CdS was discussed by Sebastian *et al* [27]. They found

that good quality films can be obtained by choosing Cd:TEA:NH_3:TU mole ratio of about 1:3.75:14.4:1 for the opto-electronic applications. They reported that the as-deposited films contained some organo-metallic impurities on the surface, which can be removed by etching of the film surface in very dilute acetic acid.

Tomas *et al* [28] studied the influence of thermal annealing in different atmospheres on the band-gap shift and resistivity of CdS thin films prepared by chemical bath deposition technique. It was found that the resistivity of the film has reduced from 10^7 ohm cm in the as-deposited state to 0.15 ohm cm when annealed in hydrogen atmosphere. Annealing in pure hydrogen, a process that has been applied to different types of CdS films, reduces the resistivities of the film by passivating the chemisorbed oxygen at the grain boundaries.

Yu *et al* [29] characterized the CdS films prepared by solution growth technique comprising of nano particles, where they confirmed the presence of quantum size effects based on the blue shift in the optical band gap of the films. The films were found to be hexagonal with a preferred (0002) orientation. They studied the variation of the particle size with the deposition time and also correlated it with the optical band gap. The reported blue shift in the band gap (E_g) were in the range of 0.01-0.02 eV for the particle size range of 20 and 25 nm and about 0.12 eV for a particle size of 5 nm.

Kale *et al* [30] have carried out extensive characterization of the chemically deposited CdS thin films. They studied the electrical and optical properties of the films by changing the parameters like the deposition temperature and the dipping time. Depending upon conditions of the deposition, chemically deposited CdS thin films showed a blue shift as high as 0.35 eV in the optical band gap. It was found that as the deposition temperature decreases from 358 to 273 K, the band gap increases from 2.4 to 2.7 eV. They have also reported the decrease in the bandgap with increasing annealing temperature, as a result of grain growth. The grain size attains a constant value of about 8nm when the films are annealed above 673 K indicating saturation in the grain growth.

Preparation of photoconductive CdS thin films by chemical bath deposition process was described by Pavaskar *et al* [31]. The photoconductive rise and decay transients were studied by them in the temperature range of 130 - 310 K with the view of identifying the nature of the traps and to determine the trap levels. Bhushan et al [32] have carried out photoconductivity measurements of Y doped CdS thin films. They showed that the ratio of the photocurrent to dark current is of the order of 10^5. They have investigated the structural dependence of photoconductivity in Nd and Pr doped CdS thin films, using SEM, XRD and absorption measurements.

Nair *et al* [33] studied the conversion of chemical bath deposited photosensitive CdS thin films to more n-type by air annealing and ion exchange reaction. They also reported both the dark and photoconductivity measurements of the annealed films. Annealing in air at 673 - 773 K converted the films to more n type. XRD and X-ray photoelectron spectroscopic depth profile studies of the films showed that the modification of the electrical characteristics is brought about by changes in composition of the surface layers in the films.

Gupta *et al* [34] studied the dark and photoconductivity measurements of nano crystalline CdS thin films prepared by magnetron sputtering method and observed that the conduction mechanism is dominated by the combined effects of thermionic emission, tunnelling and variable range hopping. The carrier concentration and the capture cross section of the trap states were estimated to be $\sim 10^6$ cm^{-3} and $\sim 10^{-18}$ cm^2, respectively.

CdS thin films have been prepared by spray pyrolysis and the effects of the substrate temperature on the electrical properties are discussed by Steve Pence *et al* [35]. They could observe a change in the resistivity of the films grown on the glass substrates at different substrate temperatures. Formation of low resistivity films of CdS by a chemical vapour transport(CVT) method was reported by Sanchez *et al* [36]. They reported that the extrinsic films showed an electrical conductivity of the order of 10 mho cm^{-1} and the films which showed intrinsic nature exhibited a conductivity of the order of 10^{-8} mho cm^{-1}. CdS thin films of high dark conductivity have been prepared by co-evaporation of CdS and In and the

physical properties of the films were investigated by Hayashi *et al* [37].

The wavelength dependent photoconductivity measurements in CdS films prepared by metal organic chemical vapour deposition (MOCVD) technique have been carried out and the results are discussed [38]. They studied the photocurrent behaviour with the intensity of the tungsten lamp and found a linear relation in the range 15 - 30 mW cm^{-2} and 68 - 75 mW cm^{-2} and a non-linear relation in the range 30 - 60 mW cm^{-2}, which is a characteristic feature of polycrystalline semiconductor thin films. Similar results are also reported in films of SnS and CdS [39]. The non-linear relationship between photocurrent and intensity of light may be either due to the existence of bubbles along grain boundaries or to the various recombination processes which arise due to complex traps.

Tsai *et al* [40] studied the grain size effects in CdS films prepared by RF sputtering technique. The temperature dependence of photoluminescence spectra of CdS microcrystals was investigated and the variations of the properties with average grain size and thickness of films were established. Blue shift in the peak positions of the photoluminescence spectra is found to be due to the decrease in film thickness.

Optical properties of ultrathin films of CdS prepared by electrochemical atomic layer epitaxy (ECALE) were studied by Boone and Shannon [41], in which they carried out resonance Raman spectroscopy and photoluminescence.

Raman investigations of the surface modes of the crystallites in thin film of CdS grown by pulsed laser evaporation and thermal evaporation were carried out by Chuu *et al* [42]. The quality of the films is investigated by resonance Raman scattering, X-ray diffraction and optical transmittance. Their results revealed that the Raman shifts of the surface phonon mode are observed at about 300 to 297 cm^{-1}. Raman shift is found to be sensitive to the changes in the crystallite sizes.

Zahn *et al* [43] reported that it is difficult to distinguish the Raman mode between the cubic and hexagonal phase of CdS as it appears at the same wavenumber. Angel *et al* [44] have

studied the Raman scattering in CdS thin films in a wide range from 0 to 1600 cm^{-1}, where they could show the multiple series of longitudinal optical (LO) modes of CdS. The analysis of Raman spectra of CdS thin films annealed in argon and sulphur atmosphere revealed that the transverse optical (TO) mode appear around 228 cm^{-1} at a temperature of 623 K.

Photoconduction, i.e., increase in conductivity due to irradiation of a semiconductor with light, is a non-equilibrium process. Photoconductivity has played a major role in the development and understanding of physics of the solid state [45, 46]. Concurrent with the basic studies of photo conductivity is the successful application of the phenomenon for a wide range of technologies and development of devices. Photoconductivity can arise due to irradiation of the semiconductor material with ultra violet, visible or infra-red source. Many non-metallic elements also exhibit photoconductivity. Some of the materials exhibiting photoconductivity include B, C, S, Ge, As; selenides, tellurides, sulfides of cadmium and zinc; many oxides like CuO, ZnO, MgO and other semiconductor compounds such as InSb, GaAs, CdS, CdTe.

Persistent photoconductivity or prolonged photoconductivity (PPC), an interesting phenomenon in semiconductors is the occurrence of photoconductivity that persists for a long period of time after the termination of the source of photoexcitation. Discovery of the room temperature PPC phenomena makes the PPC based devices feasible. It provides a non-destructive method to probe the profile of impurities in semiconductors. Hence, study of persistent photoconductivity is interesting both from the point of basic physics as well as technological applications. PPC phenomenon observed in a variety of semiconductors such as III-V and II-VI semiconductor compounds has been investigated by various researchers [47, 48, 49, 50, 51, 52]. Technologically, understanding of optical and transport properties of II-VI semiconductor thin films is also of importance for optoelectronic applications. Various models have been suggested to describe the persistent photoconductivity in semiconductors and each model has to be studied thoroughly for clear understanding and they are discussed in detail in the fifth chapter. The understanding of PPC phenomena provides insight into

the basic physical processes in semiconductors such as charge carrier excitation, storage and relaxation and they are explained with suitable examples below.

Some of the possible mechanisms of PPC are (1) random local potential fluctuations due to compositional variations (2) presence of shallow and deep levels in the bandgap region and (3) large lattice relaxation process associated with deep donor levels which are often called DX centers. PPC can be used to study common features of defects, which help us to understand the origin of defects and their properties.

It has been generally concluded that the formation of p-type CdS is very difficult because of self-compensation effects due to sulphur vacancies [53]. A few authors have reported attempts to form p-type CdS crystals by compensation of donors with copper acceptors [54, 55]. Various researchers [56, 57, 58] have tried to dope impurities by ion implantation technique to form p-type CdS and they are discussed in one of the forthcoming sections where the irradiation effects in CdS thin films are dealt with. Keitoku *et al* [59] have reported the conversion to p-type of CdS films prepared by laser ablation method. They doped copper atoms onto CdS thin film and studied the resistivity characteristics. They found that initially, the resistivity increases with increase in the concentration of copper in the target followed by a decrease at about 5 atomic percent copper content. The conduction type is also found to change from n to p-type at around the same concentration level of copper.

Fabrication of thin film p-CdS(Cu)/n-CdSe heterojunctions and their photovoltaic characteristics have been studied by Kashiwaba *et al* [60]. The electrical characteristics of copper doped p-type CdS thin films have been investigated by Kashiwaba *et al* [61]. CdS was deposited on a Cu film at about 475 K facilitating the diffusion of copper. The resistivity of the films increased with increase in Cu doping but decreased for values of the Cu/Cd atomic ratio over 0.5%. The Seebeck coefficients changed from negative to positive with increasing Cu doping. The I-V characteristics of a cell with a CdS (Cu-doped)/CdS(non doped) structure showed rectification. It is proposed that Cu compensates the donors due to sulphur

vacancies and the conductivity type of the films is converted to p-type [61].

Sebastian [62] reported the formation of p-type CdS films by in-situ copper doping in the chemical bath. It was found that the copper doped films showed amorphous nature and exhibited high electrical conductivity as compared to the undoped films. It was also found that the copper doping influenced the structure and the photoresponse, electrical and optical properties of the films. Varkey and Vijayakumar [63] reported the fabrication of homojunction using spray pyrolysed CdS thin films by copper diffusion. In their study, they prepared copper films by thermal evaporation technique where as film of CdS was coated using the spray pyrolysis process. The next section briefly discusses ion implantation, a process used for doping of semiconductors.

1.2 Ion implantation

As discussed earlier, ion implantation introduces considerable lattice disorder, which has a significant influence on the electrical and optical properties of the semiconductors. The defects produced during irradiation are normally annealed out by suitable thermal treatments. Though radiation damage is often considered as an undesirable consequence of ion implantation process, there are situations where defects are deliberately introduced into semiconductors. This technique is known as defect engineering. This section discusses the irradiation effects in semiconductors.

Ion implantation is a technique used to introduce impurities into solids in a uniform and reliable manner [1]. The technique makes use of ions with energy in the range of keV to a few MeV, which bombard the target. The ions slow down due to the interaction with the solid target and finally comes to rest at a depth normally referred to as the range. The concentration and depth of penetration of the implanted impurities can be controlled by controlling the ion current, time of implantation and beam energy. Being a non equilibrium process, there are no solubility constraints and any type of atoms can be implanted in any

target. The technique is primarily used in semiconductor technology, though it also finds applications in several other areas like surface modification for improvement of hardness, wear and corrosion resistance etc. Ion implantation is generally carried out using beam from the low energy accelerators. The typical set up for ion implantation is described in chapter II.

There exists another technique of ion implantation called plasma ion implantation, wherein the sample is immersed in a low pressure plasma of the desired implant species. A negative potential is applied to the target. The ions in the plasma get accelerated towards the target and get implanted. This technique has several advantages over the ion implantation using the accelerators. The need for beam scanning and target manipulation required for uniform implantation of complex targets does not exist. However, in plasma ion implantation, the achievable ion energies are often low (100 keV) where as in Linear Ion Beam Implantation (LIBI) using accelerators, one can easily go up to a few MeV. Further there is no control over ion species or charge states in the case of plasma ion implantation as one does not make use of mass analysis. Figure 1.1 schematically illustrates the two processes. Plasma ion implantation is generally used for surface modification in order to reduce wear and corrosion, where as linear ion implantation is more suitable for semiconductor doping and device fabrication. The next few subsections deal with the basics of penetration of energetic ions in solids and describe how the incident ions lose energy in the solid resulting in irradiation damage of the substrate. The final distribution of ions in the solid and the defect production are explained.

1.2.1 Energy loss

As an ion penetrates a solid, it loses its energy by inelastic electronic excitations as well as by elastic collisions with the target atoms. The former process is referred to as the electronic energy loss and the latter process is known as nuclear stopping. At high energies, electronic energy loss dominates whereas nuclear stopping becomes predominant as the ion slows down.

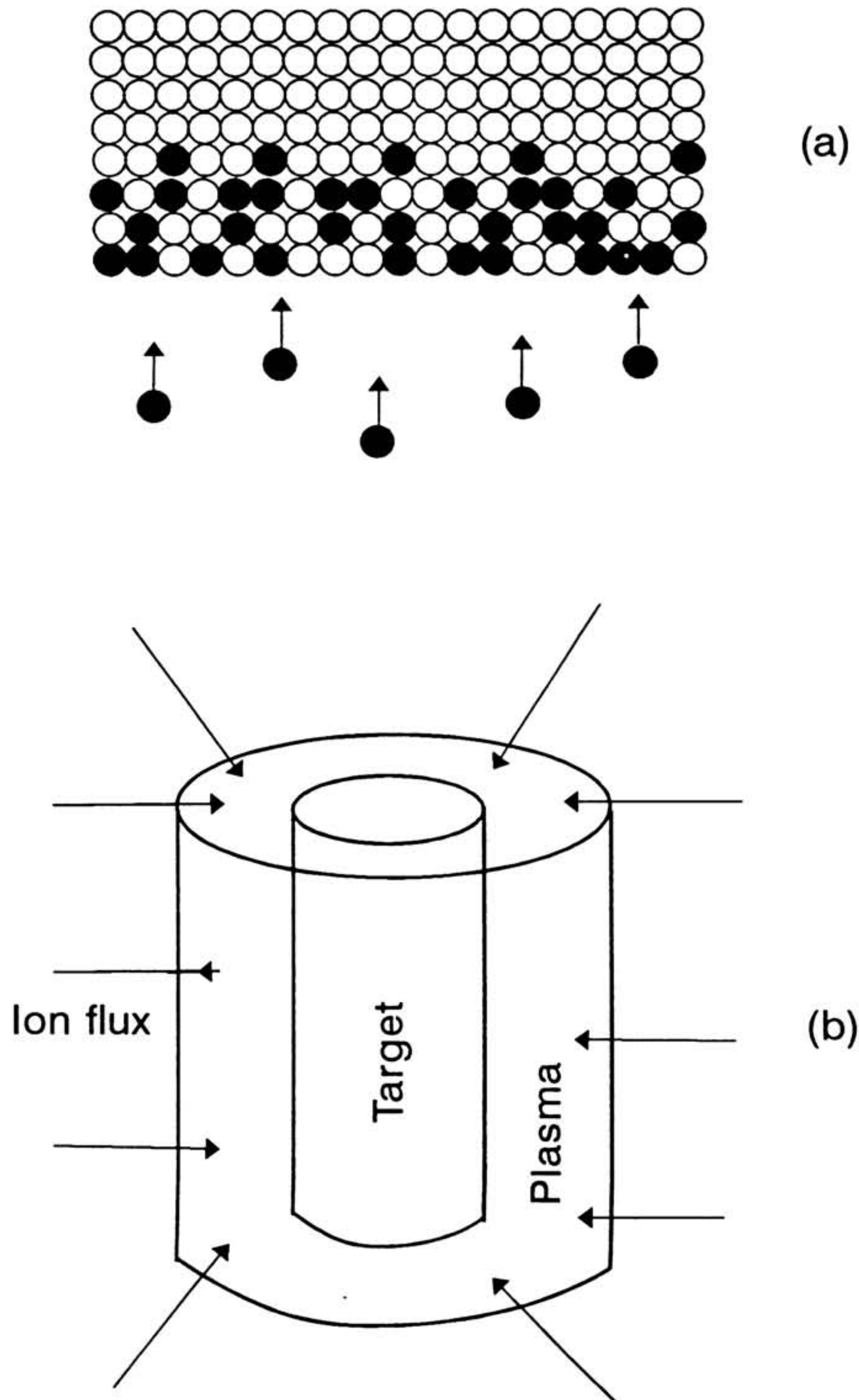

Figure 1.1: Schematic representation of the implantation processes, (a) LIBI and (b) Plasma Ion Implantation

The nuclear stopping arises out of the elastic collisions with the atoms as a whole. The total energy loss is a combination from both the process. The total stopping power is given as

$$\frac{dE}{dx} = \left(\frac{dE}{dx}\right)_e + \left(\frac{dE}{dx}\right)_n \tag{1}$$

Figure 1.2 shows the electronic stopping power and nuclear stopping power as a function of energy of the incident ions. The first unified approach to stopping and the range theory was made by Lindhard, Scharff and Schioff [64] and their approach is generally referred to as LSS theory. For practical calculations, the universal nuclear stopping is given by

$$S_n(E_o) = \frac{8.462 \times 10^{-15} Z_1 Z_2 M_1 S_n(\epsilon)}{(M_1 + M_2)(Z_1^{0.23} + (Z_2^{0.23})} \; eV/(\text{atom/cm}^2) \tag{2}$$

where ϵ is the reduced energy, Z_1 and Z_2 are the atomic number of the ion and the target atom respectively, M_1 and M_2 are the masses of the projectile and target atom, ($S_n(\epsilon)$ is given by $\ln(\epsilon)/2(\epsilon)$) where ($\epsilon$) is the reduced energy introduced by Lindhard *et al* given by

$$\epsilon = E\frac{aM_2}{Z_1 Z_2 e^2 (M_1 + M_2)} \tag{3}$$

where $a = 0.0885 a_0 (Z_1^{1/2} + Z_2^{1/2})^{-2/3}$, a_0 is the Bohr radius. Lindhard, Scharff and Schiott have given the electronic energy loss as

$$-(d\epsilon/d\rho)_e = K\epsilon^{1/2} \tag{4}$$

$$K = Z_1^{1/6} \frac{0.0793 Z_1^{1/2} Z_2^{1/2} (M_1 + M_2)^{3/2}}{(Z_1^{2/3} + Z_2^{2/3})^{3/4} M_1^{3/2} M_2^{1/2}} \tag{5}$$

where ρ is the reduced range, given by

$$\rho = RNM_2 \frac{4\pi a^2 M_1}{(M_1 + M_2)^2} \tag{6}$$

where R is the range and N is the number of atoms per unit volume.

1.2.2 Range of incident ions

The range of an ion is determined by the rate at which it loses energy. The energy loss process being statistical in nature, there is a distribution around the mean range. For non crystalline

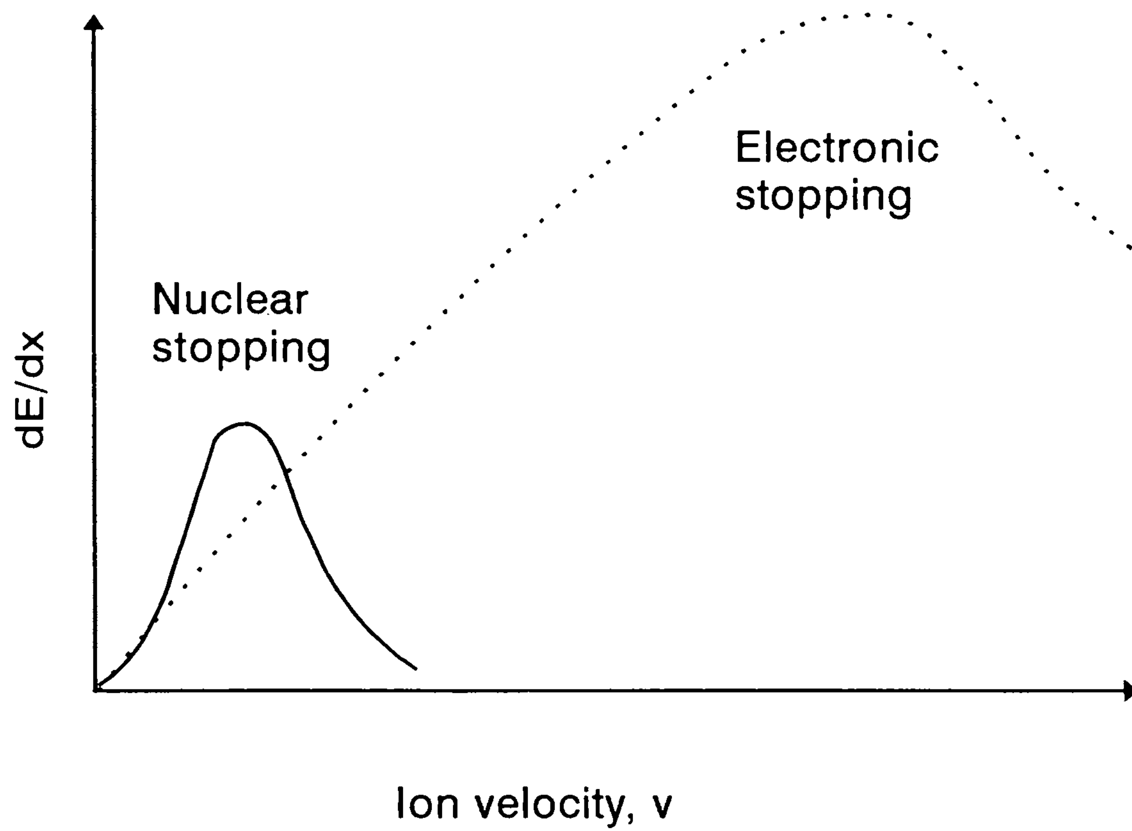

Figure 1.2: Variation of the electronic and nuclear stopping power as a function of energy of incident ions.

or amorphous materials implanted ions have a Gaussian distribution, but in single crystals it becomes more complicated because of channeling effects. There are several computer codes available for calculating the range and range straggling of ions and the most popular among them being the TRIM [65] code(Transport of ions in matter). The implantation and vacancy profile of 80 keV Ar^+ ions in CdS calculated using TRIM code is presented in the first section of the fourth chapter.

1.2.3 Radiation damage

Energy is transferred from the projectiles to target atoms and consequently, they slow down. An atom receiving sufficient kinetic energy (higher than displacement energy which is approximately equal to 20 eV) gets displaced from its lattice site. The recoiling target atom itself may be sufficiently energetic to cause further displacements resulting in a cascade of displacement collisions. The displacement damage produced during implantation consists of various types of lattice defects. A target atom which is displaced from its normal site leaves behind a vacant site which is referred to as a vacancy. The displaced atom might come to rest at interstitial positions giving rise to the formation of an interstitial. In ordered materials, the lattice displacements give rise to the reduction of the chemical order parameter, eventually leading to disorder. The process is called radiation induced disordering. Atoms could occupy sites of the wrong sublattices during irradiation giving rise to antisite defects. When large amount of energy is transferred to the lattice atom, 'collision cascades' are formed, which comprise of a vacancy rich core and an outer shell rich in interstitials . The various defects which are produced during implantation are schematically illustrated in figure1.3.

The defects produced often lead to formation of defect clusters such as vacancy and interstitial loops, which are essentially two dimensional clusters of vacancies and interstitials respectively. Three dimensional vacancy clusters also form and are referred to as voids. The defect production peaks close to the peak of the implantation profile. The defect production profile can also be evaluated by TRIM code.

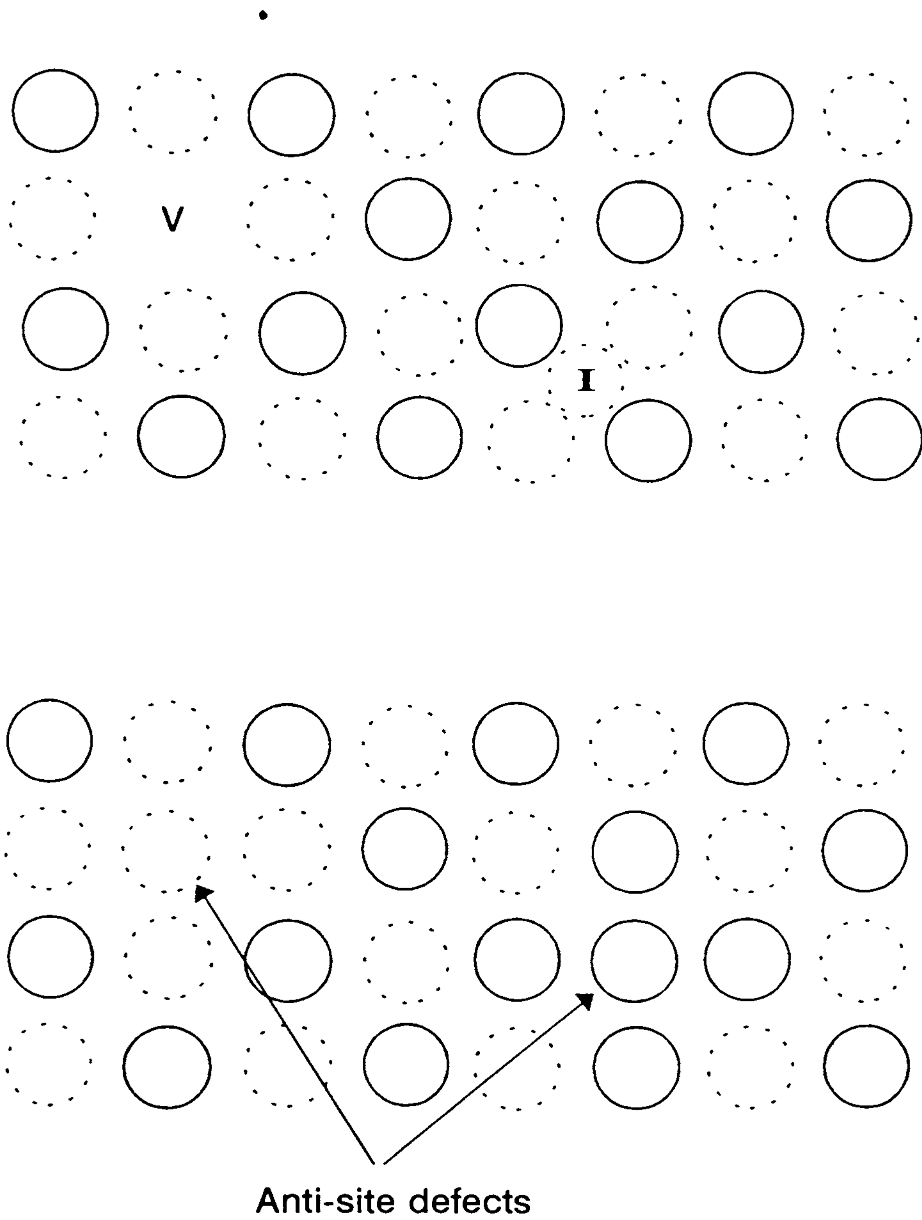

Figure 1.3: A schematic representation of various defects produced during implantation. (a) Vacancy (V) and Interstitial (I). (b) Antisite defects.

The radiation damage produced during implantation has a strong influence in the properties of the material. Significant changes in the optical and electrical properties occur on account of radiation damage. Increased optical absorption and shift of the absorption edge to lower energies and reduction in the sharpness of the absorption edge are normally observed during irradiation with energetic ions which are caused by the lattice damage. The resistivity, carrier concentration, the mobility and the type of the carriers are influenced by the implantation induced damage. In materials like ZnSe, CdS and $CuInSe_2$, ion implantation is carried out to convert the carrier type form n to p-type or vice-versa. Radiation damage is an inevitable outcome of ion implantation and may mask the desired doping effects. Post implantation annealing is resorted to, in order to remove the defects produced during implantation. The annealing involves rising the temperature of the material in order to provide thermal energy to assist the recovery of the damaged material.

1.3 Irradiation effects in semiconductors

The most widespread application of ion implantation is doping of semiconductor wafers during planar device fabrication. Irradiation causes a major change in the atomic and electronic environment, which in turn leads to change in the properties of the system. Since defects produced during implantation influence the electrical and optical properties of the system, it is important to understand the mechanism for such a change. Electrically active or inactive species can be implanted into semiconductors and the consequent changes in the properties caused by electrical activation and introduction of disorder can be studied.

Various techniques such as optical absorption spectrometry, Raman scattering spectroscopy, positron annihilation spectroscopy, the resistivity measurements and photoconductivity measurements are used to probe the implantation induced changes in semiconductors.

A detailed study of the implantation-induced damage in Si was carried out by optical absorption measurements, extending from energies above the band gap down to energies far

into the subgap regions, by Zammit *et al* [66, 67] . The changes in the optical bandgap, band-edge slopes and in the subgap features of the spectra were described. The various stages of formation and quenching of divacancies were monitored as a function of implantation conditions and annealing cycles. It was reported that the divacancies strongly affect the population of band-tail states. The annealing studies revealed that the progressive quenching of the divacancy band was followed by the appearance of another absorption band, characteristic of some intrinsic secondary defects. The studies of the structural relaxation process in implanted a-Si suggested that the process was indeed associated with annihilation of defects as well as reduction of the average strain in the material. Since the presence of defects and irradiation induced disorder significantly affect the optical properties, optical absorption spectrometry is an ideal technique for investigating the effect of irradiation in semiconductor thin films. Optical absorption studies have also been reported on ion implanted GaAs [68], and InP [69].

Several studies in the past [70, 71] have shown that Raman scattering is a very sensitive technique for studying the lattice damage produced during implantation since the thickness of the damaged layer and the optical skin depth are essentially of the same order. Raman scattering can give information regarding defects and disorder produced during irradiation. Additionally, it also has the unique advantage of using different wavelengths for incident light, thereby probing different depths of the implanted sample.

Kim *et al* [72] studied the recovery process in Ga ion implanted GaSb using the Raman scattering spectroscopy, where they found the Raman intensity of the Ga-Sb phonon mode decreases with increasing ion implantation fluence. They also carried out measurements in the samples subjected to post implantation annealing, where they found the presence of new modes which are related to Sb-Sb bond vibrations. Deneuville *et al* [73] investigated the oxygen implanted and subsequently annealed ZnSe films using the Raman measurements, in which they probed the irradiation induced damage and its recovery on annealing. Various researchers have reported the Raman measurements of irradiation induced effects in graphite

[74]. Amorphization processes in ion implanted Si was studied by Raman scattering method where it was found that the intensity of the peak at 520 cm^{-1} corresponding to crystalline Si decreased, broadened and shifted towards lower wavenumbers as the irradiation dose was increased [75].

Positron annihilation spectroscopy(PAS) is another powerful tool for a detailed characterization of defects because the presence of open volume defects could be detected in the concentration range starting from 0.1 appm to 100 appm. Variable low energy positron beams [76] could be used to study defect distribution as a function of the depth in the sample, thereby enabling the characterization of thin film structures. The technique is non destructive, because of low flux of slow positrons, coupled to the fact that positron is selective and sensitive to the presence of certain types of defects. This technique is therefore very useful in the study of semiconductor thin film layers.

Vacancy type defects produced by implantation of self ions in the energy range of MeV in Si at room temperature have been probed using depth-resolved positron annihilation spectroscopy by Nielsen *et al* [77]. It was found that the defect concentration increases linearly with dose. Measurements of line shape parameter 'S' as a function of isochronal annealing temperature for various implanted samples were carried out and the results are discussed. The positron beam studies of irradiated Si are discussed by Asoka-Kumar et al [78] and Amarendra *et al* [79].

It is well known that ion implantation causes change in the electrical properties of the system mainly due to the changes in the carrier concentration and the type conversion. Considerable literature exists on the type conversion mechanisms in different materials upon irradiation. Kohiki *et al* [80] investigated the nitrogen implantation effects in molecular beam deposited $CuIn\ Se_2$ thin films. They carried out electrical measurements in $CuIn\ Se_2$ films after nitrogen implantation to a dose of 10^{17} ions/cm^2, with an accelerating voltage of 10 kV. The films changed from n to p type, when the substrate temperature was below 515 K during implantation. The resistivity of the samples implanted and subsequently annealed

at different temperatures is reported. It was found that both the conduction type and the resistivity of the films could be changed by nitrogen implantation. Rectifying p-n junctions have been fabricated in single crystals of $CuInSe_2$ by diffusion of copper at relatively low temperatures [81].

1.4 Irradiation effects in Cadmium Sulphide

Studies of radiation effects in II-VI compound semiconductors are important in connection with the extensive applications of these compounds. Ion implantation in CdS thin films with energetic particles causes lattice damage which affects the electrical and optical properties. Ion implantation helps in converting the type of carriers responsible for the conduction phenomenon, thereby fabrication of homojunctions with CdS becomes practical and useful. Various attempts are made to form p type CdS by different routes. Ion implantation is found to be a straight forward technique to dope impurities into the material which can convert the conductivity from n to p type. Irradiation effects in CdS and attempts to make homojunction CdS are discussed below.

Lattice disorder produced by ion implantation of CdS crystals with Bi^+, Kr^+, Ar^+ and Ne^+ has been studied using RBS/Channeling and Transmission electron microscopy(TEM) by Parikh *et al* [82]. Channeling measurements of the lattice damage were carried out along both c and a axis. It was found that the damage is primarily in the form of interstitial type dislocation loops which predominately lie with a Burgers vector parallel to the a-axis. It was found that channeling measurements are consistent with the TEM observations. Amorphization was not observed during the irradiation which was confirmed by both the techniques.

Ratna sagar and Srivastava [83] studied the amorphization of thin films of CdS due to argon ion irradiation in dense plasma focus. Govind and Fraikor [84] studied the structural characteristics of CdS single crystal platelets after Bi-ion implantation with the help of

transmission electron microscopy. They reported that the ion implanted CdS does not exhibit gross degradation of the wurtzite structure to amorphous zones.

Attempts to produce p type layers in CdS by conventional doping techniques have generally been unsuccessful due to self-compensation effects [53]. Ion implantation is potentially attractive as an alternate doping technique and p type layers have been successfully formed by implanting phosphorous, arsenic, nitrogen and bismuth in CdS [56, 57, 58]. In some cases, no post-implantation annealing was required, whilst in others, annealing upto 770 K were carried out. Implantation of high energy phosphorous ion in CdS film followed by annealing,has given rise to conversion of conductivity type [85]. Thermal probe measurements were carried out on the implanted films which showed p type conductivity on the implanted surface. Diodes fabricated from implanted material showed good rectification characteristics, low voltage electroluminescence and double-injection phenomena at room temperature.

Tell and Gibson [86] implanted bismuth and xenon ions into CdS to a dose of 10^{15} ions/cm^2 and studied various properties including optical absorption, photoluminescence and photovoltage. They found that the bismuth implanted films are visibly discoloured and they could observe an increase in the absorption at room temperature. The wide bandgap II-IV semiconductors have been investigated in great detail using ion implantation technique. Annealing behaviour of the insulating layer in ion implanted CdS was investigated by Masafumi Yamaguchi [87], where he observed that the ion implanted CdS diodes showed increase in resistivity and become photosensitive after annealing above 673 K. Increase in the irradiation dose causes expansion of photoconductive region, which shows the production of various deep centres in CdS. It is reported that origin of the insulating layer is Cd vacancy, produced during ion implantation.

Chester [88] reported conductivity changes in CdS after irradiation with Co and Cs gamma rays at room temperature, which introduced donors and acceptors respectively. The radiation induced changes in electrical conductivity produced by fast neutrons at room temperature [89] and by 5 MeV electrons near 77 K were found to depend strongly on the initial carrier

concentration. Kitagawa and Yoshida [90] studied defect recovery in CdS crystals irradiated with 10 MeV electrons at 77 K and observed at least three stages of recovery between 80 and 410 K. Kittagawa and Bryant [91] reported the low temperature annealing of 200 keV electron induced defects in CdS. The carrier was found to increase by electron irradiation at a temperature near 20 K. During annealing there appeared a small reverse recovery around 20 K and a major normal recovery over a subsequent wide temperature range.

1.5 Scope of the thesis

The main aim of the present thesis is to study the effect of implantation induced damage in CdS thin films prepared by chemical bath deposition. The preparation of the films, the implantation procedure and the investigations of the implanted samples using various techniques such as electrical resistivity and photoconductivity measurements, optical absorption, Raman scattering studies and positron annihilation are discussed in detail. Some of the important observations are the conversion of n type CdS films to p type on N^+ implantation, systematic reduction in the optical bandgap and the bandedge sharpness due to implantation induced lattice disorder and persistent photoconductivity after N^+ ion implantation.

1.6 Organization of the thesis

Chapter I is an introductory chapter to the material, CdS, studied in the present investigation and to the ion implantation technique used in the present work. It also deals with the irradiation effects in semiconductors with special reference to the work carried out in CdS.

Chapter II gives a brief account of the various experimental techniques used in the present investigation. The techniques include X-ray diffraction, positron annihilation spectroscopy, Raman scattering spectroscopy, resistivity measurements and optical absorption spectrometry. The salient features of the low energy accelerator used for the implantation experiments in the present investigations are also discussed.

Chapter III deals with the preparation and characterization of CdS thin films by vacuum evaporation and chemical bath deposition method. The results of X-ray diffraction, optical absorption spectrometry and resistivity studies are discussed. Investigations of the films prepared by chemical bath deposition method reveal that on annealing, bandgap reduces and there is a phase transformation from mixed cubic-hexagonal to hexagonal phase.

Chapter IV deals with the effect of argon ion implantation in CdS thin films. Argon ion implantation effects on the films prepared by chemical bath deposition were studied using different techniques like optical absorption, X-ray diffraction, Raman spectroscopy and positron annihilation spectroscopy. Some of the salient features discussed in detail include the reduction in the optical bandgap due to implantation, variation in the intensity of the Raman peak during irradiation and post irradiation annealing , positron beam studies on irradiated CdS films etc. Raman scattering studies of the argon irradiated CdS thin films prepared by vacuum evaporation method are also discussed briefly.

Chapter V deals with the effect of nitrogen and oxygen ion implantation in CdS thin films. The electrical characterization of the nitrogen irradiated films is discussed in this chapter. The photoconductivity measurements of the nitrogen implanted CdS films prepared by CBD process are discussed in detail. Persistent photoconductivity measurements on the nitrogen ion irradiated CdS thin films prepared by chemical bath deposited films are reported for the first time. Raman scattering studies of the oxygen implanted CdS thin films prepared by vacuum evaporation method are discussed in brief. Structural investigations of the as-deposited and oxygen irradiated thin films of CdS are reported. Raman scattering studies on the oxygen ion implanted CdS thin films prepared by vacuum evaporation method are also presented in the chapter.

Chapter VI summarises the results of the systematic investigations carried out on CdS thin films and also discusses the future plan of the research in this area.

References

[1] Ion implantation in Semiconductors, J. W. Mayer, L. Eriksson and J. A. Davies, (1970) Academic Press

[2] Defects and Radiation damage in Metals, M. W. Thompson, Cambridge University Press, (1969)

[3] Application of Ion beams to Metals, S. T. Picraux, E. P. Eer Nisse and F. L. Vook (Eds), Plenum Press, (1974)

[4] Ion implantation in Semiconductors, Proceedings of US-Japan Seminar, Japan Soc. for promotion of Science, Kyoto. , S. Namba (Ed.) (1971)

[5] F.F. Morehead, Jr. and B.L.Crowder, Proceedings of the 1st International Conference on Ion Implantation, edited by L.T. Chadderton and F.H. Eisen (Gordon and Breach, New York, 1971),p 25

[6] W. Wesch, E, Wilk, and K. Hehl, Phys. Stat. Sol.(a), 70 (1982) 243

[7] Solar Materials Science, L.E. Murr, Academic Press, London, 1980

[8] S. Wagner, J. L. Shay, K. J. Bachman and E. Buehler, Appl. Phys. Lett., 26 (1975) 229

[9] J. L. Shay, S. Wagner and H. M. Kasper, Appl. Phys. Lett., 27 (1975) 89

[10] R. R. Arya, P. M. Sarro and J. J. Loferski, Appl. Phys. Lett., 41 (1982) 355

[11] V. Daneu, D.P. DeGloria, A. Sanchez, F. Tong, and R.M. Osgood, J. Appl. Phys. Lett., 49 (1986) 546

[12] M. Dagenais and W.F. Sharfin, Appl. Phys. Lett., 46 (1985) 230

[13] N. Romeo, G. Sberveglieri, and L. Tarricone, Thin Solid Films, 43 (1977) L15

[14] I. Martil, G. Gonzalez-Diaz, F. Sanchez-Quesada, and M. Rodriguez-Vidal, Thin Solid Films, 90 (1982) 253

[15] V. Canevari, N. Romeo, G. Sberveglieri, S. Azzi, A. Tosi, M. Curti, and L. Zanotti, J. Cac. Sci. Techol. A, 2 (1984) 9

[16] R. Jayakrishnan, J.P. Nair, B.A. Kuruvilla, S.K. Kulkani, and R.K. Pandey, J. Mater. Sc: Materials in Electronics, 7 (1996) 193

[17] S.G. Mokrushin, and Y.D. Tkachev, Colloid. J. USSR, 23 (1961) 336

[18] G.A. Kitaev, A.A. Uritskaya and S.G. Mokrushin, Russ. J. Physic. Chem., 39 (1965) 1101

[19] W.J. Danaher, L.E. Lyons and G.C. Morris, Sol. Energy Mater., 12 (1985) 137

[20] I. Kaur, D.K. Pandya and K.L. Chopra, J. Electrochem. Soc., 127 (1980) 943

[21] R. L. Call, N. K. Jaber, K. Seshan and J. R. White, Jr. Sol. Energy. Mater., 2 (1980) 27

[22] M. Nagao and S. Watanabe, Jpn. J. Appl. Phys., 7 (1968) 684

[23] A. Mondal, T.K. Chaudhuri, and P. Pramanik, Sol. Energy. Mater., 7 (1983) 431

[24] L. Hernandez, O. de Melo, O. Zelaya-Angel, and R. Lozada-Morales, J. Electrochem. Soc., 141 (1994) 3238

[25] R. Jayakrishnan, S.R. Kumar and R.K. Pandey, Semicond. Sci. Techol., 9 (1994) 97

[26] S. Kolhe, S.K. Kulkarni and A.S. Nigavekar, Solar Energy Mater., 10 (1984) 47

[27] P.J. Sebastian, J.Campos and P.K. Nair, Thin Solid Films, 227 (1993) 190

[28] S.A. Tomas, O. Vigil, J.J. Alvarado-Gil, R. Lozada-Morales, O.Zelaya-Angel, H. Vargas and A. Ferreira da Silva, J. Appl. Phys., 78 (1995) 2204

[29] Il Yu, Tetsuhiko Isobe and Mamoru Senna, Materials Research Bulletin, 30 (1995) 975

[30] S.S. Kale, U.S. Jadhav and C.D. Lokhande, Ind. J. of Pure & Appl. Phys., 34 (1996) 324

[31] N.R. Pavaskar, C.A. Menezes, and A.P.B. Sinha, J. Electrochem. Soc., 124 (1977) 743

[32] S. Bhushan and S.K. Sharma, Appl. Phys. Lett., 57 (1990) 884

[33] M.T.S. Nair, P.K. Nair, R.A. Zingaro and A. Meyers, J. Appl. Phys, 75 (1994) 1557

[34] P. Gupta, R. Pal, D. Battacharya, S. Chaudhuri, and A.K. Pal, Phys. stat. Sol (a) 148 (1995) 459

[35] Steve Pence, Elizabeth Varner, Clayton W. Bates Jr., Materials Letters 23 (1995) 13

[36] A. Sanchez, P. Sebastian and O. Gomez-Daza, Semicon. Sci. Technol., 9 (1994) 1

[37] Toshiya Hayashi, Takehiro Nishikura, Tatsuro Suzuki, and Yoshinori Ema, J. Appl. Phys., 64 (1988) 3542

[38] M.A. Eluruja, A.V. Adedeji, S.O.Azi, O.O. Okulaja, O.K. Osuntola, I.A. Ojo and O.B. Ajayi, J. Mater. Sci. Lett., 14 (1995) 1158

[39] Z. Paroda and Schabowska, Vacuum, 33 (1982) 179

[40] C.T. Tsai, D.S. Chuu, G.L. Chen, and S.L.Yang, J. Appl. Phys., 79 (1996) 9105

[41] B. Edward Boone and Curtis Shannon, J. Phys. Chem., 100 (1996) 9480

[42] D.S. Chuu, C.M. Dai, W.F. Hsieh and T. Tsai, J. Appl. Phys., 69 (1991) 8402

[43] D.R. T. Zahn, C. Maierhofer, A. Winter, M. Reckzugel, R.Srama, A. Thomas, K. Horn and W. Richter, J.Vac.Sci.Technol.B, 29 (1991) 2206

[44] O. Zelaya-Angel, F.de L. Castillo-Alvarado, J. Avendano-Lopez, A. Escamilla-Esquivel, G. Contreras-Puente, R. Lozada-Morales, adn G. Torres-Delgado, Solid State Communications, 104 (1997) 161

[45] Photoelectronic properties of semiconductors, (Ed.) R. H. Bube, (Cambridge University Press, Cambridge, 1992)

[46] Concepts in photoconductivity and allied problems, A. Rose, (Wiley, NewYork/London, 1963)

[47] R. J. Nelson, Appl. Phys. Lett., 31 (1977) 351

[48] D.V. Lang and R.A. Logan, Phys. Rev. Lett., 39 (1977) 635

[49] D.V. Lang, R.A. Logan, and M. Joros, Phys. Rev. B, 19 (1979) 1015

[50] H.X. Jiang and J.Y. Lin, Phys. Rev.B, 40 (1989) 10025

[51] A.S. Dissanayake, J.Y. Lin, and H.X. Jiang, Phys. Rev. B, 48 (1993) 8145

[52] A. Zareba, A.J. Szadkowski, A. Mycielski, and B. Witkowska, Phys. Stat. Sol.(b), 193 (1996) K15

[53] Fundamentals of Solar Cells, A.L. Fahrenbruch and R.H. Bube (Academic Press, London, 1983) p. 425

[54] D.C. Reynolds, L.C. Greene, R.G. Wheeler and R.S. Hogan, Bull. Am. Phys. Soc., 1 (1956) 111

[55] J. Woods and J.A. Champion, J. Electron & Contrl, 3 (1960) 243

[56] E.R. Pollard, and J.L. Hartke, Bull. Am. Phys. Soc., 14 (1969) 115

[57] Y. Shiraki, T. Shimada, abd K.F. Komatsubara, J. Appl. Phys., 43 (1972) 710

[58] F. Chernow, G. Ruse, and L.Wahim, Appl. Phys. Lett., 12 (1968) 339

[59] S. Keitoku, H. Ezumi, H. Osono and M. Ohta, Jpn. J. Appl. Phys., 34 (1995) 138.

[60] Y. Kashiwaba, A. Tada and T. Ikeda, Jpn. J. Appl. Phys., 33 (1994) L1613

[61] Y. Kashiwaba, I. Kanno and T. Ikeda, Jpn. J. Appl. Phys., 31 (1992) 1170

[62] P.J. Sebastian, Appl. Phys. Lett., 62 (1993) 2956

[63] K.P. Varkey and K.P. Vijayakumar, Jpn. J. Appl. Phys., 36 (1997) L394

[64] Lindhard, J., Scharff, M. and Schiott, H.E., Kgl. Danske Vid. Selsk. Matt-Fys. Medd., 33 (1963) 14

[65] J.P. Biersack and L.G. Haggmark, Nucl. Instr. Methods, 174 (1980) 257

[66] U. Zammit, K.N. Madhusoodanan, M. Marinelli, F.Scudieri, R. Pizzoferrato, F. Mercuri, E. Wendler and W. Wesch, Phys.Rev.B., 49, (1994) 14322

[67] U. Zammit, K.N. Madhusoodanan, F.Scudieri, F. Mercuri, E. Wendler and W. Wesch, Phys.Rev.B., 49 (1994) 2163

[68] E. V. K. Rao, Phys. Stat. Sol.(a), 33 (1976) 683

[69] T. Pankey, J. E. Darvey, J. Appl. Phys., 41 (1970) 697

[70] P. S. Peercy, Appl. Phys. Lett., 18 (1971) 574

[71] S. Ushioda, Solid. State. Commun., 15 (1974) 149

[72] S. G. Kim, H. Asahi, M. Seta, T. Takizawa, S. Emura, R. K. Soni, S. Gonda and H. Tanoue, J. Appl. Phys., 74 (1993) 579

[73] A. Deneuville, C. H. Park, P. Ayyub, T. Anderson, P. Lowen , K. Jones and P. H. Holloway, App. Surf. Sci., 50 (1991) 308

[74] K. Nakamura and M. Kitajima, Appl. Phys. Lett, 59 (1991) 1550

[75] T. Mootoka and O. W. Holland, Appl. Phys. Lett., 61 (1992) 3005

[76] P. J. Schultz and K. G. Lynn, Rev. Mod. Phys., 60 (1988) 701.

[77] Bent Nielsen, O.W. Holland, T.C. Leung, and K.G. Lynn, J. Appl. Phys., 74 (1993) 1636

[78] P. Asoka-Kmar, K. G. Lynn and D. O. Welch, J. Appl. Phys., 76 (1994) 4935

[79] G. Amarendra, G. Venugopal Rao, K. G. M. Nair and B. Viswanathan, in Proc. Of Twelth International Conference on Positron Annihilation, Missouri, USA, May 25-31, 1997 (to appear in Mater. Sci. Forum, November 1997)

[80] S. Kohiki, M. Nishitani, T. Negami and K. Nishikura, Appl. Phys. Lett., 59 (1991) 1749

[81] R. D. Tomlinson, E. Elliot, J. Parkes and M. J. Hampshire, Appl. Phys. Lett., 26 (1975) 383

[82] N.R. Parikh, D.A. Thompson, and G.J.C. Carpenter, Radiation Effects, 98 (1986) 289

[83] Ratna Sagar and M.P. Srivastava, Phys. Lett. A, 183 (1993) 209

[84] P.K. Govind and F.J. Fraikor, J. Appl. Phys., 42 (1971) 2476

[85] W.W. Anderson and J.T. Mitchell, Appl. Phys. Letts., 12 (1968) 334

[86] B. Tell and W. M. Gibson, J. Appl. Phys., 40 (1969) 5320

[87] Masafumi Yamaguchi, Jpn. J. Appl. Phys., 15 (1976) 723

[88] R.O. Chester, J. Appl. Phys., 38 (1967) 1745.

[89] R. T. Johnson Jr., J. Appl. Phys., 39 (1968) 3517

[90] M. Kitagawa and T. Yoshida, Appl. Phys. Lett., 18 (1971) 41

[91] M. Kitagawa and F.J. Bryant, Radiation Effects, 33 (1977) 181

CHAPTER 2

2 EXPERIMENTAL TECHNIQUES

This chapter describes the experimental techniques used for the present investigations. The major theme of the present thesis is to understand the structure, electrical and optical properties of ion irradiated CdS thin films. Therefore, the experimental part involves mainly the preparation of thin films of CdS and the evaluation of various properties using analytical techniques. Since the optimization of the conditions for the preparation of CdS films is discussed in detail in Chapter III, this chapter deals with all the other experimental procedure. Ion implantations of different gaseous species were carried out on CdS thin films using a 150 kV implanter. This chapter first gives a brief description of the accelerator and later, describes the experimental techniques used as analytical tools.

2.1 Details of ion implantation

The implantations were carried out using a J-15 Sames, 150 kV accelerator. In the 150 kV accelerator, the positive ions are accelerated from the high voltage terminal, the potential of which is varied from 40 to 145 kV, to the target, which is kept at ground potential. Thus, ions of any energy between 40 to 145 keV can be implanted. A schematic of the accelerator is shown in figure 2.1.

The ion source section consists of a radio frequency ion source followed by the extraction and focus systems. A controlled gas feed of about 10-20 cc/hour into the ion source is maintained. A 100 MHz, 100 W RF power supply is capacitatively coupled to the ion source bottle to ionize the gas. Applying an extraction potential of 0 to 6 kV, the ions are extracted from the source. The beam is focussed by applying a voltage of 0 to 14 kV to the focus electrode

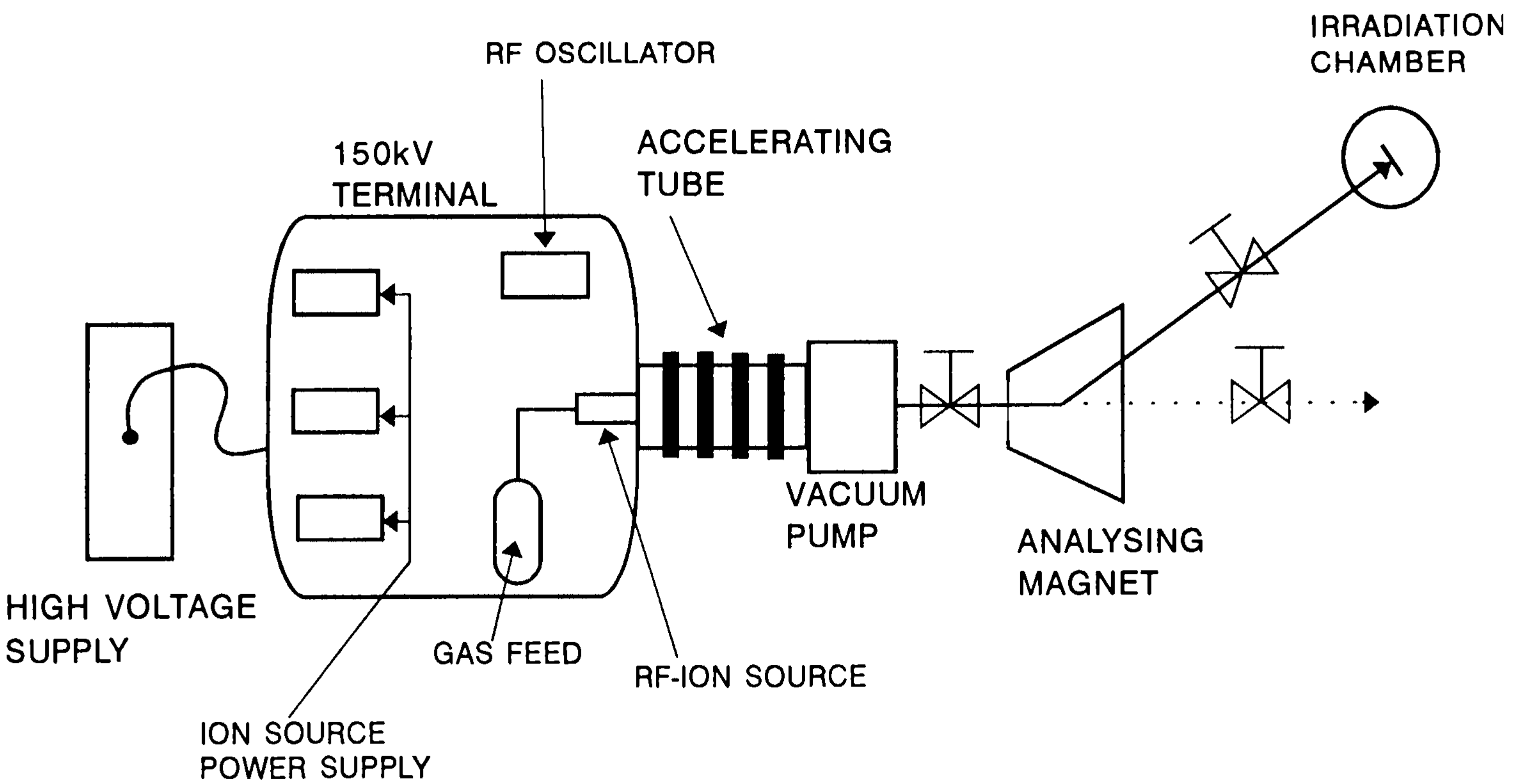

Figure 2.1: A schematic view of the 150 kV accelerator used for the irradiation experiments

at the exit of the ion source. The ion source can give intense beams of gaseous ions, typical yield being as high as 1 mA.

The ion beam is accelerated by a 10 stage accelerating tube. A vacuum of 10^{-6} mbar is maintained inside the accelerator using an oil diffusion pump (100 mm diameter). The accelerated ion beam is mass analysed using an in-house designed H shaped magnet producing a saturation field of 1.5 Tesla in the pole gap of 30 mm. Square section hollow copper conductor is used as the magnetizing coil. An in-house built 200 ampere 100 ppm stabilized power supply is used to energise the magnet coil. The mass energy product of the magnet is 15 amu·MeV. A 2 port magnet chamber is used for the ion beam transport. The 45° port is used for the analysed beam. The straight port is used for the beam alignment and for providing additional evacuation to the magnet chamber.

It is essential to maintain the sample surface clean, as the range of the implanted ions with low incident energy is only a few hundred Angstroms. Hence the beam line starting from the mass analysing magnet chamber and the implantation chamber are made compatible with ultra high vacuum (UHV). A turbo molecular pump evacuates the magnet chamber to a pressure of the order of 10^{-6} mbar. A liquid nitrogen trap is provided in the beam path to reduce contamination of hydrocarbon vapours emanating from the oil diffusion pump used for pumping the accelerator.

Figure 2.2 shows the details of the implantation chamber used for the irradiation experiments. The chamber is of small volume, pumped differentially by a turbo molecular pump to maintain a pressure of 10^{-8} mbar. It is provided with multiports having facilities for beam entry, beam viewing and vacuum measurements. The beam entry port has provision for fixing a demountable collimator of varying size to define the beam, falling on the target.

Figure 2.3 shows the sample manipulator of the 150 kV accelerator. The sample holder is attached to the top flange of the implantation chamber by means of a mini Leybold DNPS 35 UHV manipulator, capable of linear (± 10 mm) and rotary (360°) motions. The sample

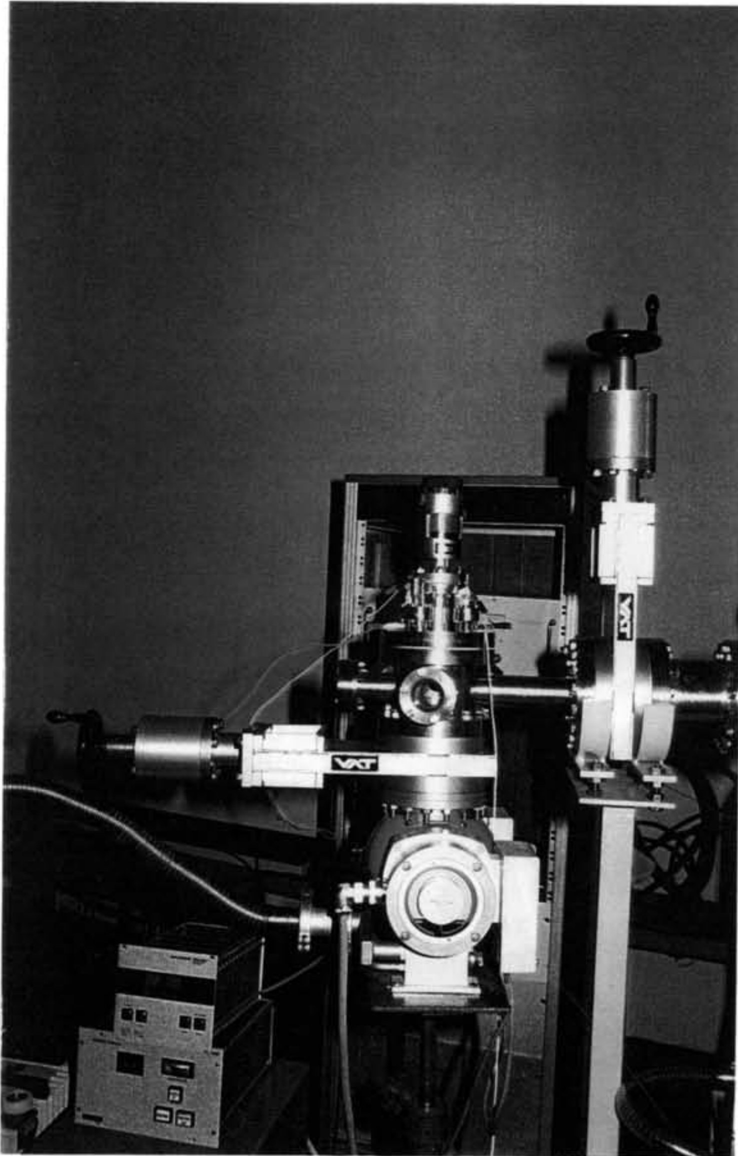

Figure 2.2: Photograph of the implantation chamber in the 150 keV machine

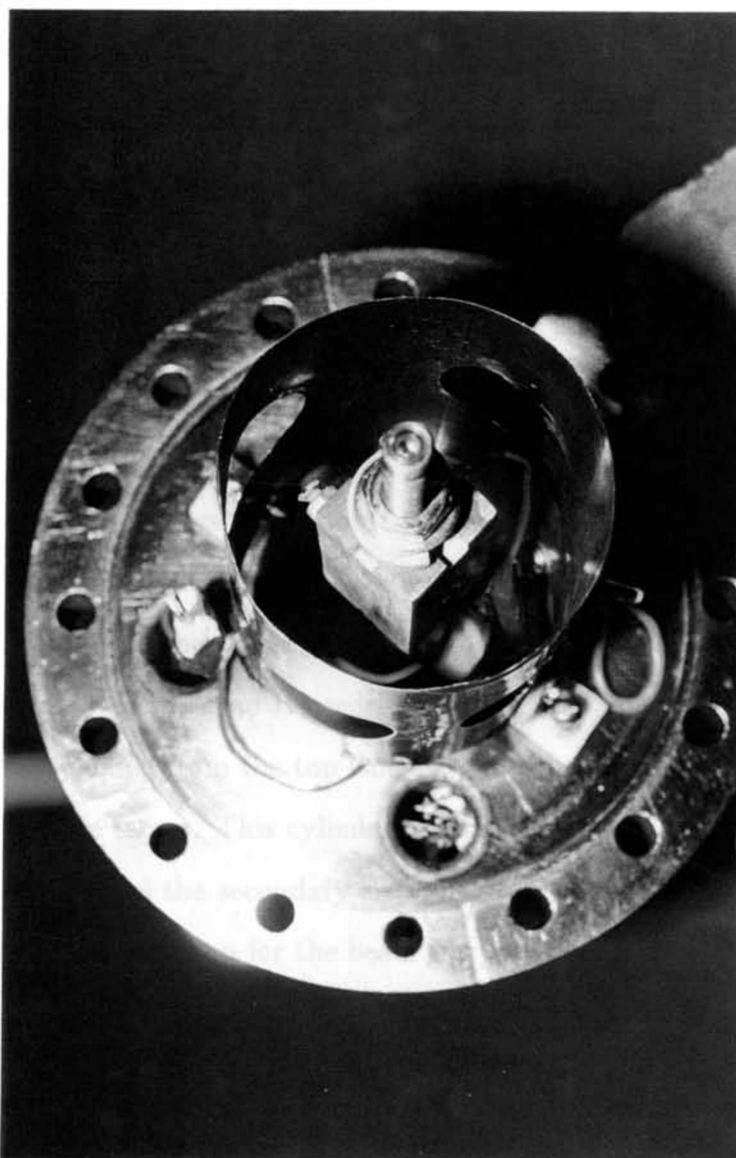

Figure 2.3: Photograph of the sample manipulator in the 150 keV machine

holder is a 25 × 25 × 40 mm copper block, fixed to the manipulator shaft. The samples are fixed on the faces of the copper block by silver paste. The copper block is electrically insulated from the manipulator shaft by a machinable ceramic (macor) disc, so that the beam current falling on the sample holder can be measured. The measurement of beam current and the integrated charge is carried out using a digital beam current integrator. The accumulated irradiation dose in terms of ions/cm^2 can be calculated by knowing the integrated charge and diameter of the incident beam.

When energetic charged particle impinges on a target, emission of secondary electrons takes place which introduces errors in the dose measurement, essentially giving rise to an overestimate of the dose. This occurs because the current integrator senses the emission of the each secondary electron from the target as the arrival of a positive ion. In order to eliminate this error, a secondary electron trap is used. This essentially consists of a thin walled stainless steel cylinder suspended from the top flange around the target. It is insulated from the top flange as well as the target. This cylinder is maintained at -60 to -70 V with respect to the target, in order to repel the secondary electrons back to the target. Openings are provided in the secondary electron trap for the beam entry and beam viewing.

2.2 Experimental techniques

A number of techniques were used for the characterization of thin films of CdS. These include X-ray diffraction, optical absorption spectrometry, Raman scattering spectroscopy, positron annihilation spectroscopy, scanning electron microscopy and transmission electron microscopy. Resistivity and photoconductivity measurements were carried out in the as-deposited and N^+ implanted films. The details of these experimental techniques are described below.

2.2.1 X-ray diffraction

Structure of the films before and after implantation was analysed by X-ray diffraction(XRD). Room temperature X-ray powder diffractograms were recorded using Siemens D- 500 diffractometer with PW 1140 X-ray generator coupled to a Cu-target X-ray tube. The diffractometer was equipped with a diffracted beam monochromator set up for accepting $CuK\alpha_1, \alpha_2$ wavelengths. The contribution from $K\alpha_2$ was eliminated by a numerical processing of the data.

2.2.2 Optical absorption spectrometry

Optical absorption spectrometry is a very important tool to study the optical band gap of the films. Optical absorption measurements of the thin films were carried out at room temperature using the UV-VIS Chemito spectrophotometer. The absorption data were collected in the wavelength range of 400 to 1100 nm.

2.2.3 Variable low energy positron beam

Depth resolved defect studies in as-grown and irradiated CdS thin films have been carried out using a variable low energy positron beam (VLEPB) system [1]. In these experiments, positrons of variable energy are used to probe the defects present at various depths. A cross-sectional view of indigenously developed LEPB is shown in Figure 2.4. It consists of a source in conjunction with $1\mu m$ thin W (100) moderator in transmission geometry to generate slow positrons, which are extracted and focussed using a lens assembly. The U-shaped magnetic bend eliminates the unmoderated fast positrons and transports the slow positrons upto the target. The target houses an ultra-high vacuum electrical feed through on which the sample is mounted. Using a remote controlled high voltage unit, the sample can be biased from -0.2 to -50 kV, thus imparting the required post-transport acceleration

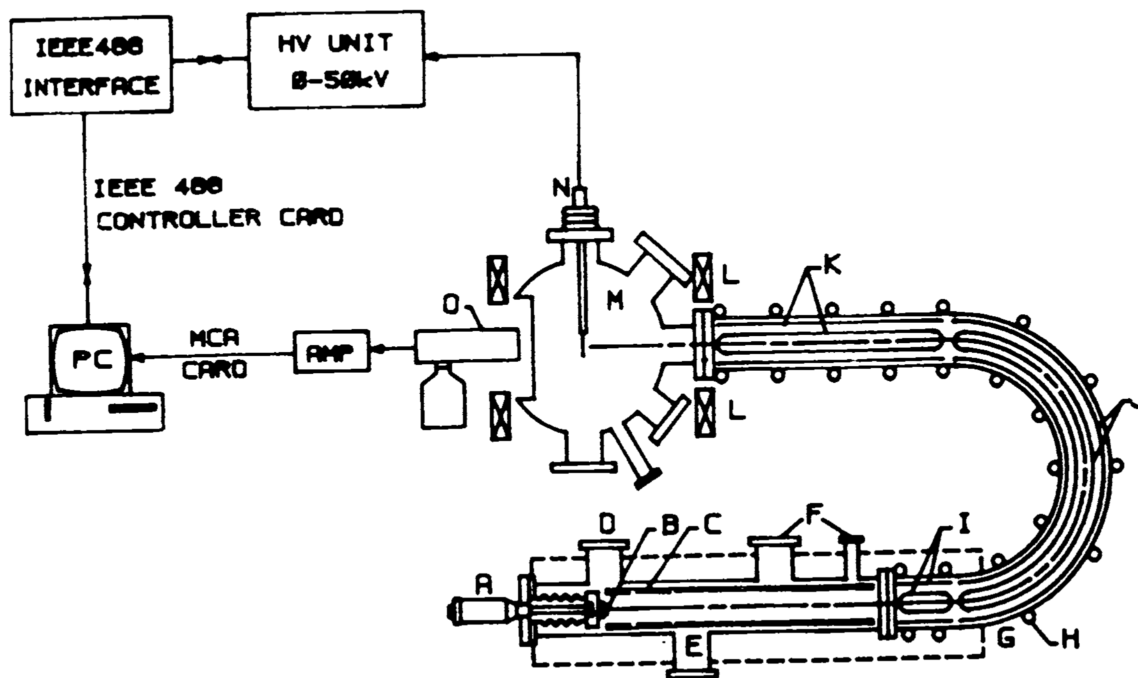

Figure 2.4: A cross-sectional view of indigenously developed low energy positron beam set-up. A - Source mounted on a linear drive; B - Moderator foil; C - Electrostatic lens elements; D - Port for vacuum monitoring; E - Pumping port; F - Electrical feedthrough port; G - Pumping shield; H - Solenoidal guiding magnetic field; I - Steering coils at the entrance; J - Orthogonal coils at the entrance; K - Steering coils at the exit; L - Helmholtz coils; M - Target chamber; N - HV feedthrough cum sample holder; O - HPGe detector

to the slow positron beam. Using the LEPB one can study the defect distribution starting from the surface to a depth of typically a few microns. The whole system is pumped using a turbo pump (500 liters/second) on target side and ion pump (60 liters/second) on source side and an ultimate vacuum of 3×10^{-8} mbar is achieved in the system. LEPB experiments comprise of measuring the Doppler broadening of annihilation γ ray energy (511 keV) as a function of positron beam energy [1]. From the measured Doppler broadening spectrum, a defect sensitive lineshape S-parameter is deduced [2, 3], which is monitored as a function of positron beam energy.

2.2.4 Raman scattering

Raman scattering is yet another technique ideally suited for probing the implantation induced lattice damage in semiconductors, mainly because the thickness of the damaged layer and the optical skin depth are essentially of the same order.

Figure 2.5 shows the block diagram of the Raman scattering set-up used in the present investigations.

The basic laser Raman setup consists of a laser excitation source, focussing lens, sample chamber, collection optics, dispersing system and a detector to analyse the scattered beam . The light source is an argon ion laser (model I-90 from M/s Coherent Inc.,USA). The experiments were carried out using the exciting source of wavelength 488 nm with a power of 50 mW. The beam diameter is about 4 mm and is focussed to a spot size of 505 μm. An Achromatic lens L_1, having a focal length of 70 mm is mounted on a xyz-translational stage used for focussing the laser. The tunable prism filter is used to filter the laser light and to eliminate other spontaneous emission lines. Mirror M which can be rotated (about its vertical axis) and translated along two perpendicular directions, is kept at an angle of 45° to the plane of incidence of the laser beam. It is used to illuminate the sample to be investigated. Distances between L_1, M and the sample are so adjusted that the beam is focussed exactly on the sample. Scattered light from the sample is collected by the Nikon camera lens L_2

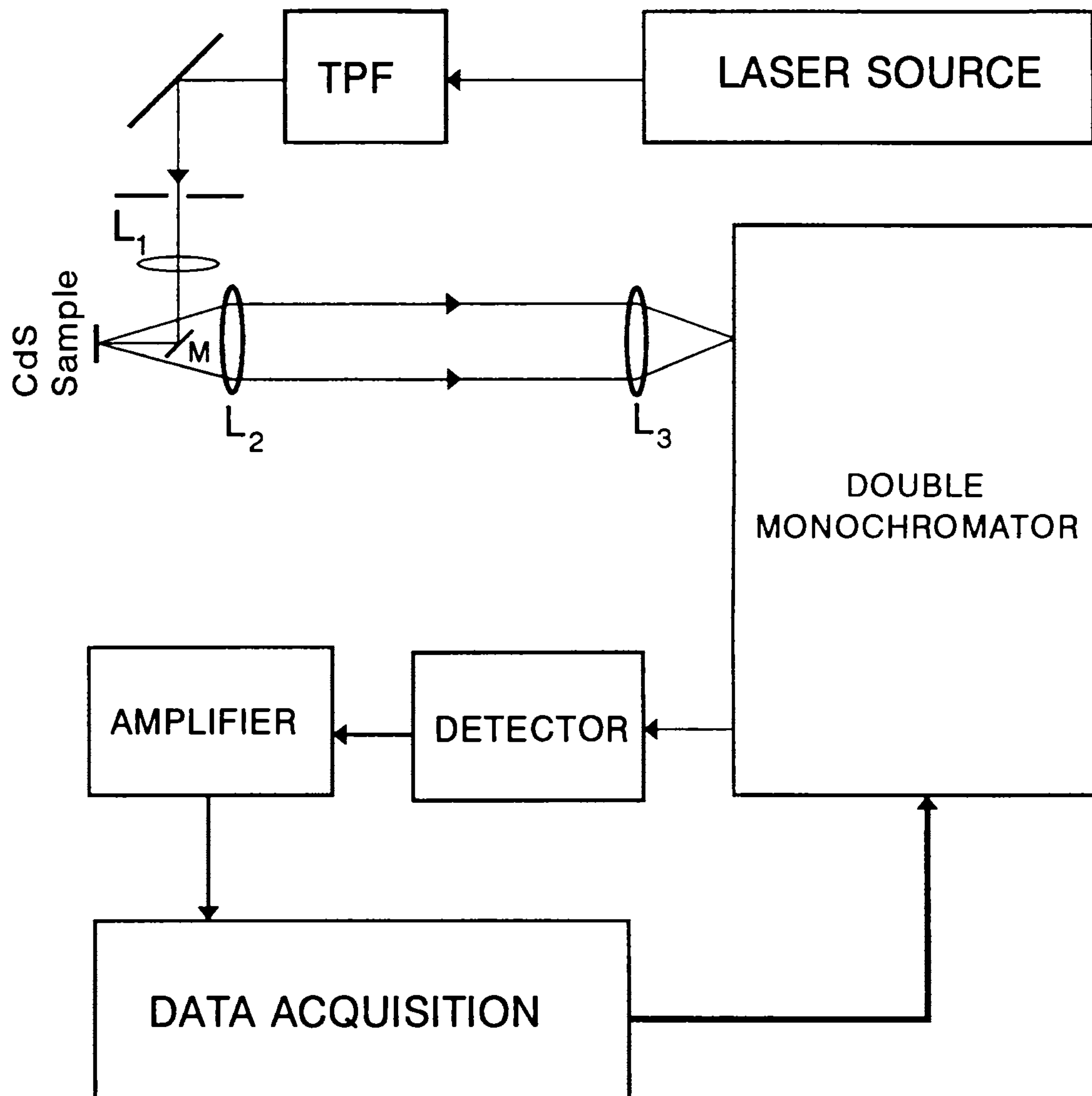

Figure 2.5: Block diagram of the Raman scattering set-up

of focal length 50 mm and is focussed onto the entrance slit of the monochromator using another Lens L_3 of focal length 400 mm. A slit width of the monochromator corresponding to 4.2 cm^{-1} in terms of FWHM of the instrument resolution function was employed. The scattered light was integrated for 10 seconds and digitally recorded at a wavelength interval of 0.5 cm^{-1}. The incident beam is vertically polarized. The unpolarized back scattered light is collected, dispersed and detected using a thermoelectrically cooled PMT model ITT - FW 130.

2.2.5 Transmission electron microscopy

A philips EM 400T transmission electron microscope was used in the present investigations for identification of structure. The accelerating voltage was 120 kV. The microscope has maximum magnification of 4×10^6 and the 'line to line' and point resolutions are 3 and 5 Å respectively. The microscope is fitted with a Link AN 10000 energy dispersive spectrometer, using which it is possible to obtain quantitative microchemical information of the samples. The heating holder (hot stage) of the microscope is capable of going upto a maximum temperature stability of ±5 °C. A liquid nitrogen trap surrounding the sample, reduces the contamination on the sample during hot stage experiments. For the TEM observations, the samples were vacuum evaporated on NaCl crystals. The films were subsequently transferred to electron microscope grid by dissolving the NaCl crystals in water.

2.2.6 Scanning electron microscopy

Surface morphology and microchemical uniformity of the films are characterized using scanning electron microscopy. These studies were carried out using a Philips PSEM 501 scanning electron microscope attached with an EDAX (Energy dispersive analysis for X-rays) 711B analyser. The minimum spot size is about 70 Å and the maximum possible magnification is 2×10^5. The accelerating voltage is at 20 kV. The three modes of operation available

are (i) secondary electron imaging mode, (ii) backscattered electron imaging mode and (iii) X-ray imaging mode. The secondary electron imaging mode provides information regarding the surface topography, whereas Energy dispersive analysis of X-rays (EDAX) attached to the microscope provides chemical information.

2.2.7 Resistivity

For electrical characterization of the films used in the present investigations, the ohmic contacts were made with silver paste. The resistivity measurements were carried out on the films in the four probe Van der pauw geometry. The resistivity measurements were carried out at room temperature using the current source (Time electronics limited DC Current calibrator). Current was applied along two contacts and the voltage was measured between other two contacts using the 195 A Keithley digital multimeter.

2.2.8 Hot probe method

Hot probe method was employed to find the conductivity type of the samples before and after irradiation. Two probes were kept on the sample out of which one probe is heated and the other probe is maintained at room temperature. A thermo emf is generated between the hot and cold probes and the polarity of the generated emf indicates the carrier type in the system.

2.2.9 Photoconductivity

The block diagram of photoconductivity set-up is given in figure 2.6. The photoconductivity measurements were carried out on the as-deposited and implanted films in the two probe geometry. The photocurrent measurements were done using the UV flash tube of power of 5 μ W. Sample was loaded inside a quartz tube which is attached to the vacuum pump.

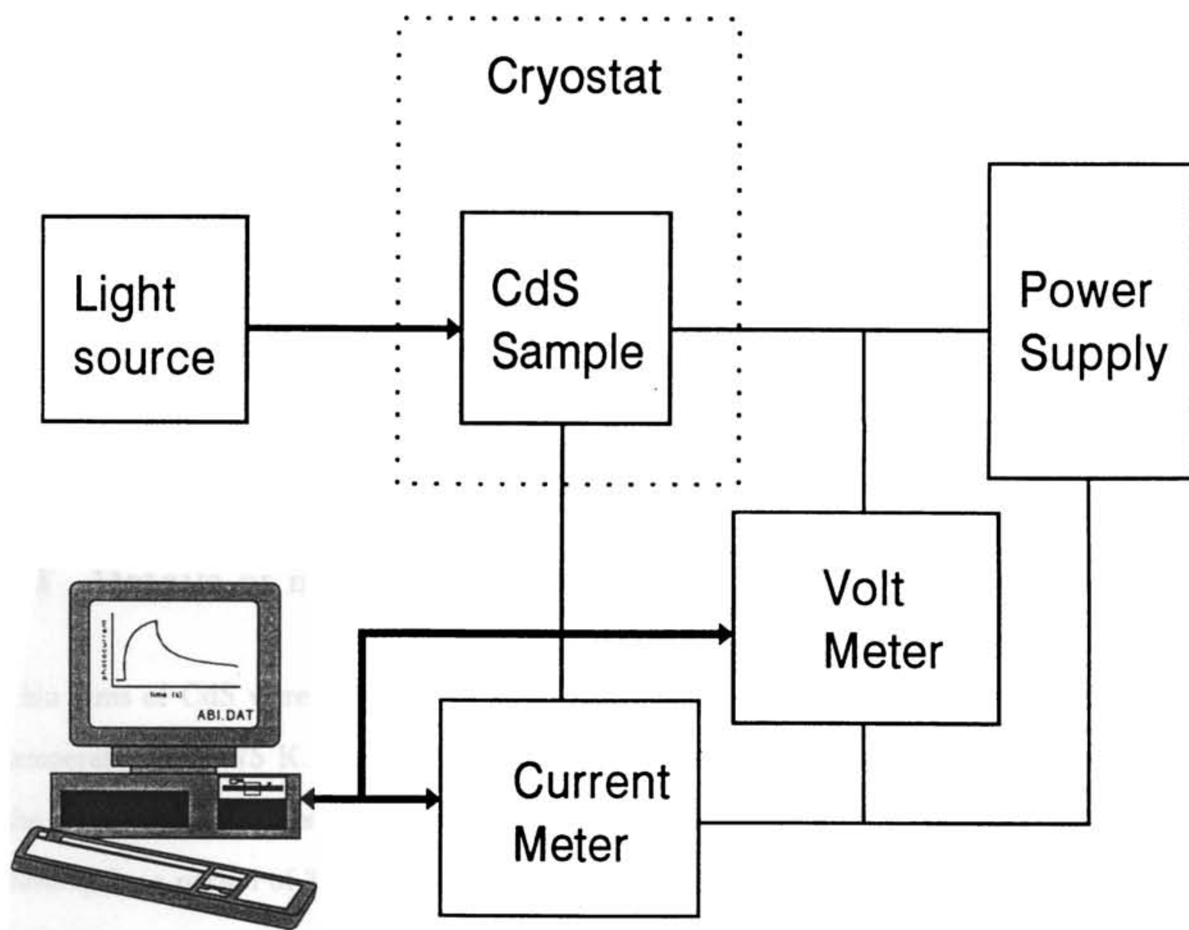

Figure 2.6: Set-up for measuring the photoconductivity of the samples

Flash was on for 5 hours to study the rising part of the photoconductivity and the decay part was monitored for several hours. These measurements were made using automated data acquisition system which accumulated data at every second and for the low temperature measurements, the data were collected for every 0.16 seconds. The photoconductivity measurements were carried out in vacuum of the order of 10^{-6} mbar. The low temperature measurements were carried out using the home built cryostat of pour-fill type. The temperature of the sample was measured using the Chromel-Alumel alloy thermocouple. Voltage was applied to the sample using the stabilizer supplied by Electronics Corporation India Limited(ECIL) - HV 4800E make. Constant voltage of 100 V was applied to the sample through out the experiment. Dark and photo currents were read using the 195 A Keithley digital multimeter.

2.3 Details of heat treatments

Thin films of CdS were annealed in an home built annealing furnace which can go upto a temperature of 1275 K. The temperature was set and the gas was allowed to flow through the quartz tube for flushing purpose. The samples were kept inside the quartz tube after flushing for a period of 30 minutes so that the impurities in the quartz tube will not interact with the sample. After the stabilization of the temperature and adequate flushing of the gas, the samples were loaded for thermal treatments. Chromel-Alumel thermocouple was used for monitoring the temperature.

2.4 Summary

Thus, the present chapter has explained the details of the various experimental stages like the irradiation, heat treatment, and the different analytical techniques like optical absorption spectrometry, positron annihilation spectroscopy, Raman scattering spectroscopy, X-ray diffraction and electron microscopy.

References

[1] G. Amarendara, G. Venugopala Rao and B. Viswanathan, Ind. J of Pure and Applied Phys., 34 (1996) 718

[2] G. Amarendara, B. Viswanathan, G. Venugopala Rao, J. Parimala and B. Purniah, Current Science, 73 (1997) 409

[3] P. J. Schultz and K. G. Lynn, Rev. Mod. Phys., 66 (1988) 814

CHAPTER 3

3 PREPARATION AND CHARACTERIZATION OF CdS THIN FILMS

Cadmium sulphide is the most suitable material for photoconductors [1], laser materials [2], homojunction and heterojunction solar cell materials [3, 4, 5, 6] due to its excellent electrical and optical properties. Considerable efforts have, therefore, been diverted to optimise the process parameters to obtain thin films of CdS with suitable electrical and optical properties. CdS thin films have been grown by a variety of techniques such as vacuum evaporation [7, 8], sputtering [9], spray pyrolysis [10, 11], and chemical bath deposition [12, 13, 14, 15]. Of these various methods, chemical bath deposition(CBD) is suitable for the preparation of thin films of large area and is a low cost process

This chapter explains the optimization of the process parameters of preparation of films of CdS using two different techniques such as vacuum evaporation and CBD. The optimization of the parameters of these two techniques was carried out by preparation of the films using various experimental conditions and their characterization using different techniques. The characterization techniques include such as X-ray diffraction(XRD), scanning electron microscopy (SEM), energy dispersive analysis of X-rays, EDAX, transmission electron microscopy (TEM) and optical absorption spectrometry. The details of the preparation of CdS films using vacuum evaporation and their characterization are presented in the first part of this chapter, which is followed by the detailed description of CBD technique. The results of the thermal annealing studies of the films prepared using CBD technique are also discussed in the chapter.

3.1 Vacuum evaporation technique

Vacuum evaporation is one of the methods used for preparing thin films. Evaporated films are formed by heating a material under vacuum to a temperature where a large number of atoms or molecules leave the surface of the material and deposit on a substrate. The condensation of evaporated materials takes place by adsorption of evaporated atoms or molecules on substrate surfaces. The nature of this primary deposit has a strong influence on subsequent growth. The main parameters that control the growth and structure of evaporated films are the type of substrate, substrate temperature,cleanliness of the substrate, evaporation temperature and angle of incidence of the evaporant.

3.1.1 Preparation of thin films of CdS using vacuum evaporation

CdS thin films were deposited on glass substrates by evaporating 99.99 % pure CdS powder. CdS powder was taken in a molybdenum boat and the evaporation was carried out by resistive heating method at a background pressure of the order of 5×10^{-5} mbar. The substrates were kept at room temperature during the evaporation. The rate of the deposition of the films was controlled and maintained in the range of 10 to 15 Å per second. The distance between the source and substrate was kept at 18 cm. The thickness and the rate of the deposition of the films were measured insitu using a quartz crystal thickness monitor. The final thickness of the films was checked using a Sloan Dek Tak 3030 surface profilometer. The substrate 'cleaning' is an important procedure prior to deposition for obtaining uniform films with good adhesion characteristics. A typical cleaning procedure of the substrates to achieve films of good quality is discussed below.

3.1.2 Substrate cleaning

The glass substrates were washed with a detergent solution, acid and base solutions, after which they were ultrasonically cleaned in distilled water and finally dried. The glass substrates were further cleaned by ion bombardment inside the vacuum chamber prior to the deposition. Ion bombardment cleaning was carried out inside the vacuum chamber prior to the deposition. The ion bombardment was required to obtain good adhesion of the film to the substrate.

3.1.3 Characterization of the films

X-ray diffraction analysis was carried out on the as-deposited films to check the crystalline structure. Figure 3.1 shows a typical X-ray diffraction pattern of the as-deposited film whose thickness was around to be 250 nm. The pattern shows the presence of a strong, sharp peak at $2\theta = 26.53^o$. This could be indexed as either (111) cubic or (0002) hexagonal. It is clear from the diffraction pattern that the films are crystalline and have a preferential orientation along (0002) hexagonal or (111) cubic direction. However it is quite difficult to conclude from the single peak appearing at 26.53 ^{o} in the diffraction pattern, whether the film is purely cubic, purely hexagonal or a mixture of the two phases as the d spacings for (0002) hexagonal and (111) cubic match well. It is well known that the CdS thin films can exist in either of these two phases or as a mixture of both the phases.

Transmission electron microscopy studies of the films were carried out to unambiguously determine the structure of the films. The films were coated on NaCl substrates under the same conditions and the NaCl crystals were dissolved in water, from which the free standing films were transferred to electron microscope grid for the TEM observation. Figure 3.2 shows a typical transmission electron micrograph of CdS thin film and its selected area diffraction pattern. It was concluded that the films are in the hexagonal phase with (0002) orientation based on the analysis of several electron diffraction patterns. Similar observation of (0002)

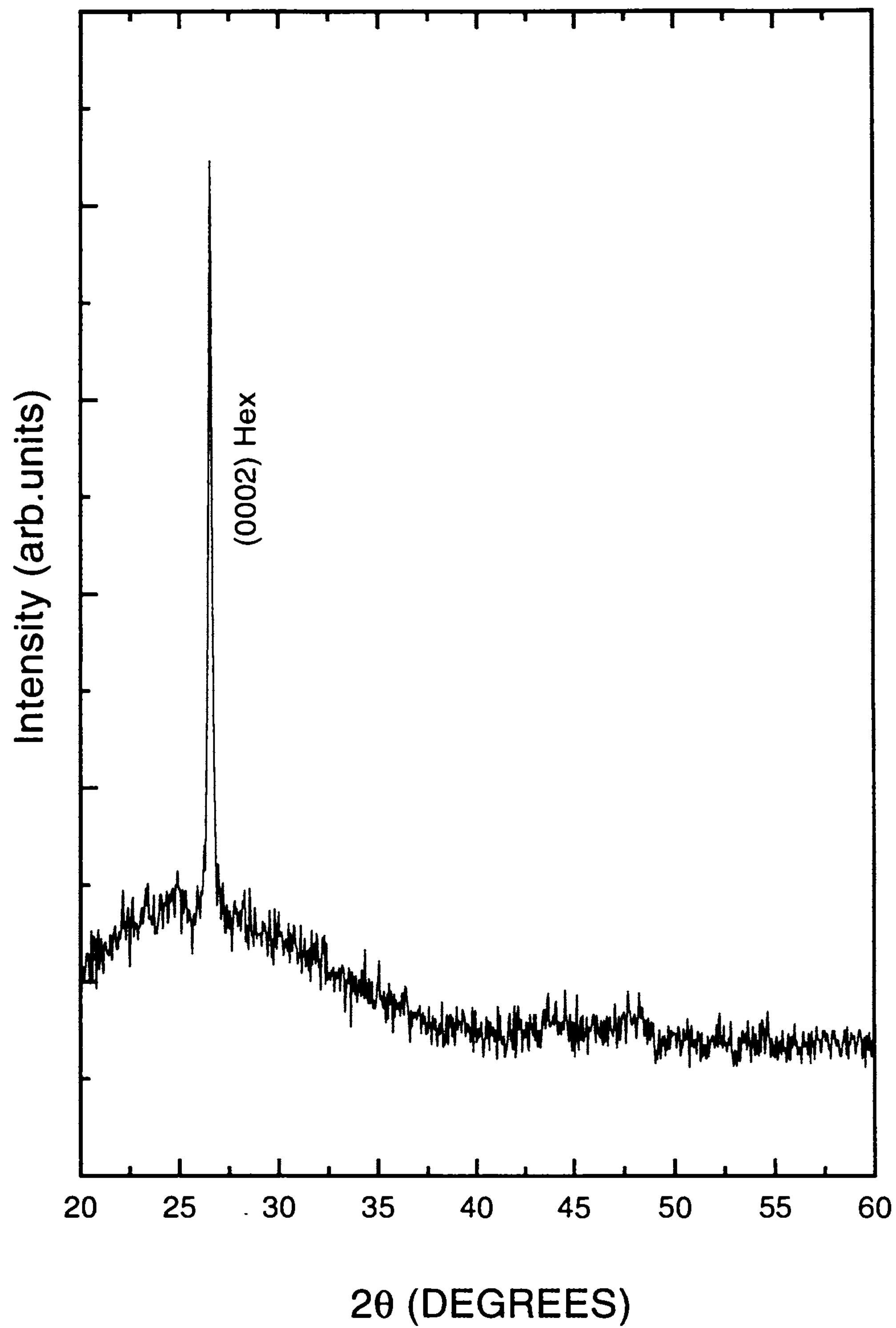

Figure 3.1: X-ray diffraction pattern of as deposited CdS thin film prepared by vacuum evaporation technique.

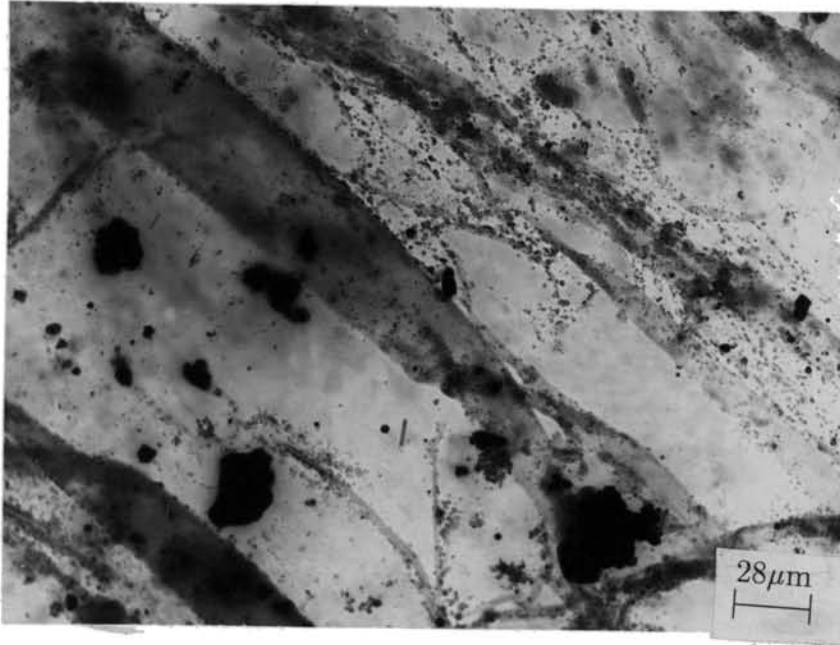

a

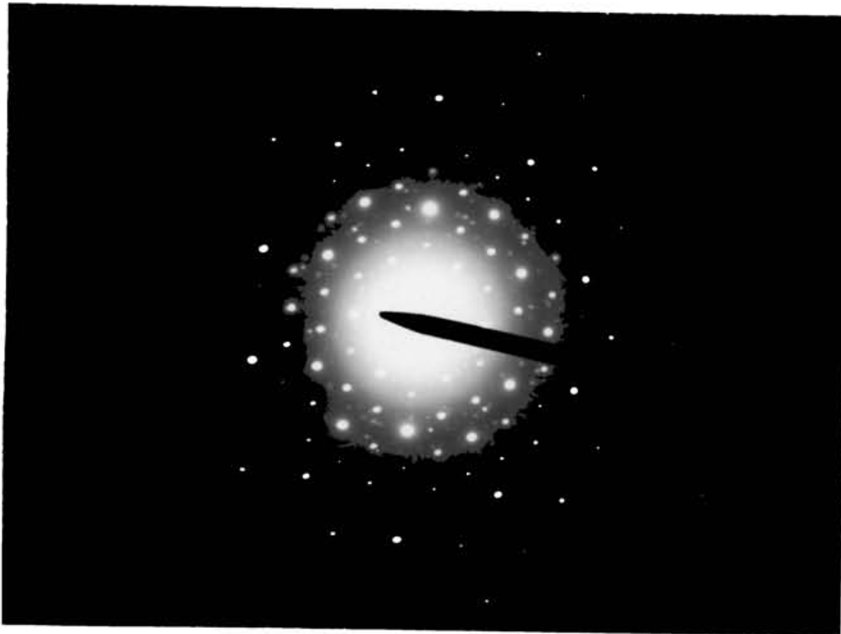

b

Figure 3.2: (a) Transmission electron micrograph of the film and (b) its selective area diffraction pattern

oriented hexagonal CdS thin films on glass substrates during vacuum deposition was reported by Ratna Sagar *et al* [16]. The preferred growth of CdS along a particular direction has also been reported, by Angel *et al* [17, 18] and Dai *et al* [19]

Optical absorption studies were carried out on the as-deposited film and a typical optical absorption spectrum is shown in figure 3.3. These studies were carried out in the wavelength range of 400 to 1100 nm to find the optical bandgap of the material. CdS is a direct bandgap semiconductor and for a direct band gap material, optical absorption coefficient, α, is given by [20]

$$\alpha = \alpha_0 \left[\frac{hc}{\lambda} - E_g\right]^{\frac{1}{2}} \quad (1)$$

where α_0 is a constant, λ is the wavelength of the incident light, c is the velocity of light, E_g is the bandgap of the material, and h is the Planck constant. The optical bandgap (E_g) of the CdS film can be determined by plotting a graph between α^2 and hν and by extrapolating the linear portion of the curve to the X-axis where $\alpha^2 = 0$ (inset of figure 3.3). The as-deposited sample is found to have an optical bandgap of 2.4 eV. The electrical resistivity of the as-deposited films was measured as a function of temperature. The resistivity was measured in the Van der pauw geometry. Ohmic contacts were made to the sample using silver paste and the ohmic nature of the contacts were checked before the resistivity measurements. An Arrhenius plot is drawn between the ln (σ) and 1/T (Figure 3.4). The activation energy of the sample is found to be around 10 meV.

Having discussed the preparation of thin film of CdS using vacuum evaporation and their characterization with respect to the crystal structure, texture developed during preparation, optical bandgap and the activation energy, the second method namely CBD will be discussed in the next section.

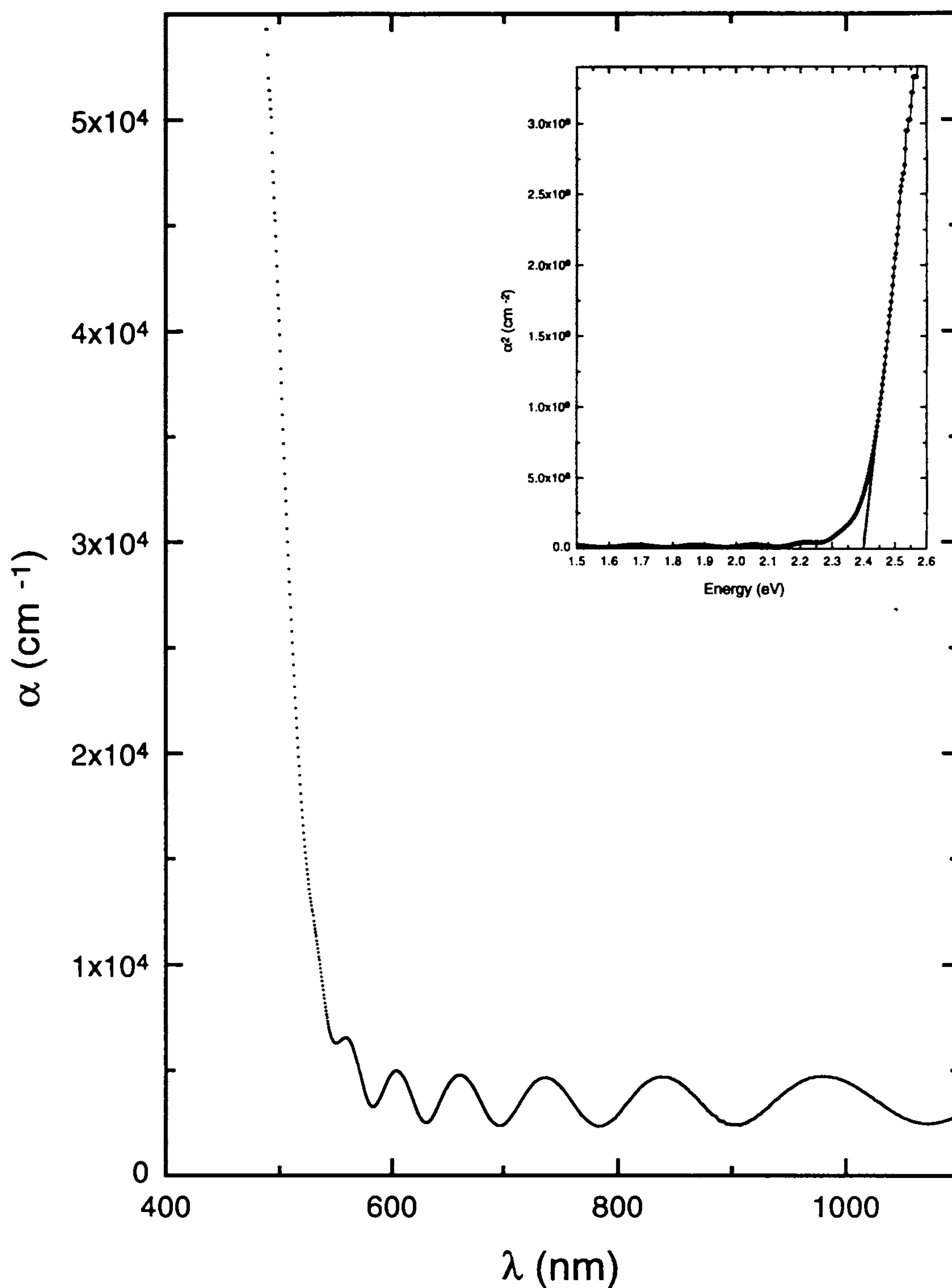

Figure 3.3: Optical absorption spectrum of as-deposited film of CdS [Inset shows the plot showing α^2 versus energy]

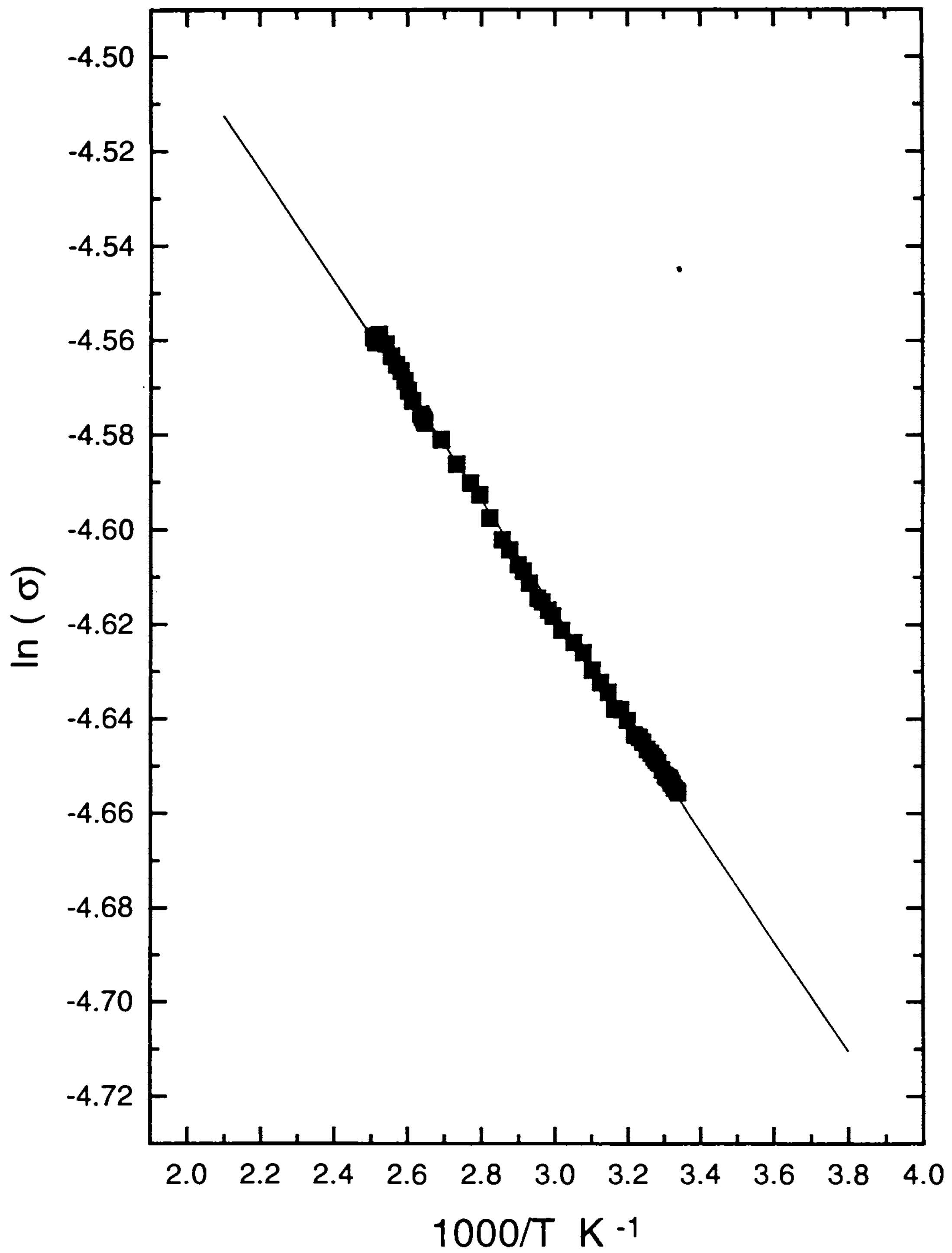

Figure 3.4: Arrhenius plot showing the variation of $\ln(\sigma)$ with $1/T$

3.2 Chemical bath deposition technique

Chemical bath deposition (CBD) is the analogue in solution of the well known chemical vapour deposition (CVD) technique in the vapour phase. It can also be considered as a particular case of heterogeneous precipitation in solution. Among the various techniques used to prepare CdS thin films, CBD is a low cost process and it is suitable for the preparation of large area thin films. Hence, there is a lot of interest in preparing compound semiconductor thin films which have applications in photovoltaics, using this simple technique. CdS films are prepared in aqueous solutions at near room temperature by a chemical reaction between dissolved precursors. The preparation of CdS thin films using CBD was initiated by the work of Mokrushin *et al* [21] and Kitaev *et al* [22] and followed by other researchers [23, 24, 25]. It has been established that the growth of the film takes place either by ion-by-ion condensation of Cd^{2+} and S^{2-} ions or adsorption of colloidal particles of CdS formed in the solution on the substrate surface, depending on the various deposition parameters such as dipping time, bath temperature and molar concentration of the reactants [26].

3.2.1 Optimization of the parameters for synthesis of CdS films

Any one of the compounds of Cd soluble in H_2O such as cadmium chloride, cadmium nitrate, cadmium sulphate or cadmium acetate could be used as a source of cadmium and similarly, thiourea can be used as the source of sulphur. In the present work, cadmium chloride and thiourea were used for the release of Cd and S ions respectively to form CdS thin films. Aqueous solutions of cadmium chloride (1M) and thiourea (1M) were mixed together in the ratio of 1:1 by volume to prepare the chemical bath. Triethanolamine was added to the bath so that a complex called cadmium triethanolamine was formed. Then ammonia solution was added drop by drop until the pH value increased to 10. The temperature of the chemical bath was maintained at 330 K. In the present investigation, microscope slides were used as substrates. Proper attention was given to the cleaning procedure of the substrates as

discussed in the earlier part of this chapter (3.1.2). These glass substrates were vertically dipped inside the chemical bath for various timings. The deposition parameters were optimized to obtain the best uniformity and adhesion properties of these films. Experiments were repeated with solutions having various values of molar concentrations. It was found that equimolar concentrations of both cadmium and sulphur containing compounds offered the best results.

3.2.2 Characterization of the films

The films prepared using chemical bath deposition technique were found to be smooth, uniform and yellow in colour. These films have good adhesion to the glass substrate. Scotch tape test was carried out on the as-deposited films. The films did not peel off from the substrate while removing the scotch tape from the substrate. Adhesion was found to be good irrespective of thickness of the films. The films were coated on glass substrates of 1.5 x 5 cm area and they were cut into small pieces for different experiments to ensure that the films were of the same batch. The thickness was measured using SLOAN Dek Tak 3030 surface profilometer. Figure 3.5 shows the variation of thickness of the films with dipping time. It is clear from the figure that the thickness increases linearly with the dipping time. Figure 3.6 shows the SEM pictures of a typical CdS thin film deposited for two hours at two different magnifications. It is seen from the scanning electron micrographs that the CdS thin film is uniform with a few isolated clusters on it. The clusters have an approximate size of 2 to 3 μm. These few well marked regions of high density growth (clusters) may be attributed to the local variation in the growth conditions. The chemical homogeneity of the films was checked using Energy Dispersive Analysis of X-rays (EDAX). A typical EDAX spectrum is shown in figure 3.7. The EDAX results revealed that the fibres and the clusters consisted of Cd and S. The composition was found to be homogeneous across the film as evidenced by the same ratio of Cd counts to S counts at various locations. EDAX spectra of the clusters reveal that they have the same composition as that of the rest of the film confirming that the

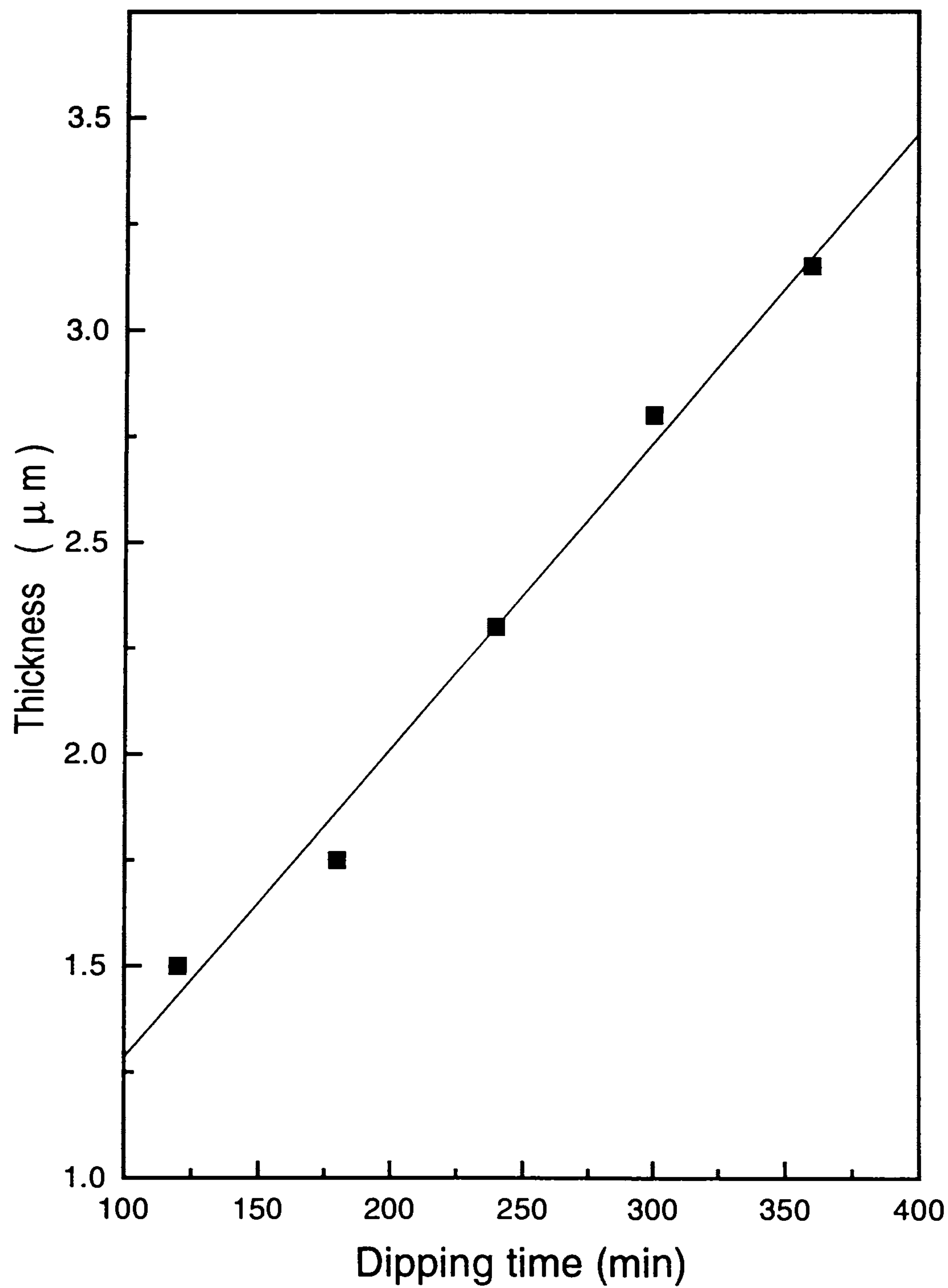

Figure 3.5: Variation of thickness of the films with dipping time

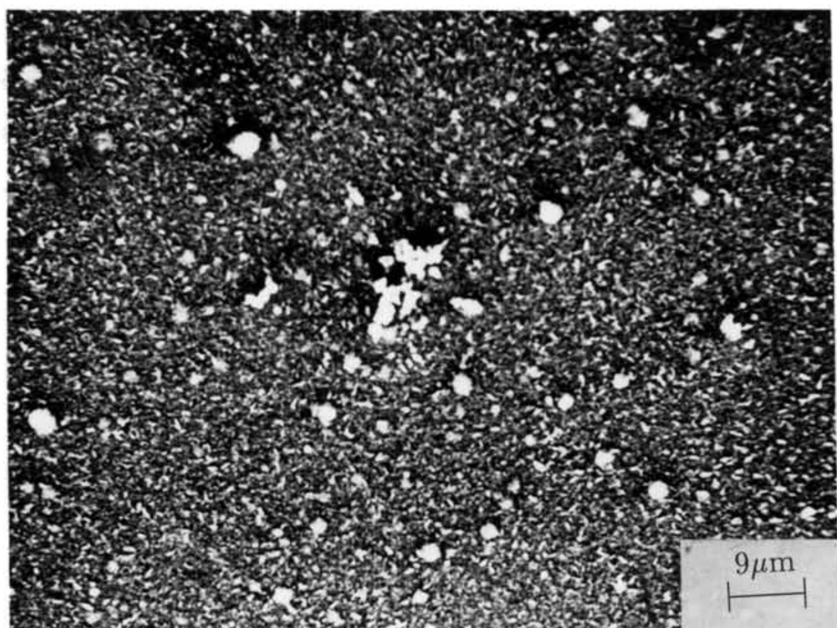

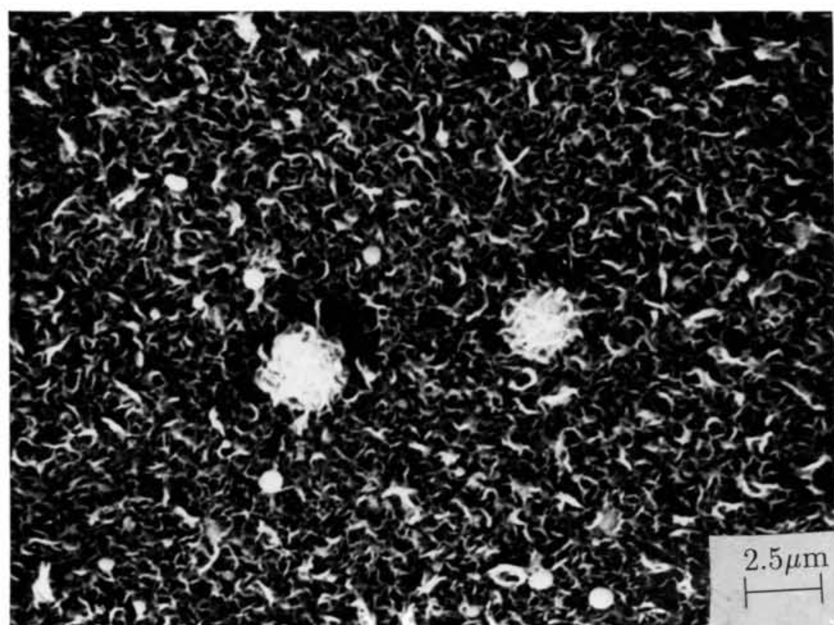

Figure 3.6: Scanning electron micrographs of CdS films. Films are prepared by chemical bath deposition method. The dipping time was 2 hours and temperature of the bath was maintained at 333 K

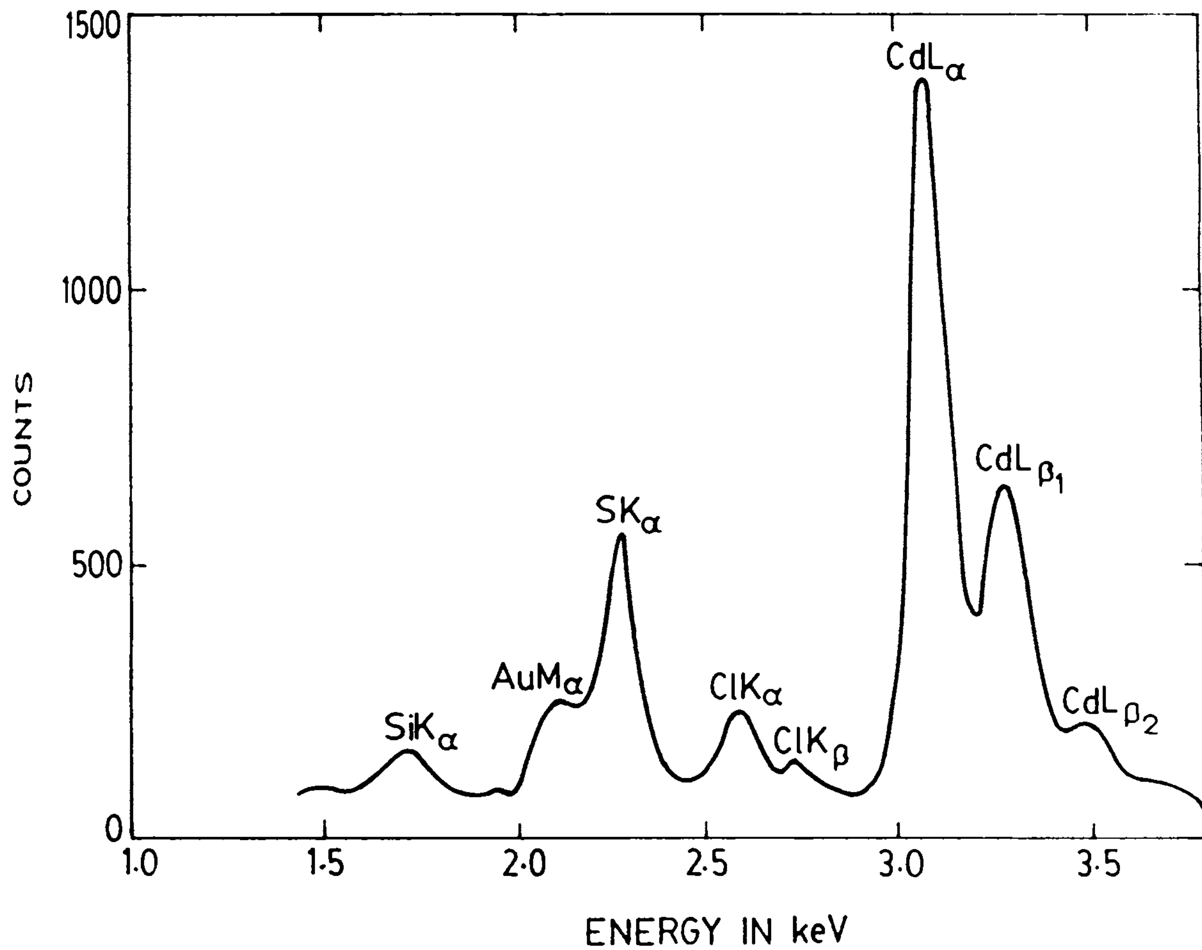

Figure 3.7: EDAX spectra of the as-deposited film of CdS

clusters are densely packed microcrystallites of CdS and are not made up of any impurity. A weak peak of chlorine is seen in the EDAX spectra. The contamination of chlorine seen on the film was attributed to cadmium chloride which is one of the reagents used for the deposition. EDAX spectra also showed the presence of gold and silicon. The gold peak arises from thin gold film coated on the samples prior to SEM observations for better conductivity and contrast. The silicon peak, probably arises from the substrate which is glass.

CdS films prepared by chemical bath deposition were found to be crystalline. Unlike in the case of films prepared by vacuum evaporation technique, no textured growth is seen in films prepared by CBD process. The detailed analysis of the structure of CBD films is discussed in the next section. The resistivity of the films was found to be very high. The observed high resistivity of the films is not surprising in the light of the fact that they are stoichiometric. The structure and properties of the films undergo significant changes during annealing to high temperatures, which are discussed in detail in the next section.

3.3 Effects of annealing on films of CdS prepared by CBD process

Figure 3.8(a) shows the optical absorption spectra of as-deposited film and the film annealed for 3 hours at 673 K. It is seen from the optical absorption spectra that the band edge shifts on annealing. The optical bandgap (E_g) of the CdS film can be determined by plotting a graph between α^2 and hν, as shown in the figure 3.8(b), and by extrapolating the linear portion of the curve to the X-axis, where $\alpha^2 = 0$.

The optical bandgap of the as-deposited and annealed films are found to be 2.3 eV and 2.2 eV respectively. The annealing was carried out at 673 K for different timings and the variation of bandgap with time is shown in Figure 3.9. It is found that the optical band gap systematically decreases with increase in annealing time. Such a decrease could be caused by either grain growth or any phase transformation during annealing. It is known that CdS

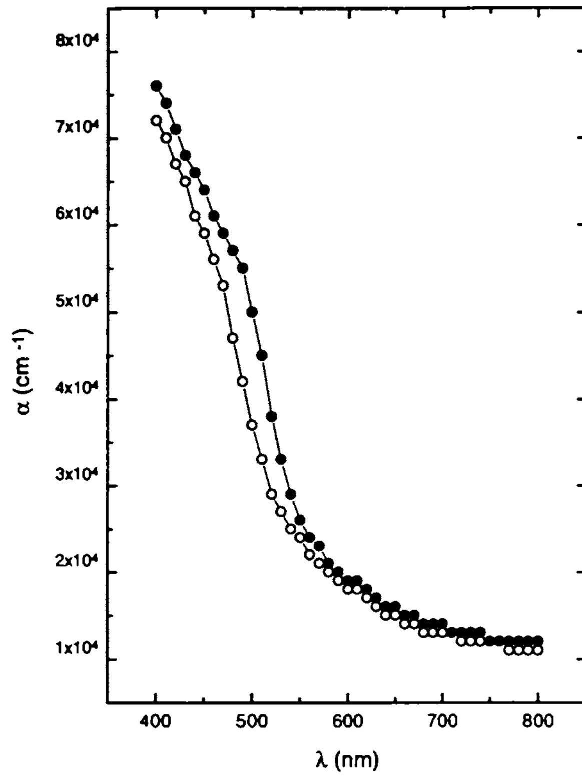

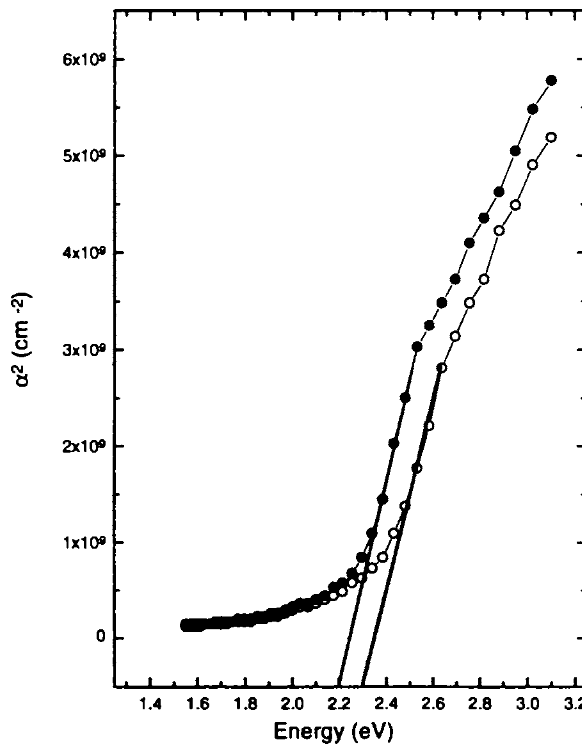

Figure 3.8: (a) Optical absorption spectra of as-deposited film (− ∘ − ∘ − ∘ − ∘ −) and annealed film (− • − • − • − • −). (b) Plot showing α^2 versus energy for the as-deposited (− ∘ − ∘ − ∘ − ∘ −) and annealing films (− • − • − • − • −)

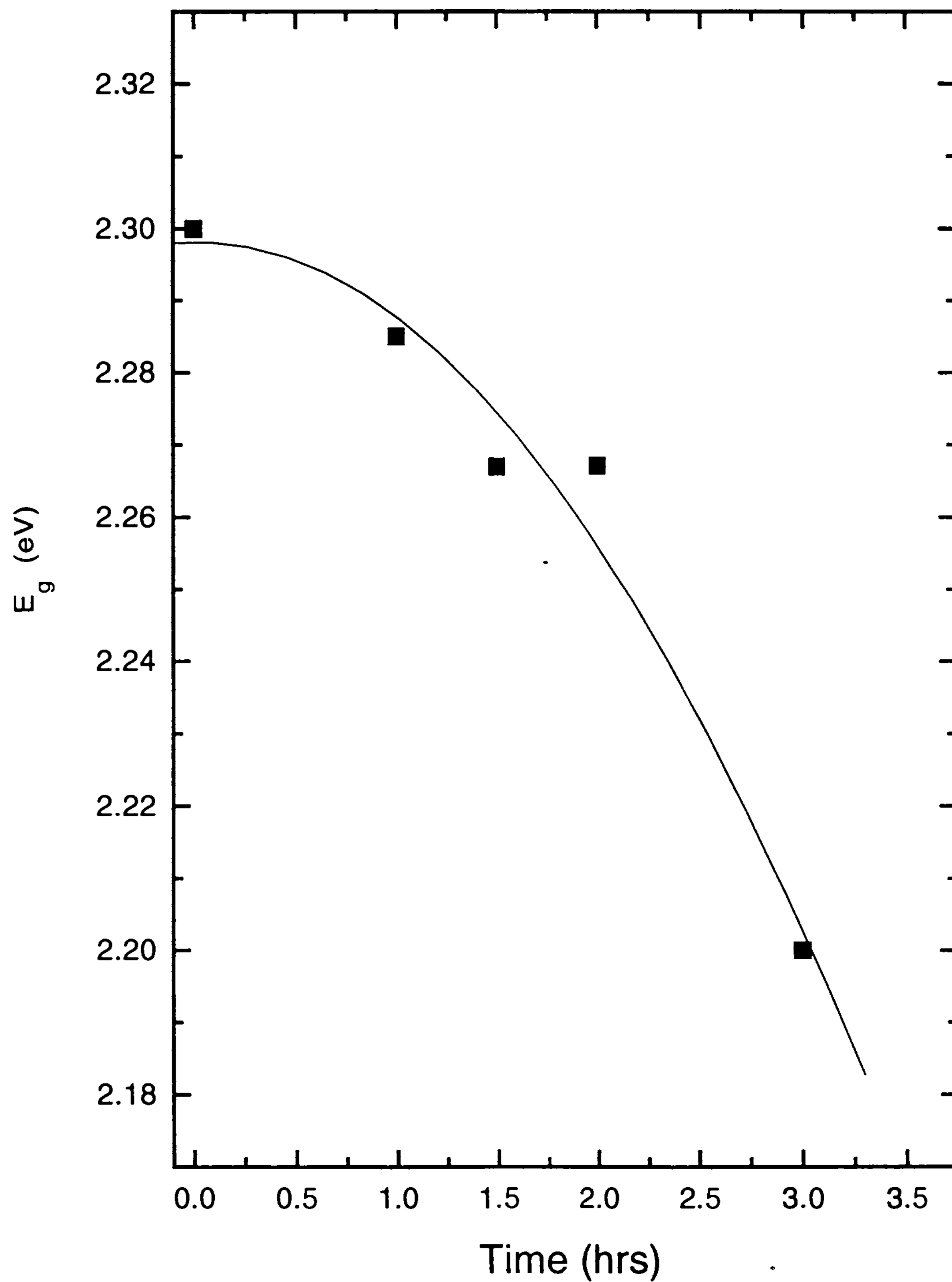

Figure 3.9: Variation of the optical band gap with the annealing time at 673 K

exists in either of two different structural phases; a stable hexagonal or a metastable cubic phase and there is a difference in the bandgap of about 0.1 eV between the two phases. Angel *et al* [17, 18] have reported a shift in the bandgap of CdS films on annealing. They found that the bandedge shift towards the higher wavelength side on annealing. They carried out photoacoustic spectroscopy to determine the change in the band gap of CdS caused by annealing. The observed reduction in the bandgap in their studies is about 0.1 eV on annealing at 573 K for 50 hours and they attributed the change in the bandgap to the cubic to hexagonal phase transformation based on X-ray diffraction evidence.

Further investigations have been carried out, in order to identify the exact cause for the reduction in the optical bandgap observed during annealing. Figure 3.10 shows the scanning electron micrographs of the CdS film in the as-deposited state and after annealing at 673 K for three hours. The microstructure of the as-deposited films shows uniformly dispersed small clusters on the film. No significant change in the microstructural features is seen on annealing. The cluster size remains more or less the same. In order to verify whether the cubic to hexagonal phase transformation had taken place during annealing, X-ray diffraction studies were carried out on the films. Since it is difficult to get good diffraction patterns from thin films, XRD was carried out in films of CdS having thickness of 1.8 μm. Films of CdS of thickness 1.8 μm were coated on glass substrates for two hours at 333 K. Figure 3.11 shows the X-ray diffraction pattern of the as-deposited CdS thin film. (For this analysis, the diffraction pattern was taken using a Philips PW 1730/10 X-ray diffractometer). It is seen from the figure 3.11, that the films are crystalline and further, the diffraction peaks observed correspond to both cubic and hexagonal phases. The peaks in the diffraction pattern are quite broad possibly due to fine size of the crystallites. It is well known that the dip-coated films, exist as a mixture of polycrystalline cubic and hexagonal phases [26, 27]. The diffraction pattern in the present investigation was compared with JCPDS data of the two phases [28, 29]. It was found that the films exist as a mixture of the two phases. The peak at 28.4^o in figure 3.11 could not be assigned to either of the CdS phases but it could be indexed as (101) peak of thiourea. Some extent of contamination due to the presence of

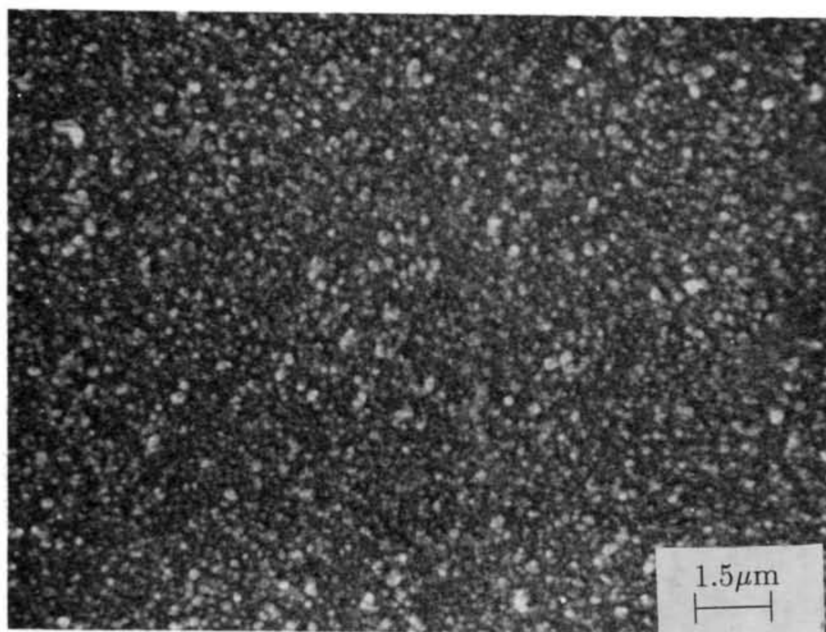

a

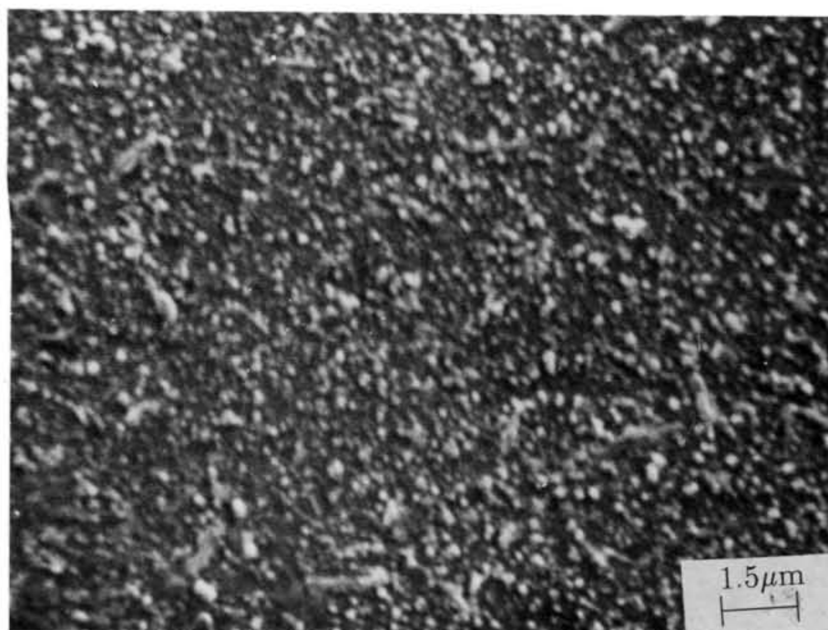

b

Figure 3.10: Scanning electron micrographs of the (a) as-deposited and (b) annealed films at 673 Kelvin for three hours [the thickness of the films is around 100 nm]

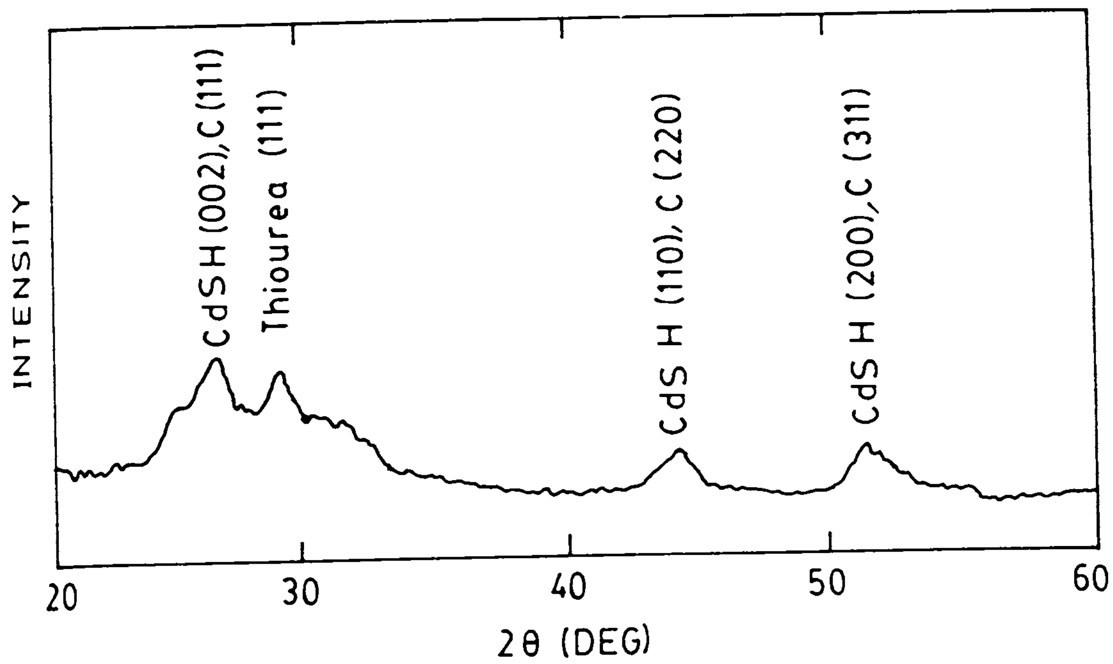

Figure 3.11: X-ray diffraction pattern of as deposited CdS thin film prepared by chemical bath deposition

thiourea is possible in films prepared by CBD, as thiourea is one of the chemical reagents used. It was found that the presence of thiourea did not affect the optical and electrical properties much. Further, thiourea is volatile and gets eliminated during high temperature annealing.

The as-deposited thin films(1.8 μm) were annealed in argon atmosphere at 673 K and the influence of annealing on the structure and optical bandgap was studied. The diffraction pattern of the annealed film is shown in figure 3.12. The appearance of a number of lines exclusively belonging to the hexagonal phase confirms that the phase transition from metastable cubic to stable hexagonal phase has occurred on annealing. Further, all the peaks have sharpened indicating the growth of grains. A few peaks corresponding to Cd_2SiO_4 are also seen in figure 3.12. The formation of cadmium silicate could be due to the reaction between the substrate and the CdS thin film . Similar observation of formation of cadmium silicate has also been reported by Zelaya Angel *et al* [17] who had carried out annealing of CdS thin films coated on glass substrates.

The decrease in the optical band gap observed in the present study during annealing could be attributed to the cubic to hexagonal phase transformation. It is well known that the volume of the unit cell has an inverse relationship with optical bandgap. The slightly higher volume of unit cell of the hexagonal phase as compared to the cubic phase may explain the difference in the optical bandgap of the two phases. The difference in the optical bandgap of the cubic and hexagonal phase is about 0.1 eV, which agrees well with the change observed in the previous investigations [17, 18].

An alternative explanation for the decrease in the band gap during annealing may be offered based on possible increase in the grain size of the CdS during thermal annealing. The effect of grain size on the optical band gap arises due to quantum confinement effects and has been investigated by Yu *et al* [30]. They carried out transmission electron microscopic investigation to study the grain size of CdS thin films and tried to correlate the grain size with optical band gap. They could observe that there was a decrease of about 0.1 eV in the

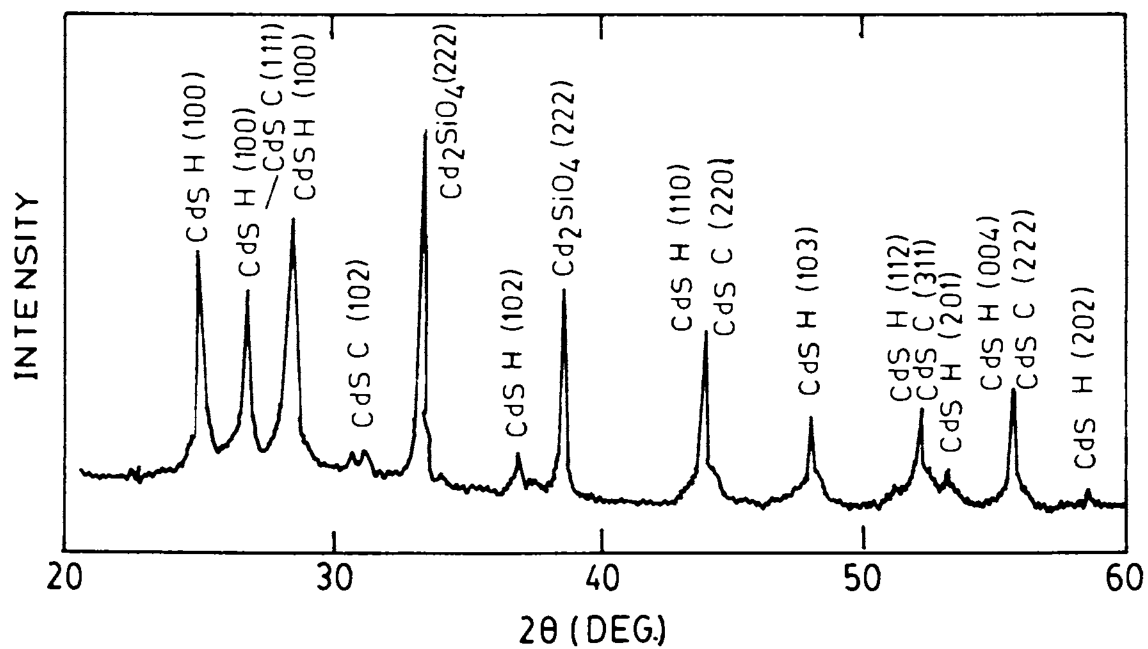

Figure 3.12: X-ray diffraction pattern of film annealed in argon atmosphere for three hours at 670 K

band gap when the grain size increased from 5 nm to 25 nm. At a grain size of about 25 nm, the band gap was within 0.01 to 0.02 eV of the bulk value.

In the present study, an estimate of the average size of the grains has been obtained from the X-ray diffraction pattern using the Debye Sherrer formula.

$$d = \frac{0.94\lambda}{\beta cos\theta} \tag{2}$$

where d is the grain size, β is the full width at half maximum(FWHM), θ is the Bragg angle and λ is the wavelength of the X-rays. The estimated grain size of the as-deposited films is about 7 nm and the bandgap be 2.3 eV. The diffraction peaks in the XRD pattern of the annealed film are considerably sharp indicating the grain growth. The approximate grain size in the annealed film turns out to be larger than 23 nm. Kale *et al* [31] studied the optical bandgap, resistivity and grain size of the films prepared at different deposition temperatures and dipping times where they could observe the bandgap to be 2.4 eV for the films of grain size of about 7nm. As the deposition temperature is decreased, the bandgap is found to increase and they attributed this effect to the nano particles of CdS.

However, an explanation based on grain growth is not tenable in the present case due to the following reasons. Firstly we observed clear evidence for a cubic to hexagonal phase transition during annealing. Such a transition can account for a shift in the band gap from 2.3 to 2.2 eV. Secondly the value of the band gap of annealed films due to coarsening [30] slowly approaches the bulk value and never goes below the bulk value. The observed value of optical band gap in the annealed films is well below 2.4 eV, the band gap of the cubic phase single crystal. Hence, it might be reasonably concluded that the observed shift in the bandgap can be attributed to the cubic to hexagonal phase transformation [14].

3.4 Partial conversion of films of CdS to CdO on annealing

X-ray diffraction pattern of the as-deposited CdS thin film is shown in the figure 3.13. The films were found to be crystalline and further they were containing both cubic and hexagonal phases of CdS similar to figure 3.11. The grain size has been calculated as 7 nm using Debye Sherrer formula. In addition, the films were found to show high resistance, with the resistivity in the range of 10^5 to 10^9 ohm cm.

The optical absorption spectra of the as-deposited CdS thin film is given in 3.14. The optical bandgap(E_g) of the CdS film can be determined by plotting a graph between α^2 and hν and by extrapolating the linear portion of the curve to the X-axis, where $\alpha^2 = 0$ (Inset of figure 3.14). The as-deposited sample is found to have an optical bandgap of 2.35 eV.

The annealing of the films in flowing air atmosphere(673 K, 2 hours) resulted in a drastic reduction of the resistivity of the films. The resistivity of the films dropped to 0.2 ohm·cm. In order to understand the origin of such a large change in the resistivity, the X-ray diffraction studies were carried out on the annealed samples. Figure 3.15 shows the diffraction pattern of the films annealed in flowing air atmosphere. The most striking feature of the XRD pattern is the sharpening of all the peaks indicating the grain growth. This is also consistent with our earlier result mentioned in this chapter. The estimate using the Debye Sherrer formula provides a grain size of 35 nm in the annealed films as against 7 nm in the as-deposited thin film. Further examination of the XRD pattern indicates the partial conversion of cubic phase to hexagonal phase of CdS as evidenced by the presence of several peaks which belong exclusively to the hexagonal phase. The appearance of the peaks at 2θ = 32.9°, 38.2° and 55.2°s suggests the formation of CdO phase. Cubic to hexagonal transformation could not have given rise to the change in the electrical conductivity of the films. In order to confirm this, annealing was carried out under inert atmosphere. The phase transformation to hcp and the grain growth were seen in the case of the films subjected to annealing in argon atmosphere. However, the films did not become conducting confirming

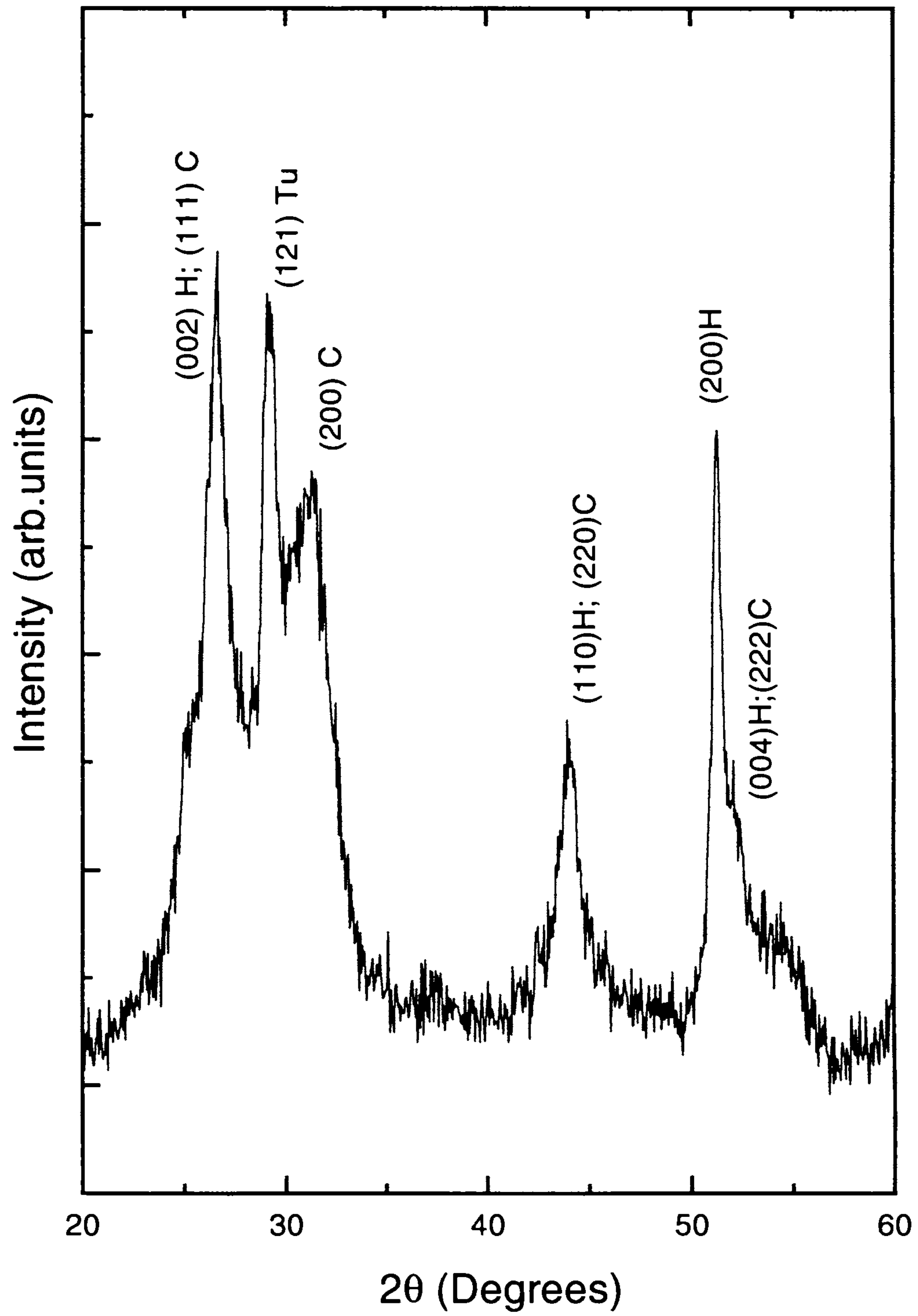

Figure 3.13: X-ray diffraction pattern of the as deposited CdS thin film prepared by Chemical bath deposition method.

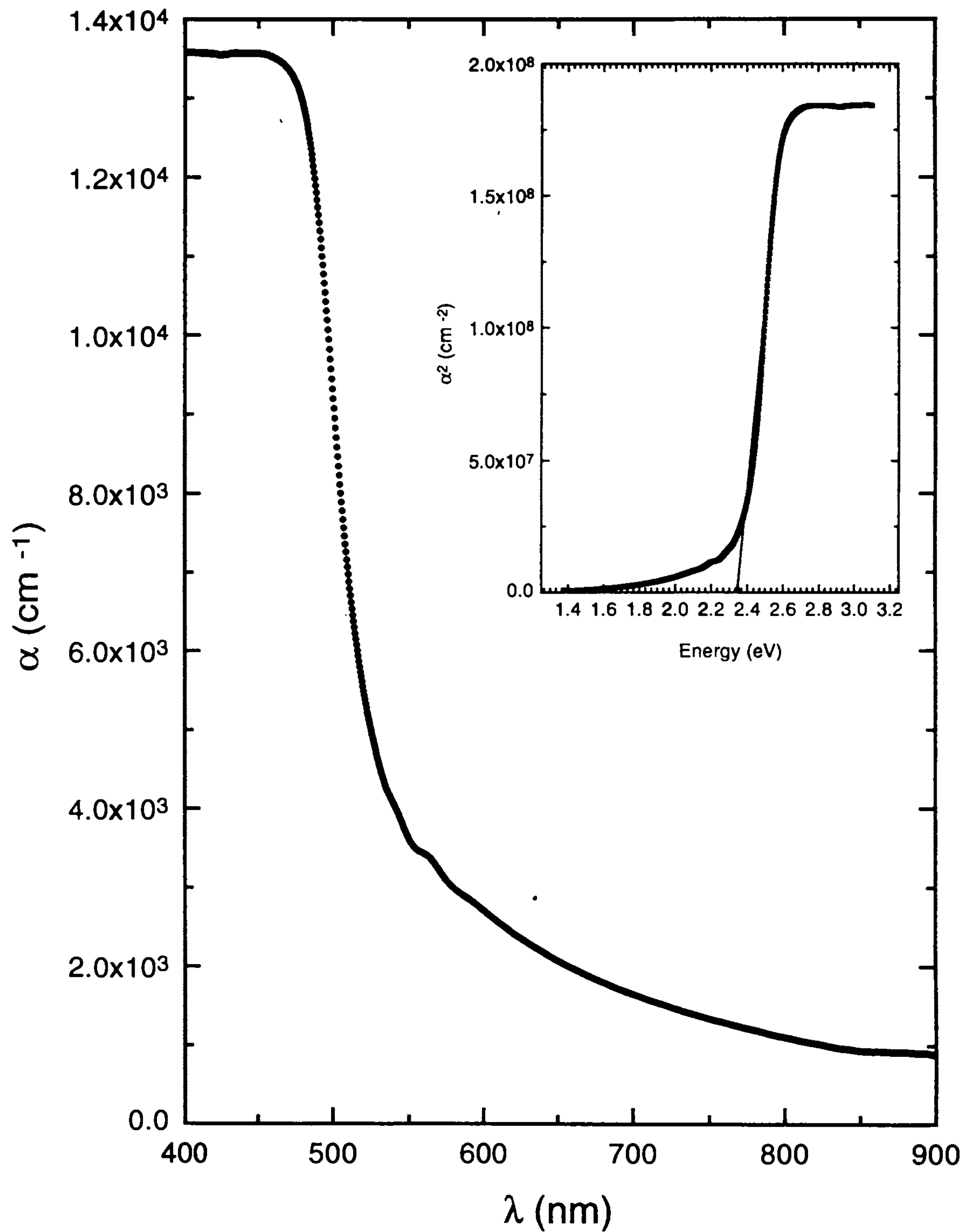

Figure 3.14: Optical absorption spectra of as-deposited film of CdS [Inset shows the plot showing α^2 versus energy]

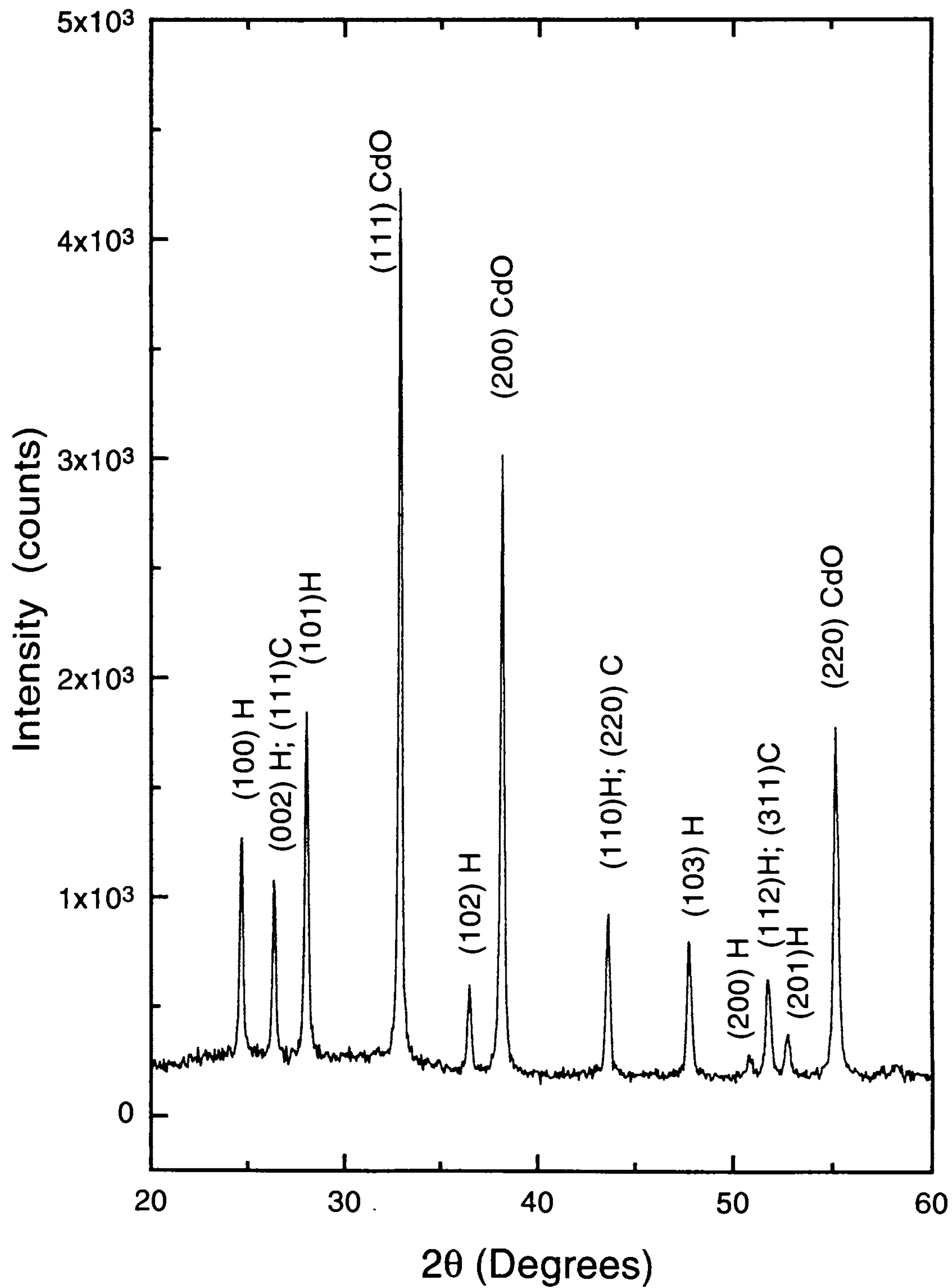

Figure 3.15:- X-ray diffraction pattern of CdS film annealed in flowing air

that observed conductivity of the films annealed in air atmosphere was solely due to the formation of CdO phase.

It is interesting to note that the decrease in resistivity is seen only in the case of films annealed in flowing air or oxygen atmosphere, where considerable fraction of CdS gets converted to CdO. This is probably because a continuity between the various CdO grains is required for obtaining good conductivity. It is possible to achieve such a condition only when a substantial volume fraction of CdS gets converted to CdO, rather than when CdO is present as isolated islands in an insulating CdS matrix. Figure 3.16 shows an XRD pattern of CdS thin film annealed in an oxygen deficient atmosphere by passing commercial grade argon through the furnace. The CdO phase is still present as can be seen from the presence of the characteristic peaks at $2\theta = 32.9^o$, 38.2^o and 55.2^o. The CdO phase could have formed due to the presence of oxygen in the gas used for flushing. However, the intensities of the diffraction peaks of CdO are small compared to the case of annealing in flowing air, indicating much lower volume fraction of CdO. In addition, the resistivity of the film did not change significantly on annealing in an argon(commercial grade) atmosphere. The CdO phase, in this case, could have formed as isolated islands on the insulating matrix, which probably explains why the resistance remained high despite the formation of the conducting CdO phase.

Nair *et al* [23] have reported the formation of highly conducting CdS phase on annealing, where they have converted CdS thin films to n type by annealing in air. It has been reported by Jayakrishnan *et al* [32] that CdS thin films of low resistivity have been formed on rapid thermal annealing of dip coated CdS thin films. They have shown that rapid thermal annealing of dip coated CdS thin films in vacuum resulted in the reduction of the film resistivity from 7×10^7 ohm cm to 0.16 ohm·cm. Jayakrishnan *et al* have attributed this reduction to the effect of desorption of adsorbed oxygen, which according to them acts as trap for mobile charge carriers in CdS [31]. Such a drastic reduction in resistance was not observed when they carried out slow thermal annealing in a vacuum of 10^{-2} mbar which they ascribe to surface contamination due to slow annealing in vacuum.

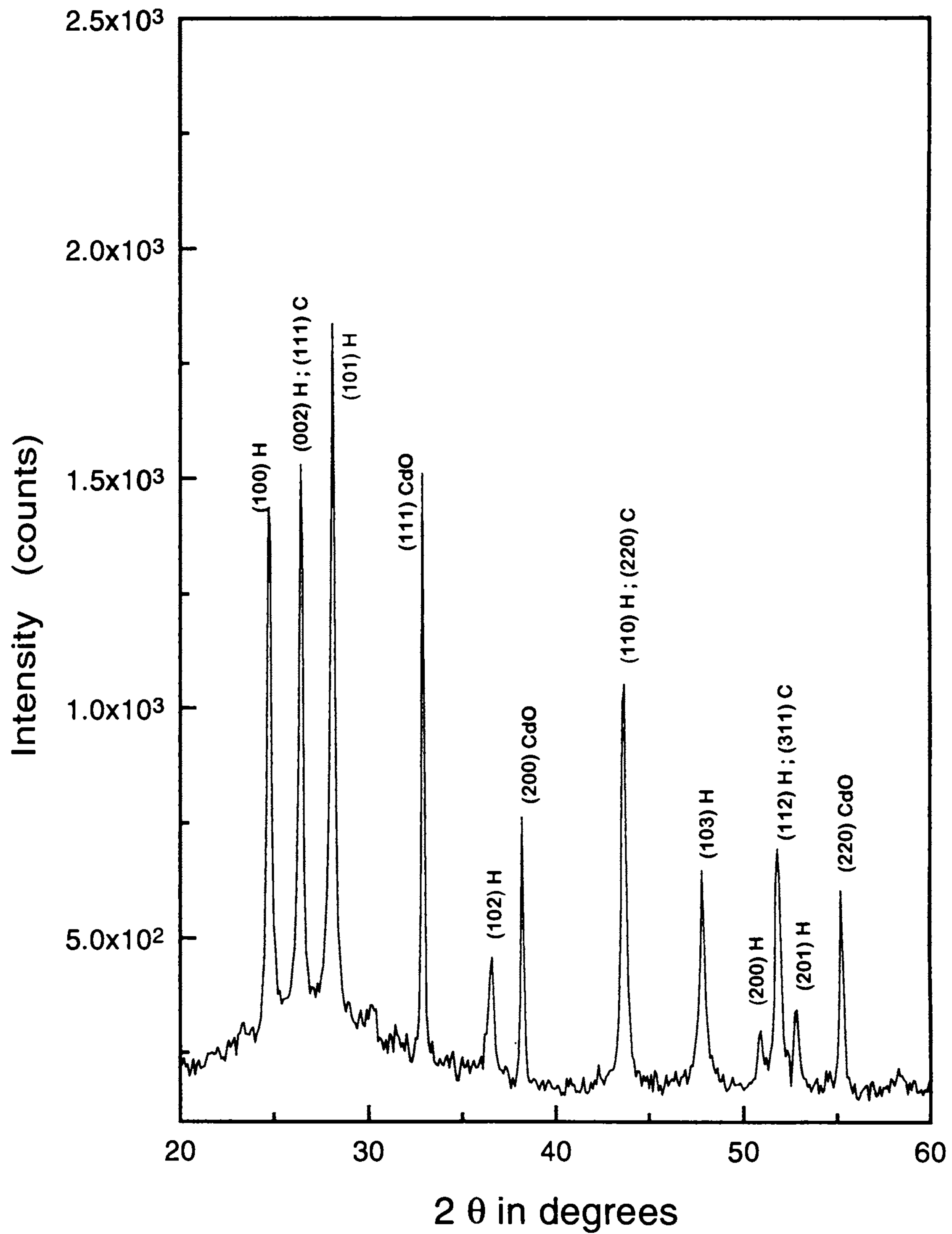

Figure 3.16: X-ray diffraction pattern of CdS film annealed in oxygen deficient atmosphere by passing flowing commercial grade argon

In the present investigation, the annealing was carried out at 673 K for three hours in vacuum of the order of 10^{-5} mbar, so as to avoid contamination effects. The time of annealing is much larger than the rapid thermal annealing carried out by Jayakrishnan *et al* [32]. The results of oxygen desorption could have manifested in our case also. However, the films remained highly resistive even after annealing and this is in disagreement with the results of Jayakrishnan. Similar observation was reported by Danaher *et al* [26] where the CBD films were found to be highly resistive even after annealing in vacuum at 603 K for 2 hours. Nair *et al* [23] have reported the formation of CdO phase on air annealing of the dip coated films. These results are in agrement with our study. They have also observed the formation of CdO phase in the annealed films which are conducting.

One of the main problems associated with the annealing of the dip coated films is the deterioration of the optical transmission. Figure 3.17 shows the optical absorption spectra of a CdS thin films after annealing. There is a significant increase in the optical absorption. The SEM micrograph of the annealed film is shown in Figure 3.18. Large number of cracks are visible in the micrograph, presumably created during annealing due to thermal stresses. The reduction in the optical transmission may be attributed to the reduction in the quality of the film.

3.5 Summary

In this chapter, a detailed account of the preparation of CdS thin films using vacuum evaporation and chemical bath deposition techniques is presented. Detailed characterization of the films is also presented in this chapter.

CdS films prepared by vacuum evaporation were found to have a preferred orientation along (0002) hexagonal direction which is in agreement with the TEM results. The optical bandgap of the films was found to be around 2.35 eV.

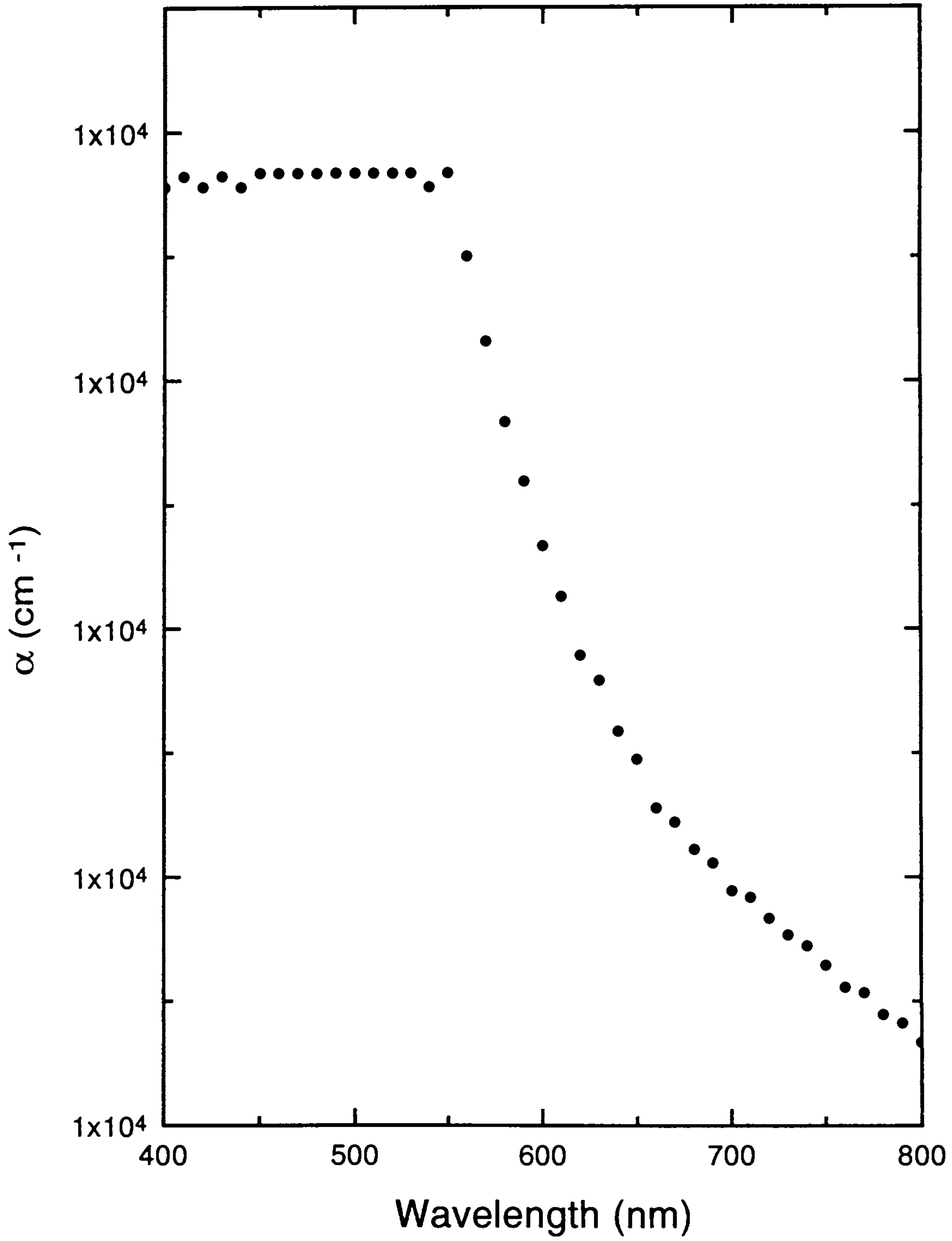

Figure 3.17: Optical absorption spectra of film annealed in vacuum for three hours at 670 K

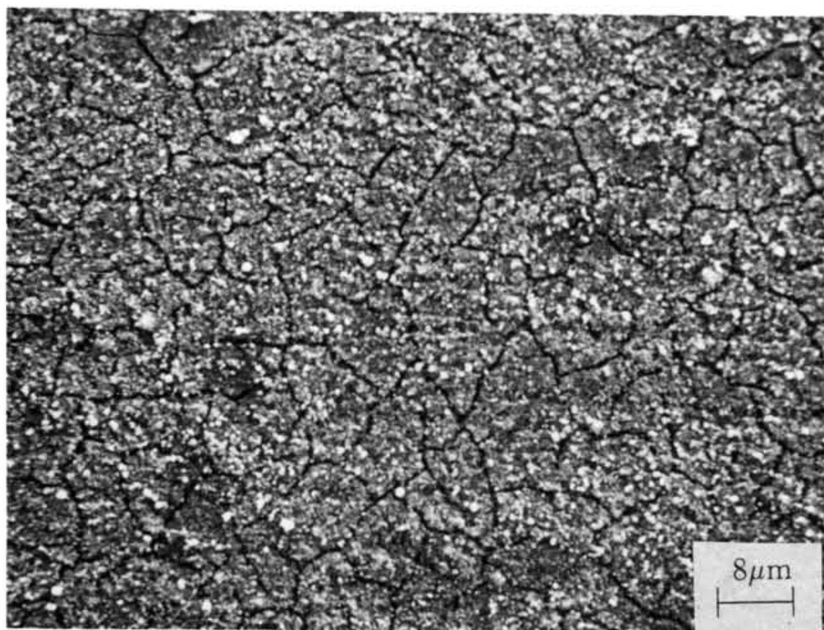

Figure 3.18: Scanning electron micrograph of the films annealed in flowing air for three hours at 673 K

Good quality, adherent films of CdS were prepared by optimizing different process parameters like molar concentration, dipping time and temperature of the bath. It was found that the best quality films of good adhesion and uniformity could be achieved with equimolar concentrations of cadmium and sulphur compounds and a bath temperature of 333 K.

The virgin samples were found to be crystalline, containing both the cubic and hexagonal phases. The films were found to show high resistance, with the resistivity in the range of 10^5 to 10^7 ohm·cm.

The effect of thermal annealing on the structure and optical bandgap is discussed in detail. Evidence for the possible causes, namely, the structural transformation of the films from metastable cubic zinc blende to the stable hexagonal wurtzite phase along with the grain growth were obtained. Optical absorption measurements carried out on the as-deposited and annealed CBD films revealed the bandgap reduction on thermal annealing. The observed shift in E_g has been found to be due to the change in the volume of the unit cell as a consequence of the phase transformation. Films annealed in air at 573 K resulted in the partial conversion of CdS to CdO and consequent decrease in resistivity.

References

[1] C. Cali, V. Daneu, A. Orioli and S. Riva-Sansevirino, Appl. Opt., 15 (1976) 1327

[2] V. Daneu, D. P. DeGloria, A. Sanchez, F. Tong, R. M. Osgood, Jr., Appl. Phys. Lett., 49 (1986) 546

[3] Britt and C. Ferekides, Appl. Phys. Lett., 62 (1993) 2851

[4] B. M. Basol, Sol. Cells, 23 (1988) 69

[5] S. K. Das and G. C. Morris, J. Appl. Phys., 73 (1993) 782

[6] A. G. Stanley, Appl. Solid State Sci., 15 (1975) 251

[7] N. Romeo, G. Sberveglieri and L. Tarricone, Thin Solid Films, 43 (1977) L15

[8] T. Hayashi, T. Nishikura, T. Suzuki and Y. Ema, J. Appl. Phys., 64 (1988) 3542

[9] I. Martil, G. Gonzalez-Diaz, F. Sanchez-Quesada, J. Vac. Sci. Technol. A, 2 (1984) 1491

[10] Steve Pence, Elizabeth Varner and Clayton W. Bates. Jr., Materials Letters, 23 (1995) 13

[11] Steve Pence, Clayton W. Bates. Jr., and Lise Varner, Materials Letters, 23 (1995) 195

[12] I. Kaur, D. K. Pandya and K. L Chopra, J. Electrochem. Soc., 127 (1980) 943

[13] R. L. Call, N. K. Jaber, K. Seshan and J. R. White Jr., Sol. Energy. Mater., 2 (1980) 373

[14] K. L. Narayanan, K. P. Vijayakumar, K. G.M. Nair, N. S. Thampi and K. Krishan, J. Mater. Sci., 32 (1997) 4837

[15] K. L. Narayanan, K. P. Vijayakumar, K. G. M. Nair and G. V. N. Rao, Bull. Mater. Sci., 20 (1997) 287

[16] Ratna Sagar and M. P. Srivastava, Phys. Lett. A, 183 (1993) 209

[17] O. Zelaya Angel, J.J. Alvarado Gil, R. Lozada-Morales, H. Vargas, A. Ferreira da Silva, Appl. Phys. Lett., 64 (1994) 291

[18] O. Zelaya Angel, L. Hernandez, O de Melo, J.J. Alvarado Gil, R. Lozada-Morales, H. Vargas, R. Ramirez-Bon, Vacuum, 46 (1995) 1083

[19] C.M. Dai, L. Horng, W. F. Hsieh, Y. T. Shih, C. T. Tsai and D.S. Chuu. J. Vac. Sci. Technol A, 10 (1992) 484

[20] Optical Processes in Semiconductors,J. I. Pankove, (Dover, Newyork, 1971) page 36

[21] S. G. Mokrushin and Y. D. Tkachev, Colloid. J. USSR., 23 (1961) 336

[22] G. A. Kitaev, A. A. Uritskaya and S. G. Mokrushin, Russ. J. Phys. Chem., 39 (1965) 1101

[23] M. T. S. Nair, P. K. Nair, R. A. Zingaro, E. A. Meyers, Appl. Phys., 75 (1994) 1557

[24] P. K. Nair, M. T. S. Nair, J. Campos and L. E. Sansores, Sol. Cells, 22 (1987) 221

[25] P. K. Nair, J. Campos, M. T. S. Nair, Semicond. Sci. Technol., 3 (1988) 134

[26] W. J. Danaher, L. E. Lyons, G. C. Morris, Sol. Energy. Mater., 12 (1985) 137

[27] A. Mondal, T.K. Chaudhuri, P. Pramanik, Sol. Energy. Mater., 7 (1983) 431

[28] PDF No: 10-454

[29] PDF No: 411049

[30] II Yu, Tetsuhiko ISOBE, Mamoru SENNA, Materials Research Bulletin, 30 (1995) 975

[31] S. S. Kale, V. S. Jadhav, C. D. Lokhande, Ind. J. Pure & Appl. Phys., 34 (1996) 324

[32] R. Jayakrishnan, S. R. Kumar, R. K. Pandey, Semicond. Sci. Technol., 9 (1994) 97

CHAPTER 4

4 EFFECT OF ARGON ION IMPLANTATION IN CdS THIN FILMS

Studies of effects of implantation in III-V and II-VI compound semiconductors are important in view of the extensive applications of these materials in the fabrication of opto-electronic and microelectronic devices. There is extensive literature available on the Raman scattering[1, 2, 3, 4], positron annihilation[5, 6, 7, 8] and optical absorption studies [9, 10, 11] of various compound semiconductors. However, there are not many reports on implantation effects in cadmium sulphide.

Generally, the implantation of ions in semiconductors produces two major effects:- (i) introduction of electrically active dopants and (ii) implantation induced lattice damage. In order to understand these two effects, detailed studies in argon irradiated CdS thin films have been carried out. Argon, being an inert gas is electrically inactive and any effect observed during implantation of argon ions can be exclusively attributed to radiation damage.

In this chapter, effect of implantation of argon ions on films of CdS prepared by chemical bath deposition(CBD) technique is discussed in detail. The films prepared by CBD process were bombarded with argon ions and the films were studied using various techniques such as optical absorption spectrometry, X-ray diffraction, Raman spectroscopy and positron annihilation spectroscopy. Studies were also carried out on the films after post implantation annealing and these results are discussed in detail, in the first part of this chapter.

The second part of this chapter deals with similar studies on the CdS thin films prepared by the thermal evaporation technique. These films of CdS were bombarded with argon ions and Raman scattering studies were carried out on the implanted films. On irradiation,

the films show an interesting phenomena called surface enhanced Raman scattering (SERS) and the results of the detailed study of this phenomenon are discussed. X-ray diffraction measurements were carried out on the vacuum evaporated films in the virgin and implanted conditions.

4.1 Experimental details

CdS thin films were prepared by chemical bath deposition and vacuum evaporation as discussed in the previous chapter. These films were coated on glass substrates which were cleaned as described in section 3.1.2 and were implanted with argon ions of energy 80 keV to different doses in the range of 10^{15} to 10^{17} ions/cm^2. In order to know the profiles of the implanted ions and the defects in CdS film during 80 keV argon implantation, TRIM programme (Transport of Ions in Matter) was used. The typical plots are shown in figure 4.1.

Vacuum in the irradiation chamber was maintained at 10^{-7} mbar. The implantation was carried out at room temperature and the beam current was maintained around 0.8 microamperes to avoid the excessive heating of the sample during implantation. Isochronal annealing of the films was carried out in flowing argon atmosphere at various temperatures in the range of 473 K to 773 K for 2 hours.

The optical absorption spectra of the as deposited and irradiated samples were recorded in the wavelength range 400 to 1100 nm by an UV-VIS-NIR(Chimito 2500) spectrophotometer. The unpolarised Raman spectra of these films were recorded in a Raman spectrometer built around a double grating monochromator(SPEX model 14018). An argon laser, lasing at 488 nm with a power of 50 mW was used as the source. X-ray diffraction analysis was carried out on the samples using Cu-Kα radiation. Positron annihilation spectroscopy measurements were carried out on the as-deposited, irradiated films and on films subjected to post irradiation annealing. Depth selective positron annihilation measurements have been

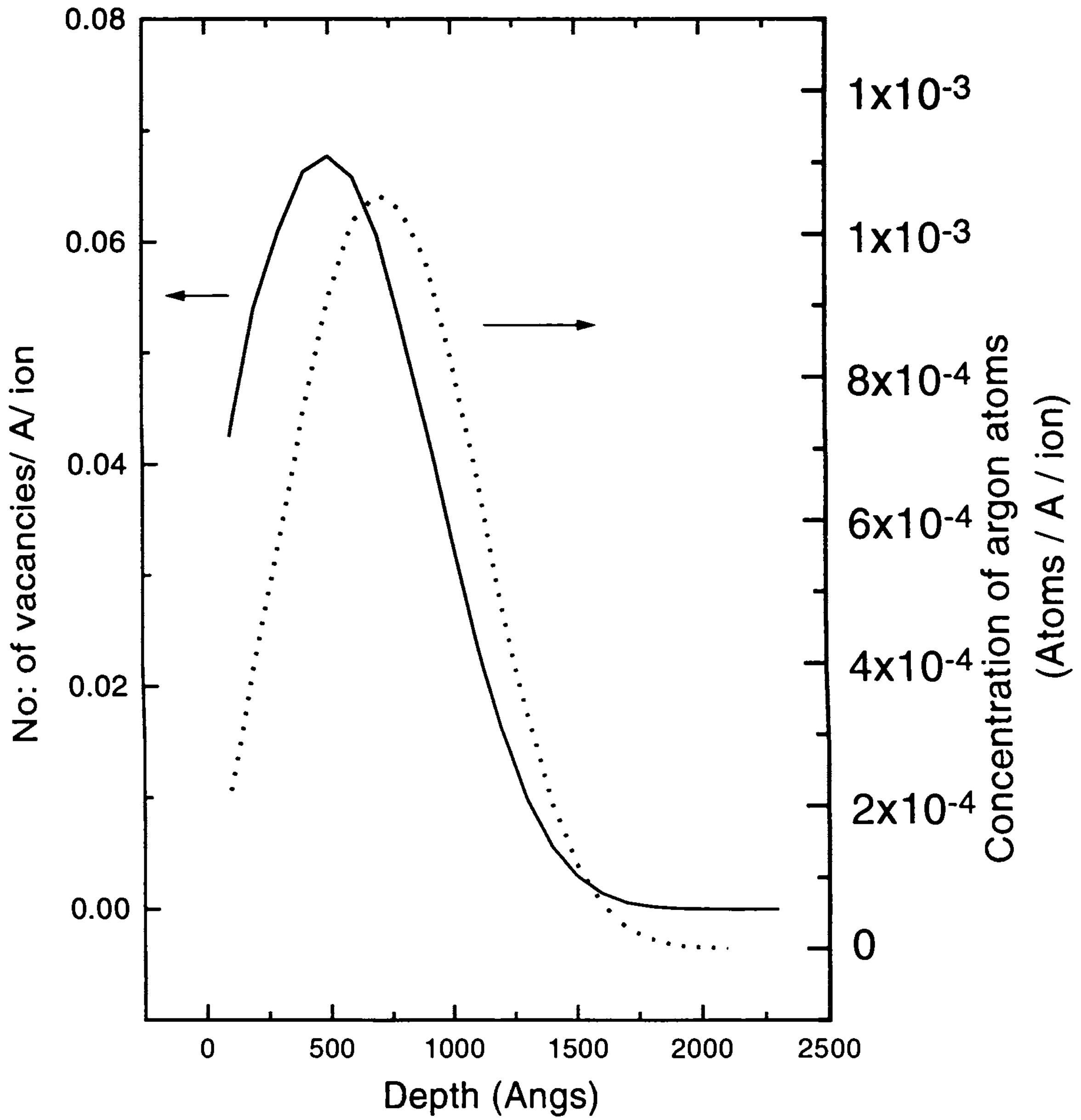

Figure 4.1: TRIM plot showing the implantation (.......) and vacancy profile (——) during argon irradiation at 80 keV in CdS.

made, using the ultra high vacuum compatible variable low energy positron beam. Doppler broadening of the 511 keV annihilation γ ray was measured using a HPGe detector based spectrometer. From these measurements, a line shape parameter (S-parameter), defined as the ratio of the area of the central portion of the Doppler broadened annihilation spectrum to the total photo peak area, is deduced.

4.2 Studies of CdS films prepared by CBD technique

The first part of this chapter presents the results of studies on CdS films, after argon ion irradiation and post irradiation annealing. The studies are mainly pertaining to (a) optical absorption, (b) X-ray diffraction , (c) Raman scattering and (d) positron annihilation measurements.

4.2.1 X-ray diffraction studies

Ion implantation induced lattice damage may give rise to changes in the crystal structure of the sample. Ratna Sagar and Srivastava reported the amorphisation of CdS films due to irradiation with argon ions in a dense plasma focus [12]. X-ray diffraction studies were carried out on the as-deposited and irradiated films as well as on films subjected to post implantation annealing. The results of these studies are discussed in this section.

4.2.2 As-deposited films

Figure 4.2 shows the x-ray diffraction pattern of the as-deposited(CBD) CdS thin film. It is observed from figure 4.2 that the films are crystalline and the films are found to have both cubic and hexagonal phases of CdS. The thiourea peak is seen in the diffraction pattern of the as-deposited film. The contamination due to thiourea in CdS thin films prepared by the chemical bath deposition technique is unavoidable as it is one of the main ingredients in the bath. However, thiourea is volatile and is removed during annealing at high temperature.

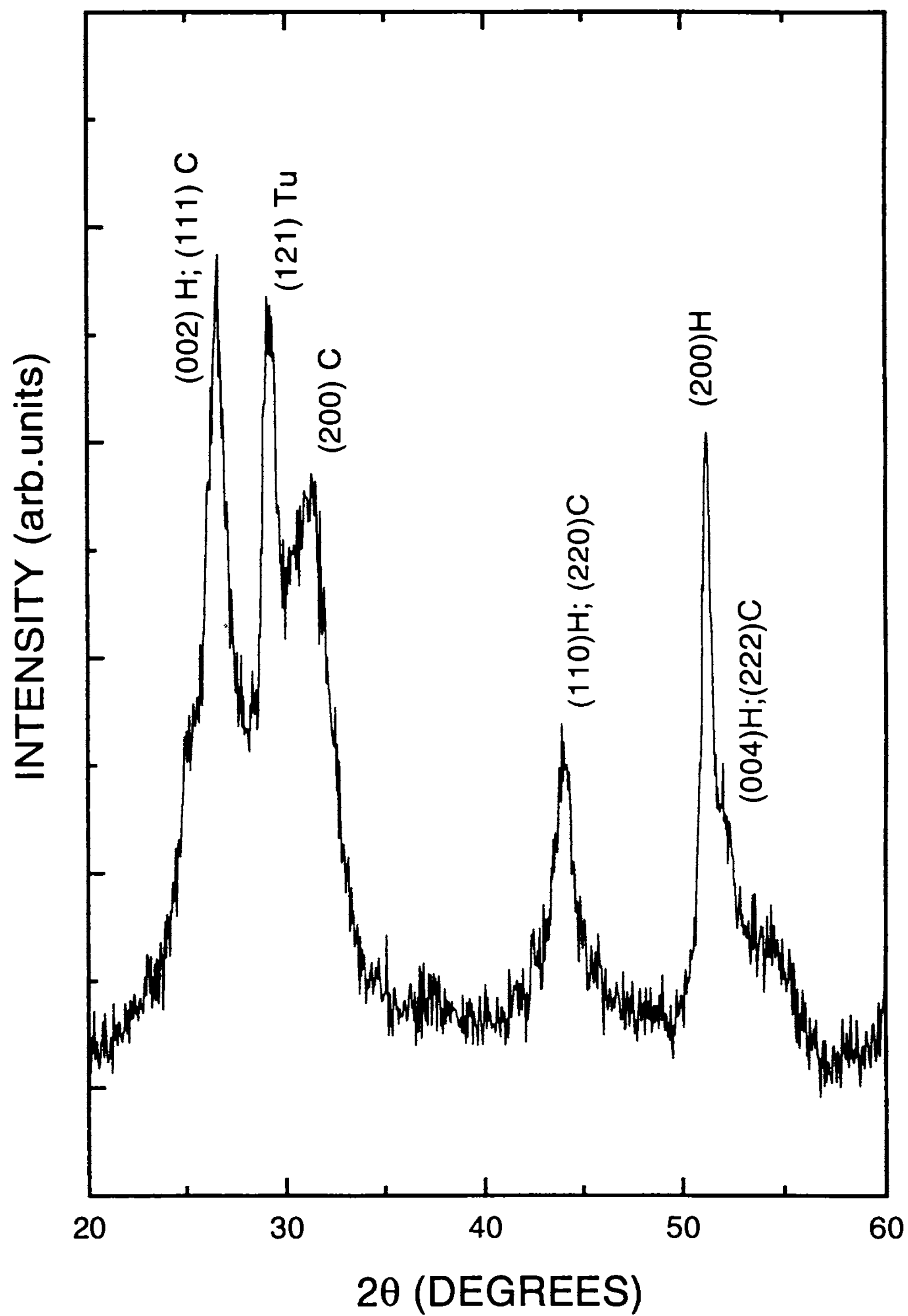

Figure 4.2: X-ray diffraction pattern of as deposited CdS thin film prepared by chemical bath deposition technique. [Cu-Kα radiation was used for the diffraction studies]

4.2.3 Effect of irradiation

Figure 4.3 shows the x-ray diffraction pattern of the argon ion irradiated thin film. In addition to the diffraction peaks of CdS, there is a peak at 38.4°. Based on careful analysis of the XRD pattern, it is seen that the peak appearing at $2\theta = 38.4^{o}$ matches well with Cd (101) as well as CdO (200). However, the formation of CdO phase is unlikely because properly mass analysed argon ion beam was used for the implantation and the vacuum during the implantation was better than 10^{-7}mbar. On argon ion implantation, there is a possibility of loss of sulphur atoms, and cadmium clusters could form in the CdS matrix. Hence, it is probable that the new peak appearing at $2\theta = 38.4^{o}$ is due to metallic cadmium clusters. Similar effect has been reported by Mady *et al* [13]. They have investigated the effect of nitrogen implantation in ZnS films and observed the formation of zinc clusters on nitrogen ion irradiation.

4.2.4 Effect of post irradiation annealing

X-ray diffraction pattern of CdS thin film after the post implantation treatment at 673 K for 2 hours in argon atmosphere is shown in figure 4.4. The peak that was exclusively due to the cubic phase at $2\theta = 30.4^{o}$ disappeared completely. The peak appearing at $2\theta = 28.4^{o}$ corresponding to thiourea also disappeared. Thiourea being volatile could have evaporated at the annealing temperature of 673 K. Many new peaks corresponding to the hexagonal phase have appeared in the diffraction pattern of the films subjected to post implantation annealing. These observations suggest that the cubic phase which is metastable, has got transformed to the stable hexagonal phase. In addition, there is a pronounced sharpening of the peaks on annealing the implanted films probably as a consequence of grain growth. A number of investigators have reported similar transition from cubic to hexagonal phase on thermal annealing [14, 15].

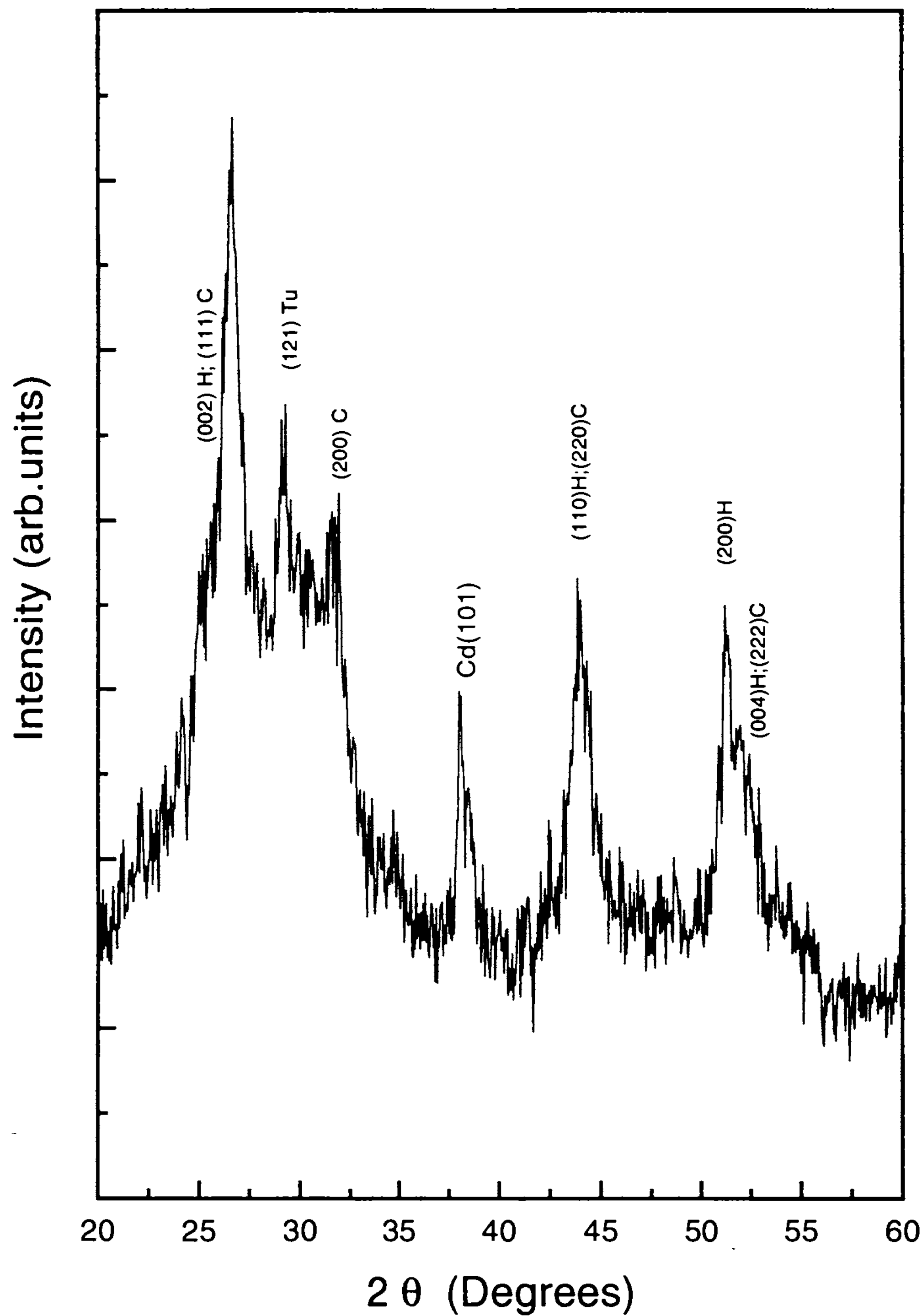

Figure 4.3: X-ray diffraction pattern of argon implanted (80 keV) CdS thin film(5×10^{16} ions/cm^2)

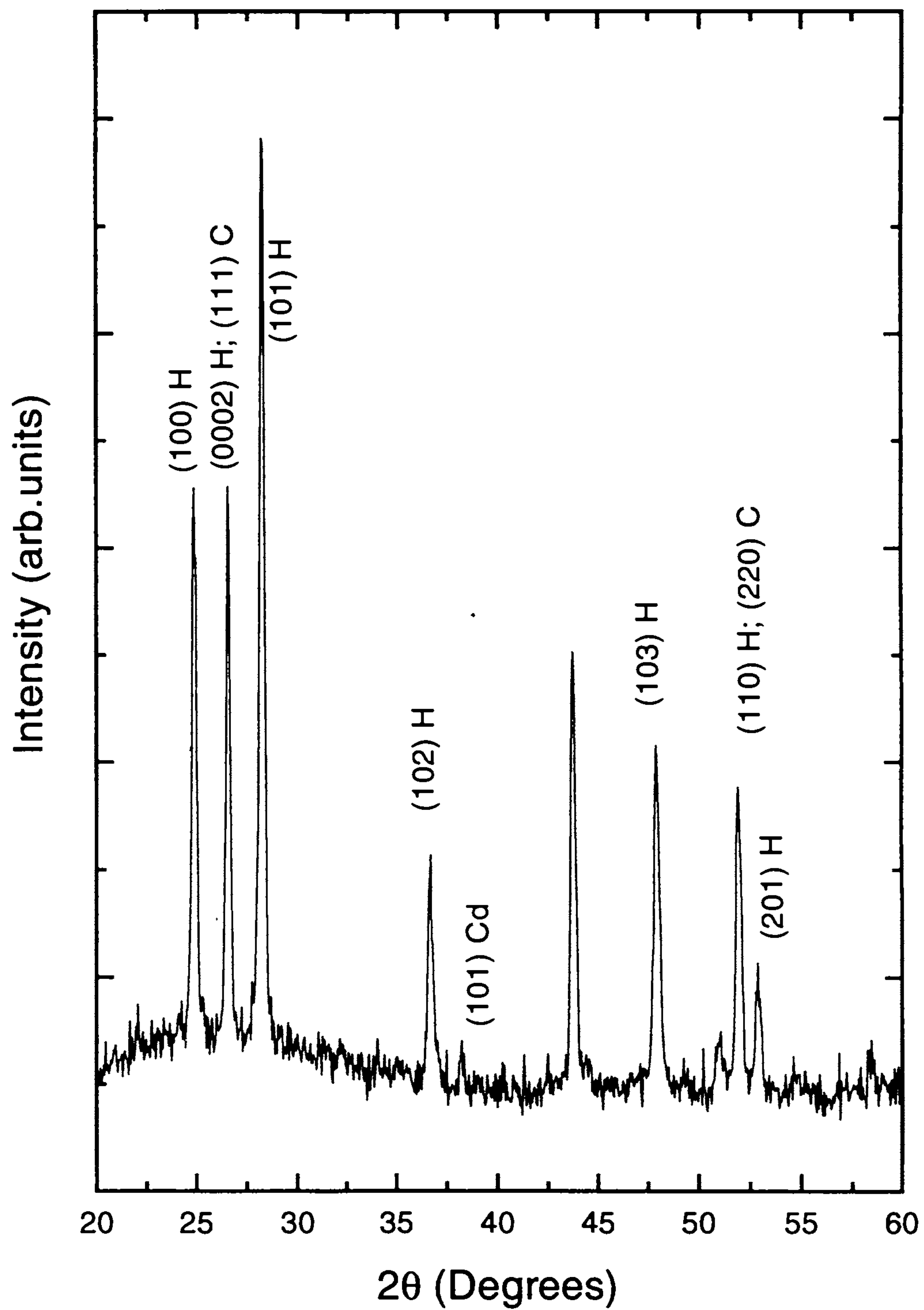

Figure 4.4: X-ray diffraction pattern of CdS thin film after the post implantation treatment at 673 K for 2 hours in an argon atmosphere

4.3 Optical absorption studies

Optical absorption measurements were carried out on the as-deposited, irradiated and subsequently annealed thin films of CdS prepared by chemical bath deposition technique. The effect of irradiation induced lattice disorder in the optical absorption spectra and the recovery of the optical properties on isochronal annealing are discussed in detail.

4.3.1 As-deposited films

Figure 4.5 shows the optical absorption spectrum of the as-deposited CdS thin film prepared by CBD. This figure is a plot between α, the absorption coefficient of the film and wavelength of the incident light. The optical bandgap can be found by plotting $(\alpha)^2$ vs $h\nu$ and extrapolating the linear portion of the curve to intersect the energy axis (inset in fig 4.5). The bandgap of the films was found to be 2.42 eV, which matches well with the earlier reports [16, 17]

4.3.2 Effect of Irradiation

Optical absorption spectra of irradiated films are given in figure 4.6. In figure 4.6, the spectrum of the as-deposited film is also given to compare with the spectra of the irradiated films. A careful examination of these optical absorption spectra reveals the shifting of the absorption edge to higher wavelengths with increase in the irradiation dose, suggesting a decrease in the optical bandgap. It is found from the figure 4.6 that the absorption coefficient has an exponential tail in the spectra of the implanted films. A plot is drawn between $(\alpha)^2$ and $h\nu$ and is given in figure 4.7. The optical bandgap can be found by extrapolating the linear portion of the curve to intersect the energy axis as done in Figure 4.5. It is clearly seen from the figure 4.7 that the sharpness of the band edge decreases with the implantation dose.

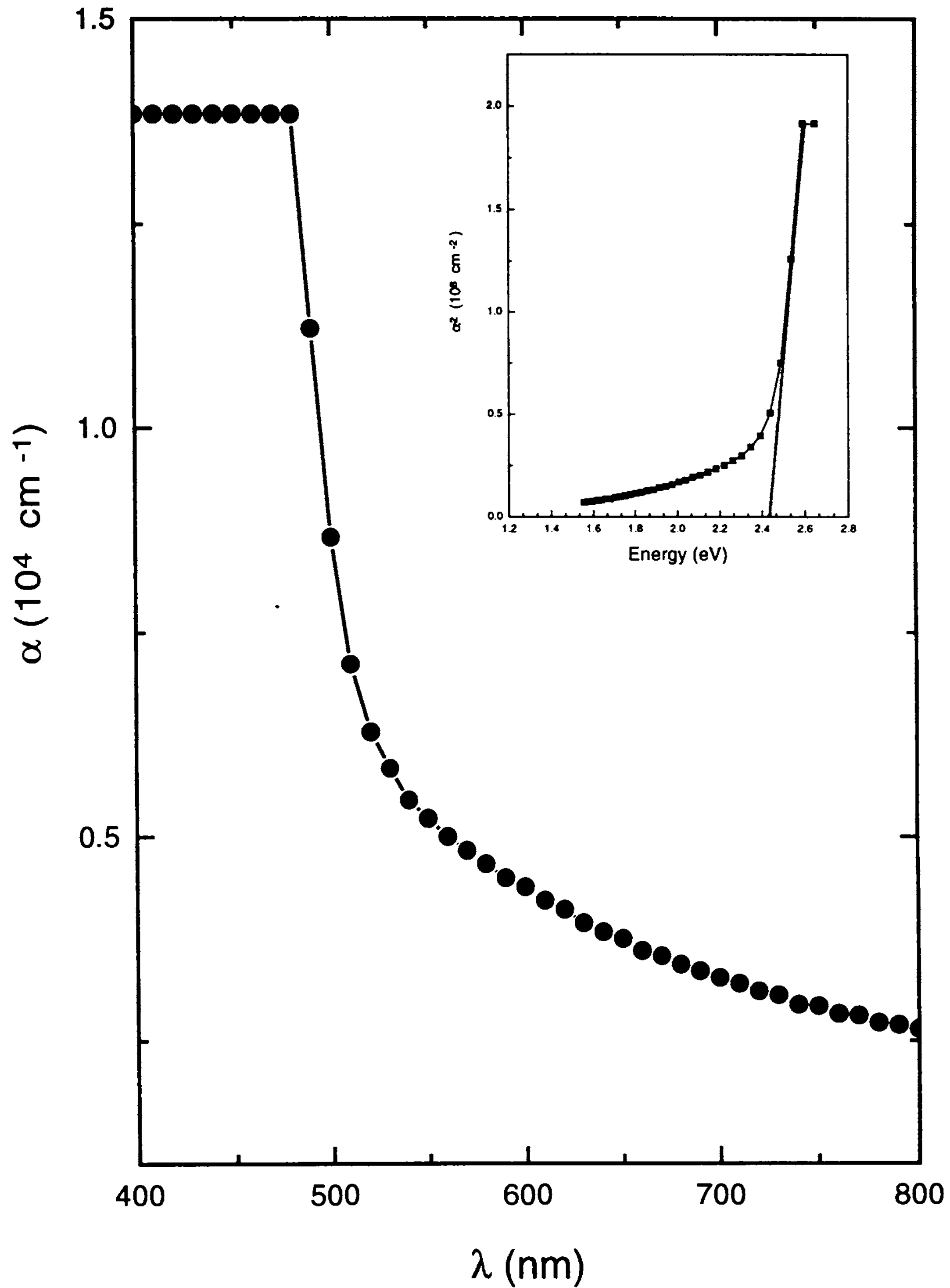

Figure 4.5: Optical absorption spectrum of as-deposited thin film of CdS. The optical bandgap(E_g) of the CdS film can be determined by plotting a graph between α^2 and hν and by extrapolating the linear portion of the curve to the X-axis (inset of figure 4.5)

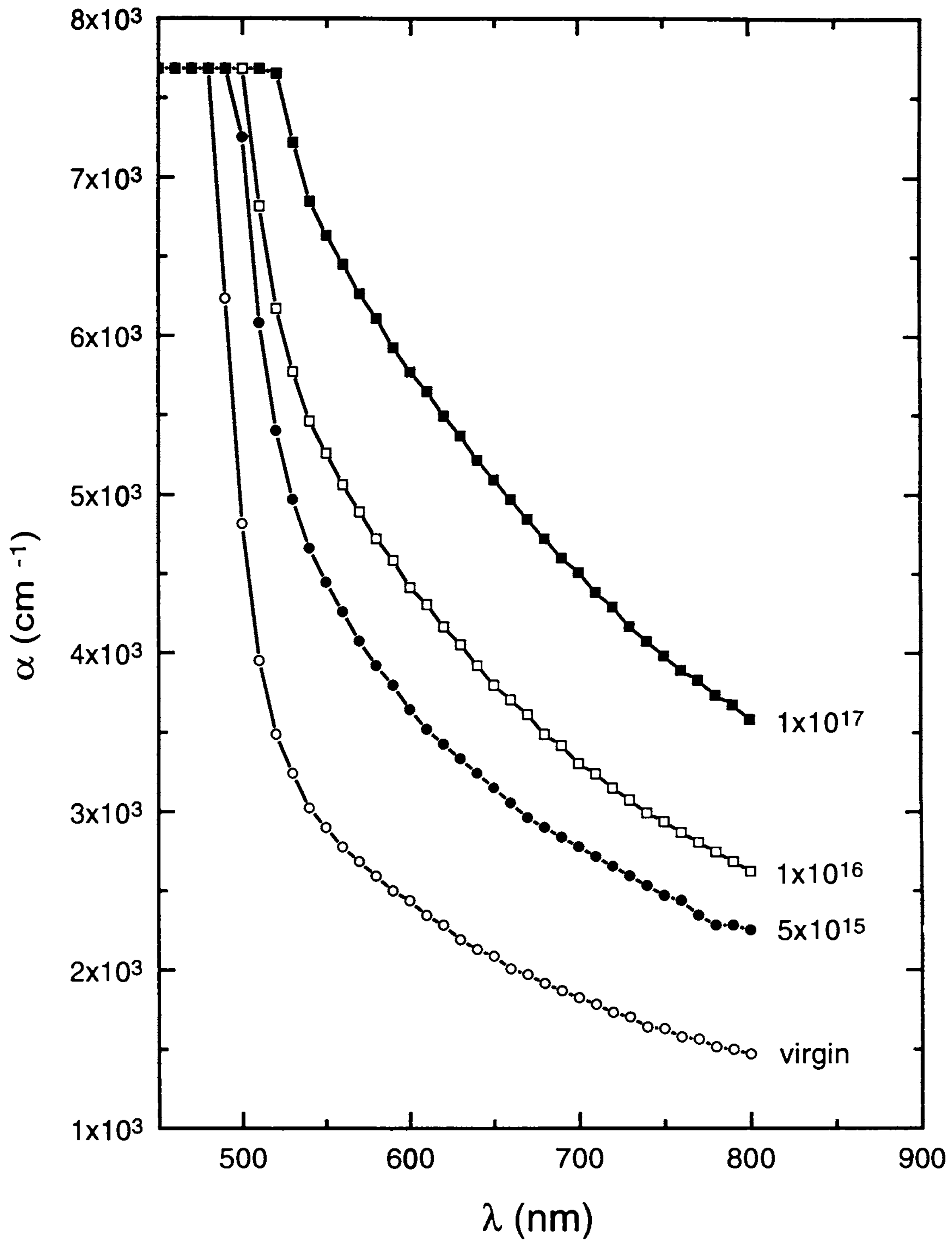

Figure 4.6: Optical absorption spectra of as-deposited and irradiated films;(o-o-o) As-deposited; (•-•-•) dose 5x10^{15} ions/cm^2; (□-□-□) dose 1x10^{16} ions/cm^2; (■-■-■) dose 1x10^{17} ions/cm^2

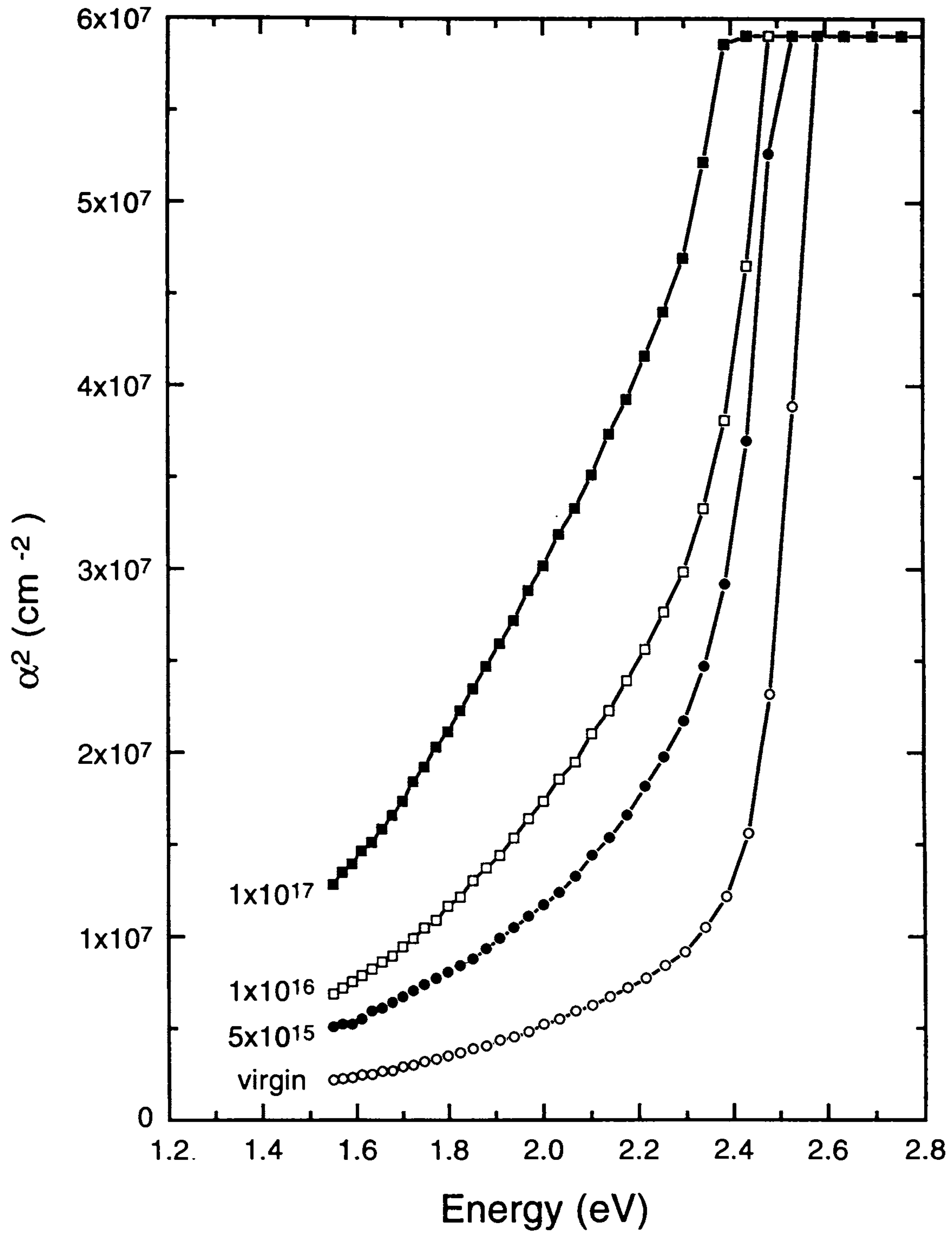

Figure 4.7: Plot showing α^2 versus energy for the as-deposited and implanted films. (o-o-o) As-deposited; (•-•-•) dose 5x10^{15} ions/cm^2; (□-□-□) dose 1x10^{16} ions/cm^2; (■-■-■) dose 1x10^{17} ions/cm^2

Exponential optical absorption edges(or Urbach edges) are frequently encountered in the study of optical properties of crystalline and amorphous semiconductors and insulators [18]. Although there are unresolved aspects in the theory, there is general agreement, that the width of the exponential tail is a direct measure of the temperature-induced disorder for crystalline semiconductors and reflects the thermal occupancy of phonon states in the crystal [19, 20].

Zammit *et al* [21] have carried out a detailed study of the implantation-induced lattice damage in Si on sapphire, using optical absorption measurements. They carefully studied the changes induced in the optical bandgap, band edge slope and the subgap features of the spectra. Optical absorption studies of structural relaxation during annealing of ion implanted a-Si were carried out by Zammit *et al* [21] and they attributed the increase in the bandgap of the material to the reduction in strain associated with the relaxation processes during annealing. They have also observed progressive sharpening of the band edge with annealing suggesting a reduction in the lattice damage.

Cody *et al* studied the disorder and its effect on the optical absorption edge of hydrogenated amorphous silicon [22]. Pankove investigated the impure GaAs using the optical absorption [23] and has attributed the exponential absorption edge of GaAs to the presence of tail states. The distribution of these tail states appeared to be exponential and varied with energy as $\exp(E/E_o)$ where E_o, the inverse logarithmic slope, increased with doping. Kekelidze has reported [11] the electrical and optical properties of InAs and InP compounds irradiated with 50 MeV electrons.

In the present study, the optical bandgap E_g is shown as a function of the irradiation dose in figure 4.8, where a progressive reduction of band gap with an increase in the irradiation dose is observed. Further, it is seen that the absorption coefficient increases with irradiation dose. The absorption coefficient of the films at 510 nm is plotted as a function of irradiation dose in figure 4.9.

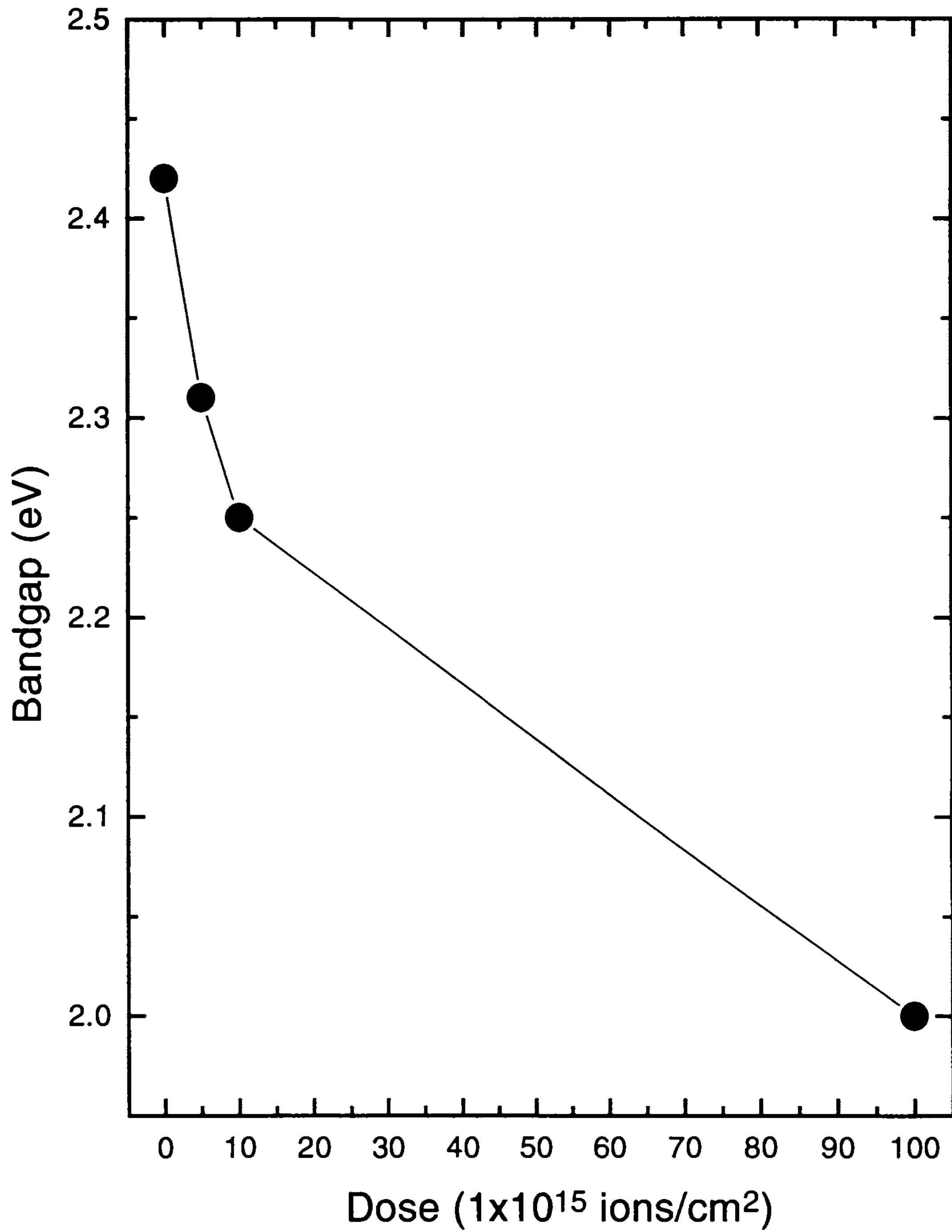

Figure 4.8: Variation of the optical bandgap E_g as a function of irradiation dose

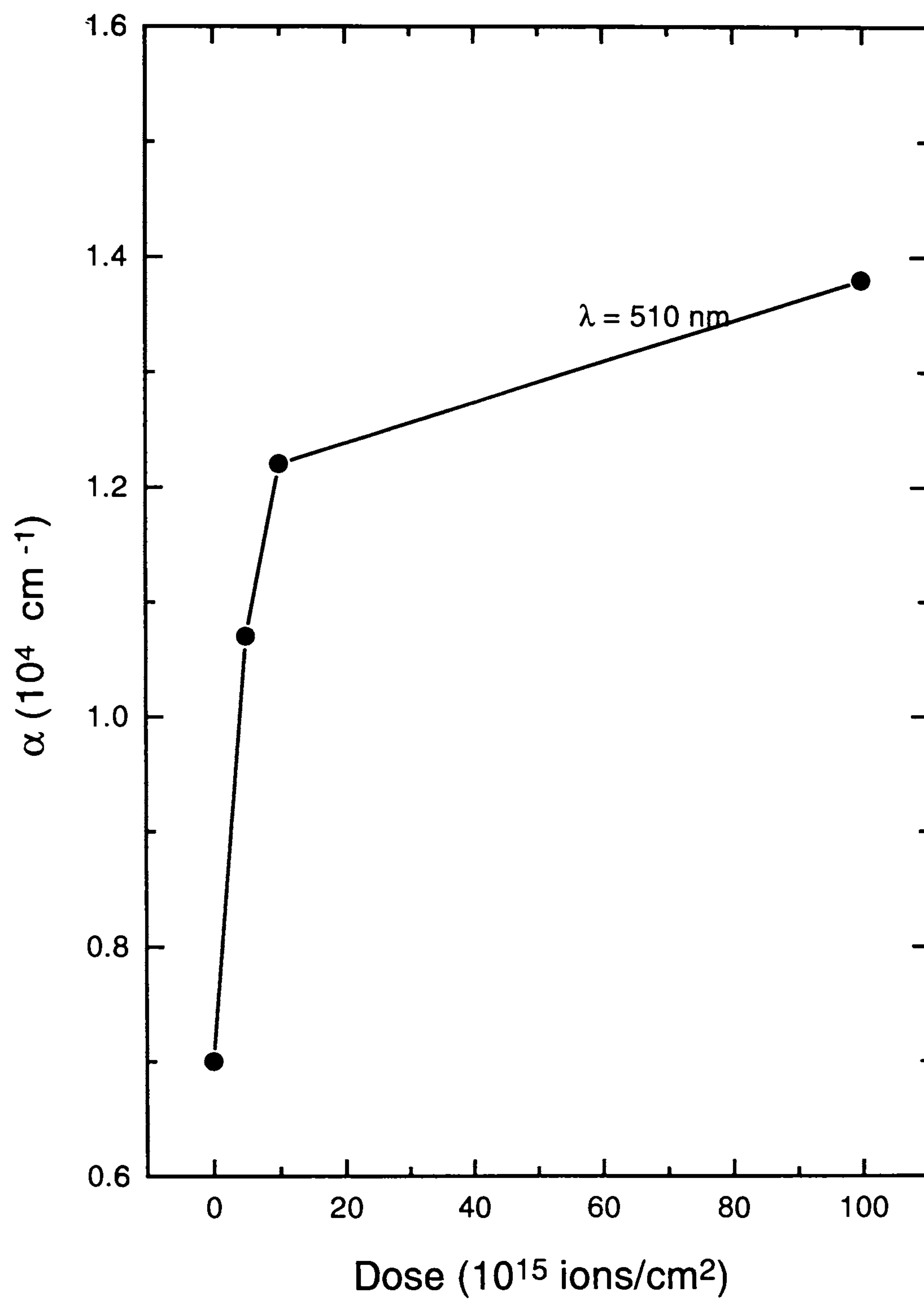

Figure 4.9: Variation of absorption coefficient of the film at 510 nm with irradiation dose

The increase in the absorption during irradiation can arise due to several factors; (i) increase in the carrier concentration due to implantation, (ii) production of metallic cadmium clusters due to the loss of sulphur or (iii) production of defect levels in the bandgap. Each of this absorption process has its characteristic energy dependence [24]. The clear exponential increase of absorption coefficient with energy in the present case strongly suggests that the increased absorption is primarily due to the production of defect levels in the bandgap.

Another parameter which is significantly affected by irradiation induced disorder is the sharpness of the band edge, which is found to reduce with the increase in the irradiation dose. In order to quantify the sharpness of the band edge, it is common practice [21] to fit the absorption coefficient, α, in the band edge region to a function of the form

$$\alpha = \alpha_o \exp(E/E_o) \tag{1}$$

E_o is normally referred to as the inverse logarithmic slope. Figure 4.10 shows the variation of E_o with irradiation dose and E_o is found to increase with irradiation dose. Irradiation with Ar^+ ions produces point defects such as vacancies, interstitials and antisite defects. Defect clusters such as argon bubbles, dislocation loops etc., can also form during irradiation. These defects produce band tailing. The observed reduction in the optical band gap as well as the loss of sharpness of the absorption edge arise due to band tailing. The relationship between the lattice disorder, the band edge sharpness and the optical band gap had been first established by Cody *et al* [22] for explaining the optical absorption characteristics of hydrogenated amorphous silicon. They considered the static structural disorder caused by defects and dynamic phonon disorder both of which have the same effect on the electronic energy levels under adiabatic approximation.

The relationship between E_o and the irradiation induced disorder has the form

$$E_o(T,X) = \frac{\theta}{\sigma_o}\left[\frac{1+X}{2} + \frac{1}{\exp(\theta/T)-1}\right] \tag{2}$$

where θ is a characteristic temperature related to the Debye temperature, $\theta = 4\theta_D/3$. $X = \langle U^2 \rangle_x / \langle U^2 \rangle_o$ is the ratio of the mean square deviation of atomic positions caused

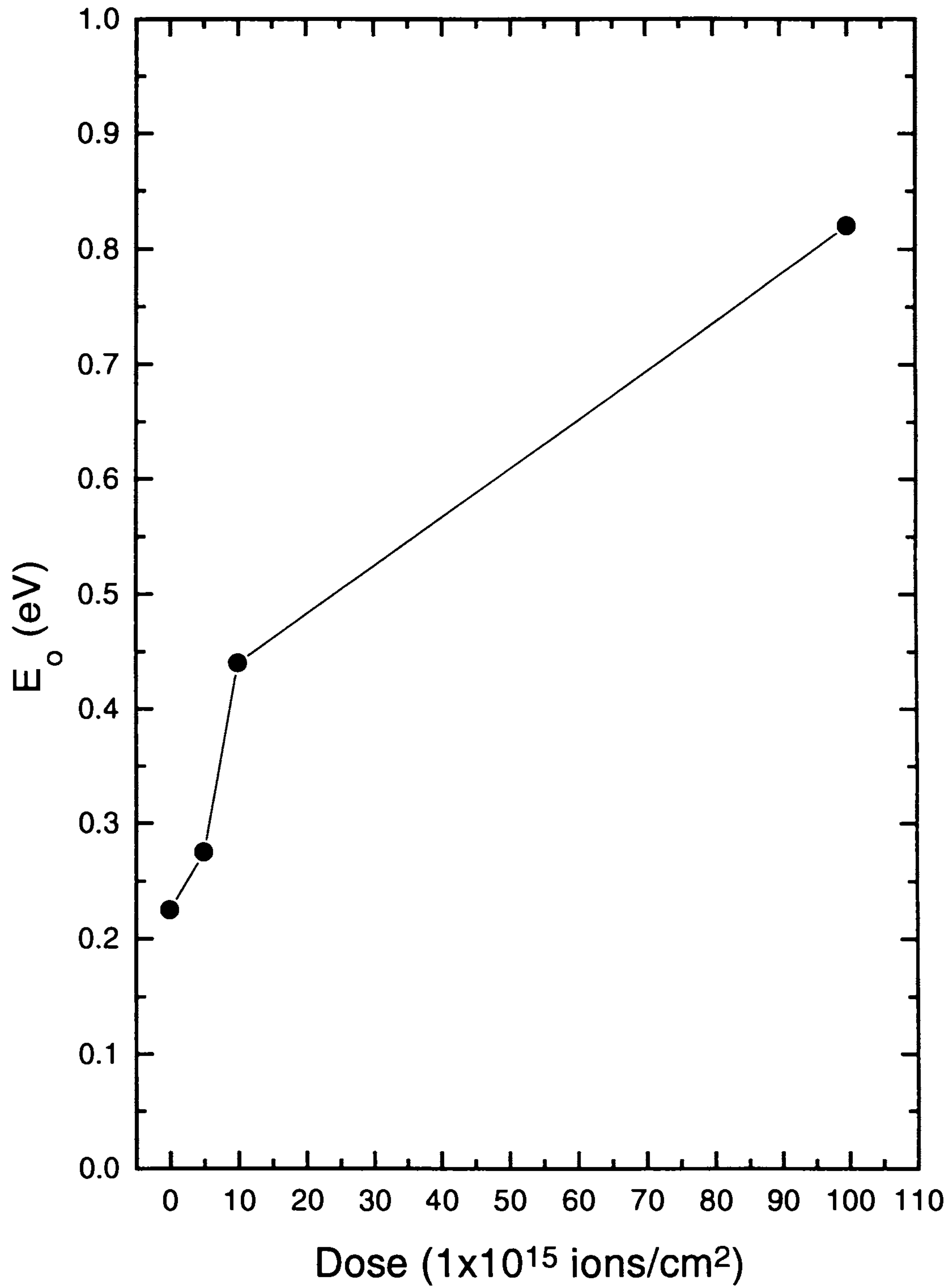

Figure 4.10: Variation of inverse logarithmic slope E_o with irradiation dose

by structural disorder to $< U^2 >_o$ the zero point uncertainty in the atomic positions, σ_o is the Urbach's edge parameter of the order of unity. They have also provided a relationship between the bandgap E_g and the width of the absorption edge E_o

$$E_g(T,X) = E_g(0,0) - < U^2 >_o D \left(\frac{E_o(T,X)}{E_o(0,0)} - 1 \right) \quad (3)$$

where $E_g(0,0)$ and $E_o(0,0)$ are the values of E_g and E_o in a defect free crystal at 0 K and D is the second order deformation potential. Equation 3 suggests a linear relationship between E_g and E_o. The optical bandgap of the unirradiated CdS film and those of irradiated samples are plotted as a function of the corresponding E_o values in figure 4.11. A good linear dependence between E_o and E_g can be seen from figure 4.11. The observed strong correlation between E_g and E_o suggests that the decrease in band gap as a result of irradiation is predominantly due to lattice disorder produced during irradiation. Similar observations have been reported in earlier studies [22, 25].

4.3.3 Effect of post irradiation annealing

Post-irradiation annealing studies were carried out on a sample irradiated with 80 keV Ar^+ ions to a dose of 5 x 10^{16} ions/cm^2 . The optical absorption spectra of the as-deposited, irradiated and annealed samples are given in figure 4.12. The isochronal annealing upto a temperature of 573 K did not give rise to any significant change in the optical absorption spectra of the sample as can be seen from figure 4.13 where the absorption coefficient at λ = 510 nm is shown as a function of annealing temperature. A sharp reduction in absorption is seen on annealing at 573 K. The bandgap is found to increase on annealing and recovers back to the as deposited value when annealed at 773 K for two hours (figure 4.14). The band edge also progressively sharpens on annealing and the inverse logarithmic slope value E_o, returns to the as deposited values at 773 K. The increase in the value of the bandgap and sharpening of the band edge suggest a reduction in the degree of lattice disorder, as a consequence of annealing of defects. The near complete recovery of these parameters to the pre-irradiation values indicates that almost complete annihilation of the defects produced

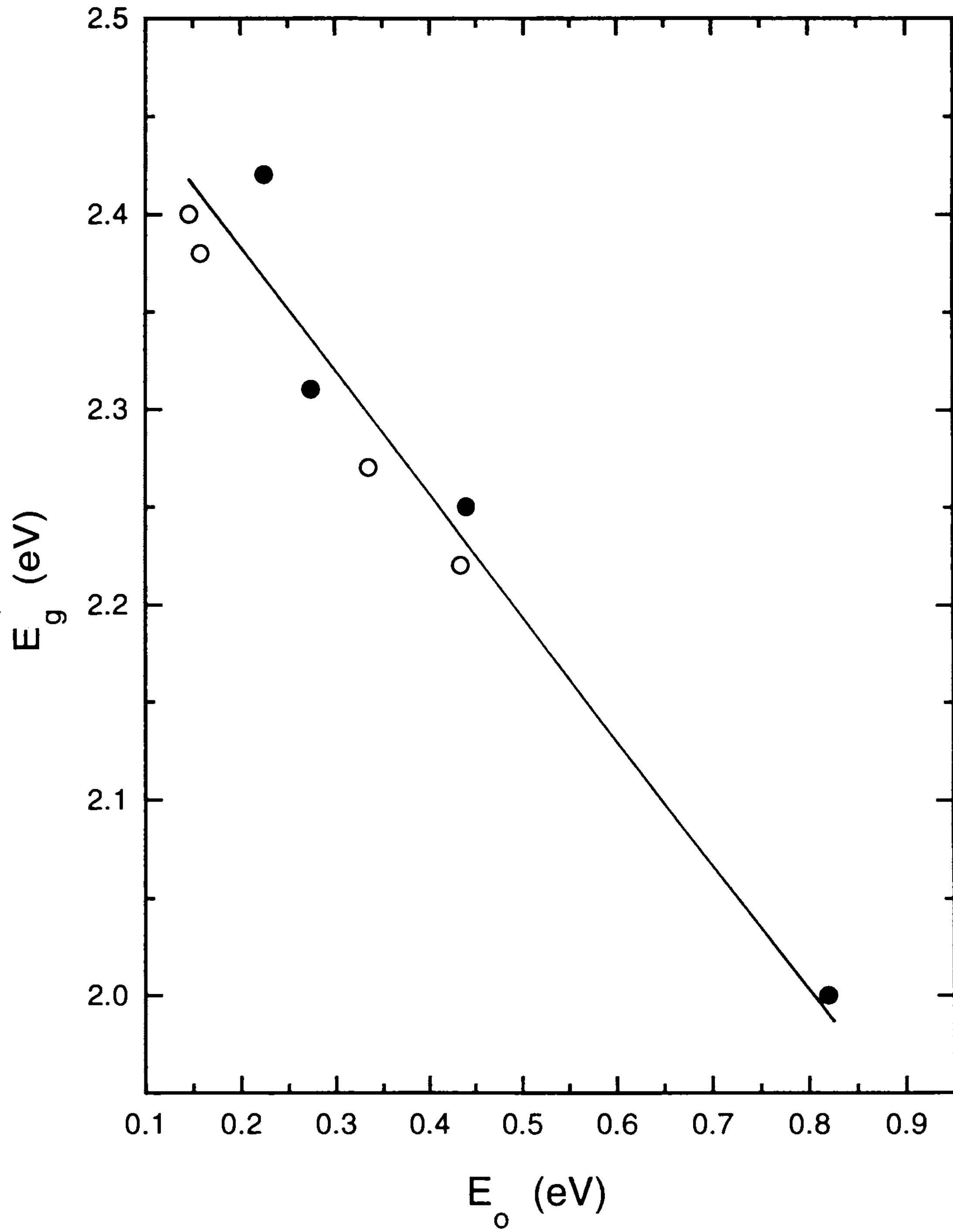

Figure 4.11: Variation of bandgap E_g with inverse logarithmic slope E_o; (o) implantation; (•) annealing;

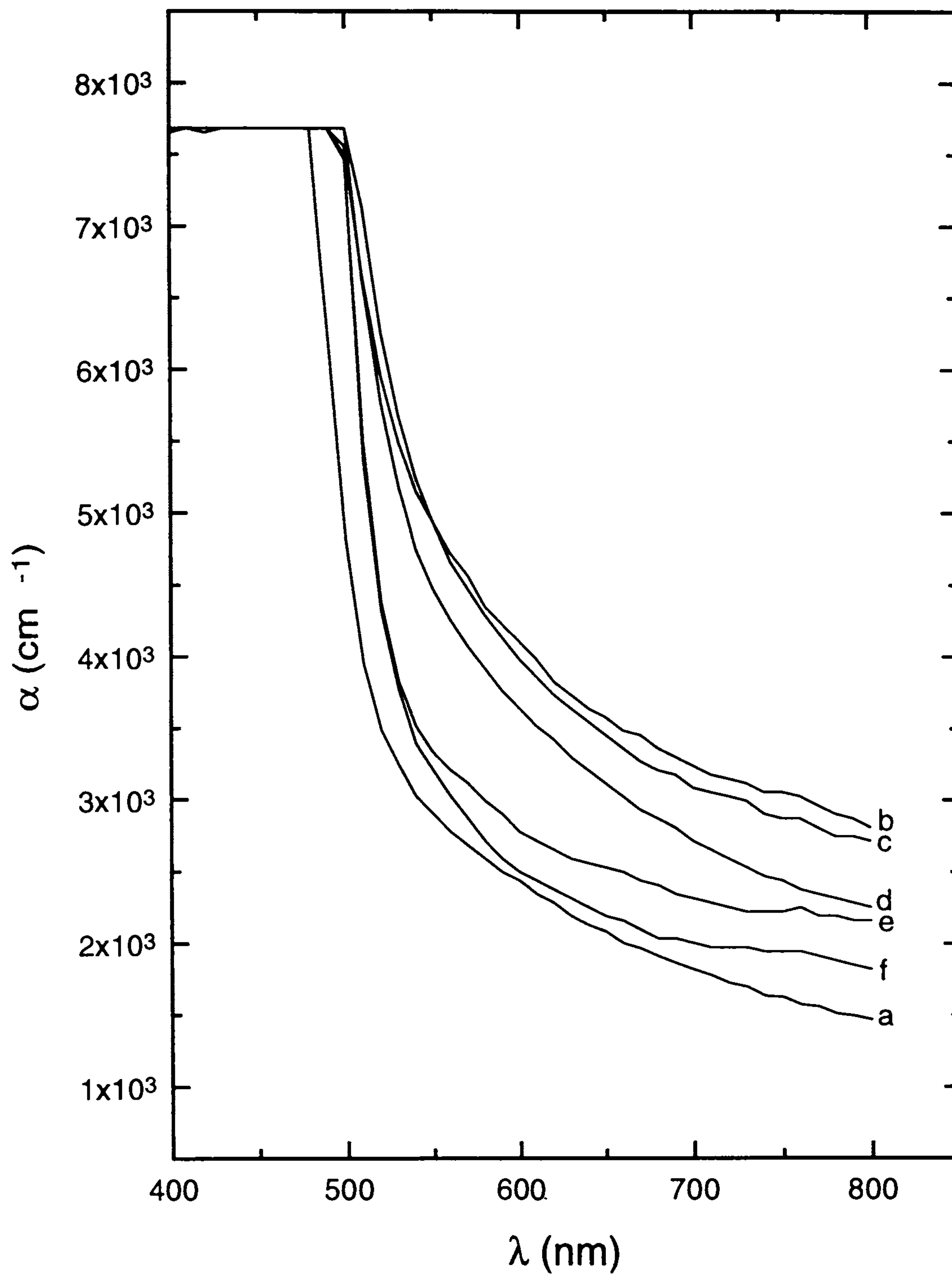

Figure 4.12: Optical absorption spectra of CdS thin film in the as-deposited condition, after implantation to a dose of $5x10^{16}$ ions/cm^2 and after various stages of isochronal annealing; (a) as-deposited; (b) implanted; (c) annealing at 473 K; (d) annealing at 573 K; (e) annealing at 673 K; (f) annealing at 773 K. [Annealing was carried out for 2 hours]

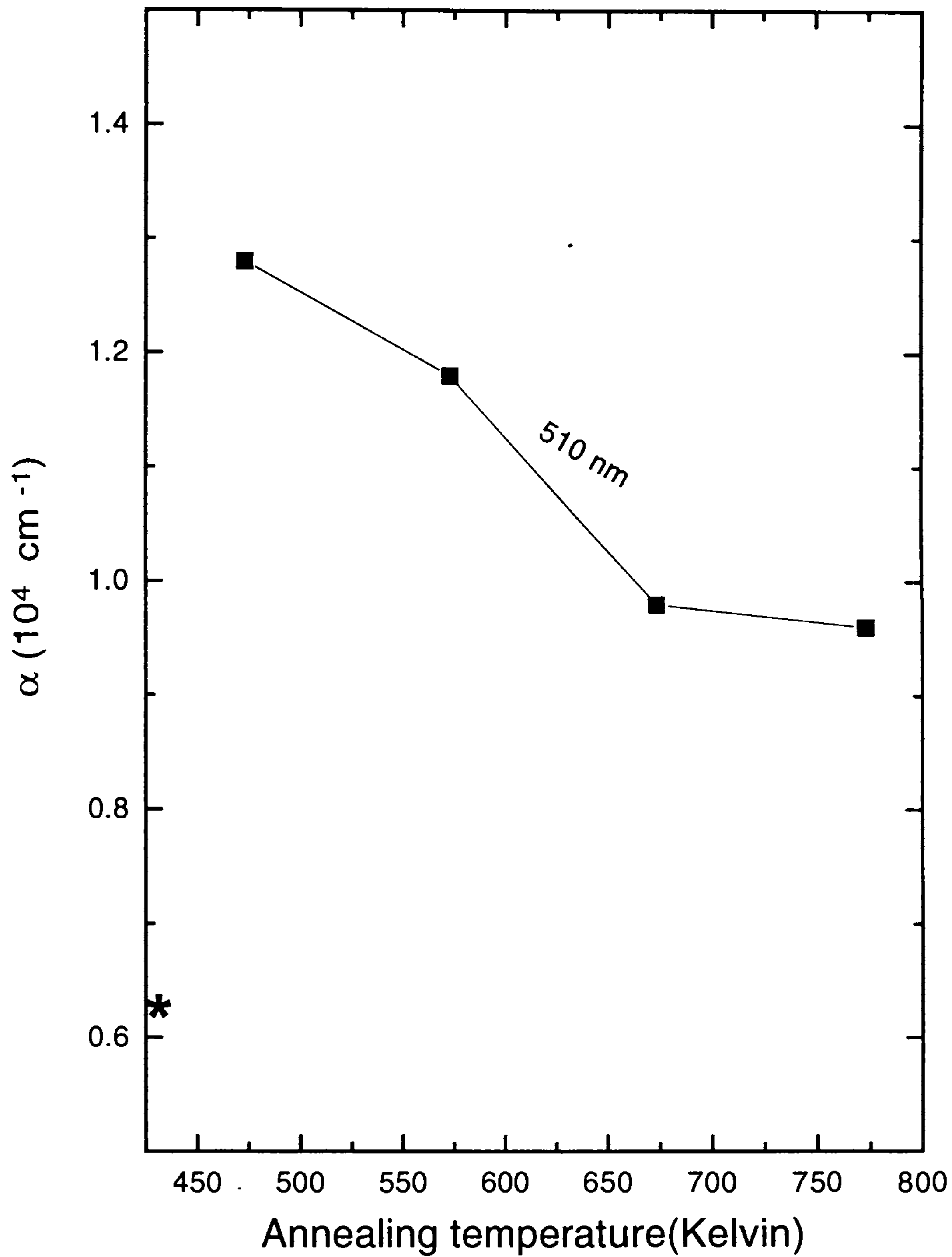

Figure 4.13: Absorption coefficient of the films at 510 nm as a function of annealing temperature. The absorption coefficient values of the as-deposited film is marked by ⋆ on the Y axis

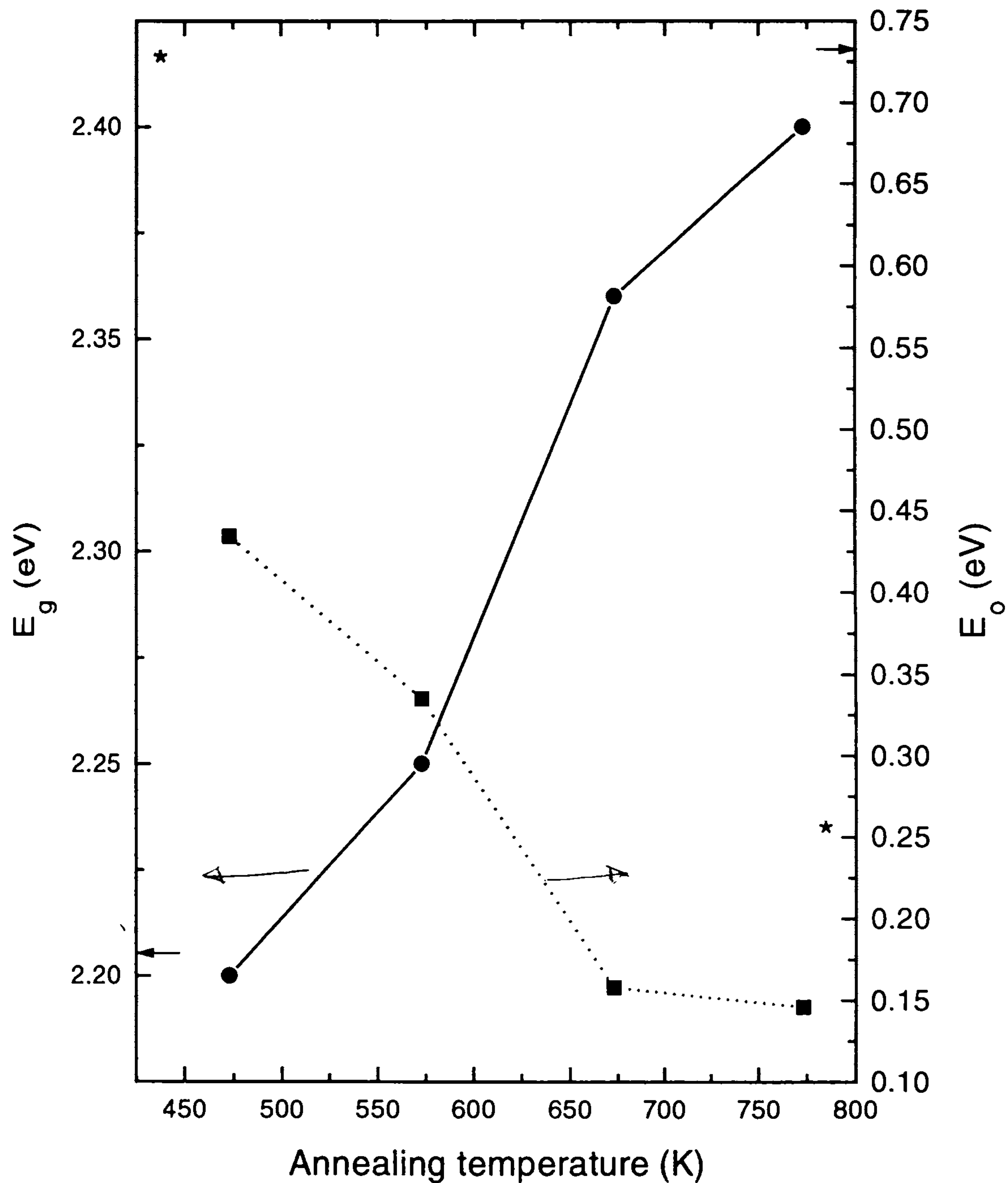

Figure 4.14: Variation of E_o and E_g during post implantation annealing shown as a function of annealing temperature.(E_o and E_g values of the as-deposited samples are marked by $\star$ on the corresponding axes. The arrow marks on the axes indicate the as-irradiated values)

during irradiation has occurred. However, the absorption coefficient does not completely recover to the as-deposited value on annealing, as seen from figure 4.13. The possible reasons for this are the following: Though most of the defects produced during implantation would get annealed, the implanted argon atoms would be still retained in the matrix. Further, the quality of the film could also reduce substantially during annealing giving rise to cracking. The remnant absorption might be attributed to such effects. It is interesting to note that though the absorption coefficient does not completely recover back to as deposited value during annealing, E_o and E_g values practically reduce to the as-deposited values. This observation is significant. If the residual absorption is due to argon atoms substitutionally incorporated in the CdS matrix, the effect of strain created by the accommodation of such atoms should also have been observed. Since E_o and E_g which are very sensitive to matrix strain recover to original values, it is unlikely that argon atoms are still retained in the matrix. However if argon atoms cluster to form bubbles during annealing, the strain due to the accommodation of argon atoms would be relieved. The bubbles may still reduce the optical quality of the film and give rise to increased absorption. The linear relationship between E_o and E_g is also obeyed during annealing, as can be seen from figure 4.11, where E_o and E_g values obtained from various absorption spectra recorded during annealing are also included. Defects produced during implantation are one of the major causes for the change in the optical properties of the system, which have been presented above.

Having discussed the effect of irradiation induced disorder in the optical absorption spectra of films of CdS prepared by chemical bath deposition method, the Raman scattering studies on the films is discussed in the next section.

4.4 Raman scattering studies

Raman scattering is yet another technique ideally suited for probing the lattice damage in semiconductors introduced during implantation. Several studies in the past [1, 2, 3, 4] have shown that Raman scattering is a very sensitive technique for studying the lattice damage

produced during implantation since the thickness of the damaged layer and the optical skin depth are essentially of the same order.

Implantation of energetic ions into a host lattice like cadmium sulphide, can cause various effects. These are (i) possibility of a contraction of the bond between the cations and anions, (ii) possibility of the bond dilation between the cations and anions and (iii) also a chance of break up of bonds between the atoms. Any one of these events or all these events combined together would shift the Raman line to the lower wave number side or decrease the intensity of the Raman peak. The broadening of the Raman line during irradiation [26] was observed by various investigators and they attribute this either to the defects present in the material or to the lattice damage/disorder of the system caused during ion implantation.

One of the most striking features of the Raman spectrum of CdS is the remarkable overtones series of the longitudinal optical (LO) phonons [27, 28]. Both cubic and hexagonal phases of CdS give rise to the A_1(LO) phonon mode at about 305 cm^{-1}. Raman scattering studies of CdS in the form of thin films [29], doped glass [30], and colloid aqueous suspensions [31] have been reported.

4.4.1 As deposited films

A typical Raman spectrum of the as-deposited CdS thin film is shown in figure 4.15. The Raman peak arises from the A_1(LO) mode of CdS and it is consistent with the earlier investigations [32, 33]. It is common in all spectroscopic studies that the observed spectrum is a convolution of the true spectrum, characteristic of the processes that take place in the system under study, and the spectrometer resolution function arising from the finite slit width of the instrument. The spectrometer resolution function can be approximated by a Gaussian, when the resolution is limited by the aberrations and diffractions at various optical components in the spectrometer, and by a triangular function when the resolution is slit width limited. Although valuable information can be obtained by analyzing the complete

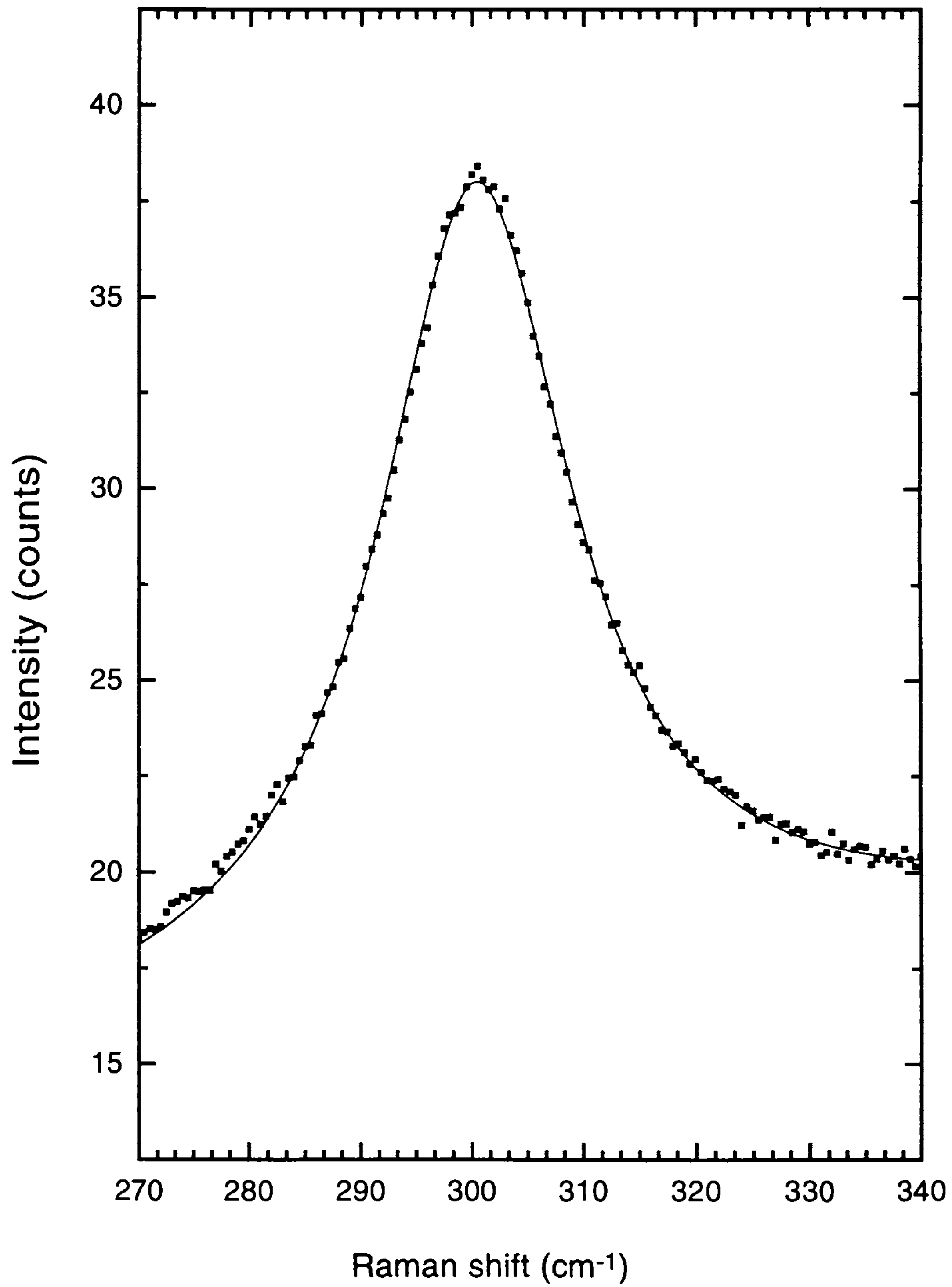

Figure 4.15: Raman spectrum of as-deposited film of CdS along with Lorentzian fitting

line shape, it is often sufficient to work with parameters like FWHM, peak intensity, or the integrated intensity of the true spectrum. The observed Raman spectrum is the convolution between the true Raman spectrum and the spectrometer resolution function having a FWHM of 4.2 cm^{-1}. The true FWHMs of the Raman modes and the true height were deduced from the observed values using the empirical relations given by Arora and Umadevi [34].

A Lorentzian line shape is fitted to the Raman spectrum from which the peak position, full width at half maximum (FWHM) and the area under the Raman peak have been obtained. No asymmetry in the lower wavenumber side of the peak is seen in the spectrum. Raman peak of CdS thin film prepared by CBD technique appears at 300.3 cm^{-1} and the true FWHM is 19.14 cm^{-1}. It is reported that the defect-free crystalline CdS films result in a peak position of about 305 cm^{-1} and FWHM of about 10 cm^{-1} [32]. A comparison of these values with the results of present studies shows that they do not match very well. The low value of peak position and the high value of FWHM in CdS thin films prepared by CBD are probably due to poor crystalline quality. It has been reported [35] that it is very difficult to distinguish the influence of cubic and hexagonal phases of CdS on Raman spectra, the A_1(LO) mode being common in both cases. Angel reported [36] the Raman scattering measurements on CdS thin films before and after thermal annealing where they presented the spectrum in the wide range from 0 to 1600 cm^{-1}. Raman response was employed in order to determine how the scattering by the phonon vibrational modes gives an indication about the phase transition mechanism in the β-α CdS structural transformation. The presence of the E_1(TO) mode shifted from 240 to 276 cm^{-1} for as grown and thermally annealed films subjected to heat treatment in Ar + S_2 ambient. [36].

4.4.2 Effect of irradiation

Figure 4.16 shows the Raman spectrum of the argon ion implanted CdS thin film and its fit to a Lorentzian lineshape. The intensity of the Raman peak has reduced significantly during implantation with argon ions in comparison to that of the as-deposited film. This can be

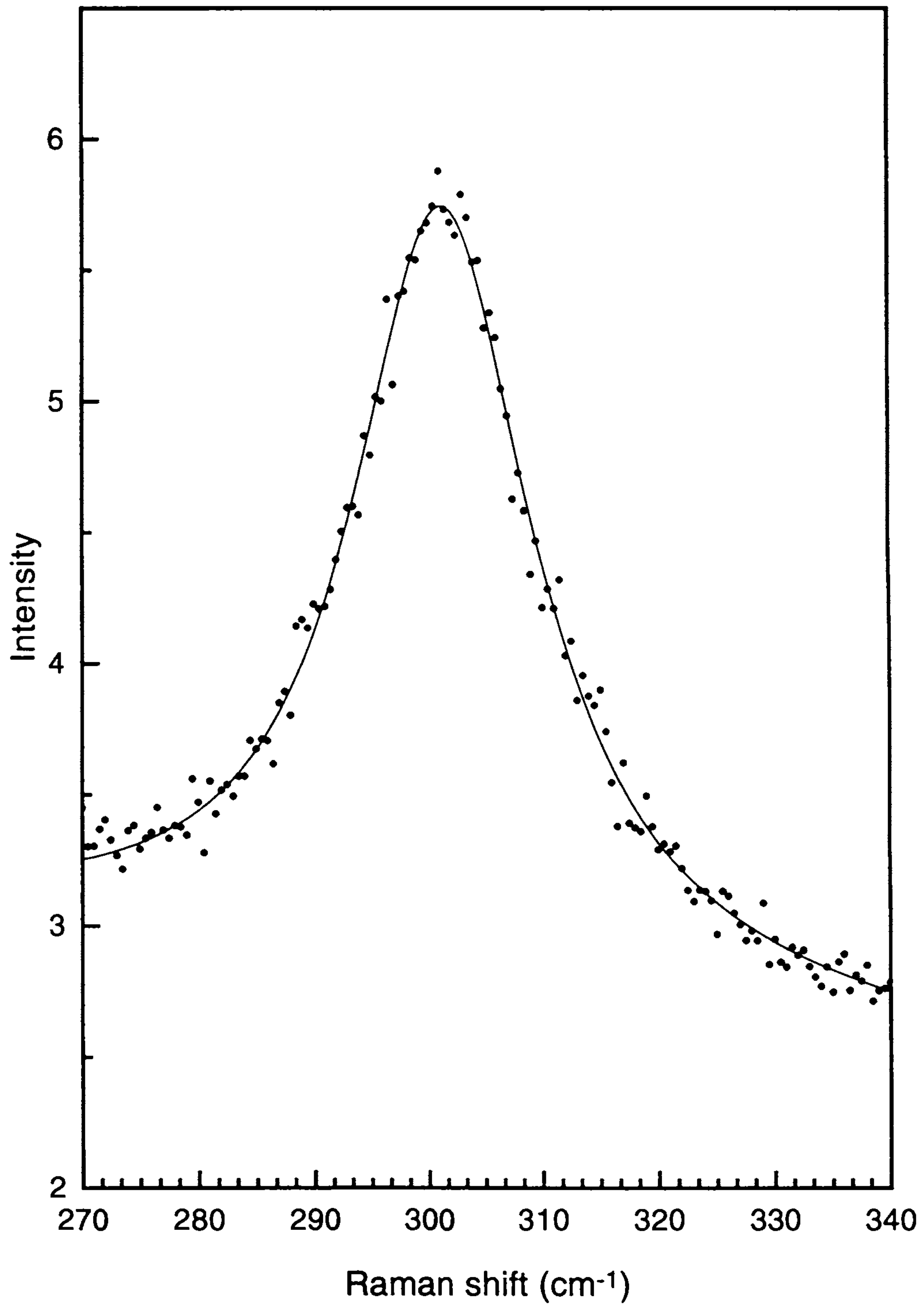

Figure 4.16: Raman spectrum of the argon implanted CdS thin film and with its fit to a Lorentzian lineshape

attributed to the lattice damage introduced by implantation of argon ions. The FWHM of the spectra of implanted film (18.31 cm^{-1}) remained more or less the same as that of the as-deposited film. The position of the peak increased from 300.3 cm^{-1} in the as-deposited film to 301.2 cm^{-1} in the implanted film. This increase in the peak position is marginal and hence not considered significant.

4.4.3 Effect of post irradiation annealing

Figure 4.17 shows the Raman spectrum of CdS thin films subjected to post implantation annealing (annealed at 673 K for 2 hours in argon atmosphere) fitted to a Lorentzian line shape. The Raman mode peaks at 301.7 cm^{-1} and has a FWHM of 12.45 cm^{-1}. The position of the Raman peak does not change significantly on annealing. It has increased from 301.2 cm^{-1} in the implanted film to 301.7 cm^{-1} in the film subjected to post implantation annealing. The peak position does not change significantly on implantation or on annealing. It is observed that the relative intensity of the A_1 (LO) mode of CdS film has increased significantly when compared to that of the implanted film. On annealing, some of the lattice defects are annihilated out and hence the defect density reduces, which causes the increase in the Raman intensity. The FWHM of the Raman spectrum of CdS thin film subjected to post implantation annealing is found to be around 12 cm^{-1} which is even smaller than that of the as-deposited film (which was about 19 cm^{-1}). This observation suggests that thermal annealing not only leads to the removal of the implantation produced damage/disorder but also anneals out the defects and strain present in the as-deposited film[37].

The effect of thermal annealing and consequent reduction in the lattice strain and improvement in the crystalline perfection have been studied by several authors by Raman scattering. Shirai *et al* [38] have studied the Raman and photoluminescence measurements of electrochemically as-deposited and annealed CdS films and they attributed the decrease in the FWHM value of the Raman mode of CdS to the improvement of the crystallinity of the films as the annealing temperature is raised. Yedave *et al* [39] have studied ion beam induced

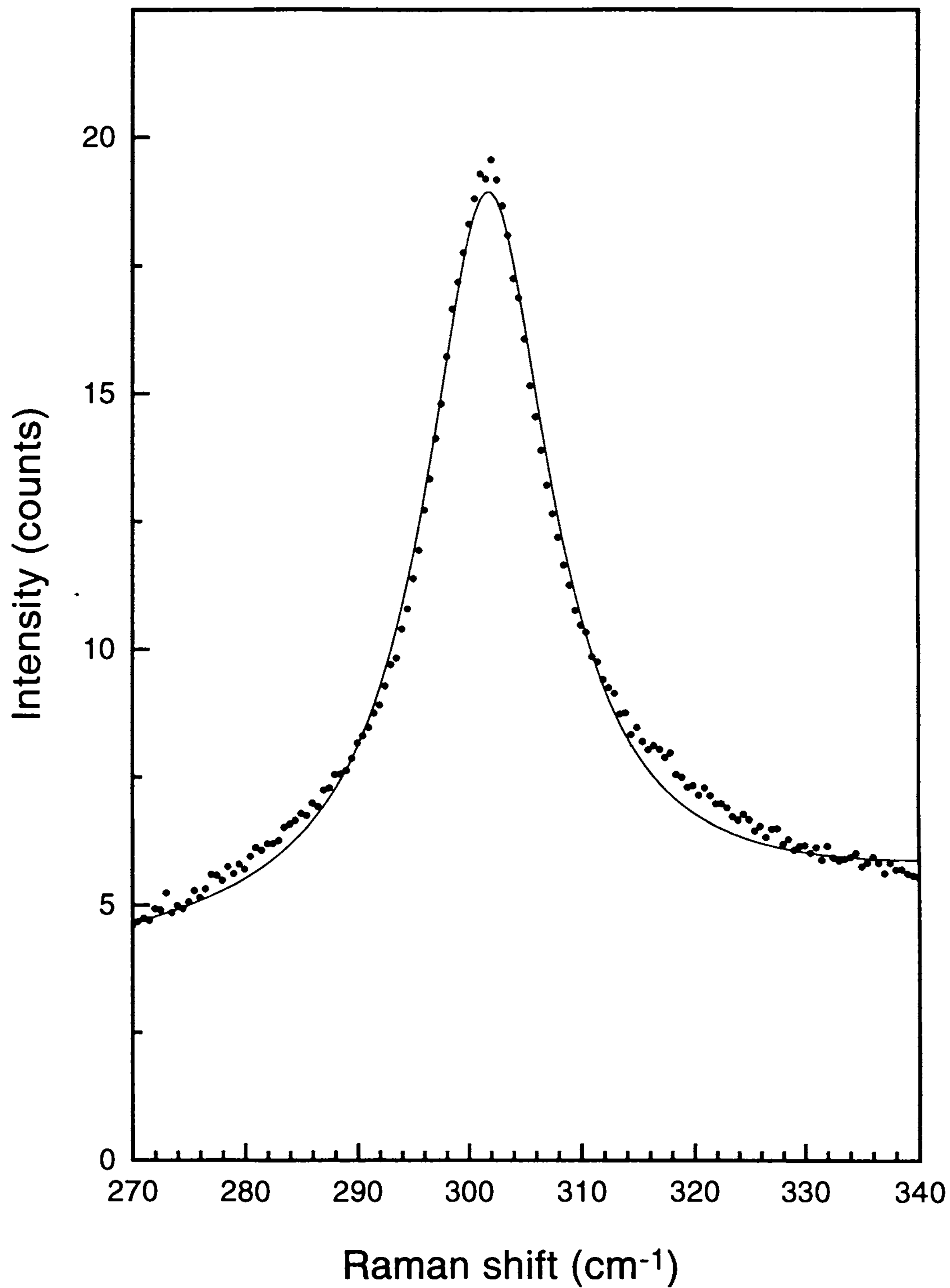

Figure 4.17: Raman spectrum of CdS thin films subjected to post implantation annealing (annealed at 673 K for 2 hours in argon atmosphere) fitted to a Lorentzian line shape

structural transformation in hydrogenated microcrystalline silicon using X-ray diffraction and Raman spectroscopy. Deneuville *et al* [40] studied the bulk and near-surface regions of oxygen ion implanted heteroepitaxial ZnSe films where they found that FWHM is very sensitive to the strain in the films. Wagner *et al* [41] have used Resonance Raman scattering by two longitudinal optical(LO) phonons in GaAs to probe ion implantation induced lattice damage and its annealing where it was found that the intensity of the Raman line depends strongly on the lattice perfection of the material. Nakumara *et al* have investigated the electrical activation and local vibration mode from Si-implanted GaAs [42] where they found that on annealing, structural recovery takes place in the implanted samples. Su *et al* [43] have studied the Raman scattering studies of Si implanted GaSb with various doses and energies. Samples implanted at room temperature showed disorder or amorphous layer and on furnace annealing as well as rapid thermal annealing, they could get a better structural recovery with increasing annealing temperature or time.

So far, extensive experimental studies on x-ray diffraction, optical absorption and Raman scattering of CdS thin films prepared by chemical bath deposition method have been discussed. The lattice damage caused during implantation changes the properties of the system and the results have been presented and discussed in detail.

In the following section of this chapter, the results of the positron beam studies on the as-deposited and implanted films and films subjected to post implantation annealing are discussed. The positron technique was chosen to probe the nature of the defects produced during implantation.

4.5 Positron annihilation studies

When energetic positrons from a radioactive source enter the condensed medium, they rapidly lose their energy by collisions with electrons and ions. After a somewhat longer period, characteristic of the medium, their annihilation is announced by the emergence of

energetic photons, whose energy, momenta and time of emission can be measured with great precision with modern day detector systems. Positron annihilation spectroscopy (PAS) is a powerful tool for the detailed characterisation of defects because the presence of open volume defects could be detected in the concentration range starting from 0.1 appm to 100 appm [44]. The technique which is non destructive, because of low flux of slow positrons, coupled to the fact that positron is selective and sensitive to the presence of certain types of defects, is very useful in the study of semiconductor thin film layers. This technique does not require any special preparation of the samples as do many other defect-characterization techniques, such as Capacitance-Voltage (C-V) measurements [45] and Deep level transient spectroscopy [46]. In addition, positron annihilation spectroscopy does not impose any restriction on the conductivity of the semiconductor material, like that imposed in Electron Paramagnetic Resonance (EPR) measurement [47].

Positron annihilation spectroscopy, as the name suggests, uses the photons emerging from the annihilation of positrons and electrons. Positron-electron annihilation produces high energy photons which are very penetrating. Hence, these photons will escape the semiconductor structure without any final state interaction. The kinematics of the emerging photons are determined by the initial energy and momentum of the electron-positron pair participating in the annihilation. Because positrons thermalise rapidly after entering a solid (within 1-10 ps), the energy and momentum of the emitted photons are largely decided by electrons participating in the annihilation process. Hence, the photon spectra can be analyzed to determine the properties of the electrons.

Due to the coulomb repulsion between the positrons and the positive ion cores, and also because of the large diffusion length of thermalised positrons, appropriately charged open-volume defects can trap positrons very efficiently. The trapped positrons more often encounter valence electrons than core electrons, producing significant differences in the energy and momentum of the emitted photons; this leads to two observable characteristics, viz., Doppler broadening and angular correlation of the annihilation photons. In the case of

Doppler broadening measurements, in principle, the shape of the annihilation spectra can be deconvoluted to obtain the electron-momentum distribution, more often it is quantified by shape parameters, such as S or W. The S-parameter measures the number of events in the central region of the annihilation peak, while the W-parameter measures the number of events in the wing region. Positron annihilation with core electrons produce a broad annihilation peak, and those with valence electrons produce a narrow peak. Hence, the W and S parameters reflect predominantly the contributions from the core and valence electrons, respectively.

Thin film samples of CdS have been prepared by chemical bath deposition (CBD) method [48]. These films were implanted to a dose of 5×10^{14} cm^{-2} and 5×10^{16} cm^{-2}. These implantations are carried out at room temperature. Positron beam studies of the as-deposited, argon ion irradiated and films subjected to post irradiation annealing were carried out and the results are presented in detail.

4.5.1 As deposited films

The variation of S-parameter as a function of positron beam energy, E_p, is shown in figure 4.18. The X-axis at the top shows the sample depth probed by the beam. In the case of as-grown CdS film, the S- parameter is low at the surface, increases upto E_p of 3 keV, beyond which it decreases gradually. In compound semiconductors such as CdHgTe [49], variation of S-parameter similar to the present one has been observed. This behaviour can be understood by considering scattering of epithermal positrons, positrons annihilating from trapped surface states and bulk states. The initial increase may be due to reduction in the fraction of scattered epithermal positrons. The gradual decrease beyond 3 keV is due to decrease in the fraction of positrons diffusing back to surface states. On the other hand, in pure Si, it was found that the S-parameter is low at the surface and it gradually increases and stabilises at a constant value characteristic of bulk Si [8, 50]. More work is required towards understanding of e^+ behaviour in single and compound semiconductors.

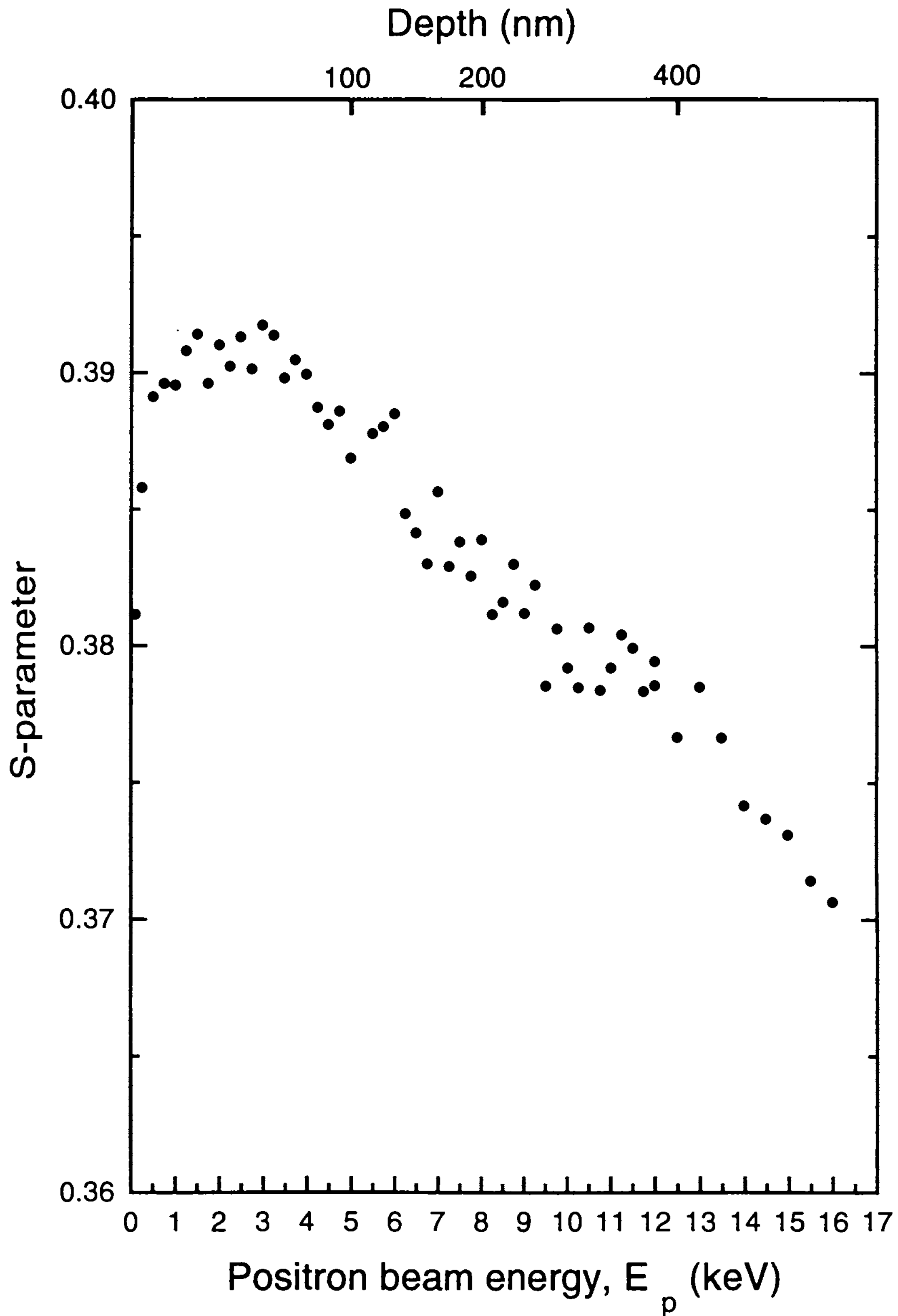

Figure 4.18: Doppler broadening Line shape S-parameter as a function of positron beam energy E_p for as-grown CdS thin films. Mean depth probed by positron beam is indicated on the top axis.

4.5.2 Effect of irradiation

The variation of S-parameter as a function of positron beam energy, E_p, is shown in figure 4.19 for three cases, viz., i) as-grown CdS ii) Ar^+-irradiated CdS (dose: $5x10^{14}$ cm^{-2}) and iii) Ar^+-irradiated CdS (dose: $5x10^{16}$ cm^{-2}). An interesting observation in figure 4.19 is that the irradiated sample exhibits lower S-parameter value, as compared to the as-grown CdS sample, throughout the sample depth investigated in the study. The observed broad reduction in S parameter vs. E_p curve on irradiation in the present studies, is in contrast to that observed in ion implanted Si [8, 50], where a sharp maximum in S-parameter is seen at a depth corresponding to the maximum damage layer. If the lattice damage in CdS created by the Ar-ion irradiation were to be predominantly Cd vacancies, then the S-parameter would have shown an increase as compared to that of as-grown sample. The opposite behaviour in S observed upon irradiation in the present study, rules out positron trapping at Cd vacancies.

The reduction in S-parameter would suggest that the atomic environment of the positron trapping site in irradiated CdS film is core-electron rich, as compared to that in the as-grown film. This leads to the following plausible explanation. Upon irradiation, sulfur vacancies are produced at sufficient concentrations. Radiation induced segregation of Cd atoms takes place around sulfur vacancies. This Cd clustering results in enhanced high momentum (core electron) contribution, leading to a broadening of the Doppler curve with a reduced S-parameter. Indeed, our XRD studies [37] carried out on similar CdS films, upon Ar irradiation, have revealed a characteristic new peak attributable to Cd clusters. This Cd peak is not found in the XRD pattern of the unirradiated CdS film. Formation of Zn clusters, upon nitrogen ion irradiation of ZnS films has also been reported [13]. Thus, the present observation is in accordance with earlier reported results [13, 37]. With respect to the observed broad profile for S vs. E_p in figure 4.19, it may be stated that the CdS films in the present study have nanocrystalline structure [48, 51] as the XRD analysis of the as-deposited CdS thin films reveals the grain size to be around 7 nm. The grain boundaries of sufficiently high density might well provide a favourable diffusion path for the long range migration of

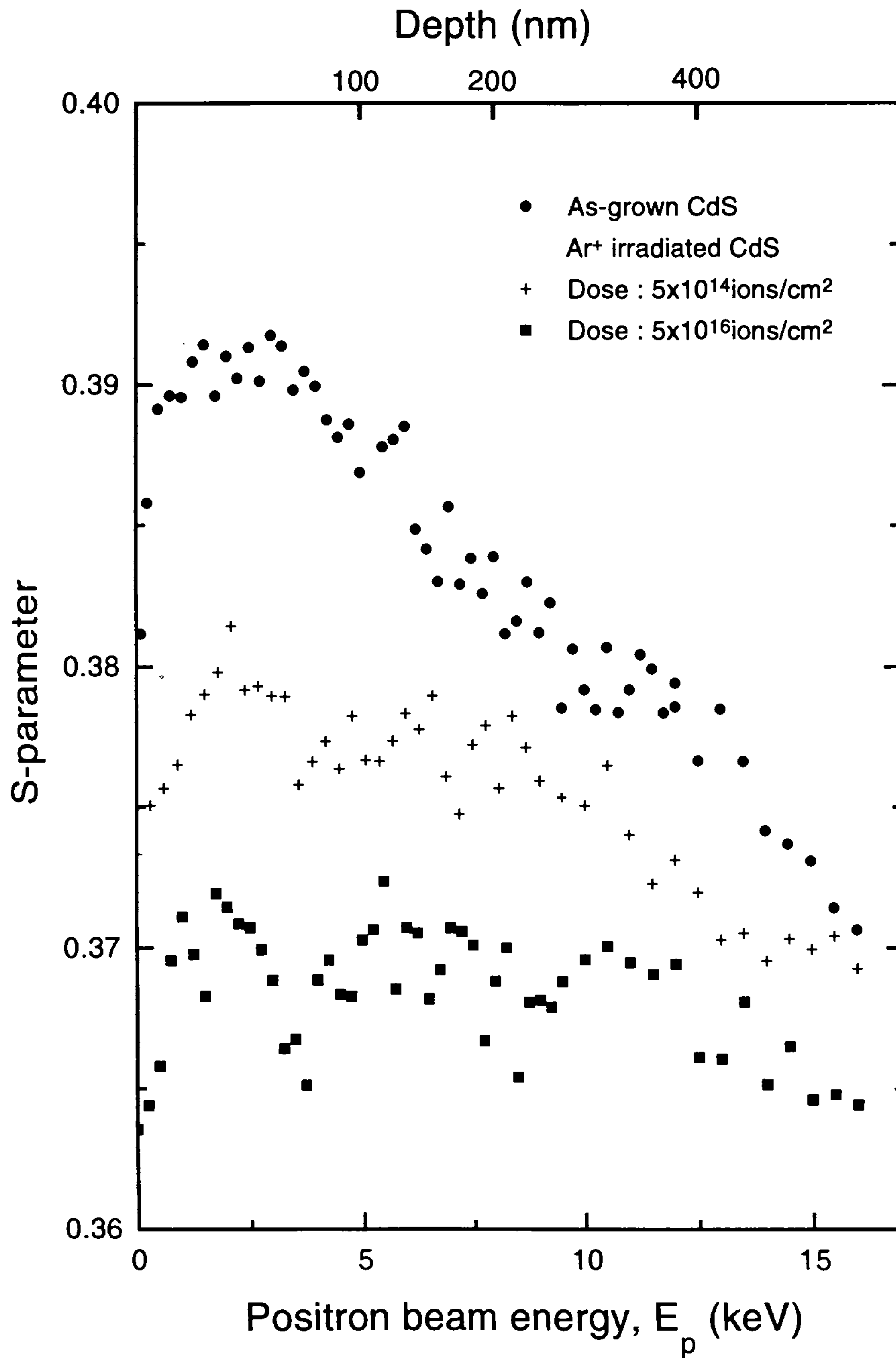

Figure 4.19: Doppler broadening Line shape S-parameter as a function of positron beam energy E_p for as-grown and irradiated CdS thin films. Mean depth probed by positron beam is indicated on the top axis

Cd. Hence, it is conceivable that a rather homogenous distribution of Cd cluster complexes is formed throughout the sample depth, which explains the flattening of S vs. E_p profile in figure 4.19. When the irradiation dose is increased to 5x10^{16} Ar/cm^2, there is a further reduction of S- parameter, indicating that the concentration of irradiation induced cluster complexes has increased. It is worth commenting here that coincident Doppler measurements [52, 53] based on two Germanium detectors would enable a study of the core-electron environment of the defect complex with greater precision. This would help in better identification of the nature of irradiation induced defect complexes seen in the present study.

4.5.3 Effect of post irradiation annealing

In order to investigate the thermal stability of the irradiation induced defect complexes, isochronal measurements have been carried out on CdS thin films irradiated to a dose of 5x10^{14} Ar/cm^2 these results are shown in figure 4.20. As the irradiated sample is annealed at 370 K, noticeable reduction is seen in the S-parameter throughout the sample thickness as compared to that of as-irradiated sample. This could be understood as due to the dissociation of the irradiation induced Cd cluster complexes. However, considering the fact that the sample has nanocrystalline grains, annealing of interfacial defects due to the grain growth might also contribute to the observed reduction in S-parameter. This would be discussed below. It is seen from figure 4.20, that as the annealing temperature is increased, it is found that the amount of reduction in S-parameter decreases gradually. Between 570 K and 670 K, there is not much change in the S-parameter variation. However, it is noticeable that in spite of the removal of the irradiation-induced defects at high temperatures like 670 K, the S-parameter values have not recovered to the extent of that of the as-grown sample. This would mean that the sample has undergone irreversible changes during the isochronal annealing with respect to its microstructure.

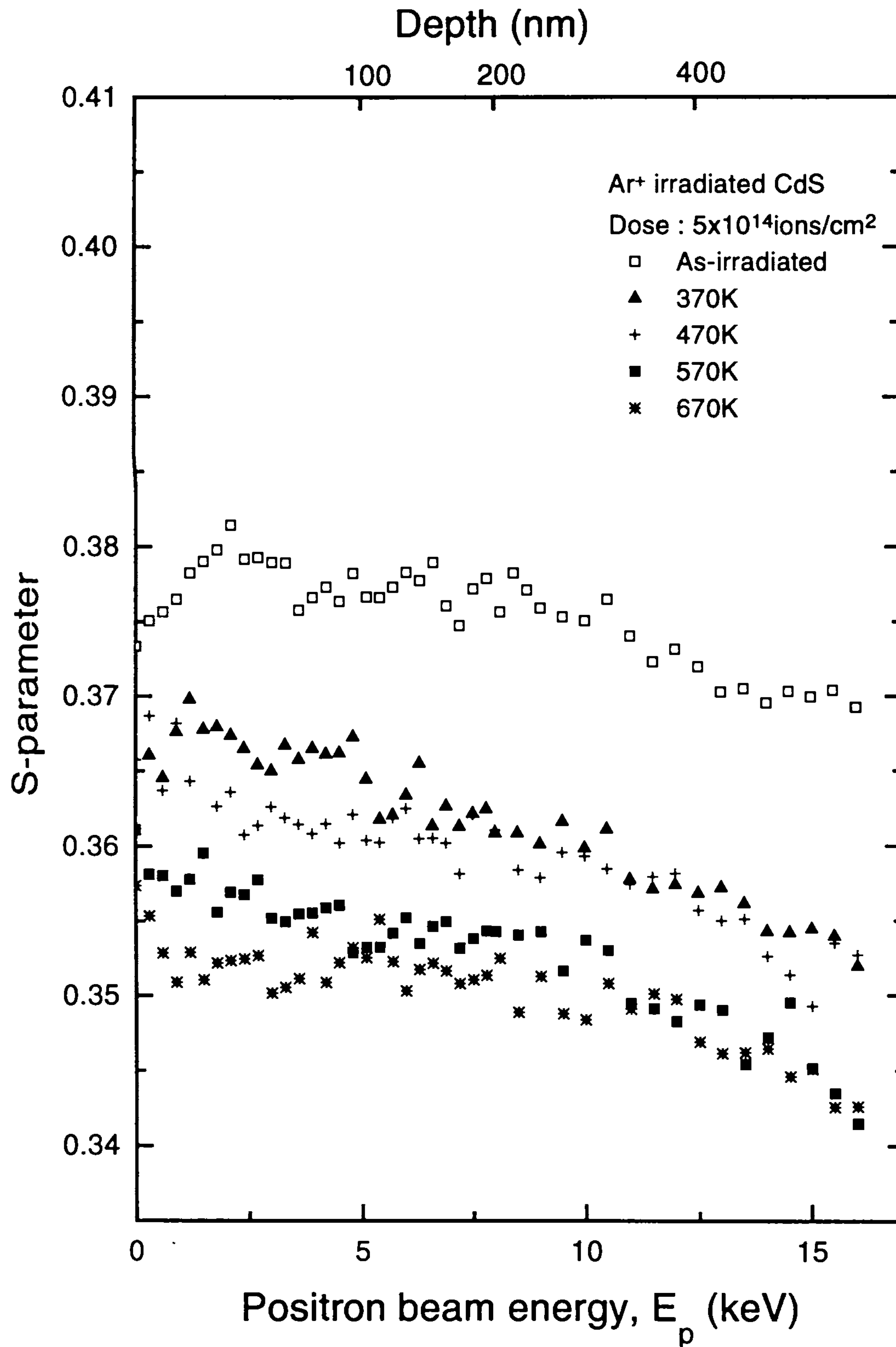

Figure 4.20: Doppler broadening Line shape S-parameter as a function of positron beam energy E_p for irradiated CdS thin film and the films after annealing at various annealing temperatures for 2 hours

4.5.4 Effect of annealing the as-deposited films

Towards delineating the effects of irradiation- induced defects and structural defects (present in the as-grown sample), similar isochronal annealing measurements have also been made on as-grown CdS sample. These results are shown in figure 4.21. A comparison of figures 4.20 and 4.21 reveals that the change observed from room temperature to 370 K is smaller in the as-grown sample as compared to the irradiated sample. This would indicate that the large reduction seen in irradiated sample in this temperature range is predominantly due to the annealing of irradiation-induced Cd cluster complexes. Further, changes seen in S-parameter beyond 370 K are mainly due to the annealing of interfacial defects, as the nanocrystalline grains of CdS thin film start growing. By about 570 K, this grain growth results in large grains whose size is greater than the positron diffusion length in the sample. This results in positron probing more of the interior of the grains, rather than the grain boundaries, giving rise to stabilisation of S-parameter values with respect to annealing temperature. Thus, the present positron beam results indicate that the isochronal annealing of the CdS thin films results in a change of microstructure, consistent with our earlier SEM and XRD studies [48].

In the next section of this chapter, studies of CdS thin films prepared by vacuum evaporation method are discussed. Raman scattering studies and XRD investigations on the as-deposited and implanted films have been carried out and the results are discussed in detail below.

4.6 Studies of CdS films prepared by vacuum evaporation

CdS thin films were prepared by vacuum evaporation onto glass substrates at room temperature. These films (of thickness 250 nm) were implanted with 100 keV Ar^+ ions to various doses in the range of 10^{14} ion/cm^2 to 10^{16} ion/cm^2. Raman scattering and X-ray diffraction studies were carried out on the as-deposited and implanted films to probe the lattice damage during ion implantation.

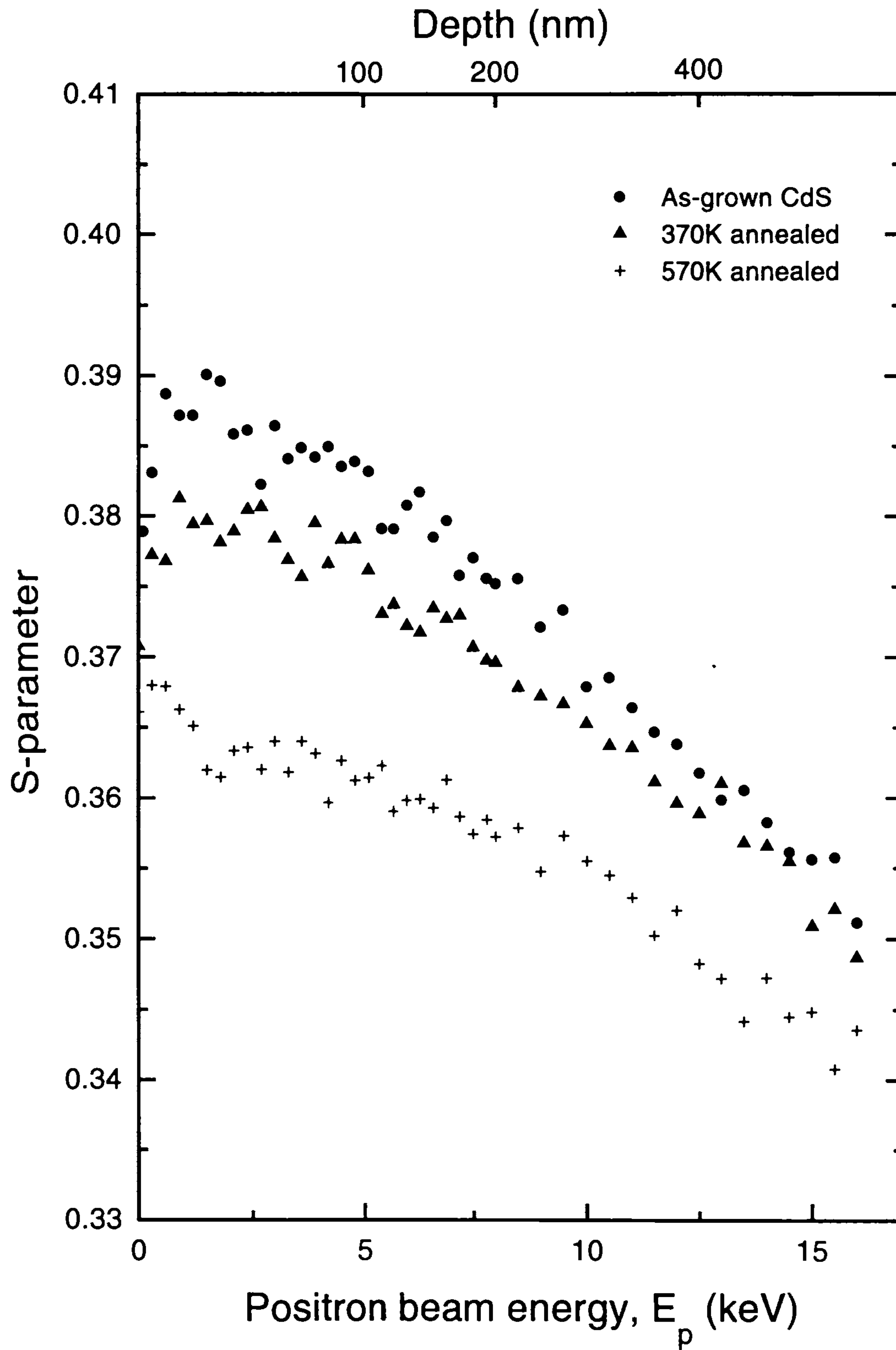

Figure 4.21: Doppler broadening Line shape S-parameter as a function of positron beam energy E_p for as-grown CdS film and annealed at various temperatures

4.6.1 As-deposited thin films

Figure 4.22 shows the X-ray diffraction pattern of the as-deposited CdS thin film prepared by vacuum evaporation technique. The characterisation of these films using XRD and TEM to determine the crystalline structure of the films have already been explained in the previous chapter. The oriented growth of hexagonal CdS thin films on glass substrates similar to that of present observation has been observed by various investigators [52, 53]. In the present study, the films are found to have a preferred growth along (0002) hexagonal orientation.

A typical Raman spectrum of the as-deposited CdS thin film is shown in figure 4.23. A Lorentzian line shape is fitted to the Raman spectrum from which the peak position, full width at half maximum (FWHM) and the area under the Raman peak have been obtained. No asymmetry in the lower wavenumber side of the Raman peak is seen in the spectrum. The spectrum showed a single peak at about 303 cm^{-1} which corresponds to $A_1(LO)$ mode of CdS.

The Raman peak of as-deposited thin film appears at 303.12 cm^{-1} and the FWHM is around 8.38 cm^{-1}. These values are comparable to those observed in single crystalline CdS [32]. It has been reported that the increase in FWHM(to about 20 or 30 cm^{-1}) often results either from the poor crystalline quality or from the polycrystalline effects [32]. The low value of the FWHM in the present case is an indication of the good crystalline quality of the film.

4.6.2 Effect of irradiation

X-ray diffraction pattern of the film implanted with 100 keV argon ions to a dose of 5×10^{16} ions/cm^2 is shown in figure 4.24. The sharp peak representing hexagonal structure with a preferred orientation along (0002) direction appears at 26.5° in both the as-deposited and implanted CdS thin film. However, the peak height is reduced and its width is slightly increased. This might be attributed to the lattice damage caused during ion implantation.

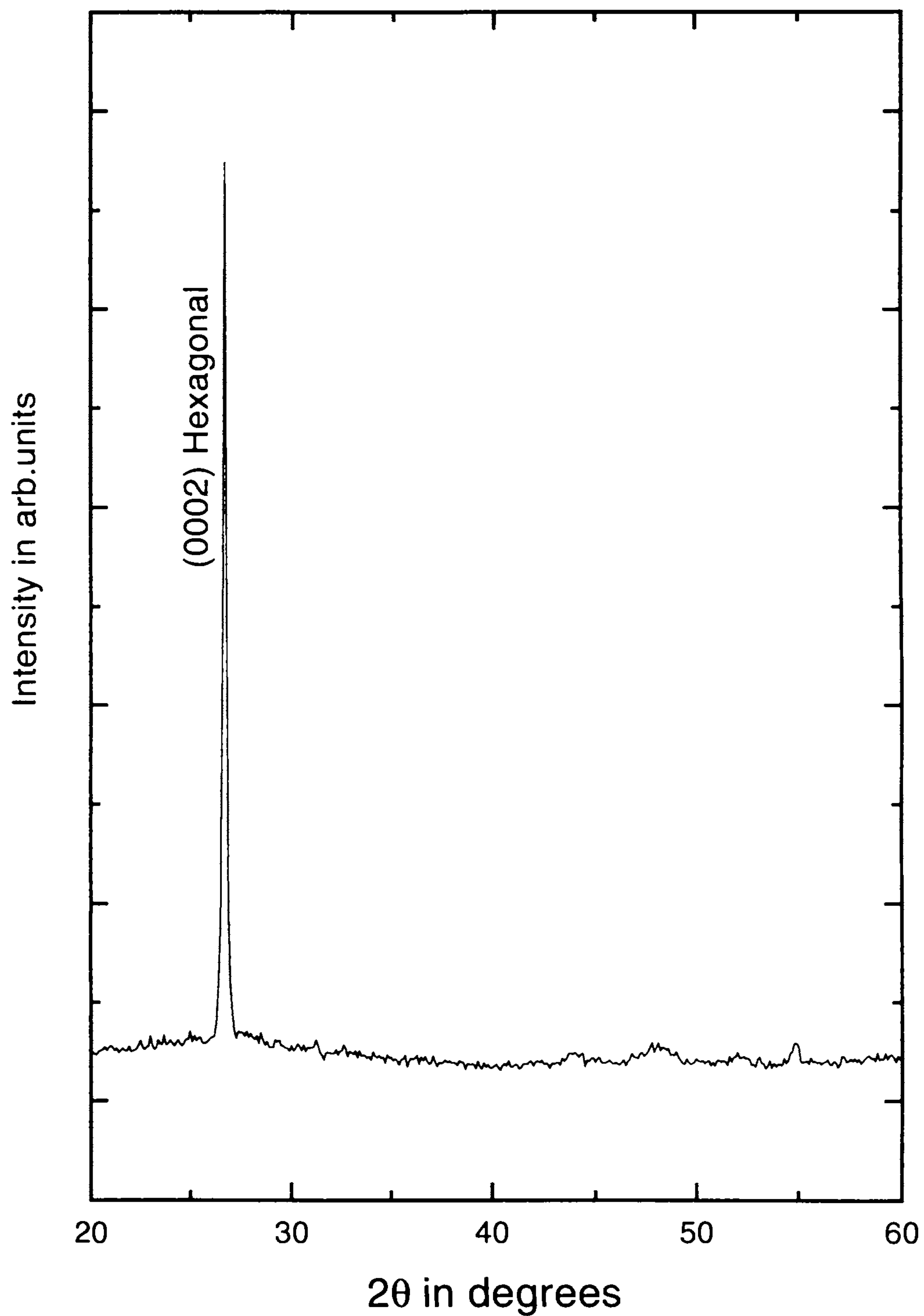

Figure 4.22: X-ray diffraction pattern of the as-deposited CdS thin film prepared by vacuum evaporation method

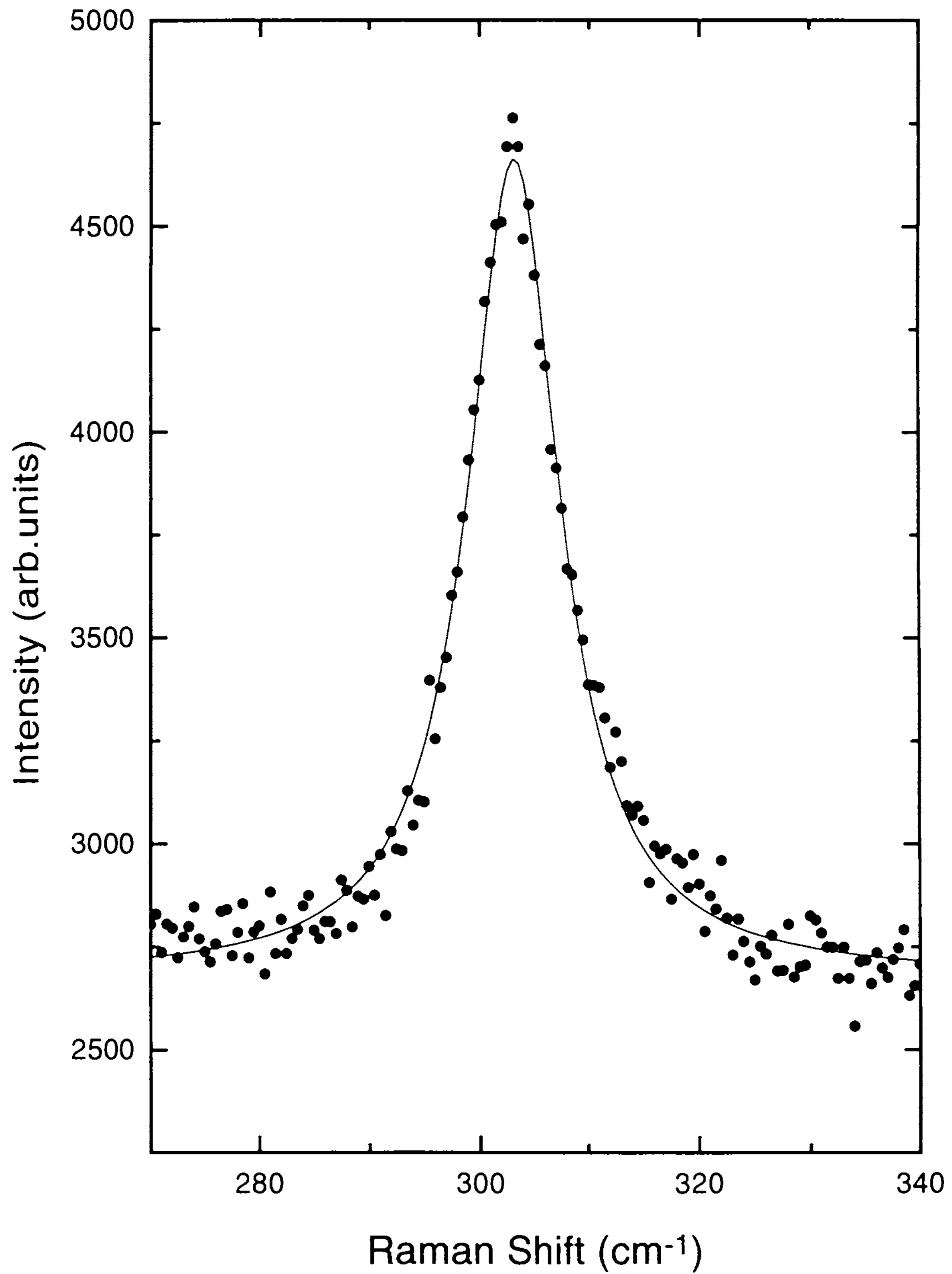

Figure 4.23: A typical Raman spectrum of the as-deposited CdS thin film

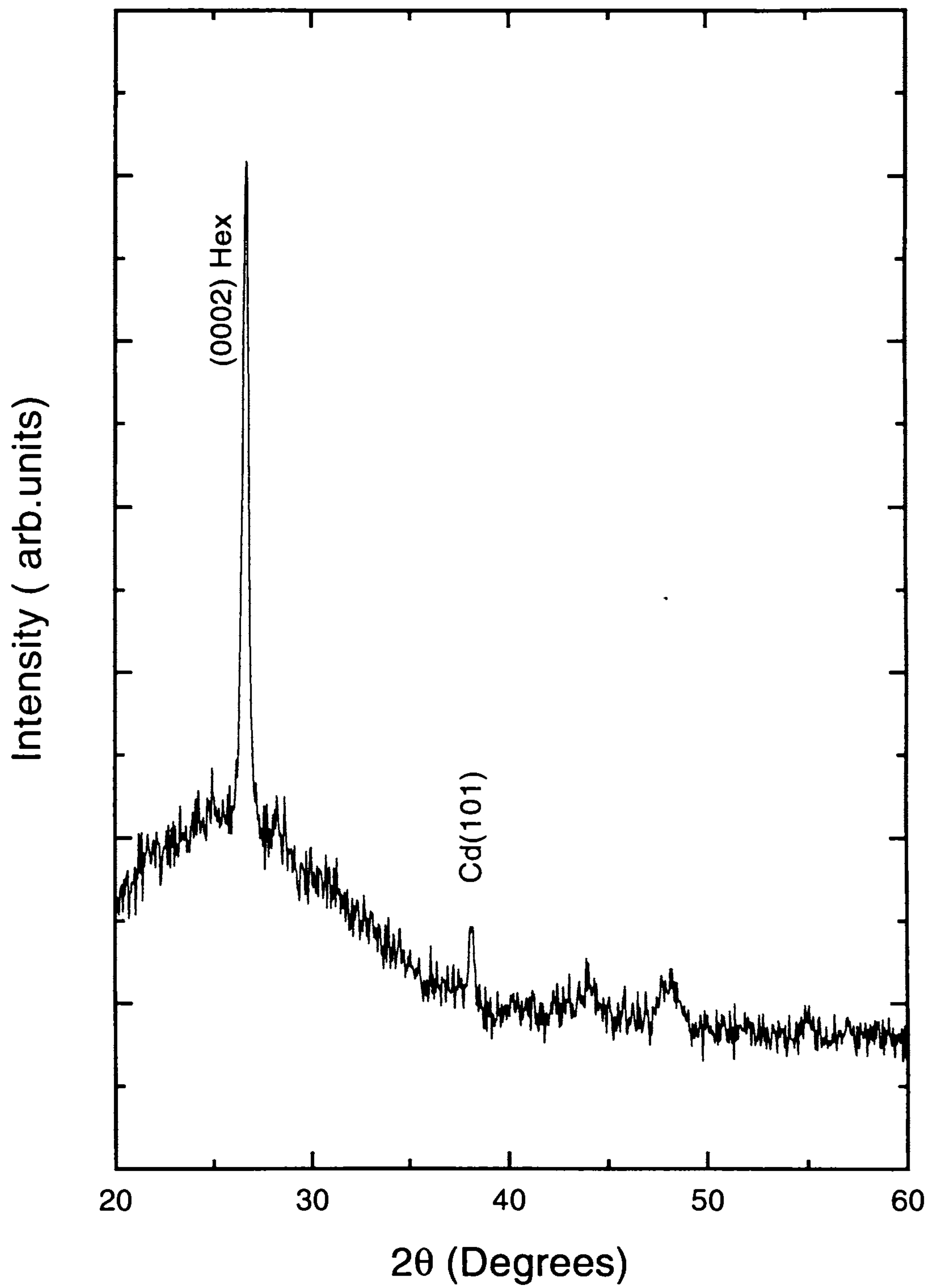

Figure 4.24: X-ray diffraction pattern of the film implanted with 100 keV argon ions to a dose of $5x10^{16}$ ions/cm^2

A peak is seen at 38.4^o in the pattern and is attributed to metallic cadmium. Similar results are observed in CdS films prepared by chemical bath deposition which was discussed earlier.

Raman spectra of the films implanted to various doses and their fits to Lorentzian line shape are shown in figure 4.25. It is observed from figure 4.25 that the position of the peak remains more or less the same. Table IV.1 lists the true height and width of the virgin and implanted films. It is seen from the Table IV.1 that the area under the peak of Raman mode and its FWHM values increase on implantation. The increase in FWHM with irradiation dose can be attributed to the radiation damage produced during Ar^+ ion irradiation.

Table IV.1 Calculated true width and true area under the Raman peak for the as-deposited and implanted films

Sl. No.	Dose (ions/cm^2)	FWHM (cm^{-1})	Area (arb.units)
1	As deposited film	8.38	18983.3
2	10^{14}	14.2	72460.2
3	10^{15}	13.8	75568.8
4	$5x10^{16}$	16.22	101780.5

It is clearly seen from the table that the full width at half maximum increases with implantation dose which is due to the lattice disorder caused during implantation. The position of the peak appears to be less sensitive to the implantation while the FWHM is relatively more sensitive. A decrease of 0.4 cm^{-1} in FWHM between the samples irradiated to different doses like 10^{14} and 10^{15} is less and ignored. Interestingly the area under the Raman peak is also found to increase with the implantation dose [33]. The observed increase in the Raman intensity (area under the peak) is rather surprising since it is known that the irradiation induced lattice disorder normally cause a decrease the intensity of the Raman line [43].

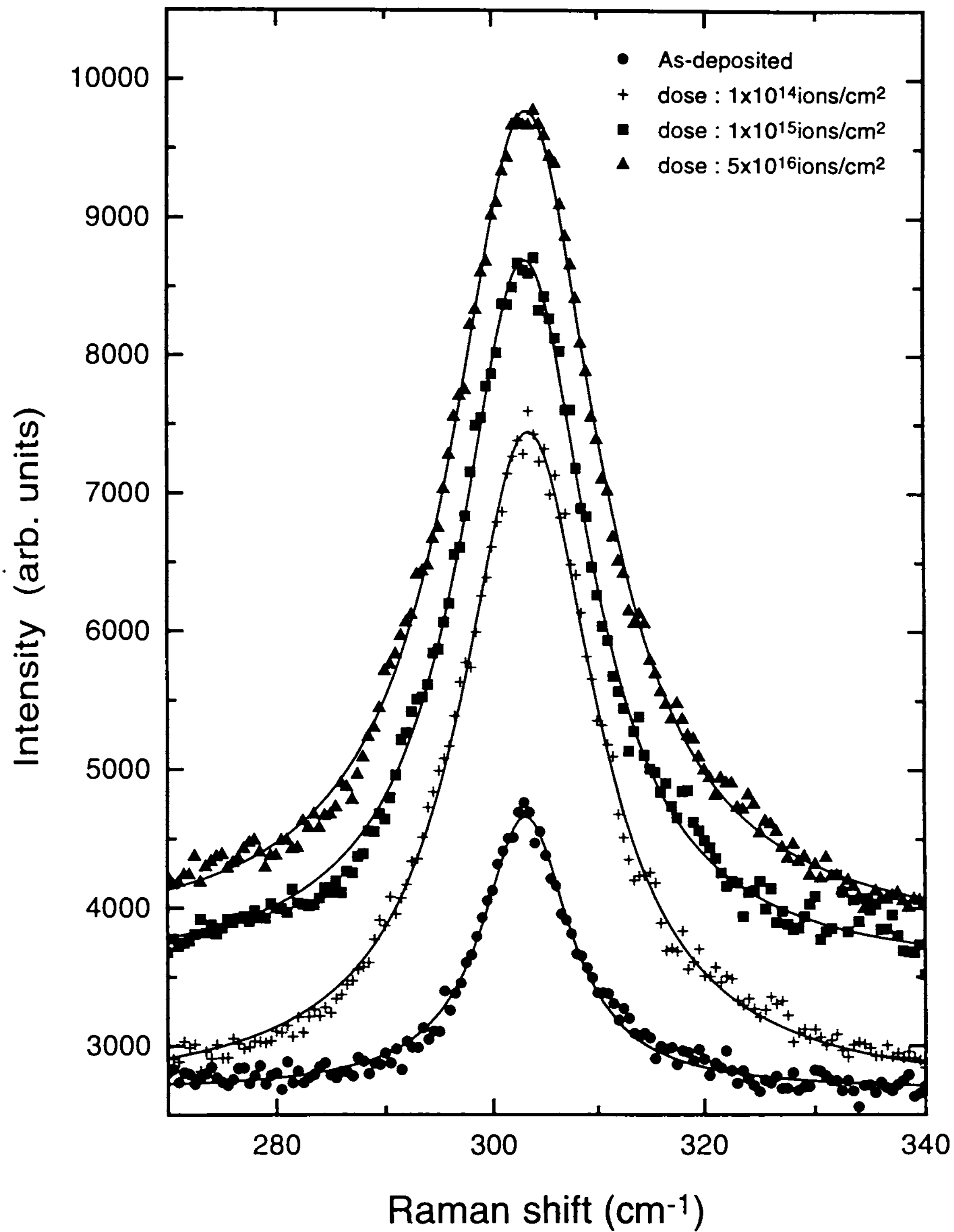

Figure 4.25: Raman spectra of the films implanted to various doses and their fits to the Lorentzian curve

Various possibilities for such an increase in the relative intensity (area under the Raman peak) are considered here. The intensity enhancement of the peak can be due to Resonance Raman scattering(RRS) effect, which essentially is the enhancement of the Raman intensity when the wavelength of the exciting radiation closely matches the band gap. The resonance between the incident energy and the bandgap of the system of interest plays a major role in enhancing the intensity. In the present study, the as-deposited CdS thin film has a band gap of 2.4 eV and Raman scattering studies were carried out using the 4880 Å wavelength of the argon laser whose energy corresponds to 2.54 eV. RRS is expected to occur in the implanted CdS thin films, if the bandgap of the implanted film approaches the energy of the exciting radiation. Various researchers have reported the RRS effect in CdS thin films [27, 28]. However, optical absorption studies have clearly established that the bandgap of CdS decreases on implantation due to irradiation induced lattice disorder [37]. The red shift thus produced, increases the difference between the energy of the laser light and the optical band gap, making the Resonance Raman effect unlikely cause for the observed rise in the intensity.

Another possibility for the increase in intensity is enhanced Raman scattering effect resulting from surface roughness introduced during ion implantation. In order to check this possibility, the surface roughness of the as-deposited and implanted films were measured using a Sloan Dek-Tak 3030 stylus depth profilometer. The roughness profiles are shown in figure 4.26. The average roughness of the as-deposited CdS thin film (figure 4.26 a) is found to be 49 Å and that of the implanted film (figure 4.26 b) is about 410 Å. The surface roughness has increased considerably in the implanted film . Hence, this suggests that the increase in Raman intensity could be possibly due to the increase in the surface roughness and the consequent enhanced Raman scattering effect. In the case of as-deposited films prepared by chemical bath deposition process, the films are found to have a high surface roughness which will in turn enhance the relative intensity of the Raman mode of CdS [53].

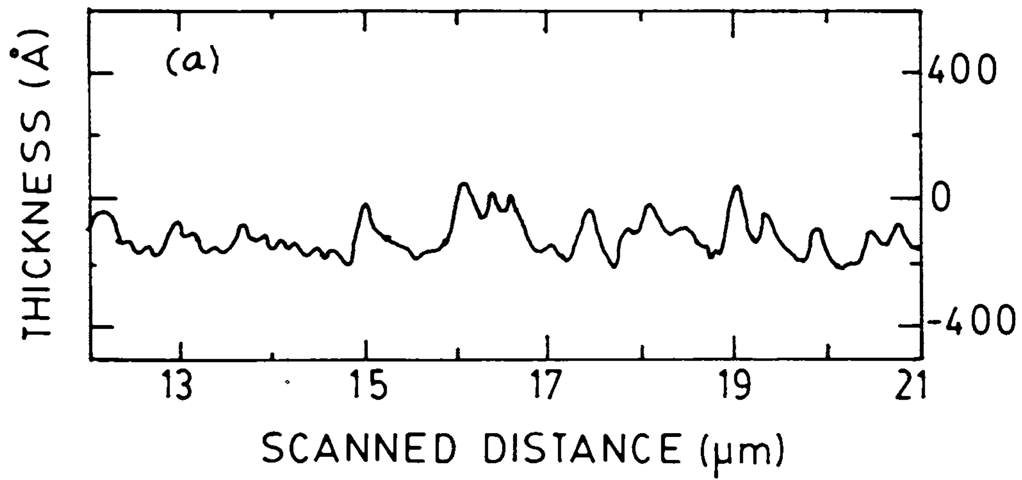

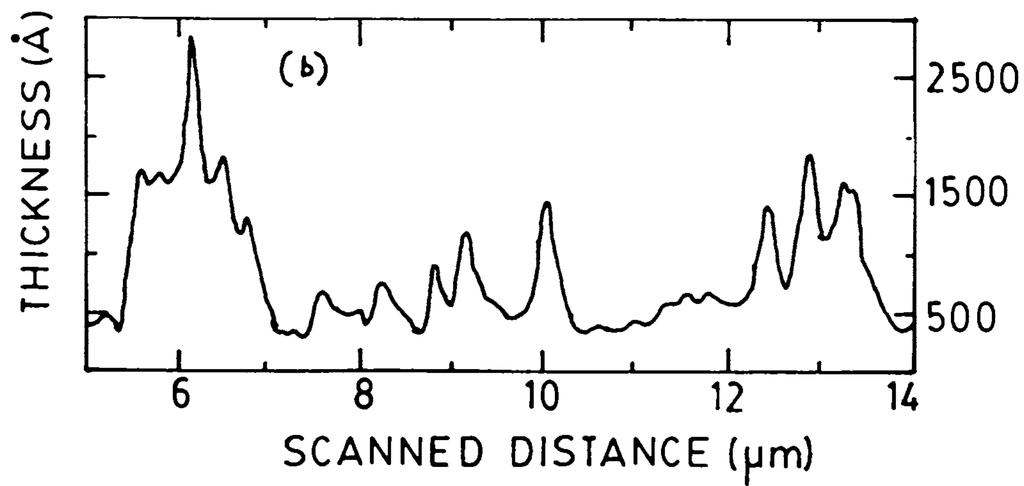

Figure 4.26: The roughness profiles are shown; (a) as-deposited condition; (b) irradiated condition; The average roughness of the as-deposited CdS thin film is found to be 49 Å and that of the implanted film is about 410 Å

4.7 Summary

This chapter reports the irradiation effects of CdS thin films prepared by CBD process and vacuum evaporation. Different techniques such as optical absorption, Raman scattering spectroscopy, X-ray diffraction and positron annihilation spectroscopy were used in the study and the results are discussed in detail.

A brief report on the observation of Surface enhanced Raman scattering effect(SERS) on the argon irradiated CdS films prepared by vacuum evaporation is also presented.

The effect of irradiation on the optical absorption spectra of CdS thin films prepared by CBD has been investigated. A progressive reduction in the band gap and the band edge sharpness is observed with increasing irradiation dose. This has been attributed to lattice damage produced by irradiation. The dependence of bandgap on the irradiation induced lattice disorder might be profitably used in tailoring the properties of semiconductor materials. On annealing the irradiated films, a recovery of the bandgap accompanied by a decrease in inverse logarithmic slope (E_o) is achieved which is due to the removal of defects during annealing.

Raman peak of the as-deposited CdS thin film appears at 300 cm^{-1} due to the CdS A_1 (LO) mode. The relative intensity of the Raman peak decreases on argon ion implantation due to implantation induced lattice disorder. Annealing of the implanted films, resulted in the recovery of the relative intensity of the Raman peak with no appreciable shift in the position of the peak.

X-ray diffraction studies of the as-deposited films reveal the presence of both cubic and hexagonal phases. Argon ion implantation possibly results in the removal of sulphur leading to formation of Cd clusters in the implanted zone of CdS. Post implantation annealing at 673 K for 2 hours in argon atmosphere resulted in the complete transformation of the film, from cubic to hexagonal phase accompanied by substantial grain growth.

Depth sensitive positron beam studies in the as-grown and Ar irradiated CdS nanocrystalline thin films are reported. A comparison of the Doppler broadening lineshape S-parameter variation as a function of sample depth for the irradiated and unirradiated films indicates a reduction in S-parameter which is in contrast to the behaviour usually observed in ion implanted layers. This experimental observation may be explained by the fact that irradiation results in the formation of Cd clusters. Isochronal annealing studies on irradiated and as-grown samples indicate that Cd clusters formed during irradiation are annealed out at about 370 K, while the interfacial defect annealing due to the grain growth in the sample continues up to about 570 K.

Vacuum evaporated CdS thin films were irradiated with argon ions and the Raman measurements were carried out. The Raman scattering studies of the implanted films showed steady increase in the intensity of CdS A_1 (LO) Raman mode with the irradiation dose accompanied with an increase in the full width at half maximum. The position of the peak of the A_1(LO) Raman mode of CdS did not change on implantation. Ion implantation induced surface roughness is the cause for the intensity enhancement and ion implantation induced lattice damage is the cause for the increase in the full width at half maximum of the Raman mode of cadmium sulphide thin films. X-ray diffraction studies of the argon ion implanted films revealed that the films did not loose their crystallinity on implantation and cadmium clusters formed in the implanted region.

References

[1] P. S. Peercy, Appl. Phys. Lett., 18 (1971) 574

[2] S. Ushioda, Solid. State. Commun., 15 (1974) 149

[3] S.G. Kim, H. Asahi, M. Seta, J. Takizawa, S. Emura, R.K. Soni, S. Gonda, and H. Tanoue, J Appl. Phys., 74 (1993) 579

[4] J. M. Zhang, S. C. Shen, S. P. Guo and S. X. Yuan, J. Phys. D: Appl. Phys., 29 (1996) 2162

[5] M. Fujinami, A. Tsuge and K. Tanaka, J. Appl. Phys., 12 (1996) 9017

[6] B. Nielsen, O.W. Holland, T.C. Leung and K.G. Lynn, J. Appl. Phys., 74 (1993) 1636

[7] P.J. Schultz and K.G. Lynn, Rev. Mod. Phys., 60 (1988) 701

[8] P. Asoka-Kumar, K.G. Lynn and D.O. Welch, J. Appl. Phys., 76 (1994) 4935

[9] E. V. K. Rao, Phys. Stat. Sol. A, 33 (1976) 683

[10] T. Pankey, J. E. Darvey, J. Appl. Phys., 41 (1970) 697

[11] N. P. Kekelidze, Radiation Effects, 32 (1977) 113

[12] Ratna Sagar and Srivastava, Phys. Letts. A, 183 (1993) 209

[13] KH.A. Mady, Z. S. Moustafa, M. S. Selim and A. A. Gabr, J. Mater. Sci., 23 (1988) 2403

[14] O.Zelaya Angel, L.Hernandez, O de Melo, J.J Alvarado-Gil, R.Lozado-Morales, C.Falcony, H.Vargas and R.Ramirez-Bon, Vacuum, 46 (1995) 1083

[15] O.Zelaya Angel, J.J Alvarado-Gil, R.Lozado-Morales, H.Vargas, Appl.Phys.Lett., 64 (1994) 291

[16] Solid State Electronic Devices, B. G. Streetman (Prentice Hall, New Jersey, 1980), p.443

[17] G. Hodes, Phys. Rev B., 36 (1987) 4215

[18] Amorphous and Liquid Semiconductors, J. Tauc (Ed), Plenum, London (1976), refer Chapter 6

[19] M. V. Kurik, Phys. Stat. Solidi(a), 8 (1971) 9

[20] H. Sumi and Y. Toyozawa, J. Phys. Soc. Jpn., 31 (1971) 342

[21] U. Zammit, K.N. Madhusoodanan, M. Marinelli, F.Scudieri, R. Pizzoferrato, F. Mercuri, E. Wendler and W. Wesch, Phys.Rev.B., 49 (1994) 14322

[22] G. D. Cody, T. Tiedje, B. Abeles, B. Brooks and Y. Goldstein, Phy. Rev. Lett., 47 (1981) 1480

[23] J. I. Pankove, Phy. Rev., 140 (1965) A2059

[24] Optical processes in semiconductors, J. I. Pankove, , Prentice Hall, Englewood Cliffs, NJ, pp-34-86.(1971)

[25] K. L. Narayanan, K. P. Vijayakumar, K. G. M. Nair and N. S. Thampi, Physica B, 240 (1997) 8

[26] T. Mootoka and O. W. Holland, Appl. Phys. Lett., 61 (1992) 3005

[27] R. C. C. Liete, J. F. Scott and T. C. Damem, Phys. Rev. Lett., 22 (1969) 780

[28] M. V. Klein and S. P. S. Porto, Phys. Rev. Lett., 22 (1969) 782

[29] J. F. Scott and T. C. Damem, Opt. Commun., 5 (1972) 410

[30] J. V. Baranov ,Y. S. Bobovich, N. I. Grebenshchikova, V. I. Petrov and M. Y. Tsenter, Opt. Spectrosc., 60 (1986) 685

[31] R. Rosetti, S. Nakahara and L. E. Brus, J. Chem. Phys., 79 (1983) 1086

[32] Michel Froment, Marie Claude Bernard, Robert Cortes, Bandombele Mokili and Daniel Lincot J.Electrochem.Soc., 142 (1995) 2642

[33] K. L. Narayanan, K. P. Vijayakumar, R. Kesavamoorthy, K. G. M. Nair and N. S. Thampi, Solid State Phys.(India), 39C (1996) 159

[34] A. K. Arora and V. Umadevi, Appl. Spectros., 36 (1982) 424

[35] D.R. T. Zahn, C. Maierhofer, A. Winter, M. Reckzugel, R.Srama, A. Thomas, K. Horn and W. Richter, J. Vac. Sci. Technol. B, 29 (1991) 2206

[36] O. Zelaya-Angel, F. de. Castillo-alvarado, J. Avendano-Lopez, A. Escamilla-Delgado, G. Contreras-Puente, R. Lozado-Morales, G. Torres-Delgado, Solid State Commun., 104 (1997) 161

[37] K. L. Narayanan, K. P. Vijayakumar, K. M. Nair and G. V. N. Rao, Nucl. Instr. Meth. Phys. B, 132 (1997) 61

[38] Katsunori Shirai, Fumitaka GOTO and Masaya Ichimura, Jpn. J. Appl. Phys., 35 (1996) L1483

[39] S. N. Yedave, S. B. Ogale, R. O. Dusane, S. V. Rajarshi, V. G. Bhide, S. T. Kshirsagar, J. Appl. Phys., 71 (1992) 3773

[40] A. Deneuville, C. H. Park, P. Ayyub, T. Anderson, P. Lowen , K. Jones and P. H. Holloway, App. Surf. Sci., 50 (1991) 308

[41] J. Wagner, Ch. Hoffman, Appl. Phys. Lett., 50 (1987) 682

[42] T. Nakamura and T. Katoda, J. Appl. Phys., 57 (1985) 1084

[43] Y. K. Su, K. J. Gan, J. S. Hwang and S. L. Tyan, J. Appl. Phys., 68 (1990) 5584

[44] Positron Solid State Physics, W. Brandt and A. Dupasquier (eds) (North Holland, Amsterdam, 1983)

[45] MOS (Metal Oxide Semiconductor) Physics and Technology, Eds. E.H. Nicollian and J.R. Brews, Wiley, New York, 1982

[46] Lang, D.V., J. Appl. Phys., 45 (1974) 3023

[47] Growth and Characterization of Semiconductors, Newman, R.C., Eds. R.A. Stradling and P.C. Klipstein, Adam Higler, New York, 1990, p. 119

[48] K. L. Narayanan, K. P. Vijayakumar, K. G. M. Nair and G. V. N. Rao, Bull. Mater. Sci., 20 (1997) 287

[49] C. Smith, P.C. Rice Evans and N. Shaw, Fifth International Workshop on Slow Positron beam Techniques for Solids and Surfaces, Eds. E. Ottewitte, A.H. Weiss, (AIP Press, New York, 1994), p.78

[50] G. Amarendra, G.Venugopal Rao, K.G.M. Nair and B. Viswanathan, in Proc. of Twelth International Conference on Positron Annihilation, Missouri, USA, May 25-31, 1997 (to appear in Mater. Sci. Forum, Noveber 1997)

[51] K. L. Narayanan, K. P. Vijayakumar, K. G. M. Nair, N. S. Thampi and K. Krishan, J. Mater. Sci., 32 (1997) 4837

[52] A. Sanchez, P. J. Sebastian and O. Gomez-Daza, Semicond. Sci. Technol., 9 (1994) 1

[53] K.L. Narayanan, K. P. Vijayakumar, B. Sundarakkannan, R. Kesavamoorthy, K. G. M. Nair, Phys. Stat. Soli(a) [In Press]

CHAPTER 5

5 EFFECT OF NITROGEN AND OXYGEN ION IMPLANTATION IN CdS THIN FILMS

Ion implantation provides an alternative method of introducing dopant atoms into the lattice. The major factors governing the successful exploitation of ion implantation are the range of distribution of the implanted atoms, the amount and nature of the lattice disorder that is created, the location of the implanted atoms and ultimately the changes in structural, electrical and optical characteristics that result from the implantation and subsequent annealing treatment. Ion implantation into compound semiconductors has been investigated with increasing vigour in the last few decades. The accomplishments include demonstration of type conversion and p-n junction formation in some compounds like CdS, $CuInSe_2$ which can be formed neither by growth nor by thermal diffusion. CdS normally exhibits n type conductivity which arises from a departure in stoichiometry, specifically from a sulphur deficiency. Ion implantation of impurities like bismuth, phosphorus, nitrogen and arsenic in CdS has been reported to result in p type conversion and p-n junction formation [1, 2, 3, 4]. Extensive research work has been done on CdS because of the potential applications in the field of opto-electronic devices. However, only a few of these investigations have been addressed to the study of type conversion phenomenon in CdS [1, 2, 3, 4]. Defects produced during implantation cause drastic changes in the electrical and optical properties of the semiconductors [5, 6], where one can expect changes in the optical band gap and in the conductivity type.

The effect of nitrogen ion implantation in CdS thin films is discussed in this chapter. The structural investigations of the as-deposited, implanted and subsequently annealed thin films of CdS are reported here. Nitrogen implantation induced changes in the electrical properties of the films and in particular an increase in conductivity of the films with an increase in the

nitrogen fluence is reported. On nitrogen irradiation, type conversion from n to p in CdS films was achieved for the first time and the results are discussed. The photoconductivity i.e., increase in conductivity due to irradiation of a semiconductor with light, is one of the non-equilibrium processes which gives a lot of information about the trap levels and decay constants of the carriers. The Persistent photoconductivity or prolonged photoconductivity is one that persists for a very long period of time after the termination of the photoexcitation. The observation of persistent photoconductivity in the nitrogen irradiated CdS thin films prepared by chemical bath deposition (CBD) method is reported. The phenomenon of persistent photoconductivity is of technological importance and hence a detailed analysis of the measurements is presented with various fittings of the data. Optical absorption measurements of the nitrogen irradiated and subsequently annealed films are discussed in this chapter.

Optical absorption and Raman scattering studies of the oxygen irradiated CdS thin films prepared by vacuum evaporation are reported. Oxygen irradiation was done on the samples at different fluences. The effect of irradiation dose on the optical properties are discussed.

5.1 Experimental details

CdS thin films were prepared by chemical bath deposition as discussed in the third chapter. These films were implanted with N^+ ions of energy 130 keV to different doses in the range of 10^{14} to 10^{17} ions/cm^2. The CBD CdS thin films were bombarded with oxygen ions at an energy of 50 keV to doses in the range of 5×10^{15} to 1×10^{16} ions/cm^2 and optical absorption measurements were carried out. Oxygen implantation was done on CdS films at an energy of 90 keV to different doses in the range of 10^{14} to 10^{17} ions/cm^2 and the Raman measurements were carried out and the results are discussed.

Vacuum in the irradiation chamber was maintained at 10^{-7} mbar. The implantation was carried out at room temperature and the beam current was maintained around 0.8 microam-

peres to avoid the excessive heating of the sample during implantation. Annealing of the films was carried out in flowing helium atmosphere at about 673 Kelvin for 2 hours. The optical absorption spectra of the as deposited and irradiated samples were recorded in the wavelength range 400 to 1100 nm by an UV-VIS-NIR (Chimito 2500) spectrophotometer. X-ray diffraction analysis was carried out on the samples using Cu-K_α radiation. The conductivity measurements of the nitrogen implanted films were carried out on in the Van der Pauw geometry. Hot probe and photoconductivity measurements were carried out in the N^+ irradiated films and the relevant experimental details are given in chapter 2, section 2.2.8.

5.2 Characterization of structural modifications

In order to understand the structural modifications of the implanted films and the films subjected to post implantation annealing, x-ray diffraction was carried out on the samples and the results are discussed.

5.2.1 As deposited films

X-ray diffraction studies were carried out on the as-deposited films as well as on the high dose nitrogen ion irradiated films and on films subjected to post implantation annealing and the results are discussed below. Thin films of thickness of about 1.5 μm were coated on glass substrates. Figure 5.1 shows the x-ray diffraction pattern of the as-deposited thin film of CdS prepared by chemical bath deposition method. Films were coated on the glass substrates. It is observed from the figure 5.1 that films are crystalline and the films are found to have both cubic and hexagonal phases. The grain size of the films was calculated to be around 7 nm and the details are given in the third chapter (section 3.4).

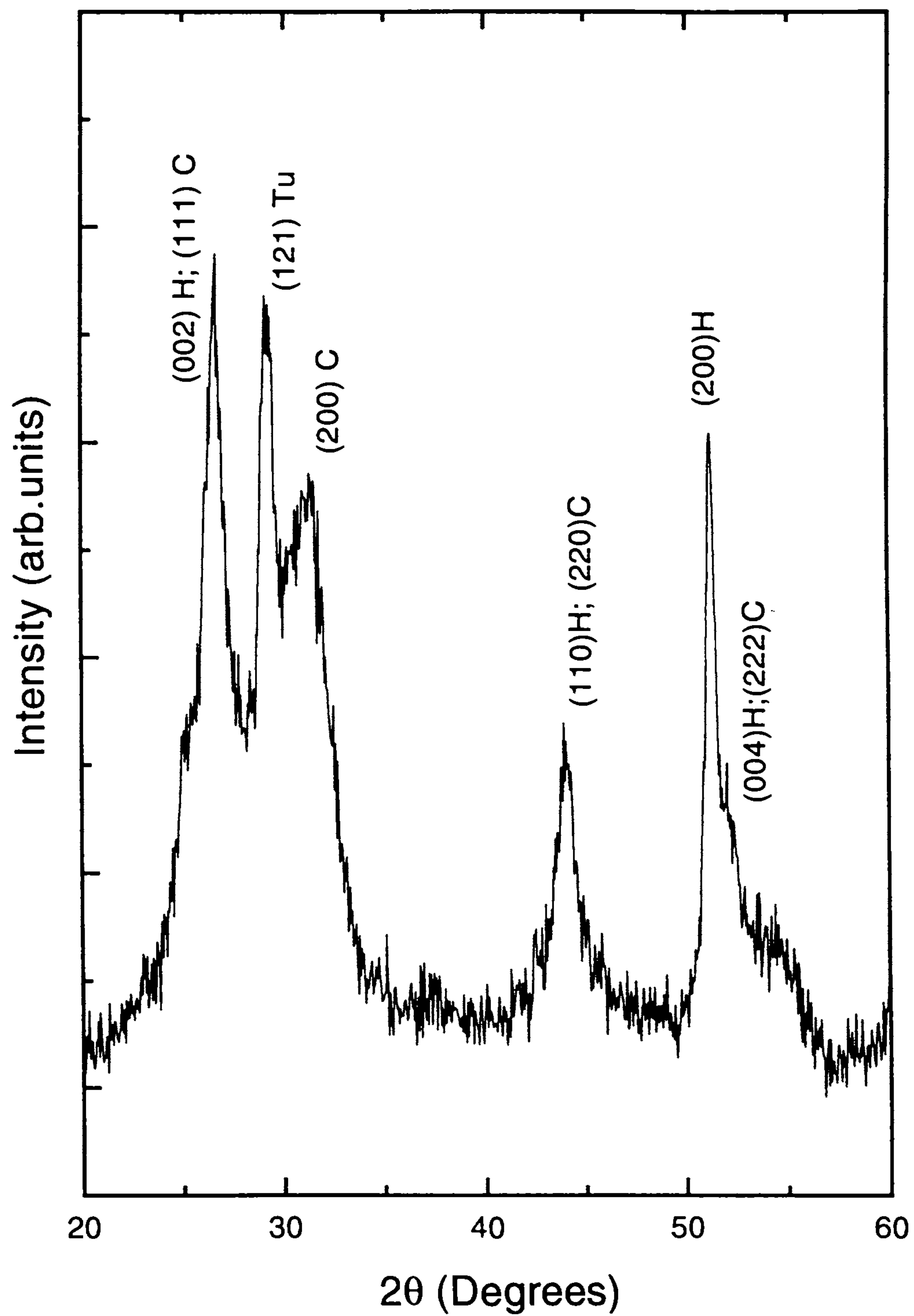

Figure 5.1: X-ray diffractogram of the as-deposited thin film of CdS

5.2.2 Effect of ion implantation

The films were found to acquire a metallic lustre on nitrogen ion irradiation. In order to understand the structural modifications of the implanted films, x-ray investigations are carried out. Figure 5.2 shows the x-ray diffraction pattern of the nitrogen ion implanted films of CdS. It is evident from the figure that new peaks have arisen, and they are attributed to the Cd phase. This is similar to the x-ray diffraction pattern obtained in the argon irradiated CdS thin film (see section 4.4.2). The only difference is that in the nitrogen irradiated case, the formation of Cd phase is more predominant than that in the argon irradiated films.

5.2.3 Effect of post implantation annealing

Figure 5.3 shows the x-ray diffraction pattern of films subjected to post implantation annealing.. Annealing was carried out on the implanted films for a period of three hours at 673 Kelvin in helium atmosphere. It is seen from figure 5.3 that films transform from mixed cubic-hexagonal phase to exclusively hexagonal phase. Such a structural transformation has been reported by many researchers [7, 8, 9]. There are two peaks attributable to cadmium nitride as marked in the figure 5.3. The formation of cadmium nitride arise due to the reaction of cadmium with the implanted nitrogen ions.

5.3 Electrical characterization of N^+ irradiated CdS films

The electrical conductivity of the films on nitrogen irradiation has increased as a function of dose. The mechanism for such a change in the electrical conductivity is discussed below.

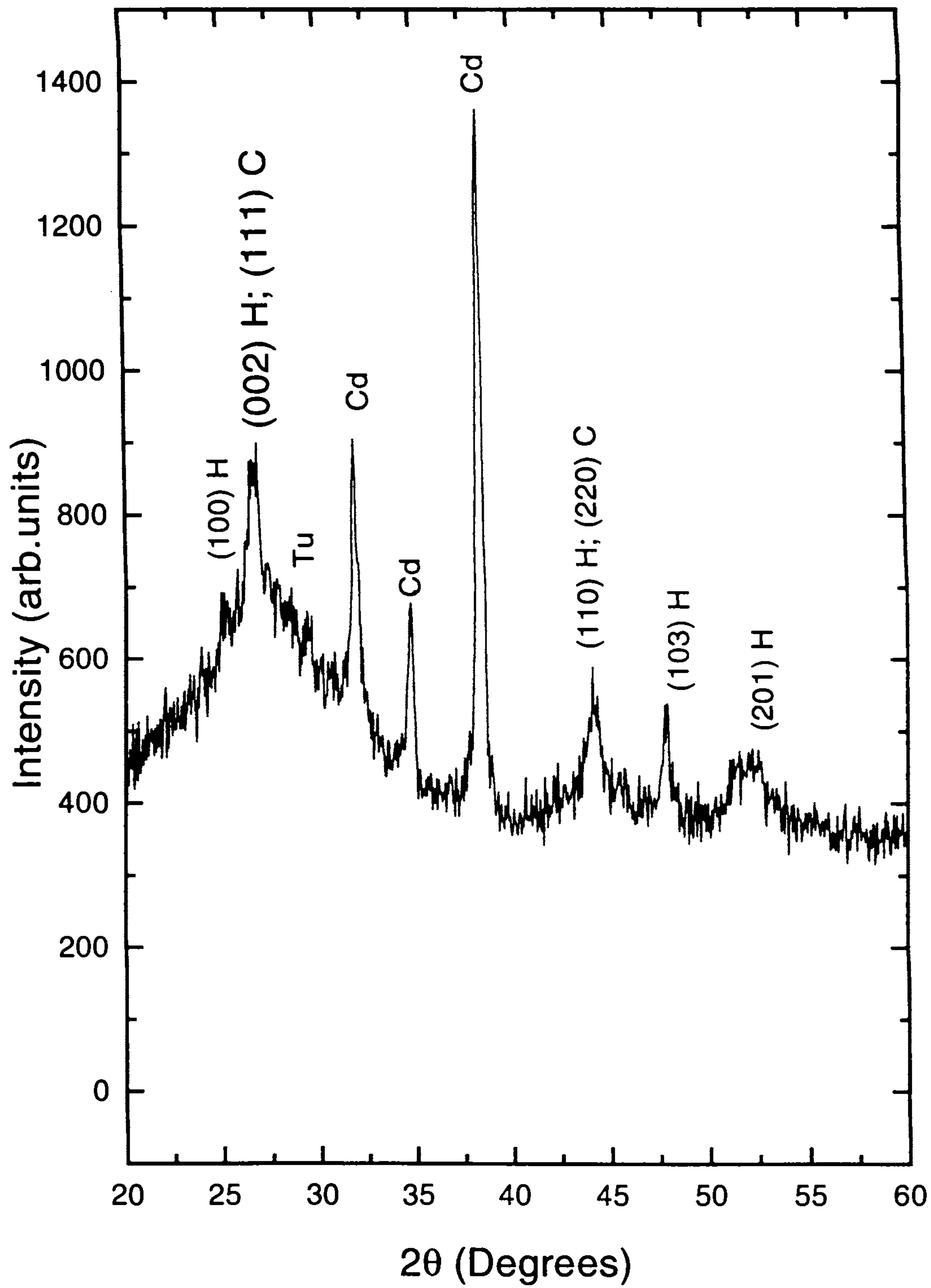

Figure 5.2: X-ray diffraction pattern of nitrogen ion implanted CdS thin films. The films are prepared by chemical bath deposition technique

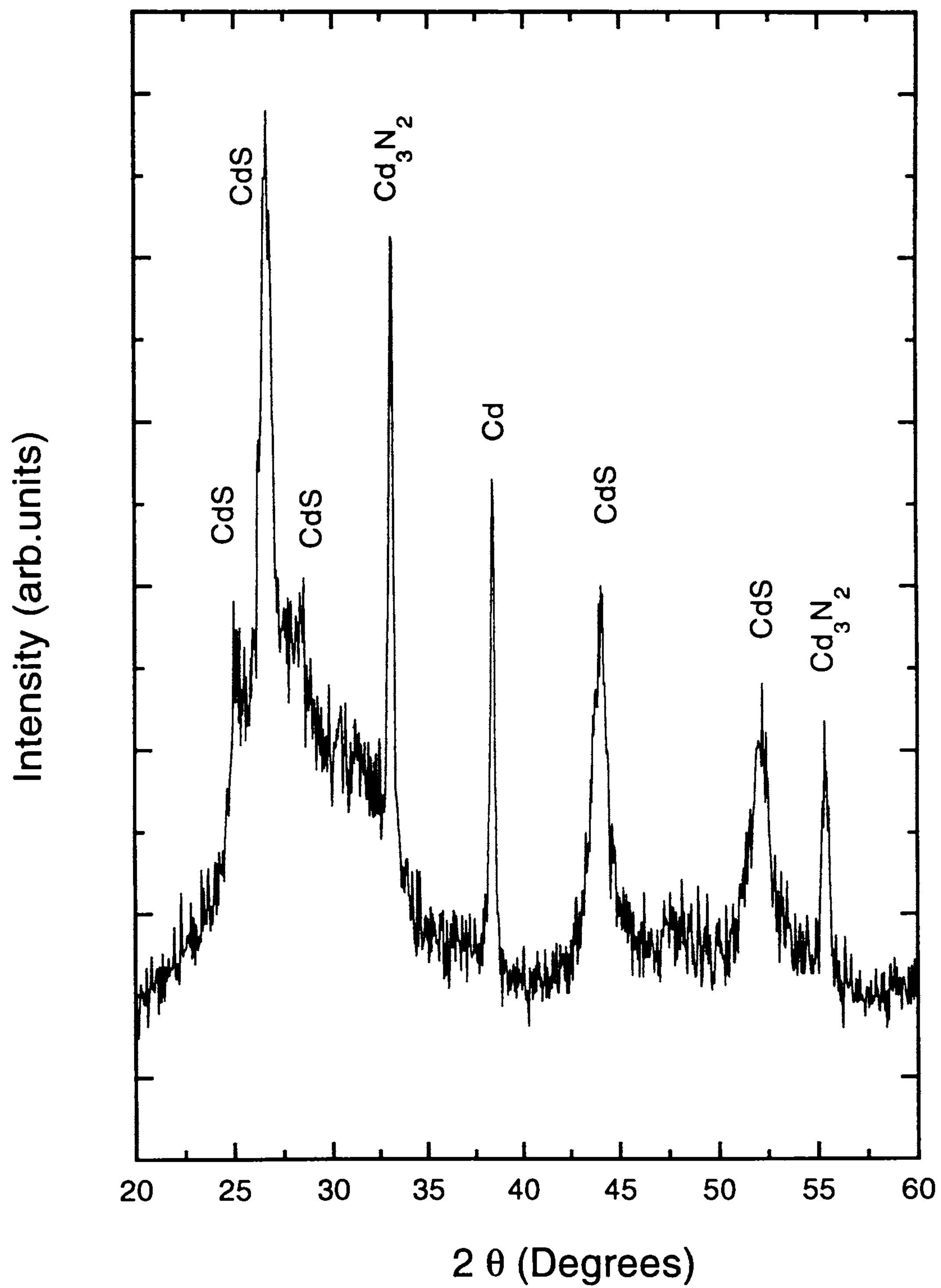

Figure 5.3: X-ray diffraction pattern of films subjected to post implantation annealing. The implanted films were annealed in flowing helium atmosphere for two hours at 673 Kelvin.

5.3.1 Conductivity measurements on N^+ irradiated films

Silver paste was used as the ohmic contact for the electrical measurements. The ohmic character of the contact was verified by doing I-V measurements and a typical I-V characteristics curve of the irradiated film is presented in the figure 5.4. The resistivity of the as-deposited film is found to be around 10^7 $\Omega\cdot$ cm. The high resistivity of the films is not surprising because of the stoichiometric nature of the film. On nitrogen irradiation, the conductivity of the films is found to increase systematically. Figure 5.5 shows the variation of the conductivity of the films with the nitrogen ion fluence. It is found that the resistivity of the films decreases from 10^{-7} mho cm^{-1} to about 10^{-3} mho cm^{-1}. On nitrogen irradiation, the metallic lustre on the film surface increases which can be seen by the naked eye. The samples subjected to irradiation of nitrogen ions to a dose of 10^{17} ions/cm^2 showed the conductivity of the order of 0.1 mho cm^{-1}. The increase in conductivity of the samples due to nitrogen ion irradiation is attributed to the formation of acceptor levels on nitrogen irradiation. The conductivity of the films subjected to high dose implantation was studied at different temperatures. The plot drawn between the $\ln(\sigma)$ and the inverse of temperature is given in figure 5.6. From figure 5.6, the activation energy was found to be 0.06 eV.

5.3.2 Hot Probe measurements

In order to understand the nature of the carriers (n or p type), before and after irradiation, Hall effect measurements were attempted on the as-deposited and implanted films. However, no measurable voltage drop was discernible when the magnetic field was applied making the Hall measurement difficult. Hence, hot probe method (thermo electric power) was used as an alternative technique to probe the conductivity type of the films before and after ion implantation. It was found that in the as-deposited thin films of CdS, electrons are majority carriers and it is n type. On implantation, p type conductivity of CdS films was established by hot probe method. Though there are various reports on the type conversion

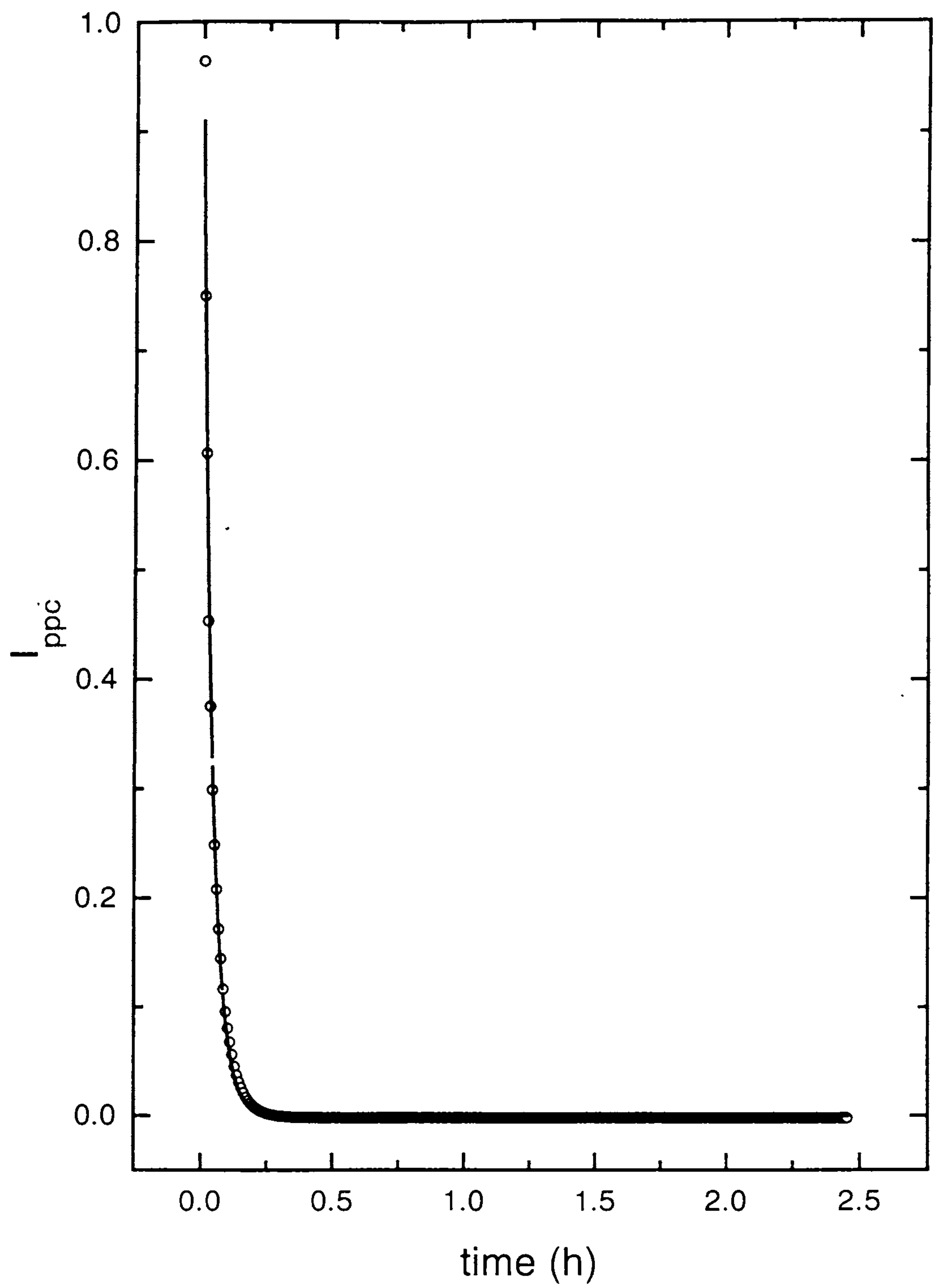

Figure 5.8: PPC decay of the as-deposited films of CdS at room temperature

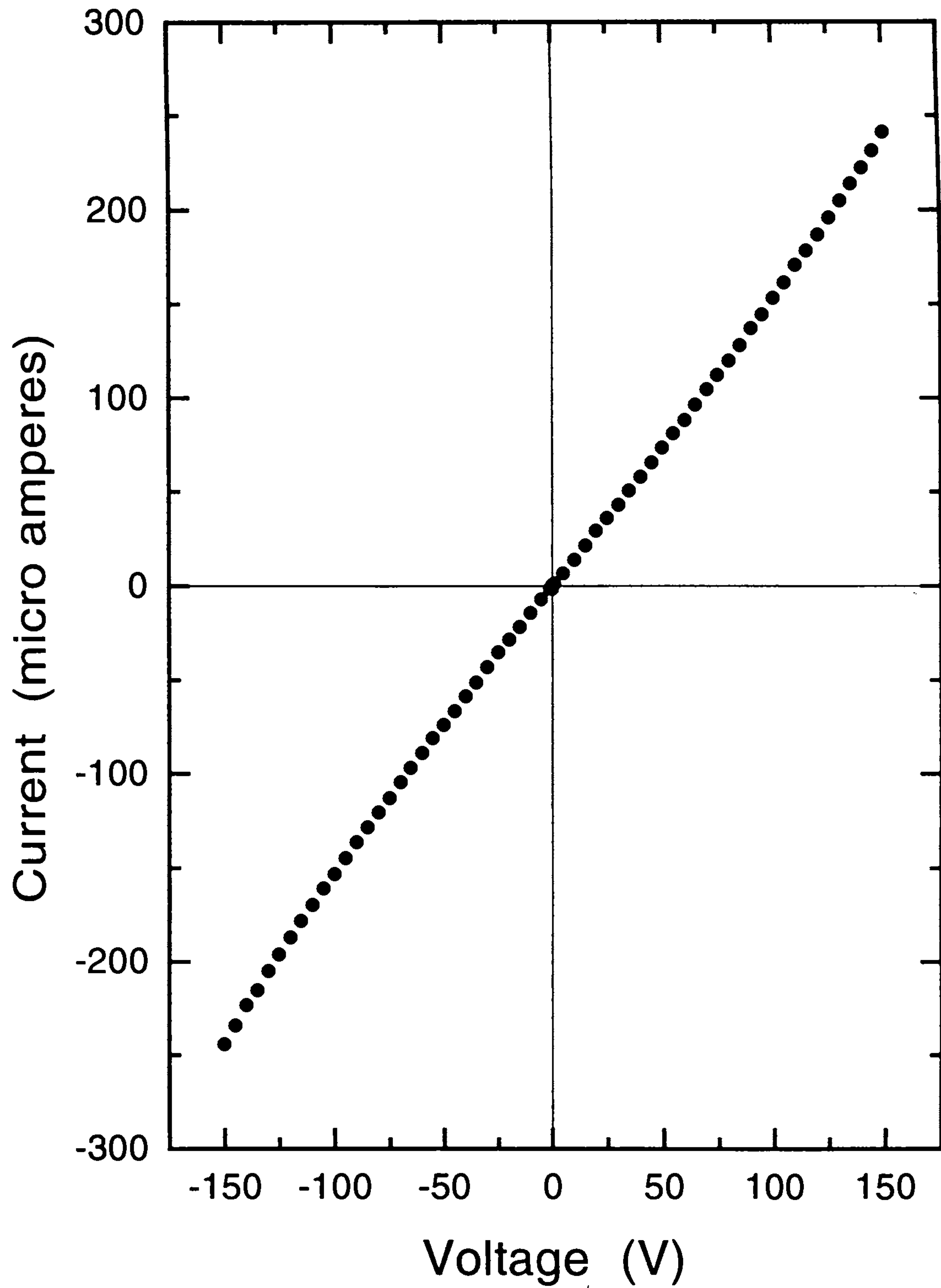

Figure 5.4: I-V characteristics of nitrogen ion implanted CdS thin film showing that the silver contact is ohmic.

of CdS material on irradiation [1, 2, 3, 4] or by diffusion process [10, 11, 12, 13] there are no reports on the type conversion in CdS thin films prepared by chemical bath deposition due to nitrogen irradiation. This is the first report of such a type conversion (ie., to p-type CdS) to the best of the authors knowledge. This conversion arises from the formation of acceptor levels produced by nitrogen implantation.

5.4 Photoconductivity

Photoconduction, i.e., increase in conductivity due to irradiation of a semiconductor with light, is a non-equilibrium process. Photoconductivity has played a major role in the development and understanding of physics of the Solid state [14]. Concurrent with the basic studies of photoconductivity have been the emergence and successful exploitation of a wide range of technologies and devices utilizing this phenomenon.

The persistent photoconductivity is nothing but the persistence of photoconductivity for a long time even if the optical excitation is removed and it is observed in many systems. The fundamentals of persistent photoconductivity, its effect in various systems and a few models for explaining the photoconductivity are discussed in the next section.

5.5 Persistent Photoconductivity:

Persistent photoconductivity or prolonged photoconductivity (PPC), an interesting and puzzling phenomenon in semiconductors is the occurrence of photoconductivity that persists for a very long period of time after the termination of the photoexcitation. PPC phenomenon observed in a variety of semiconductors such as III-V and II-VI compound semiconductor alloys has been investigated by various researchers [15]. Discovery of the room temperature PPC phenomena-makes the PPC based devices feasible. It provides a non-destructive method to probe the profile of impurities in semiconductors. Technologically, understand-

ing of optical and transport properties of II-VI semiconductor alloy thin films is also of importance for optoelectronic applications. PPC exists upto room temperature and can be optically quenched by infrared radiation in II-VI semiconductor alloys, which makes them very important materials for device applications such as infrared detectors [17]. Hence, study of persistent photoconductivity is interesting both from the point of basic physics as well as technological applications.

A relaxation time constant as long as 10^{13} seconds has been observed at 10 K in $Al_{0.3}Ga_{0.7}As$ [16]. In contrast, a decay time constant of the order of 1000 seconds has been found in II-VI semiconductor alloys and also in many other systems like superconducting compounds [18, 19, 20, 21] and C_{60} [22, 23, 24]. Various models have been suggested to describe the persistent photoconductivity in semiconductors and each model has to be dealt thoroughly for a clear understanding. The persistent photoconductivity can arise due to the presence of the metastable states or shallow or deep traps or due to complex defect centers.

The understanding of PPC phenomena will provide insight into mechanisms for basic physical processes in semiconductors such as charge carrier excitation, storage and relaxation and they are explained with suitable examples in Appendix A. Some of the possible mechanisms are (1) random local potential fluctuations due to compositional variations,(2)presence of shallow and deep levels in the bandgap region and (3) large lattice relaxation process associated with deep donor levels which are often called DX centers. Studying common features of defects in different materials through the use of PPC could help us to understand the origin of the deep level formation as well as their properties. This in turn may help to establish a common description for all defects in different materials. Carriers are spatially separated due to different mechanisms and those will be discussed in detail with appropriate examples in Appendix A. Depending upon the defects distribution, the relaxation kinetics can be described either by single or double exponential, power law or stretched exponential. It is well known that the presence of disorder in the material leads to non-exponential decay. The time dependence of photoconductivity is described in Appendix B.

5.6 Data Analysis of the Photoconductivity measurements

The photoconductivity measurements were carried out on the nitrogen implanted films and the results are discussed in this section. The experimental details of the photoconductivity measurements are given in the chapter section 2.2.9.

In order to show that CdS is highly photosensitive, the variation of the photocurrent with flash OFF and ON conditions was monitored. Throughout this experiment, a constant bias of 100 Volts was applied to the sample. Figure 5.7 shows the photocurrent of the typical case of CdS thin film, irradiated to a dose of 10^{15}ions/cm^2, as a function of time before, during and after exposure to light. The photocurrent was monitored during different FLASH ON and OFF periods. After turning ON the flash, a fast growth in the photocurrent is seen. Upon turning OFF the light, a decay is seen and again when the flash is turned ON, the growth of photoconductivity takes place, thus showing that the films are photosensitive.

In figure 5.7, the voltage is given in the right ordinate. The voltage is fixed at 100 volts for normal photoconductivity measurements and is switched OFF and ON to check its effect on the behaviour of decay process, as shown in the figure. It is to be carefully noted from the figure that decay behaviour of photoconductivity is unaffected by the presence or absence of bias voltage. Upon turning the flash OFF, the decay of the photoconductivity occurs in a slow non-exponential manner. The decay of such a kind is not surprising as the implanted films have more defects. The slow non exponential relaxation mechanism of the carriers is attributed to the persistent photoconductivity and is discussed in Appendix A.

Figure 5.8 shows a typical plot of PPC decay at room temperature for the as-deposited thin film of CdS. The dark conductivity level has been subtracted from the data points, and the decay curve has been normalized to unity at t = 0, the moment the illumination is terminated. Therefore, PPC as a function of time can be expressed as

$$I_{ppc} = [I(t) - I_d]/[I_0 - I_d] \quad (1)$$

where I_0 is the conductivity level immediately after the termination of the light source, I(t)

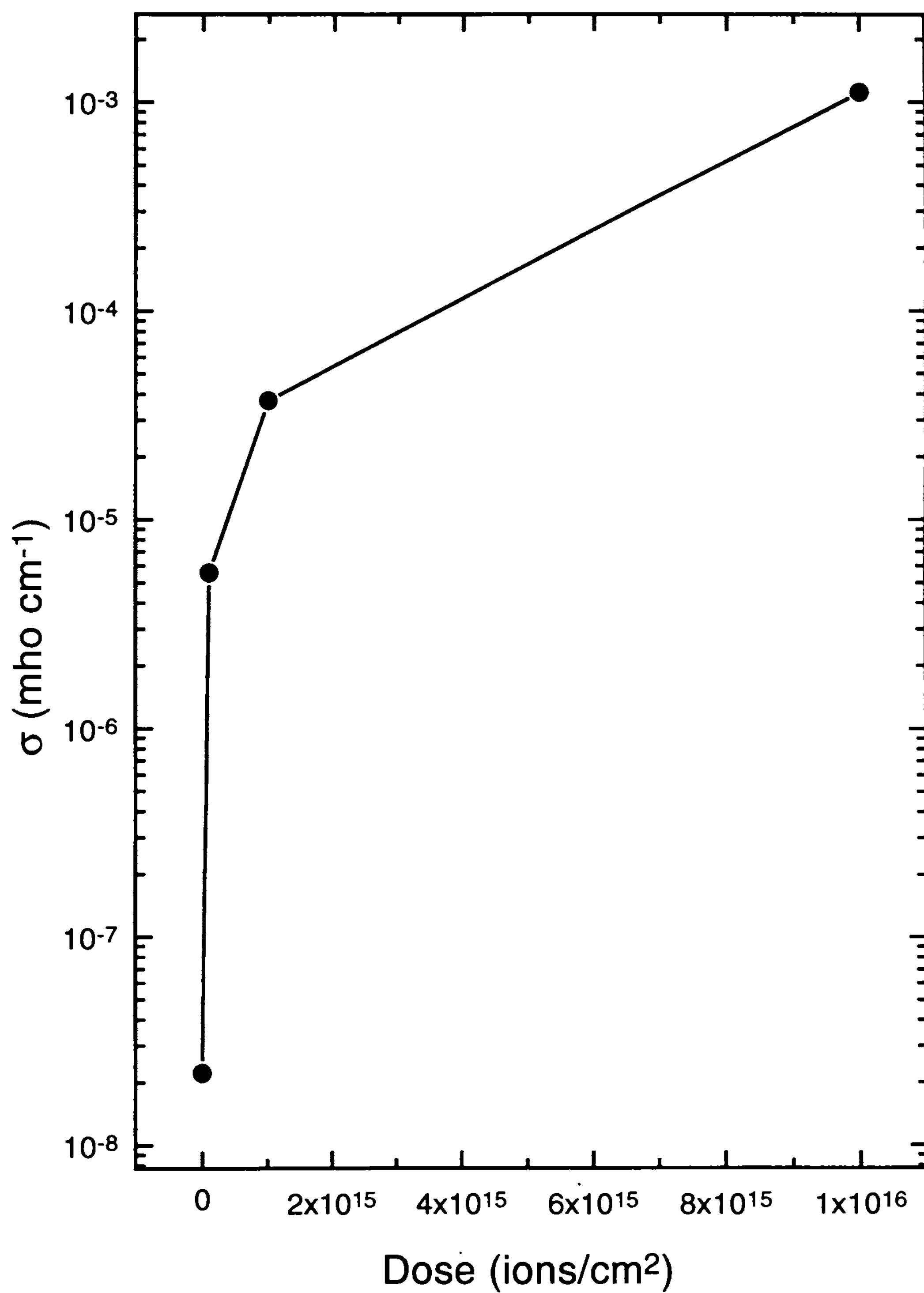

Figure 5.5: Variation of conductivity of the films with the irradiation dose.

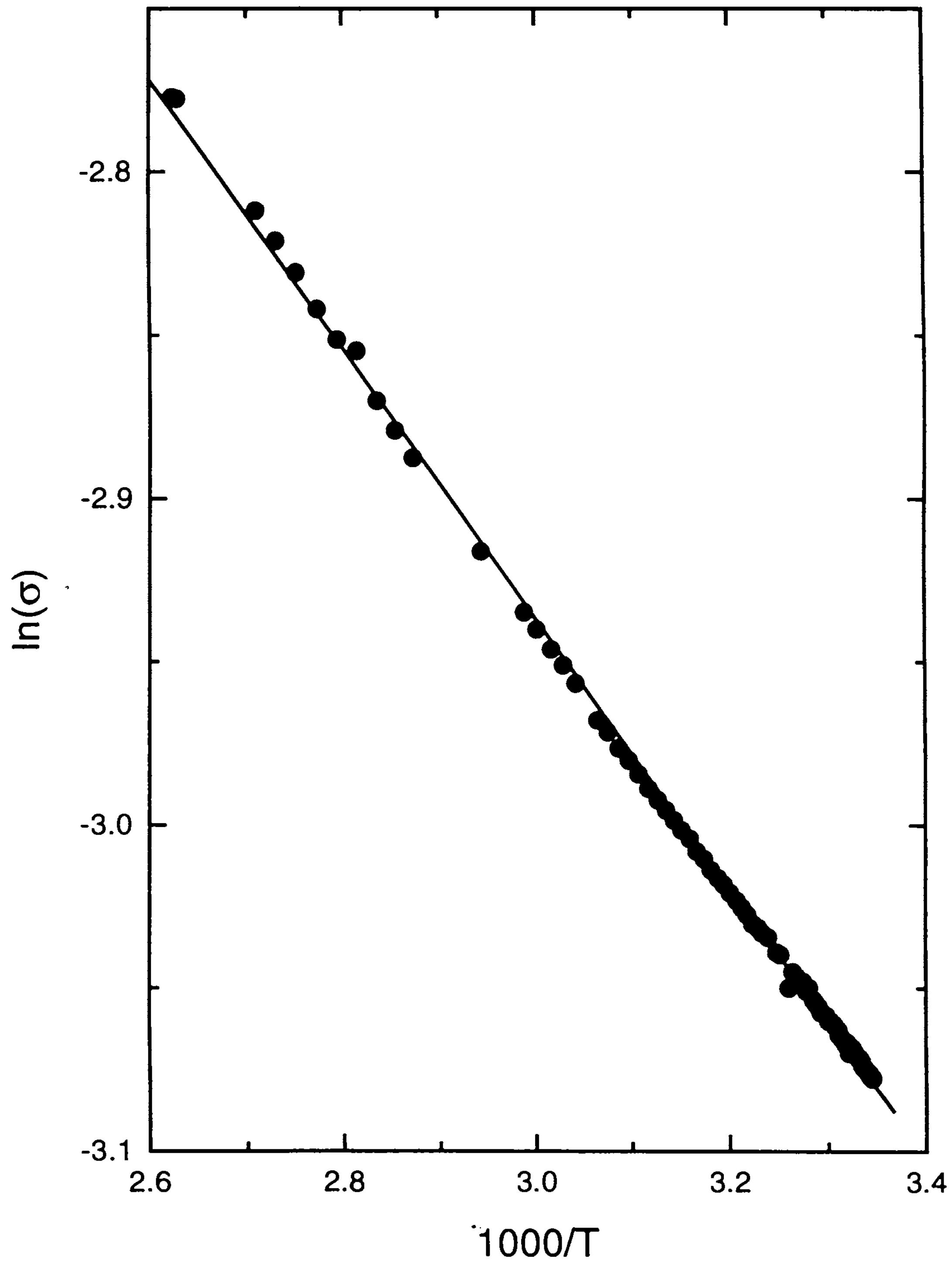

Figure 5.6: Arrhenius plot showing the variation of $\ln(\sigma)$ with 1000/T.

the conductivity at time t, and I_d the initial dark conductivity level. I_{ppc} is calculated in this manner for all the experiments and the plots are drawn between I_{ppc} and the time.

The decay constant can be found by fitting the decay curve with either of the following functions namely, single exponential, double exponential, stretched exponential and power law. There are some situations where one can expect the experimental data to be best fitted to one of the above mentioned functions. These fits were tried with all the functions and the results are given below. Figure 5.9 shows the decay curves of the as-deposited and irradiated films. Irradiation dose was varied from 10^{14} to 10^{17} ions/cm^2. It is interesting to note from the figure 5.9 that the decay rate is different in the irradiated samples. The decay rate of the films irradiated to low dose levels is not found to be as fast as in the case of the as-deposited films. Moreover, the decay rate is very slow in the high dose irradiated films. It can be concluded that the decay rate decreases with the increase in doping concentration. The systematics in the variation of the decay constants, obtained from the fits, are discussed below.

The as-deposited and irradiated decay curve data were fitted with the single exponential function $I_{ppc} = I_o exp(-t/\tau)$. The decay curve of the as-deposited film with the single exponential function fit is given in figure 5.10. It is found that the decay constant of the carriers in the as-deposited film is 0.0399 hours. All the other data were also similarly fitted to this function and the results are given in figure 5.11. A systematic increase of the time constant of the carriers with the irradiation dose is observed from the figure 5.11. Similarly, the decay curves of the as-deposited and irradiated films were fitted with the double exponential function which is of the form $I_{ppc} = I_1 exp(-t/\tau_1) + I_2 exp(-t/\tau_2)$. The decay constants are plotted with the irradiation dose in figures 5.12 (a & b) from which it is observed that the decay constants, both τ_1 and τ_2, have a systematic dependence on the irradiation dose. The analysis shows that there are two decay constants, one of faster decay and the other of slower decay.

In fact, the experimentally observed relaxation kinetics in a wide range of materials can often

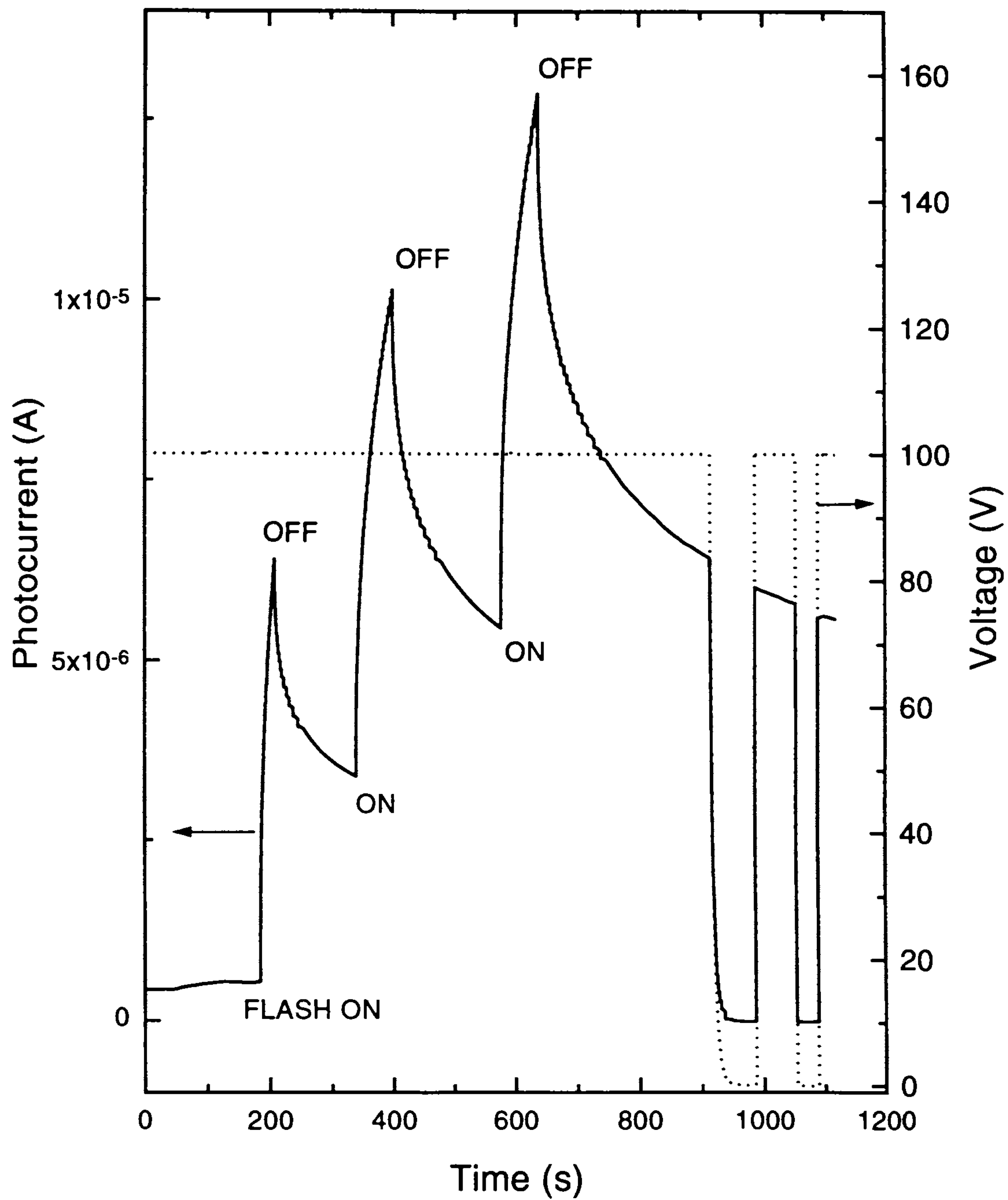

5.7: Variation of photocurrent during different flash ON and OFF conditions. The line shows the bias voltage

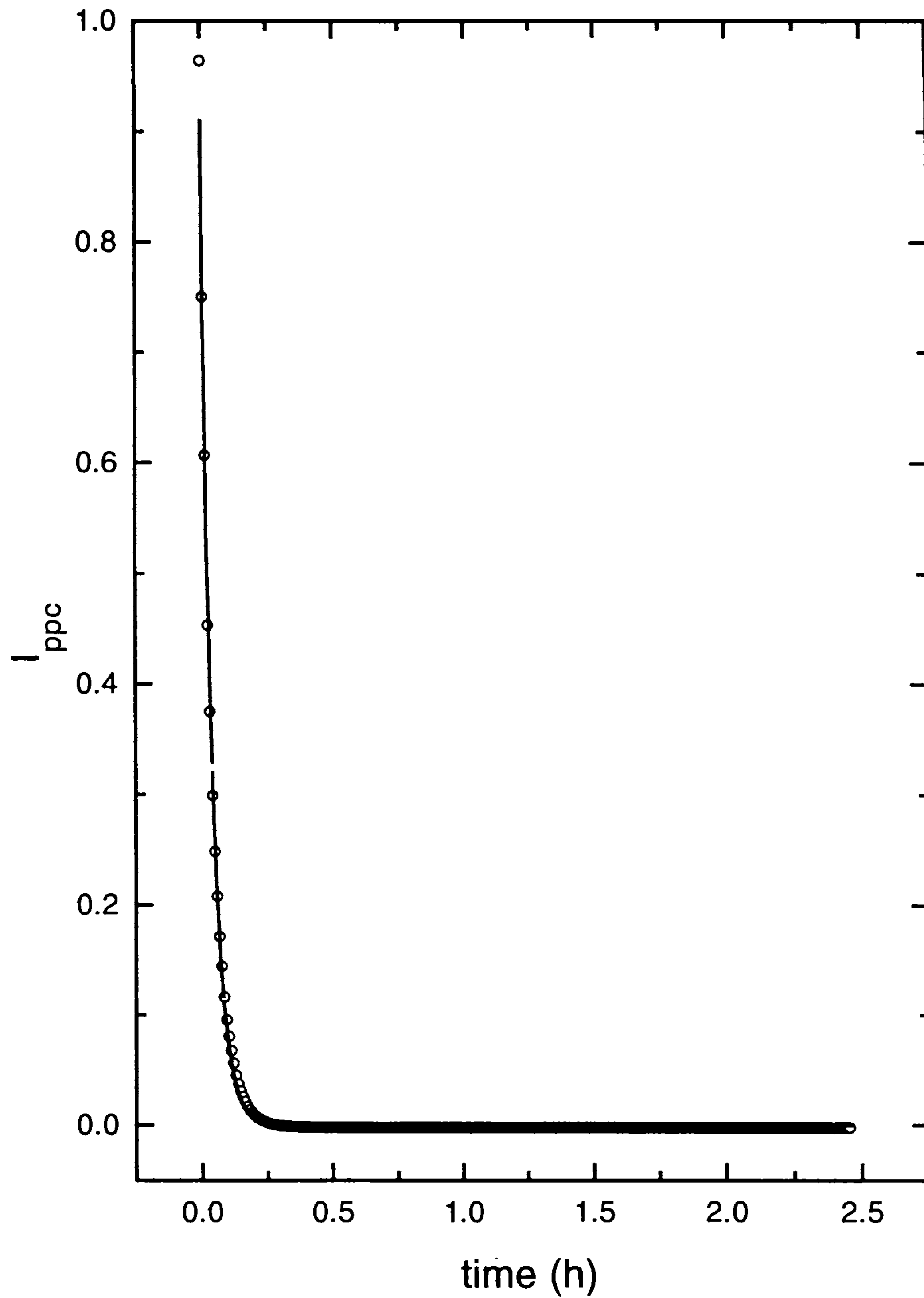

Figure 5.10: Plot showing the single exponential fit to the PPC decay curve of the as-deposited sample.

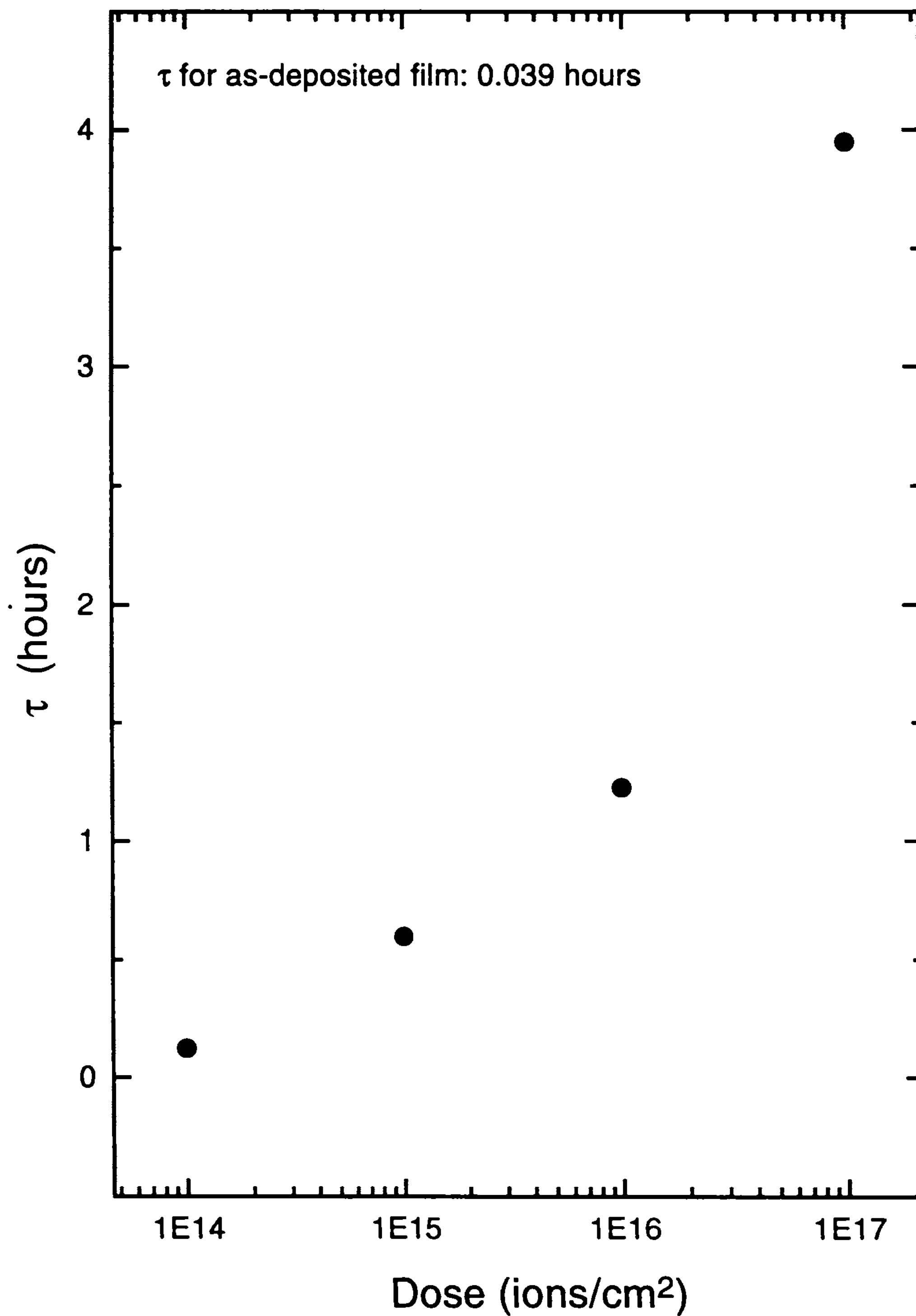

Figure 5.11: Variation of the decay constant with the irradiation dose. The decay constant was obtained by fitting the data to the single exponential function

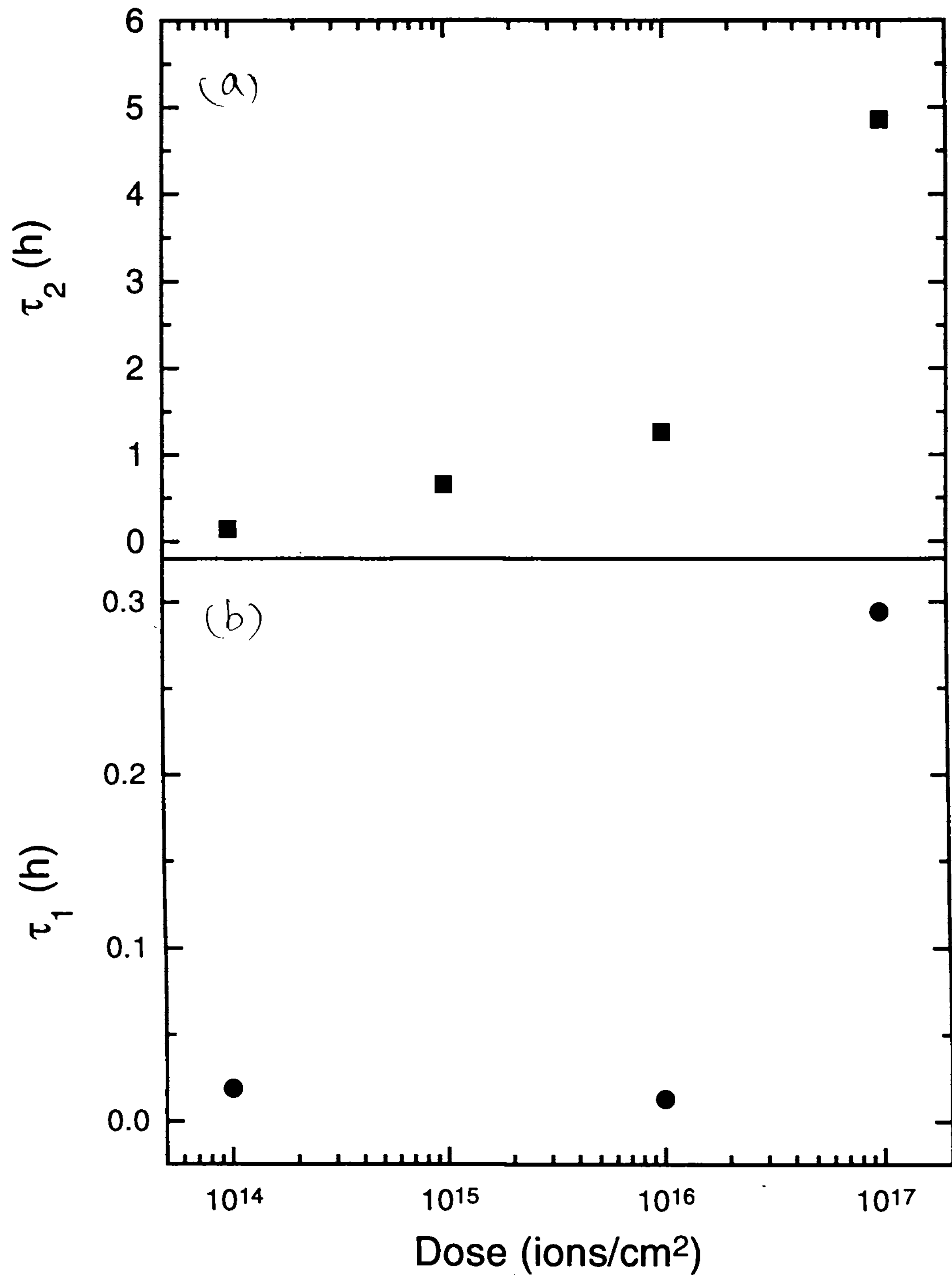

Figure 5.12: Variation of the PPC decay constants of the as-deposited and irradiated films. The decay constant was obtained by fitting the data to the double exponential function

be described either by the stretched exponential function or by power law. It is believed that these decay forms may be asymptotic forms of same kind of relaxation kinetics which describe a wide class of materials toward equilibrium under different conditions. It is widely accepted that the presence of disorder in the material leads to non exponential decay.

PPC decay behaviours were studied by fitting the data with the stretched exponential function, which is described by a time dependence, $I_{ppc} = \mathrm{I}_o \exp\left[-(t/\tau)^{\beta}\right]$, where τ is the decay constant and β is an exponent. Such a behaviour is commonly observed in disordered systems. Figure 5.13 shows the plot drawn between the implantation dose and the decay constant obtained from the stretched exponential fitting. It is observed that the decay constant has a linear dependence on the log(dose). The decay constant of the films is found to increase with the irradiation dose which is expected. The increase in the time constant is due to the highly disordered nature of the sample caused by irradiation. The decay constant of the as-deposited film is found to be around 0.035 hours whereas the decay constant of the high dose irradiated films is found to be around 1.8 hours. The high decay constant value is suitable from the application point of view. The decay curves were also fitted with a function $I_{ppc} = \mathrm{A} + \mathrm{I}_o \exp\left[-(t/\tau)^{\beta}\right]$, where A is the background parameter. Similar results are obtained from the fitted curves and the results are plotted in figure 5.14. It also has a linear dependence with the log(dose). The exponent values are found to be in the order of 0.5 to 0.9 in both the fittings for the as-deposited and irradiated films.

The photoconductivity measurements were carried out on the low dose implanted films at different low temperatures. Fits to the functions mentioned earlier were tried to the photoconductivity data obtained for different temperatures. The experiments were carried out in a vacuum of the order of 10^{-6} mbar to do the measurements at low temperatures. The non-Debye relaxation mechanism of the photoconductivity measurements obtained at low temperatures establishes the fact that the system is in a highly disordered state. Therefore, one can expect the decay to follow the stretched exponential decay rather than single or double exponential function. It is assumed that only the carrier concentration of the material

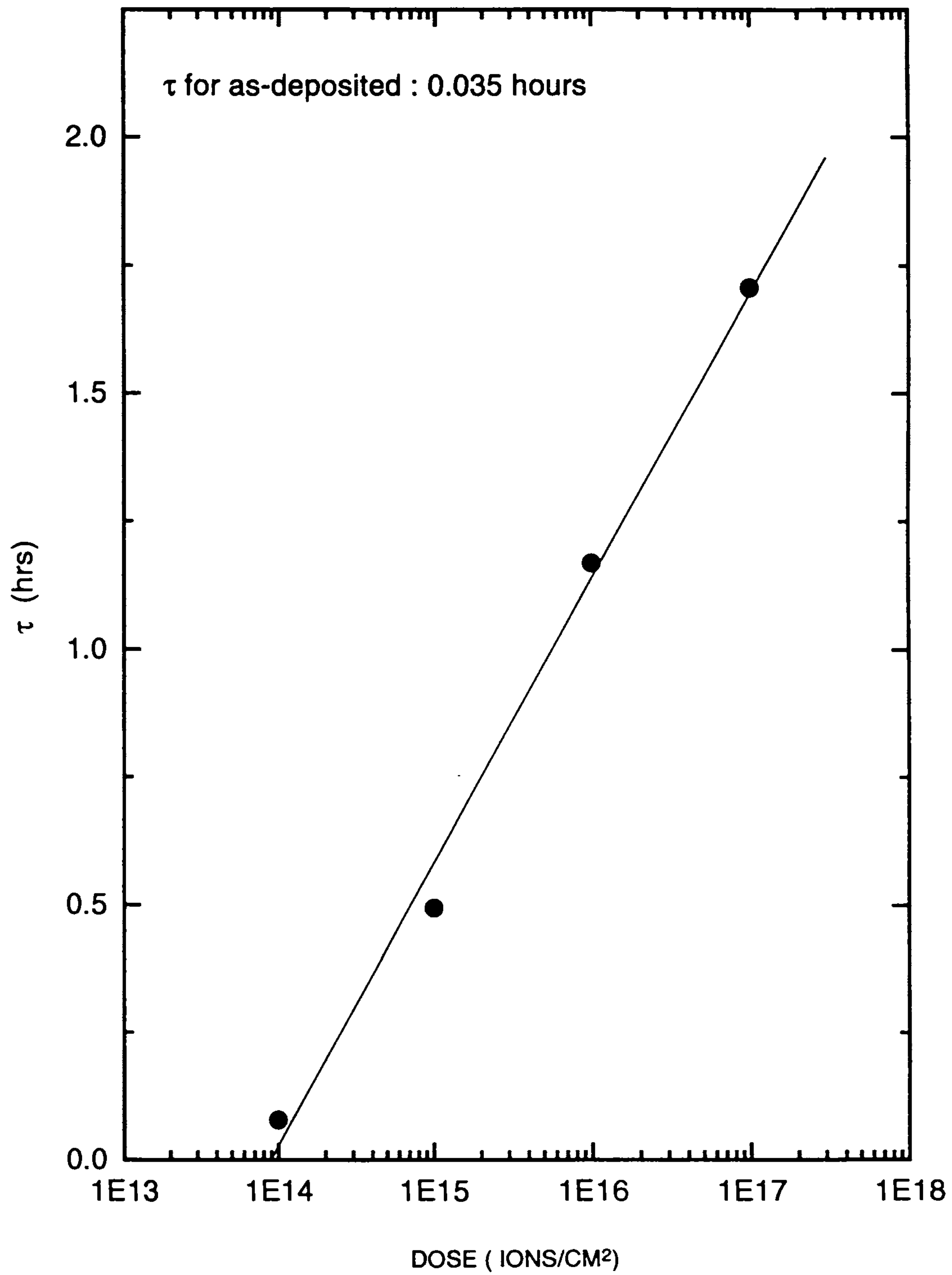

Figure 5.13: Plot drawn between the implantation dose and decay constant. The values are obtained by fitting the data to the stretched exponential function

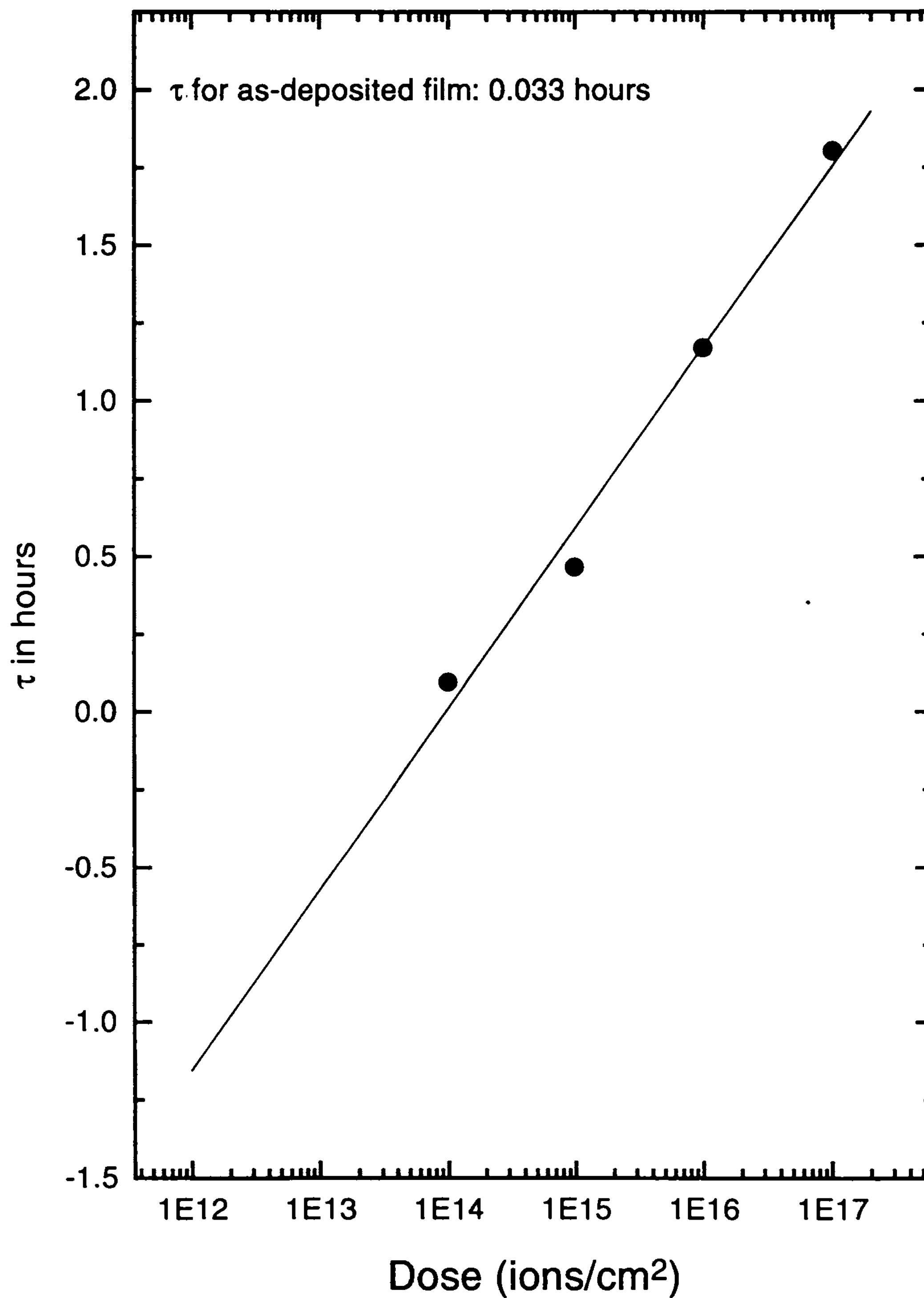

Figure 5.14: PPC decay of the as-deposited and irradiated films. Nitrogen ion was irradiated at an energy of 130 keV at room temperature. The data were fitted with a a stretched exponential function with a constant background parameter

gets affected and not their mobility. Better fits were not obtained when fitted with I_{ppc} = A + $I_o \exp[-(t/\tau)^\beta]$. The decay curves obtained at low temperatures were then fitted to a linear combination of stretched exponential and single exponential functions and the fits were found to be good. The PPC decay at low temperatures can thus be described by an initial rapid decay followed by a stretched exponential decay [25]. The decay constants τ thus generated from the fits were plotted as a function of temperature in figure 5.15. It is found from the figure 5.15 that the decay constant increases as the temperature is lowered, which is understandable. At 300 K, the decay constant is found to decrease drastically to 0.18 hours. Recombination of carriers is easily possible as the temperature is increased and hence the lower time constant at high temperature. Similar observations are reported in various systems [25, 17]. Figure 5.16 shows the Arrhenius plot drawn between $\ln(\tau)$ and 1000/T, where τ is the decay constant and T is the temperature. A straight line is evident from the figure 5.16. The electron capture barrier of 0.06 eV is found from the curve. In the case of $Zn_{0.04}Cd_{0.96}Te$, the electron capture barrier has been determined from the PPC decay measurements to be 0.125 eV [26]. The capture barrier has been determined in Si doped $Al_{0.3}Ga_{0.7}As$ [16], as 160 meV whereas in the case of CdS_xSe_{1-x}, the barrier is found to be 0.01 eV [27].

It is obvious that at low temperatures, the mobility of the carriers will get affected and hence power law fit was tried to the data of the low temperature measurements. One would expect that disorder would influence the mobility of the carriers at lower temperatures as discussed in the Appendix B. All the low temperature data were fitted to the power law and the fit is found to be good when compared to the stretched exponential function. The expression $I(t) = \frac{a}{b+t^c}$ for power law decay can be rewritten in the form $I(t) = I_0/\left[1 + (t/\tau)^c\right]$ where $I_0 = a/b$ and $\tau = b^{1/c}$. From this formula, it is evident that τ describes the characteristic time for the decay of transients. When t is much greater than τ, the decay of current follows the pure power law $I(t) = at^{-c}$. Unlike in the case of exponential decay, there is no unique time scale for power law decay. This can be seen by calculating the time required for the current to decay from a chosen level to half of its value. The time t_1 at which the current

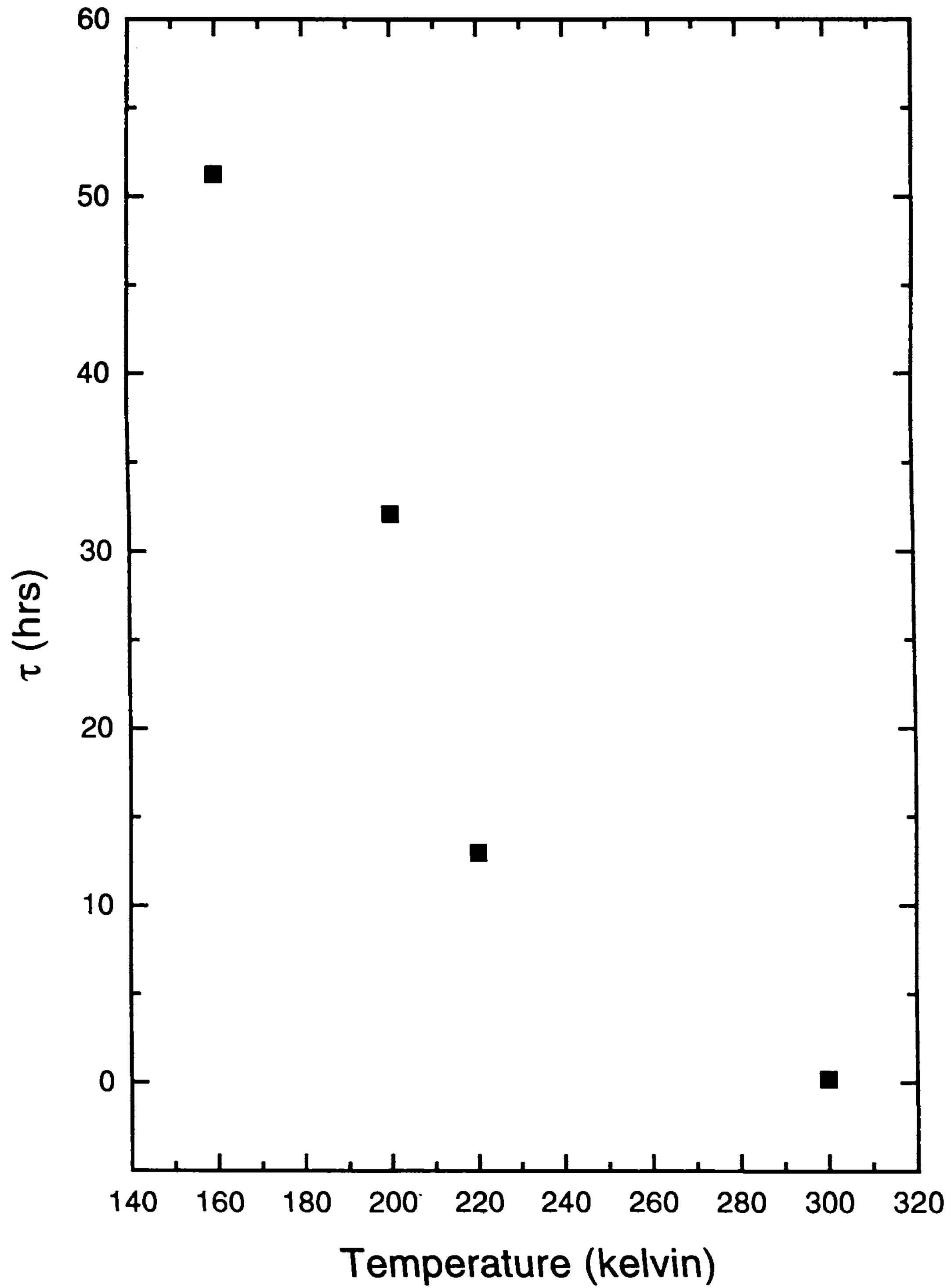

Figure 5.15: Decay constants of the films as a function of temperature. The data were fitted with the linear combination of single exponential function and stretched exponential functions.

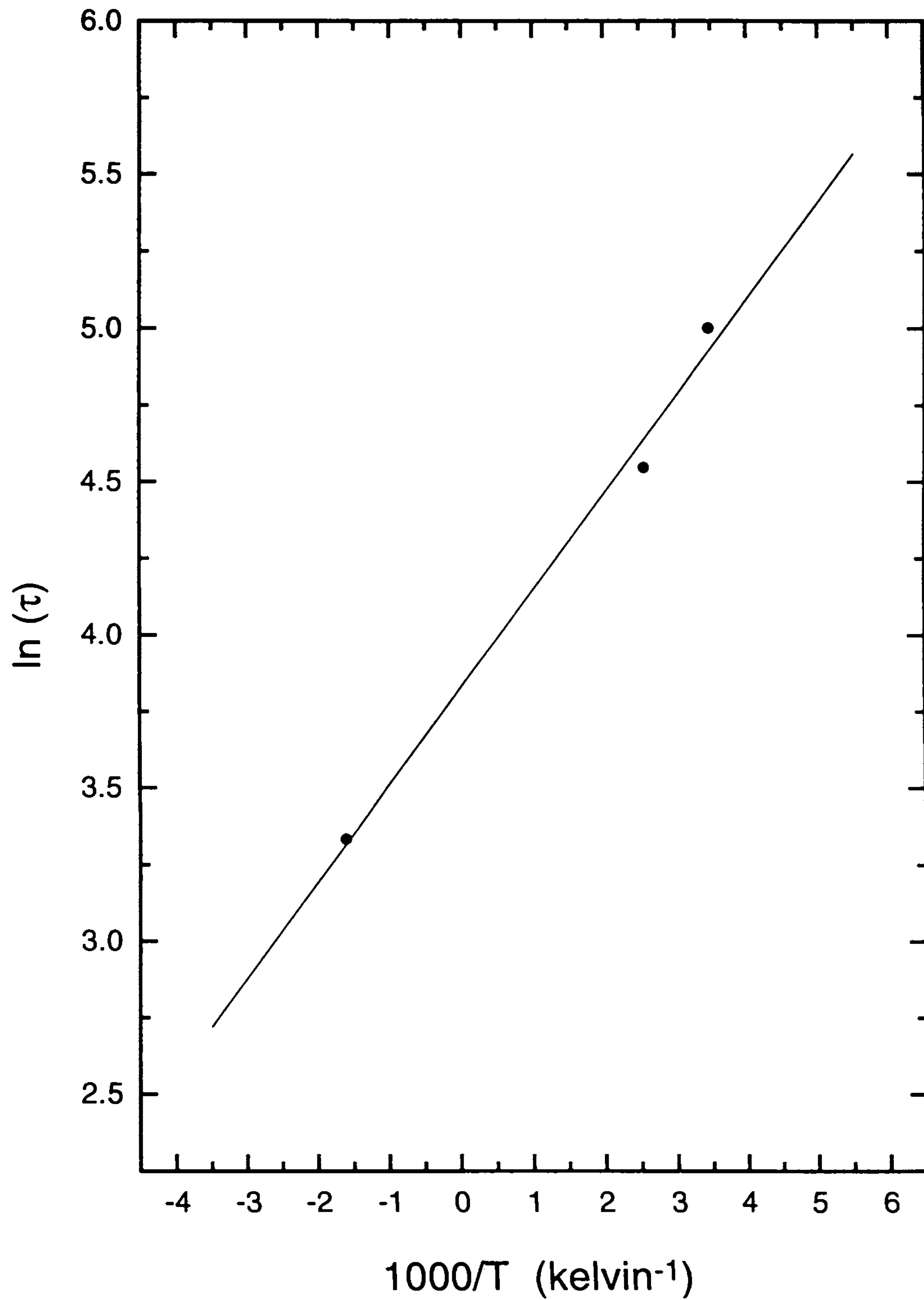

Figure 5.16: Arrhenius plot showing the variation of $\ln(\tau)$ with 1000/T.

decays from I_0 to $I_0/2$ is given by $b^{1/c}$. The time t_2 to decay from I_0 to $I_0/4$ is given by $b^{1/c}3^{1/c}$ which is greater that $2b^{1/c}$ when $c < 1$. Similarly, the time t_n for th current to decay from I_0 to $I_0/2^n$ is given by $b^{1/c}(2^n - 1)^{1/c}$. Thus the ratio t_{n+1}/t_n for the current to decay to $1/2^{n+1}$ and $1/2^n$ of its value at zero time tends to $2^{1/c}(\equiv\ exp(1/c)log(2))$ as n becomes large. Thus the time taken for the current to decay from the present level to half of its value increases exponentially with $1/c$ as the level decreases. The low temperature data were fitted with the power law expression. Figure 5.17 shows the variation between $1/c$ and the temperature. It is clearly seen from the figure that as temperature increases $1/c$ decreases. This implies that slowing down of the relaxation becomes more and more as the temperature decreases as can be intuitively expected from the power law.

So far, the persistent photoconductivity measurements of the nitrogen implanted films were elaborately discussed. The effect of nitrogen ion implantation on optical absorption measurements are discussed in the next section.

5.7 Optical absorption studies of nitrogen irradiated CdS thin films

Optical absorption studies were carried out on CdS thin films of thickness 1.5 μ m. Films were prepared by chemical bath deposition method. The films were bombarded with nitrogen ions to different doses in the range of 10^{15} to 10^{17} ions/cm^2 at an energy of 130 keV. The results are similar to the results of argon irradiated CdS thin films which are reported in the fourth chapter.

Figure 5.18 shows the optical absorption spectra of the as-deposited CdS thin film and irradiated films. It is observed that the absorption edge shifts towards higher wavelength region indicating the reduction in the bandgap. In order to estimate a reduction in the bandgap, a plot is shown between α^2 and the energy of the photons and is given in Figure 5.19. The bandgap of the as-deposited thin film of CdS is found to be 2.38 eV. It is clearly

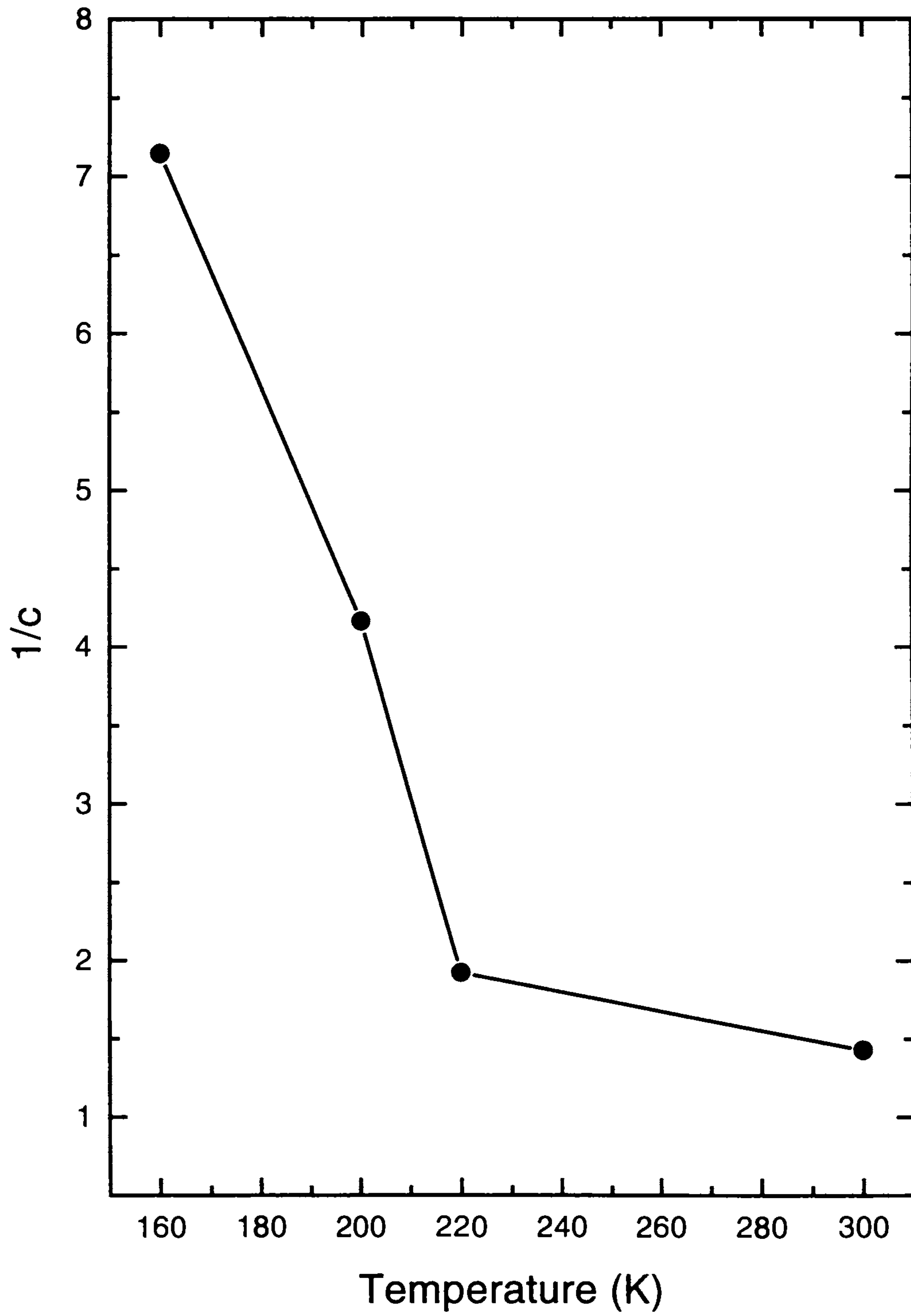

Figure 5.17: Variation of 1/c with temperature.

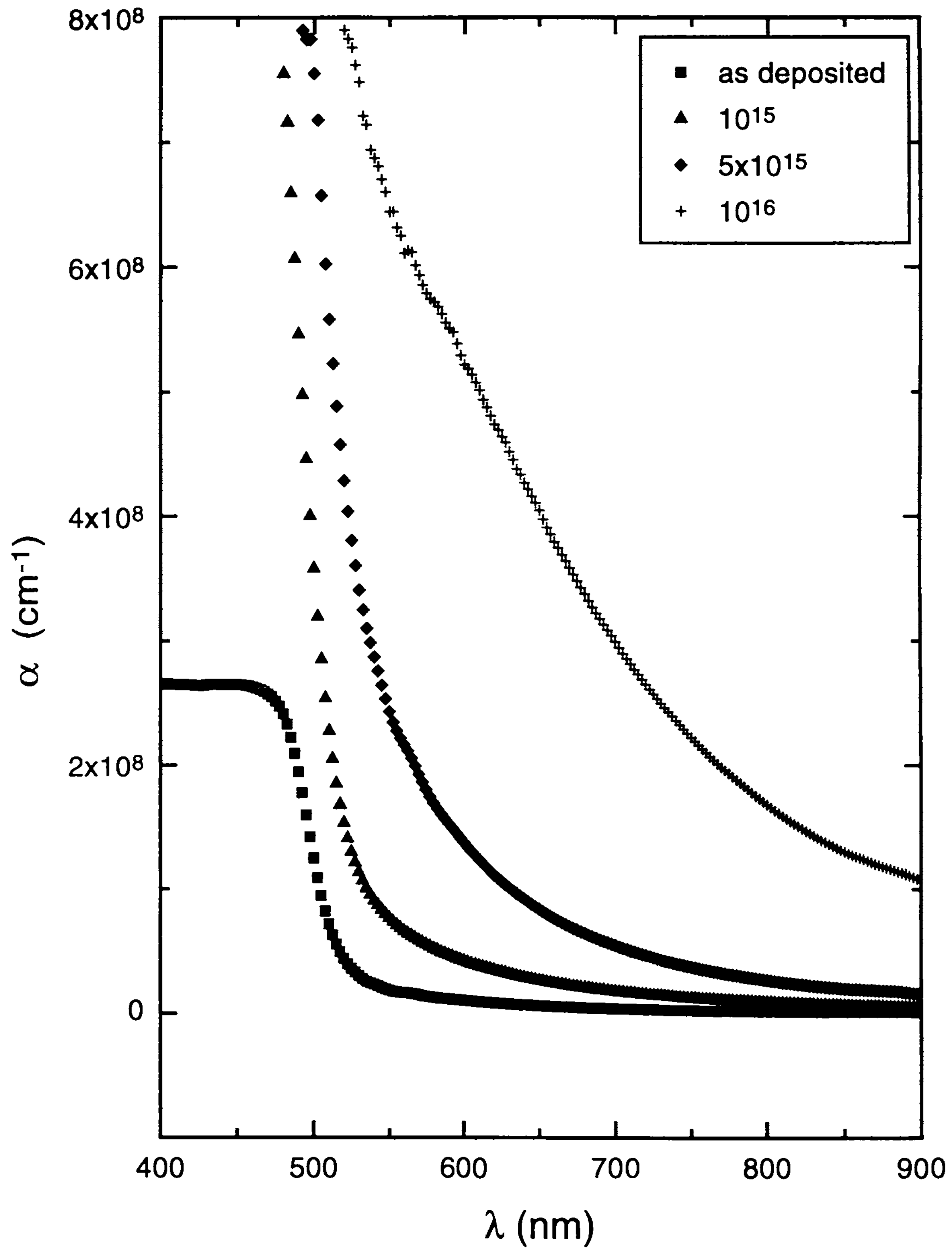

Figure 5.18: Optical absorption spectra of the as-deposited and irradiated thin films. Implantation energy: 130 keV)

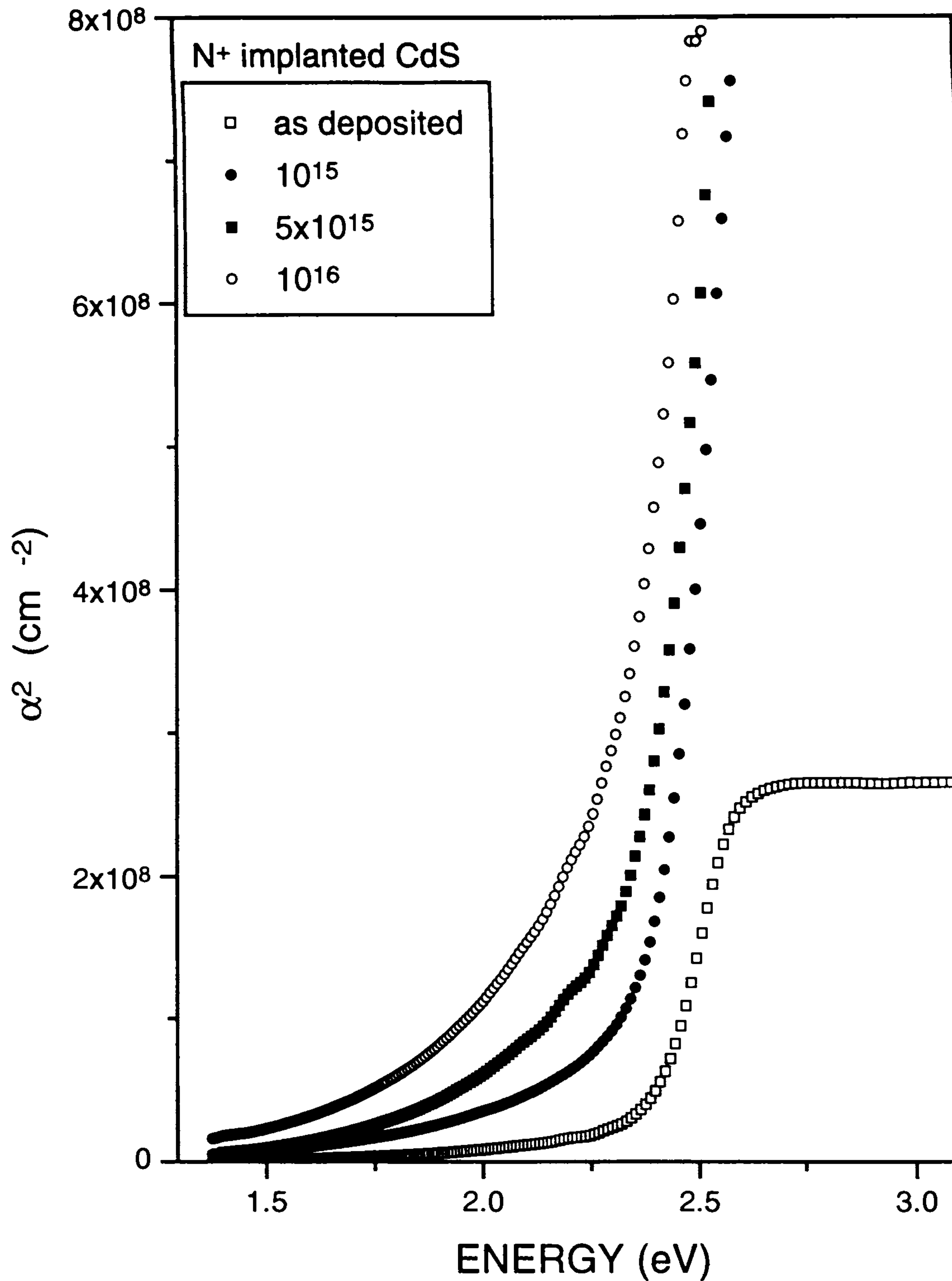

Figure 5.19: Plot drawn between between α^2 and the energy of the photons; (Extrapolation of the linear portion to the X- axis gives the bandgap of the films)

seen from the figure 5.20 that the bandgap decreases with the increase in the irradiation dose. In order to quantify the sharpness of the band edge, it is common practice [28] to fit the absorption coefficient, α, in the band edge region to the function

$$\alpha = \alpha_o \exp(E/E_o) \tag{2}$$

E_o is normally referred to as the inverse logarithmic slope. Figure 5.20 also shows the variation of E_o with irradiation dose and E_o is found to increase with irradiation dose. The reduction in the gap and the increase in E_o values are similar to the earlier reports where the authors have studied the effect of argon irradiation on optical absorption spectra of CdS thin films prepared by chemical bath deposition [29, 30]. The results are consistent with the earlier reports. The high dose sample (10^{16} ions/cm^2) was annealed at 673 K for three hours. The optical bandgap of the films subjected to post implantation annealing was found to recover from the as irradiated value of 2.18 eV to 2.3 eV. This indicates the implantation induced disorder was annihilated during subsequent annealing process. The E_o value of the films subjected to post implantation annealing also recovered to 0.199 eV.

5.8 Optical bandgap shift in oxygen ion implanted CdS films

The optical absorption measurements of the O^+ irradiated CdS thin films are reported here. The films were prepared by chemical bath deposition method. Oxygen ions were bombarded with 50 keV O^+ ions from a low energy accelerator at room temperature to various doses in the range of 5×10^{15} ions/cm^2 to 1×10^{16} ions/cm^2.

The optical absorption spectra of the as deposited and irradiated films are given in figure 5.21 from where it is seen that the absorption increases with irradiation dose which is attributed to the production of defect levels. It is seen in figure 5.21 that the the absorption edge shifts to higher wavelengths with increasing implantation dose suggesting a decrease in the optical bandgap. The optical bandgap E_g as a function of the implantation dose is given in table IV.2, where we find a progressive reduction of band gap with the implantation dose.

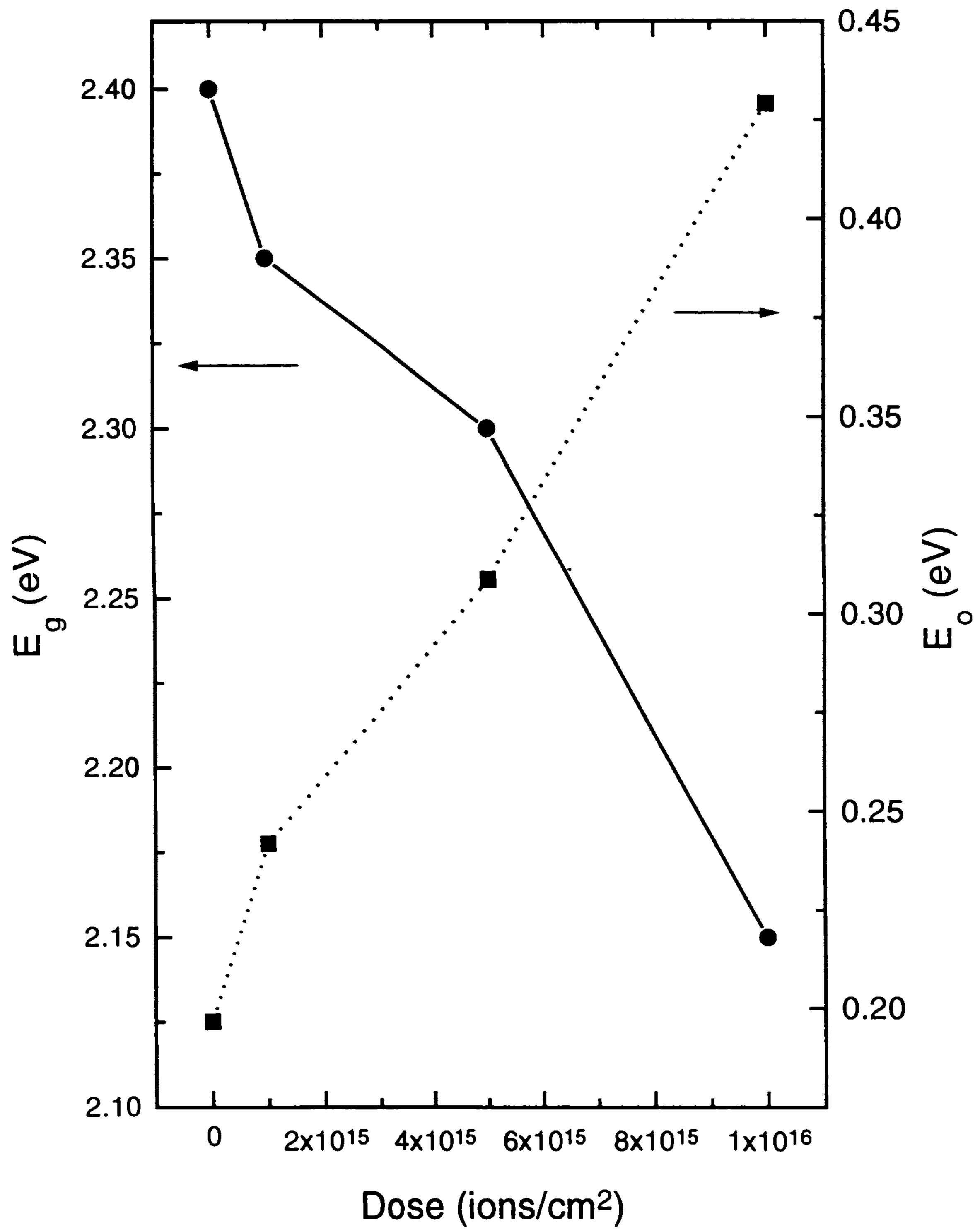

Figure 5.20: Variation of bandgap and inverse logarithmic slope E_o with irradiation dose

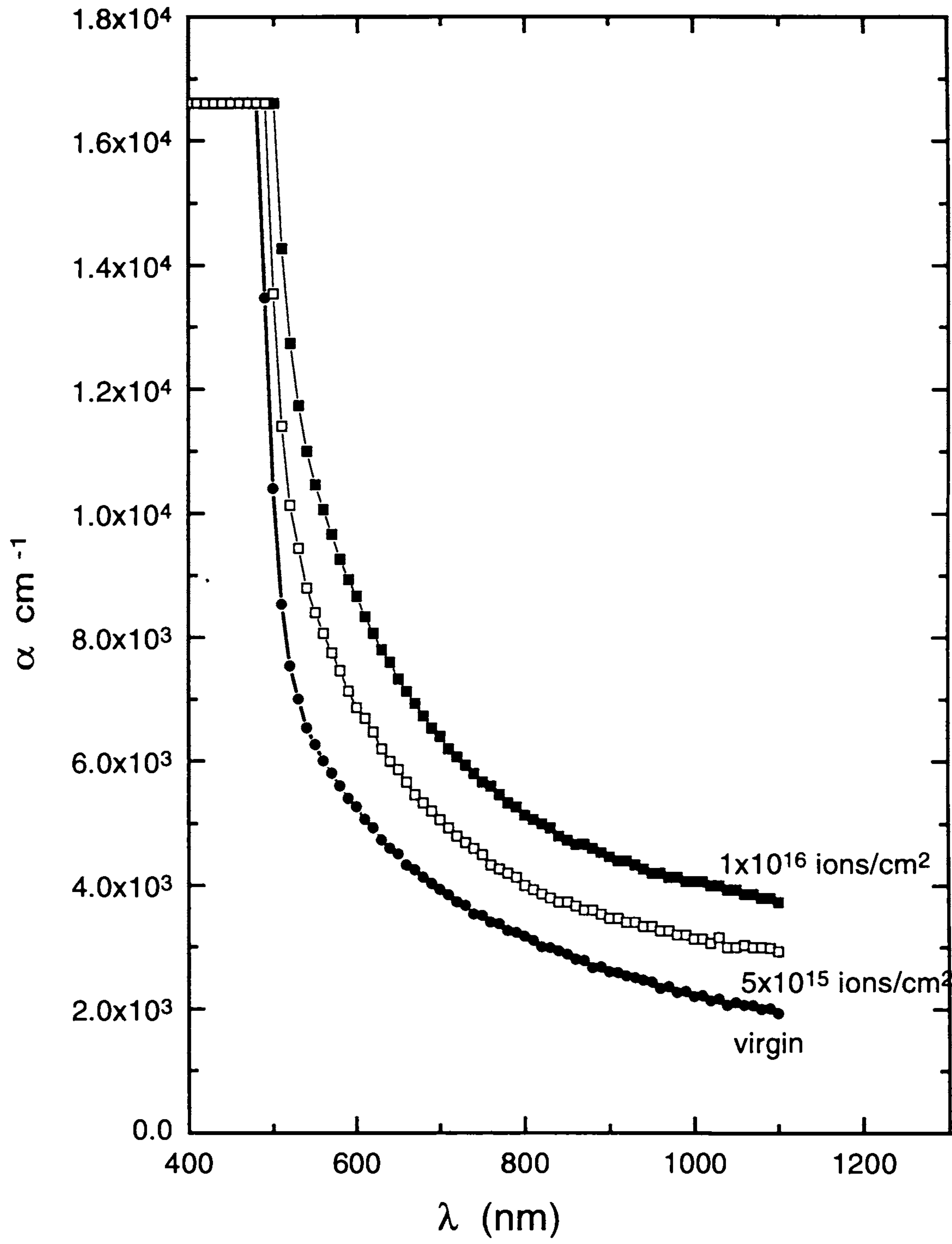

Figure 5.21: Optical absorption spectra of the as-deposited and oxygen ion irradiated films

Table V.1 Optical bandgap and E_o values as a function of the oxygen irradiation dose.(The energy used was 50 keV)

Sl. No.	Dose (ions/cm^2)	E_g (eV)	E_o (eV)
1	As deposited film	2.41	0.108
2	5x10^{15}	2.3	0.142
3	10^{16}	2.21	0.161

Another parameter which gets significantly affected by irradiation induced disorder is the sharpness of the band edge, which is found to reduce with the increase in the irradiation dose. The quantification of the bandedge sharpness was done similar to the argon and nitrogen irradiated cases, and the values of E_o are also tabulated in the table V.1 It is seen from the table, that E_o increases with implantation dose as in the case of the previous observations [29, 30]. The decrease in the optical bandgap and the reduction in the bandedge sharpness are attributed to implantation induced lattice damage as in the case of N^+ and Ar^+ irradiation.

So far, we have discussed the electrical characterisation, photoconductivity and optical absorption measurements of the nitrogen implanted CdS thin films prepared by chemical bath deposition method. The bandgap reduction induced by O^+ implantation in the CdS thin films was also discussed briefly. In the following section, the Raman scattering studies of the oxygen irradiated CdS thin films prepared by vacuum evaporation method is discussed.

5.9 Raman scattering studies of O^+ irradiated CdS films

Thin films of CdS were prepared by vacuum evaporation technique. Raman scattering spectroscopy was carried out on the samples before and after oxygen implantation to study the effect of lattice damage in the system. The results of Raman scattering studies on vacuum

evaporated CdS thin films of thickness 6000 Å irradiated with low energy (80 keV) O^+ ions at room temperature to various doses in the range of 10^{15} to 10^{17} ions/cm^2 are discussed below.

5.9.1 X-ray diffraction studies

X-ray diffraction patterns of the as-deposited and oxygen implanted films are shown in figure 5.22 (a,b). It shows a single dominant peak at 26.53^o and it is ascribed to (0002) hexagonal structure. The results are quite similar to that of argon implanted CdS film. The Cd peak is seen clearly in the XRD pattern of the high dose implanted film and it shows the formation of Cd clusters. XRD investigations of the implanted films reveal that hexagonal wurtzite phase has not got affected due to ion implantation.

5.9.2 Raman scattering studies

A typical Raman spectrum of as-deposited CdS thin film is shown in figure 5.23(a). This Raman peak arises due to A_1(LO) phonon mode of CdS. The absence of asymmetry in the lower wavenumber side of the peak implies that there is no surface mode excited in the CdS thin film. A lorentzian line shape is fitted to the Raman spectrum and the peak position, full width and half maximum (FWHM) and the area under the peak have been obtained. The higher value of FWHM (15.6 cm^{-1}) and the lower value of peak position (301.8 cm^{-1}) as compared to that of thermally evaporated CdS thin films of thickness 2500 Å(FWHM 8.3 cm^{-1} and the peak position 303 cm^{-1}) [31] indicate that the present 6000 Å thick CdS films have a lot of defects. The deposited CdS thin film has been cut into many pieces and different pieces have been implanted with different doses viz., 5 x 10^{14}, 5 x ^{15}, 1 x 10^{16}, 5 x 10^{16} and 1 x 10^{17} ions /cm^2.

Figure 5.23(b) shows the O^+ implanted CdS thin film with a dose of 1 x 10^{16} ions/cm^2. This is also fitted to a lorentzian line shape. The FWHM remains almost the same. The

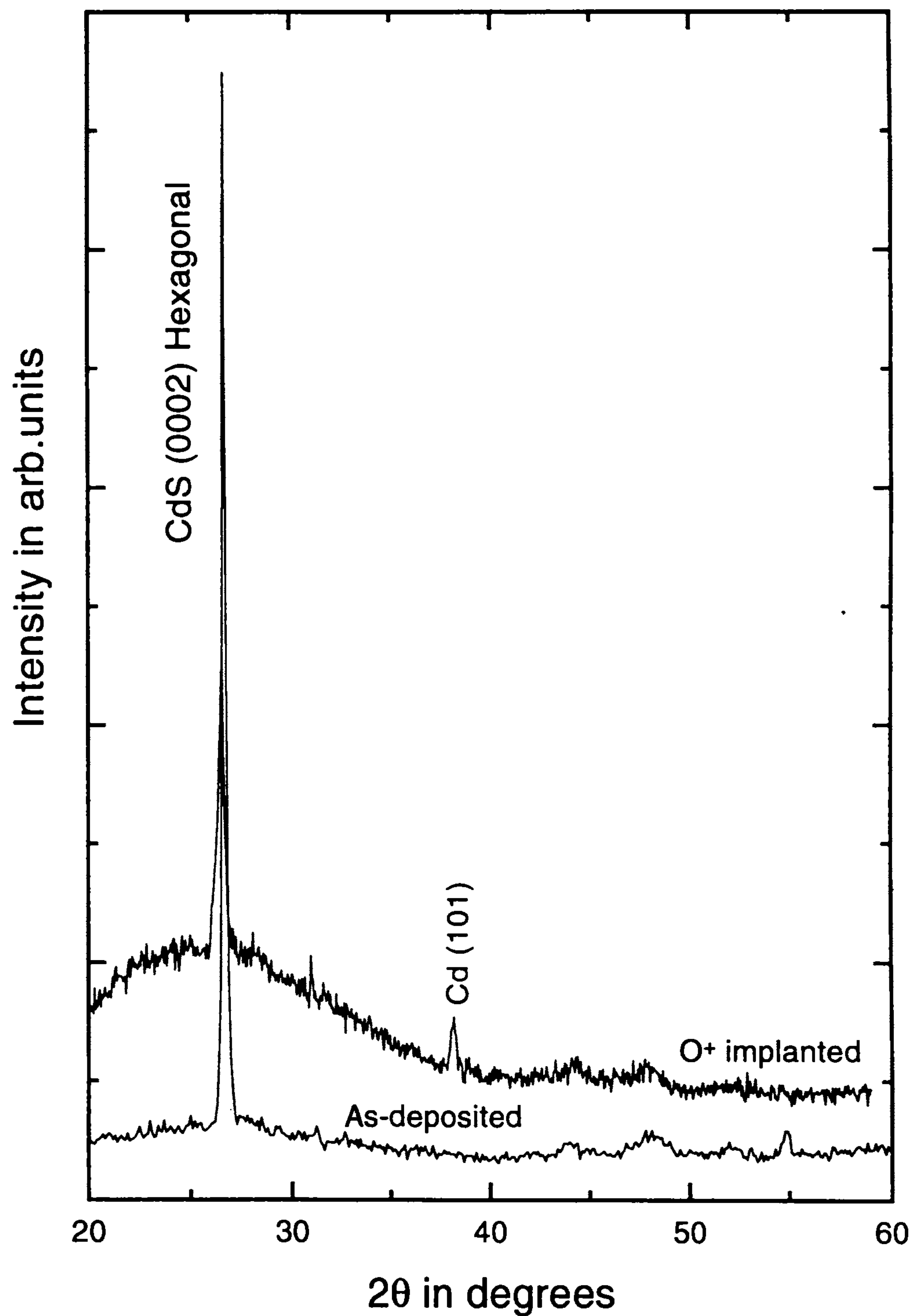

Figure 5.22: X-ray diffraction patterns of the (a) as-deposited and (b) oxygen ion irradiated CdS thin films prepared by vacuum evaporation method.

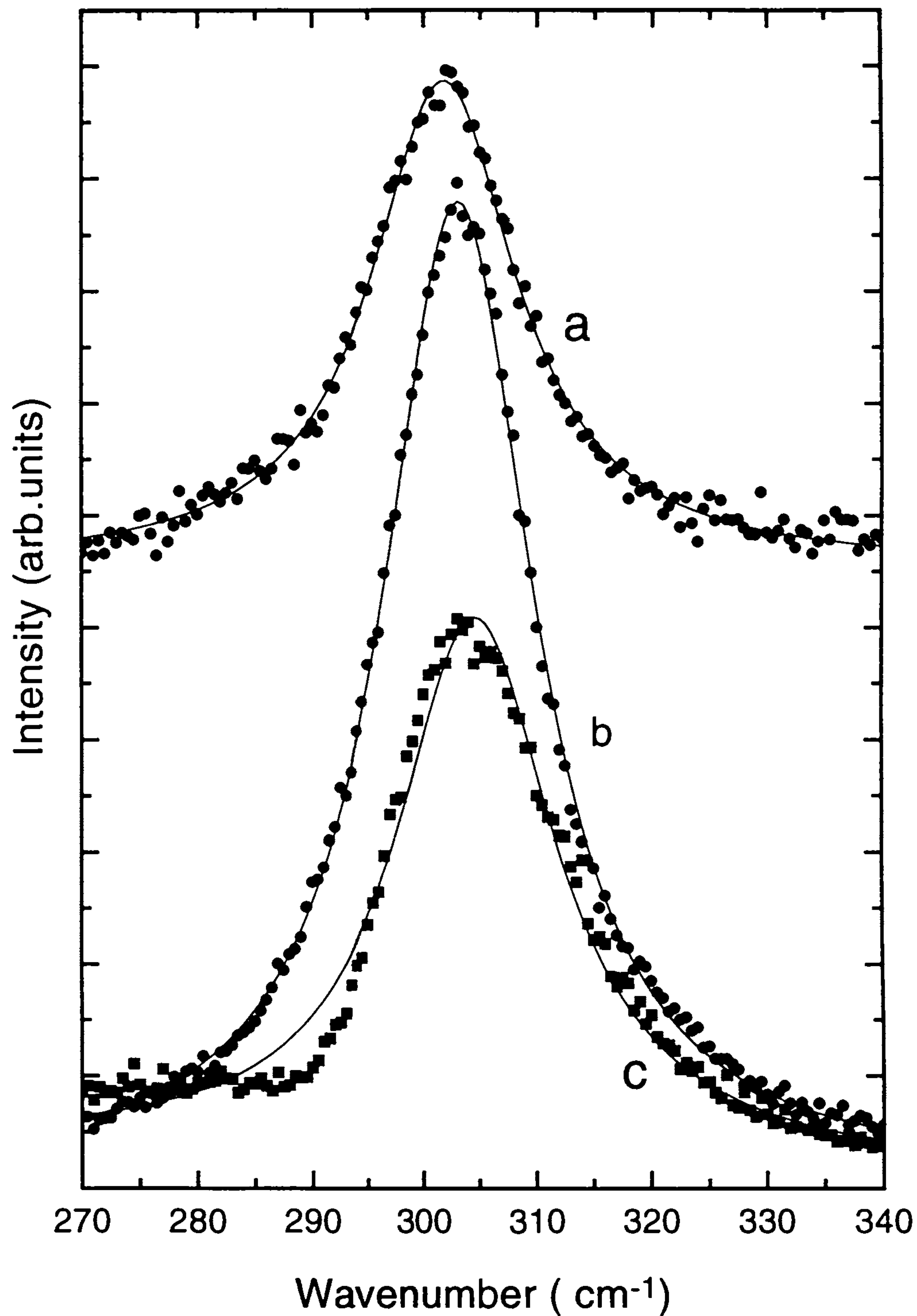

Figure 5.23: The Raman spectra of the (a) as-deposited thin film; (b) of the O^+ implanted ($1x10^{16}$ ions/cm^2) film; (c) of the O^+ implanted ($1x10^{17}$ ions/cm^2) film; The dots are the experimental data points and the solid line going through the data is the Lorentzian fit)

peak position increases and the area under the peak also increases. Figure 5.23(c) shows the Raman spectra of the high dose (1 x 10^{17} ions /cm^2) O^+ implanted CdS film. The lorentzian fit is not satisfactory as seen in Fig.5.23(c). However, for the sake of comparing the peak position, FWHM and the area of Raman mode for various doses, this single lorentzian fit is considered. The peak position further increases while the FWHM remains almost the same. The background intensity in the Raman spectra of the ion implanted CdS film has decreased considerably as seen in Fig.5.6(b). This can be explained due to ion beam induced annealing effects where one can expect the decrease in the background intensity.

Figures 5.24 (a) and (b) show the FWHM and the peak position of A_1(LO) CdS mode with implantation dose. Generally ion implantation results in lattice damage which would decrease the peak area, decrease the peak position and increase the FWHM value. On contrary, we observed here an increase in peak position as shown in Fig.5.24. This might be due to the replacement of sulphur ions by oxygen ions in the CdS lattice during implantation which results in increased vibrational frequency of Cd-O bonds as compared to that of Cd-S bonds due to mass defect. It is known that if a lighter atom replaces a heavier atom, then the vibrational frequency would increase due to mass defect. The vibrational frequency would be decided by the mass defect, the possible force constant change and the extent of atom replacement. As the dose increases, more and more sulphur ions are replaced and hence the frequency continues to increase. The observed FWHM almost remains the same indicating the lattice damage is not very high. However, the tendency of the FWHM is to increase with implantation dose as shown in figure 5.24 is in agreement with the increased lattice disorder. The area under the peak increases first to about 2.5 times at the dose of 1 x 10^{16} ions/cm^2 as compared to that of as-deposited thin film and then decreases at higher doses as shown in figure 5.25. This behaviour might be due to a competition between the Raman enhancement due to implantation induced surface roughness and the Raman intensity decrease due to increased lattice disorder. Surface roughness measurement using SLOAN DEK-TAK 3030 profilometer reveals that the surface roughness increase on ion implantation. At low doses, the Raman enhancement due to implantation induced surface roughness competes over the

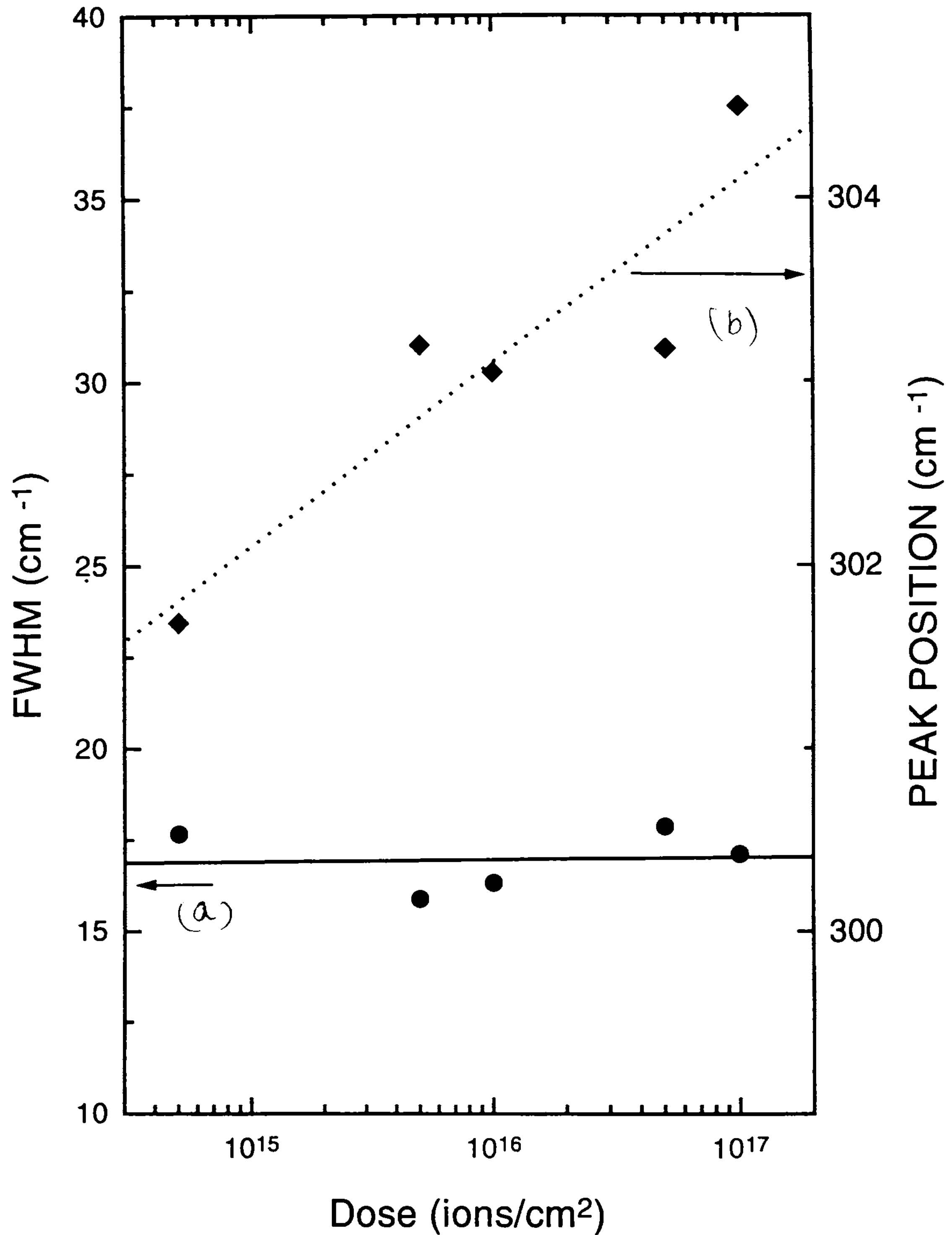

Figure 5.24: (a) FWHM; (b) Peak frequency of the Raman mode as obtained from the Lorentzian fit to the data of oxygen ion implanted CdS thin films as a function of dose. The straight lines going through the data are guide to the eyes

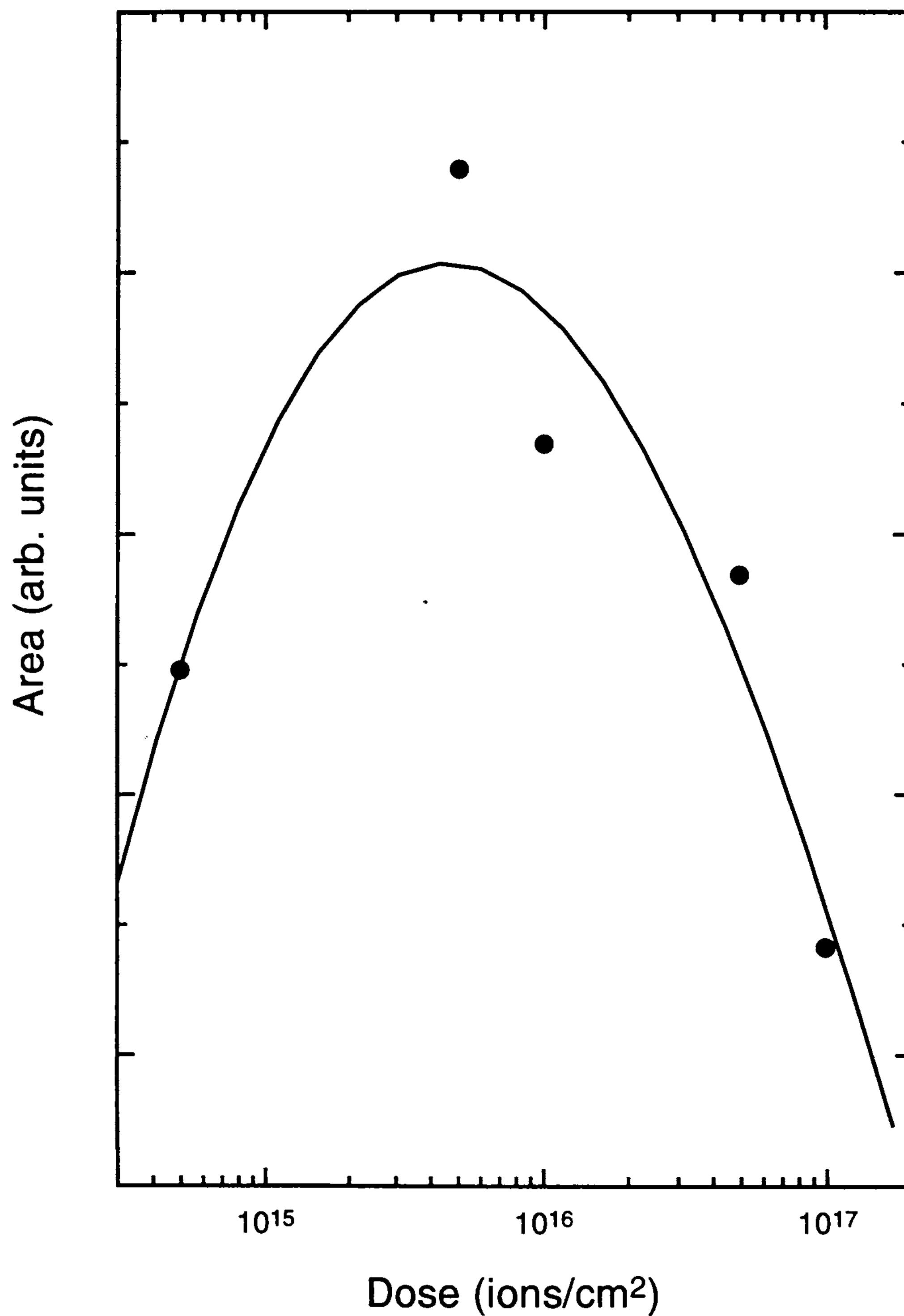

Figure 5.25: Area of the Raman mode as obtained from the Lorentzian fit to the data of oxygen ion implanted CdS thin film as a function of dose. The solid line going through the data are guide to the eyes.

lattice damage but at higher doses, the effect of lattice damage overtakes.

5.10 Summary

This chapter reports the effect of nitrogen and oxygen irradiation on CdS thin films. Nitrogen ion irradiation leads to two important results (i) A change in the conductivity type from n to p type CdS thin film is achieved and the type conversion is attributed to the formation of acceptor levels due to the nitrogen ion irradiation. (ii) Nitrogen irradiation induced persistent photoconductivity in CdS thin films is observed for the first time and the PPC effect on irradiation increases with the irradiation dose which is due to the random local potential fluctuations caused by irradiation induced compositional variations.

The activation energy of the nitrogen ion irradiated films was found to be 0.06 eV which is due to shallow level and not due to deep level. The detailed analysis of the photoconductivity measurements in the present investigations reveal that the observed time dependence of persistent photoconductivity is consistent with the random local potential fluctuations, being the rate controlling mechanism. The occurrence of RLPF provides the random distribution of time constants necessary for the occurrence of stretched exponential decay. The power law behaviour seen in the low temperature runs can occur only in the strong disorder limit. This together with the fact that there is no evidence for deep levels and can be taken for the satisfactory evidence for the presence of RLPF.

Optical absorption measurements on the nitrogen and oxygen ion irradiated CdS thin films were carried out and reduction in the bandgap of the films was seen on irradiation. Raman scattering studies of the oxygen irradiated CdS thin films prepared by vacuum evaporation technique were carried out. It was found that the peak position of the Raman mode of CdS increases with the irradiation dose and it is explained on the basis of the replacement of heavier sulphur ions by lighter oxygen ions.

5.11 Appendix A: Causes of Persistent photoconductivity

5.11.1 Random local potential fluctuations

Compositional variations can cause fluctuations in the local potential of the system. Time evolution of persistent photoconductivity observed in some materials is similar to transport in disordered systems, which suggests that random local potential variations that arise due to the compositional fluctuations might be present in these systems. The microscopic random local potential fluctuation model was frequently used to describe the charge transport properties of strongly compensated, inhomogeneous and amorphous semiconductors [32]. According to this model, the Fermi level falls in the localized region, and the charge transport occurs via activated electron hopping between localized states or by activation of electrons into the percolation state region, while holes remain localized. Therefore, a transition from localized to delocalized states is expected on the basis of this model. A percolation transition has been observed in II-VI semiconductor alloys in the PPC mode, which suggests that the spatial separation between stored charge carriers by random local potential fluctuations(RLPF) is responsible for PPC observed in these materials [33, 34, 25]. More detailed explanation of the RLPF observed in various systems is dealt with in the later part of this section.

A schematic of the real space potential profile at the conduction band edge of a II-VI mixed crystal is given in figure 5.26. In this model, the photoexcited charge carrier density is highly inhomogeneous. Spatially, electrons fall into localized states, which form due to the variations in composition or variation of band gap from one spatial region to another. The low potential sites in the conduction band are spatially separated from those in the valence band leading to very long carrier lifetimes. It is known that as temperature increases, PPC is induced by electron hopping between localized states; as temperature increases to above a critical value, T_c, electrons can be activated, become

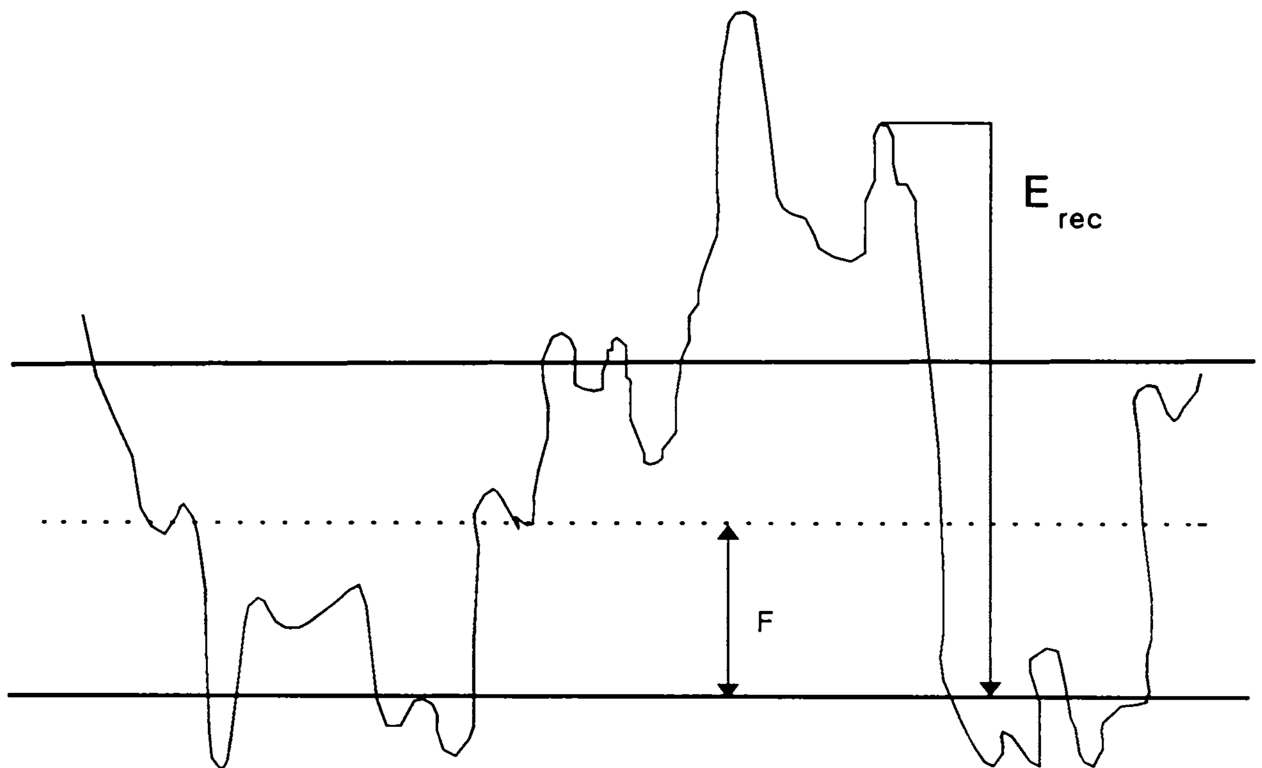

Figure 5.26: A schematic of the real potential profile at the conduction band edge.

delocalized(activated to levels above the mobility edge) and the charge transport occurs via the electrons percolating through the conduction network, while holes remain localized because of their heavier mass. Electrons are localized in the sites or percolate through the network of the potential minima and are spatially separated from the localized holes because the potential minima for electrons are the potential maxima for holes. This leads to long recombination lifetimes for the photoexcited charge carriers and hence the effect of PPC. A further increase in temperature would give electrons sufficient thermal energy to transfer to the maximum barrier height, E_{rec}, to recombine with holes soon after photoexcitation and cause a thermally activated PPC decay behaviour. Thus, the electron-hole recombination barrier E_{rec} depends predominantly on the degree of the fluctuation of the sample. In mixed crystals, large compositional fluctuations are known [35, 36, 37] to cause local potential fluctuations.

An unique property for PPC in II-VI semiconductor alloys is expected - infrared PPC quenching [17]. As indicated in the figure 5.26 the charge carriers (say electrons) stored in potential minima, can be transferred past the potential barrier to radiatively recombine with holes by illumination with long wavelength infrared radiation even at room temperature. This will result in a quenching of PPC and a stimulated emission of photons with energy of the order of E_g. PPC induced in II-VI mixed crystals by visible illumination can be quenched by long wavelength infrared radiation even at room temperature, which supports the interpretation that PPC in II-VI semiconductor mixed crystals is caused by random local potential fluctuations induced by composition fluctuations.

Dissanayake [27] studied the persistent photoconductivity in $CdS_{0.5}Se_{0.5}$ semiconductor alloy and their experimental results are consistent with the interpretation that persistent photoconductivity is caused by random local potential fluctuations. The relaxation time constant of PPC is systematically measured as a function of temperature. They observed that PPC decays faster at 45 K than at 8.6 K. Dependence of the PPC relaxation behaviour on excitation dose was also investigated for $CdS_{0.5}Se_{0.5}$, where they could observe an increase in

relaxation time constant τ with the increase in the excitation photon dose. These experimental results suggest that PPC in $CdS_{0.5}Se_{0.5}$ is caused by conduction of charge carriers stored in random local potential wells induced by compositional fluctuations.

Persistent photoconductivity has been investigated in detail in a $Zn_{0.3}Cd_{0.7}Se$ mixed crystal [25]. Relaxation of stored charge carriers, which contribute to PPC has been studied at different conditions and has been reported. At T < 220 K, the relaxation time increases with increase of temperature. They also studied the persistent photoconductivity at a constant temperature but as a function of excitation photon dose. It is found that at constant temperature, the relaxation time increases with increase of excitation photon dose. The PPC observed in $Zn_{0.3}Cd_{0.7}Se$ exhibits phenomena characteristic of disordered systems, which suggests that the random local potential fluctuations, which arises from the compositional fluctuations, are responsible for PPC.

5.11.2 DX centres

The name "*DX CENTRE*" was originally proposed [38] to account for the dual observation that the defect concentration was nearly always proportional to the shallow donor concentration (hence the relation to the donor impurity D) and the defect behaved in a decidedly non-effective mass way (hence the supposed association with an unknown defect X). The details of DX centres are reviewed by D. V. Lang [40].

The *DX CENTRES* in III-V alloys such as AlGaAs and GaAsP are prototypes of an interesting new class of semiconductor defects which is well characterised by the dominant role of lattice relaxation effects in determining the carrier capture and emission transitions. Defects exhibiting large lattice relaxation effects have been reported in a wide variety of semiconductor systems and have been reviewed by Langer [39]. One of the more striking phenomenon associated with *DX CENTRES* is persistent photoconductivity.

PPC is often explained by large lattice relaxation (LLR), i.e. by the atomic displacements

accompanying the electronic transitions between deep centres and the bands. The energy barrier associated with those displacements is responsible for the strong dependence of the recombination rate and the very slow kinetics at low temperatures. The 'electron-type' PPC has been observed in some II-VI compounds doped with Cl, In, or Ga [41, 42, 43]. In all these cases, the crystals were n type and the PPC was described by a widely accepted, LLR type model of the so called *DX CENTRES.*

One of the most fascinating consequences of lattice relaxation around deep centres is the possibility of negative - U centres. The quantity U refers to the energy change that accompanies the addition of an electron to the centre while it is partially occupied. If no relaxation is involved, the energy change is positive, reflecting the repulsive nature of electron-electron interactions. The energy change is usually called the Hubbard U after Hubbard who first explored its consequences in a variety of systems[44].

The phenomenon of persistent photoconductivity in $Zn_{0.04}Cd_{0.96}Te$ was observed upto room temperature [26] by Dissanayake *et al.* The results of their investigation indicated the deep centers are responsible for the PPC observed in thin films. Deep centers in a wide class of materials, whether they are introduced during the growth process or doping, exhibit a common phenomenon, ie., PPC. Deep centers are found to be responsible for the PPC effect in $Zn_{0.04}Cd_{0.96}Te$ thin film samples [26]. The photoconductivity measurements were carried out on both the bulk and thin films and the results are discussed. PPC decay is very fast in the case of bulk material which is contrary to the behaviour of thin films. The decay rate of PPC decreases as temperature increases in the temperature region investigated, which is once again contrary to the behaviour observed in thin films [26].

5.11.3 Traps and metastable states

Bhattacharya *et al* [45] studied the persistent photoconductivity behaviour on ion irradiated carbon films prepared by plasma assisted chemical vapour deposition. A very complex

distribution of traps created mostly by random displacement of carbon atoms by energetic ion beam, from its polymeric matrix showed a persistent photoconductivity at low temperature. The decay constant estimated from the photocurrent is around 15 seconds at 10 K. They calculated the density of traps and corresponding activation energies from the time constants and the intensity of photocurrent. This report shows how the slow decay of photocurrent can be applied to probe distribution of traps in the amorphous carbon during the process of ion irradiation.

Chiu [24] have studied the temperature dependence of persistent photoconductivity in C_{60} single crystals. PPC effect has been observed in C_{60} polycrystalline thin films by Hameed *et al* [23] and the underlying mechanism is not elucidated. It is found that PPC decays faster as the temperature decreases for temperatures below 260 K, which is the temperature of the rotational disorder/order phase transition. Kakalios and Fritzsche [46] reported persistent photoconductivity in doping modulated amorphous semiconductors which consist of alternating layers of n and p type doped, hydrogenated amorphous carbon. These structures are found to exhibit, after a brief illumination, a photoinduced conductivity that is several orders of magnitude larger than the dark conductivity and the current decays only very slowly on a time scale of days or weeks. Such PPC has been predicted to occur in crystalline doping superlattices on the grounds that the internal fields associated with doping modulation would spatially separate the photocarriers and thus prevent or greatly inhibit their recombination. The PPC effect reported by them for doping modulated a-Si:H is not restricted to low temperatures but is observed at temperatures as high as 400 K. Dohler has attributed the PPC effect of amorphous doped superlattices [47] in the following way. It is a fact that photoexcited electron-hole pairs are separated by the $p - n$ junction fields. The electrons get preferentially trapped in the n layers and holes in the p layers. The recombination lifetime becomes exceedingly long because recombination is hindered by the spatial separation of electrons and holes and the potential barriers.

Persistent photoconductivity in low energy argon ion bombarded semi-insulating GaAs was

studied [48]. It is well known that low energy ion bombardment produces a highly disordered region near the surface of the target material. Chemical analyses of the disordered regions indicated As deficiency as a result of preferential sputtering of arsenic, and an increased surface chemical reactivity [49]. Ion beam etching introduces discrete trap levels over a region deeper than ion range predicted by the LSS range distribution theory [50]. A possible mechanism for the PPC is the existence of longer lifetime electron traps in the damaged and partly amorphous near the surface region. At lower temperatures, the photoexcited electrons face an energy barrier for recapture. Upon terminating the excitation source due to insufficient energy for recapture, the traps remain ionized resulting in higher conductivity existing for an extended period of time. A second mechanism for the PPC could be the photogeneration of metastable states which had smaller capture cross sections for electrons [48].

5.12 Appendix B: Time dependence of the photoconductivity: A Mathematical Approach

In this section, we take a closer look at the time dependence of photoconductivity. The build up and the decay of photoconductivity are related to the relaxation kinetics of carriers in presence of recombination, trapping and detrapping. The approach towards equilibrium does not occur with the usual Debye relaxation but it occurs through many types of non-Debye relaxation functional forms. For example, the decay can be adequately described by a double exponential, stretched exponential or a power law in different classes of materials or for different states of materials. In this section, we will first consider rate equations describing the kinetics of carrier concentrations for various recombination and trapping scenarios. These equations will be solved to obtain the time dependence of photoconductivity.

5.12.1 Donor level excitation without traps

Let $\Delta n_(t)$ be the concentration of excess electrons at time t and G be the rate of production of electrons by photoexcitation. Here, it is assumed that there are no trapping centres. The rate equation is given as

$$\frac{d\Delta n}{dt} = G - \Delta n/\tau \tag{3}$$

where τ is the relaxation time with which the system tends to equilibrium

The rise curve is given by the solution of the above equation with the initial condition $\Delta n(0) = 0$. The solution reads as

$$\Delta n(t) = G\tau[1 - e^{-t/\tau}] \tag{4}$$

With $G = 0$, equation (3) transforms to

$$\frac{d}{dt}\Delta n = -\frac{\Delta n}{\tau} \tag{5}$$

The decay curve is the solution of (5) with initial condition $\Delta n(0) = G\tau$ and is given by

$$\Delta n(t) = G\tau e^{-(t/\tau)} \tag{6}$$

Thus, the rate equation follows a single exponential both in rise and fall regions. In the following section, the rate equations for electron density with recombination, trapping and detrapping will be dealt with.

5.12.2 Rate equations for electron density with recombination, trapping and detrapping

Let $\Delta n^{(f)}$ and $\Delta n^{(t)}$ be the concentrations of free and trapped electrons and G be the rate of production of electrons, τ_r, τ_t and τ_d be the recombination, trapping and detrapping time constants. Considering the production and loss of each of the species, we get the rate equations:

$$\frac{d\Delta n^{(f)}}{dt} = G - \frac{1}{\tau_r}\Delta n^{(f)} - \frac{1}{\tau_t}\Delta n^{(f)} + \frac{1}{\tau_d}\Delta n^{(t)} \tag{7}$$

$$\frac{d\Delta n^{(t)}}{dt} = \frac{1}{\tau_t}\Delta n^{(f)} - \frac{1}{\tau_d}\Delta n^{(t)} \tag{8}$$

These equations have to be solved with the initial conditions,

$$\Delta n^{(f)}(0) = \Delta n^{(t)}(0) = 0 \tag{9}$$

to obtain the build of photoconductivity

$$\Delta\sigma(t) = |e|\mu_n \Delta n^{(f)}(t) \tag{10}$$

Solution:

Equation (8) gives

$$\Delta n^{(f)} = \tau_t \dot{\Delta n}^{(t)} + \frac{\tau_t}{\tau_d}\Delta n^{(t)} \tag{11}$$

where the overdot denotes differentiation with respect to time,

Putting (11) in (7), yields the equations

$$\ddot{\Delta n}^{(t)} + \left(\frac{1}{\tau_r} + \frac{1}{\tau_t} + \frac{1}{\tau_d}\right)\dot{\Delta n}^{(t)} + \frac{1}{\tau_r\tau_d}\Delta n^{(t)} = \frac{G}{\tau_t} \tag{12}$$

Substituting

$$\frac{G\tau_r\tau_d}{\tau_t} + \psi = \Delta n^{(t)}, \tag{13}$$

in equation (12), gives

$$\ddot{\psi} + \alpha\dot{\psi} + \beta\psi = 0$$

$$\alpha = \left(\frac{1}{\tau_r} + \frac{1}{\tau_t} + \frac{1}{\tau_d}\right), \beta = \frac{1}{\tau_t\tau_d}$$

The general solution of this equation is

$$\psi = Ae^{-\lambda_1 t} + Be^{-\lambda_2 t}$$

with $\lambda_{1,2}$ given by

$$\lambda_i^2 - \alpha\lambda_i + \beta = 0$$

Thus we get

$$\Delta n^{(t)} = \frac{G\tau_r\tau_d}{\tau_t} + Ae^{-\lambda_1 t} + Be^{-\lambda_2 t} \tag{14}$$

Substituting (14) in (11)

$$\Delta n^{(f)} = G\tau_r + A\tau_t e^{-\lambda_1 t}\left[-\lambda_1 + \frac{1}{\tau_d}\right] + B\tau_t e^{-\lambda_2 t}\left[-\lambda_2 + \frac{1}{\tau_d}\right] \tag{15}$$

Using the initial conditions (see equation (9)), A and B are found to be

$$A = \frac{G\lambda_2\tau_r\tau_d}{\tau_t(\lambda_2 - \lambda_1)} \tag{16}$$

$$B = -\frac{G\tau_r\tau_d}{\tau_t}\left[\frac{\lambda_2}{\lambda_2 - \lambda_1} + 1\right] \tag{17}$$

Decay of photoconductivity is denoted by the set of equations

$$\frac{d\Delta n^{(f)}}{dt} = -\frac{1}{\tau_r}\Delta n^{(f)} - \frac{1}{\tau_t}\Delta n^{(t)} + \frac{1}{\tau_d}\Delta n^{(t)} \tag{18}$$

$$\frac{d\Delta n^{(t)}}{dt} = \frac{1}{\tau_t}\Delta n^{(f)} - \frac{1}{\tau_d}\Delta n^{(t)} \tag{19}$$

We take the initial condition to be the steady states of the species

$$\Delta n^{(f)}(0) = G\tau_r$$

$$\Delta n^{(t)}(0) = G\frac{\tau_r\tau_d}{\tau_d}$$

A similar analysis gives,

$$\Delta n^{(f)} = A'e^{-\lambda_1 t} + B'e^{-\lambda_2 t} \tag{20}$$

$$\Delta n^{(f)} = A'\tau_t e^{-\lambda_1 t}\left[-\lambda_1 + \frac{1}{\tau_d}\right] + B'\tau_t e^{-\lambda_2 t}\left[-\lambda_2 + \frac{1}{\tau_d}\right] \tag{21}$$

The constants of integration A' and B' can be obtained from the equation.

$$G\frac{\tau_r\tau_d}{\tau_t} = A' + B' \tag{22}$$

$$G\tau_r = A'\tau_t\left[-\lambda_1 + \frac{1}{\tau_d}\right] + B'\tau_t\left[-\lambda_2 + \frac{1}{\tau_d}\right] \tag{23}$$

Thus the decay of photoconductivity for donor level excitation in the presence of recombination, trapping and detrapping is given by a double exponential.

If there are n types of traps having trapping and detrapping time constants, then one can easily write down the rate equation for the build-up and decay of the carrier concentration. It is easy to show that the build-up is given by

$$\Delta n^{(f)}(t) = \sum_{i=1}^{n+1} A_i e^{-t/\tau_i} + A_o \tag{24}$$

For the decay of carriers, one gets

$$\Delta n^{(f)}(t) = \sum_{i=1}^{n+1} A_i' e^{-t/\tau_i} \tag{25}$$

Thus the build up and decay of photoconductivity are given by a sum of $(n+1)$ exponentials for this scenario of trapping.

5.12.3 Excitation of intrinsic semiconductor

Let Δn and Δp be the carrier concentration of photogenerated electrons and holes. In the presence of recombination, and no traps, the concentrations are governed by the equations,

$$\dot{\Delta n} = G - \Delta n h \frac{1}{s_{r1}} \tag{26}$$

$$\dot{\Delta p} = G - \Delta p n \frac{1}{s_{r2}} \tag{27}$$

where s_{r1} and s_{r2} are the constants.

Putting $p = p_0 + \Delta p$, $n = n_0 + \Delta n$; where n_0 and p_0 are equilibrium concentrations of electrons and holes respectively.

$$\dot{\Delta n} = G - \Delta n \Delta p \frac{1}{s_{r1}} - \Delta n \frac{p_0}{s_{r1}} \tag{28}$$

$$\dot{\Delta p} = G - \Delta n \Delta p \frac{1}{s_{r2}} - \Delta p \frac{n_0}{s_{r2}} \tag{29}$$

For small values of G, the production rate, (ie., when the intensity of photons is small) these equations get decoupled. $\Delta n \ll n_0$ and $\Delta p \ll p_0$.

$$\dot{\Delta n} \sim G - \Delta n \frac{p_0}{s_{r1}} = G - \Delta n \frac{1}{\tau_{r1}} \tag{30}$$

$$\dot{\Delta p} = G - \Delta p \frac{n_0}{s_{r1}} = G - \Delta p \frac{1}{\tau_{r2}} \tag{31}$$

With the initial conditions, $\Delta n(0) = 0 = \Delta p(0)$, The solutions are given by

$\Delta n(t) = G\tau_{r1}(1 - e^{-t/\tau_{r1}})$

$\Delta p(t) = G\tau_{r2}(1 - e^{-t/\tau_{r2}})$

The photoconductivity can be obtained using the relation,

$$\Delta\sigma = |e|[\mu_n \Delta n + \mu_h \Delta n] \tag{32}$$

The steady state value of $\Delta\sigma_{st}$ is given by

$$\Delta\sigma_{st} = |e|\,(\mu_n \tau_{r1} + \mu_h \tau_{r2})\,G \tag{33}$$

Hence $\Delta\sigma_{st}$ is proportional to intensity of the light., I_{ph}. When I_{ph} is not very small, we have to solve the non linear equations (28) and (29) to obtain Δn and Δp.

We will solve the problem for the case $n_o = h_o$; $s_{r1} = s_{r2}$

With $x = \Delta n/n_0$ and $y = \Delta p/p_0$,

$$\dot{x} = a - bxy - bx \tag{34}$$

$$\dot{y} = a - bxy - by \tag{35}$$

where $a = G/n_0$ and $b = n_0/s_{r1}$. The initial conditions are given by

$$x(0) = y(0) = 0 \tag{36}$$

from eqns (34) and (35)

$$(\dot{x - y}) = -b(x - y) \tag{37}$$

$$(x - y)(t) = e^{-bt}(x - y)(0) \tag{38}$$

Put $(x - y)(0) = 0$, Thus we get,

$$x(t) = y(t) \qquad \forall\, t \tag{39}$$

Substituting for $y(t)$ in (34), we get the equation

$$\dot{x} = a - bx - bx^2 \tag{40}$$

The solution of this equation is obtained to be

$$x(t) = \left(\sqrt{c+1/4} - 1/2\right) \left[\frac{1 - e^{-2b\sqrt{c+1/4}\ t}}{1 + \frac{\sqrt{c+1/4}-1/2}{\sqrt{c+1/4}+1/2}\ e^{-2b\sqrt{c+1/4}\ t}} \right] \tag{41}$$

where $c = a/b$. The steady state value of x is $\sqrt{c+1/4} - 1/2$ which is proportional to $\sqrt{I_{ph}}$ where I_{ph} is the intensity of photons.

5.12.4 Decay

$$\dot{x} = -bx - bx^2 \tag{42}$$

$$\frac{dx}{-(x^2+x)} = bdt \tag{43}$$

$$x = \frac{1}{\frac{x(0)+1}{x(0)}\ e^{bt} - 1} \tag{44}$$

Thus we find that eventhough the decay is non-exponential at short times, it asymptotically tends to a single exponential even for the non linear case if there are no traps.

5.12.5 Stretched Exponential Decay

The previous analysis shows that the non-constant part of the photoconductivity and the decay part can in general be expressed in the form of

$$\Delta\sigma = \sum_i A_i e^{-\lambda_i t} \tag{45}$$

where the summation is to be performed over all the types of recombination and trapping centres and λ_i are the respective decay constants.

When the system is highly disordered, we can expect a continuous distribution of these decay

constants. In that event, the photoconductivity will have to be described by a functional form

$$\Delta\sigma(t) = \int d\lambda \rho(\lambda) e^{-t\lambda} \tag{46}$$

where $\rho(\lambda)$ describes the probability density for the decay rates. If $\rho(\lambda)$ goes like $\frac{1}{\lambda^{\beta+1}}$ (for $\lambda \gg 1$), , we get $\Delta\sigma(t) = Aexp[-(t/\tau)^{\beta}]$ which is of the form of stretched exponential function.

Stretched exponential relaxation [51], which is described by a time dependence given by $I = I_0 \exp\left[-(t/\tau)^{\beta}\right]$, is commonly observed in disordered systems. Relaxation of non-equilibrated systems toward equilibrium often obeys a time law which is not exponential. The rate of change is instead initially rapid, but becomes continually slower as time progresses.

This long-standing problem of interpreting nonexponential relaxation has recently found renewed attention. Dielectric relaxation has been thoroughly discussed and its universal non-Debye type behaviour has been stressed [52]. The dynamics of glassy relaxation has recently investigated by Palmer, Stein, Abrahams and Anderson(PSSA) [53].

As mentioned earlier, traditionally this type of relaxation has been modelled by invoking statistical distributions [54]. However, there have been attempts to 'derive' stretched exponentials without invoking statistical distributions. In hydrogenated amorphous silicon(a-Si:H), for instance, the relaxation has been attributed to the motion of hydrogen [55], which was found to exhibit time dependent diffusion. Walle [56] has given an simple explanation for the relaxation phenomenon in the context of amorphous silicon. He modelled the process as one in which an hydrogen ion that is released from a trap being retrapped at the same or another trap site. Considering the reactions describing the trapping and release of hydrogen, and after some approximations, one arrives at a solution which contains two parameters. This solution turns out to behave much like stretched exponential and also provided a good fit to the experimental data available for a limited duration. In view of this agreement, he concluded that his model is a stretched exponential decay that does not invoke statistical distribution of traps. It can however, be shown that his solution actually

yield an exponential decay at long times(asymptotically).

The time dependence of persistent photoconductivity of $Zn_{0.3}Cd_{0.7}Se$ was studied by Jiang and Lin [34] at different temperatures. They observed the reduction in the decay constant with the decrease in temperature upto a temperature of 220K, and after 220 K, τ increases with increase in temperature. In the low temperature regime, they could fit the data with the stretched exponential relation. They got the straight line between ln[In $I_{ppc}(o)$-In $I_{ppc}(t)$] versus ln(t). The perfect linear behaviour of the plots demonstrates the PPC decay is well described by the Kohlrausch expression. The value of β is about 0.85$\pm$0.03 below 120 K and it is decreased near 120 K. The decay constant τ also shows a transition at 120 K. At temperatures above 220 K. the decay of PPC is no longer well described by the stretched exponential. The PPC relaxation rate increases as temperature increases in the region of T> 220 K. Since the stretched exponential relaxation is due to the disordered nature of the system, it is implied that microscopic random-potential fluctuations could possibly be the cause of the observed time dependence of PPC.

5.12.6 Power law decay

So far we have considered scenarios wherein the mobility of the charge carriers is assumed to be a constant (independent of time) and the time dependence of the conductivity arose out of the time dependence of the carrier concentration. When the degree of disorder is high, this approximation becomes untenable - the motion of the charge carriers are no longer diffusive with a constant drift velocity. Their mobility now acquires a non trivial time dependence. This point has been clearly established by Scher and Mentroll by considering a simplified model for the decay of photoconductivity in amorphous materials [57].

In an amorphous material, there is a dispersion in the spatial separation between nearest-neighbour localized sites available for hopping carriers. Also a dispersion is possible in the potential barriers between these sites. Both of these variables strongly affect the hopping

time which is nothing but the time between arrival of a carrier on successive sites. The distribution of these hopping times, $\psi(t)$, is expected to have a long tail. Scher and Montroll had developed a stochastic transport model [57] for the photocurrent $I(t)$, where they describe a carrier packet executing a time-dependent random walk in the presence of a field-dependent spatial bias and an absorbing barrier at the sample surface. They proposed the hopping time distribution to be of the form

$$\psi(t) = constant \times t^{-(1+\alpha)}, 0 < \alpha < 1. \tag{47}$$

A consequence of the above long tailed distribution is that a fraction of the carriers remain at the point of their formation for a long time. Those carriers whose local environment at their initial point permits their immediate motion (fast hops) will sooner or later find themselves immobilized at some site (long hops), thus reducing their contribution to the current, until they escape. According to this model,

$$I(t) \sim A \quad t^{-(1-\alpha)} \tag{48}$$

for an infinite system. If the sample is finite, then there exists two power law regimes.

It could be observed in their case, that the sum of two exponents will be equal to -2 for the later case. For As_2S_3, Scher and Montrol found the slopes in the I versus $ln\ t$ plot to be -1.8 and -0.2 and which on adding gives the value of -2.

$$I(t) \sim At^{-(1-\alpha)} \quad \text{for} \quad \text{t} < \tau(\text{L}) \tag{49}$$

$$I(t) \sim At^{-(1+\alpha)} \quad \text{for} \quad \text{t} > \tau(\text{L}) \tag{50}$$

where τ is a characteristic time depending upon the thickness of the sample.

Somnath *et al* [45] studied the persistent photoconductivity on ion irradiated carbon films. The slow decay of photocurrent indicates the presence of traps which can be filled by the carriers generated by the optical source. The photocurrent is proportional to $\tau^{-\beta}$, where $\beta = T/T_c$, $0 < \beta < 1$ and T_c corresponds to the critical temperature of carrier recombination.

They plotted ln (I_p) versus ln t which never showed a single straight line. At 10 K, longer decay time is observed at the beginning of photodecay curve, followed by a few segments with different values of β, indicating that the distribution of traps is complex.

References

[1] N.R. Parikh, D.A. Thompson, and G.J.C. Carpenter, Radiation Effects, 98 (1986) 289

[2] Y. Shiraki, T. Shimada, abd K.F. Komatsubara, J. Appl. Phys., 43 (1972) 710

[3] F. Chernow, G. Ruse, and L.Wahim, Appl. Phys. Lett., 12 (1968) 339

[4] E.R. Pollard, and J.L. Hartke, Bull. Am. Phys. Soc., 14 (1969) 115

[5] Electronic Structure and Properties of Semiconductors, Materials Science & Technology, A Comprehensive treatment, Vol. 4 Ed. W. Schroter (VCH, New York, 1991)

[6] N.P. Kekelidze, Radiation Effects, 32 (1977) 113

[7] K. L. Narayanan, K. P. Vijayakumar, K. G. M. Nair and G. V. N. Rao, Bull. Mater. Sci., 20 (1997) 287

[8] K. L. Narayanan, K. P. Vijayakumar, K. G. M. Nair, N. S. Thampi and K. Krishan, J. Mater. Sci., 32 (1997) 4837

[9] O.Zelaya Angel, L.HErnandez, O de Melo, J.J Alvarado-Gil, R.Lozado-Morales, C.Falcony, H.Vargas and R.Ramirez-Bon, Vacuum, 46 (1995) 1083.

[10] Y. Kashiwaba, A. Tada and T. Ikeda, Jpn. J. Appl. Phys., 33 (1994) 1613

[11] Y. Kashiwaba, I. Kanno and T. Ikeda, Jpn. J. Appl. Phys., 31 (1992) 1170

[12] P.J. Sebastian, Appl. Phys. Lett., 62 (1993) 2956

[13] K.P. Varkey and K.P. Vijayakumar, Jpn. J. Appl. Phys., 36 (1997) L394

[14] Photoelectronic properties of semiconductors, (Ed.) R. H. Bube, (Cambridge University Press, Cambridge, 1992).

[15] M.K. Sheinkman and A.Ya. Shik, Fiz. Tekh. Poluprovdn., 10 (1976) 209 [Sov. Phys. Semicond., 10 (1976) 128]

[16] J.Y. Lin, A. Dissanayake, G. Brown, and H.X. Jiang, Phys. Rev. B, 42 (1990) 5855

[17] H.X. Jiang, G. Brown, and J.Y. Lin, J. Appl. Phys., 69 (1991) 6701

[18] A. Hoffmann, Ivan K. Schuller, A. Gilabert, M.G. Medici, F. Schmidl and P. Seidel, Appl. Phys. Lett., 70 (1997) 2461

[19] V.I. Kudinov, A.I. Kirilyuk, N.M. Kreines, R. Laiho, ànd E. Lahderanta, Phys. Lett. A, 151 (1990) 358

[20] G. Nieva, E. Osquiguil, J. Guimpel, M. Maenhoudt, B. Wuyts, Y. Bruynseraede, M.B. Maple and I.K. Schuller, Appl. Phys. Lett., 60 (1992) 2159

[21] D. Lederman, J. Hansen, I.K. Schuller, E. Osquiguil, Y.Bruynseraede, Appl. Phys. Lett., 64 (1994) 652

[22] E.A. Katz, V. Lyubin, D. Faiman, S. Stutina, A. Shames and S. Goren, Solid State Communications., 100 (1996) 781

[23] Hameed, A., Rasmussen, H. and Hor, P.H., Phys. Rev. B, 48 (1993) 14760

[24] K.C. Chiu, J.S. Wang, Y.T. Dai, and Y.F. Chen, Appl. Phys. Lett., 69 (1996) 2665

[25] J.Y. Lin, H.X. Jiang, Phys. Rev. B, 41 (1990) 5178

[26] A.S. Dissanayake, J.Y. Lin, and H.X. Jiang, Phys. Rev. B, 48 (1993) 8145

[27] A.S. Dissanayake, S.X. Huang, H.X. Jiang and J.Y. Lin, Phys. Rev. B, 44 (1991) 13343

[28] U. Zammit, K.N. Madhusoodanan, M. Marinelli, F.Scudieri, R. Pizzoferrato, F. Mercuri, E. Wendler and W. Wesch, Phys.Rev.B., 49 14322 (1994)

[29] K. L. Narayanan, K. P. Vijayakumar, K. G. M. Nair and N. S. Thampi, Physica B, 240 (1997) 8

[30] K. L. Narayanan, K. P. Vijayakumar, K. M. Nair and G. V. N. Rao, Nucl. Instr. Meth. Phys. B, 132 (1997) 61

[31] K. L. Narayanan, K. P. Vijayakumar, K. M. Nair and R. Kesavamoorthy, Phys. Stat. Sol. A (In press)

[32] S.M. Ryvkin and I.S. Shlimak, Phys. Status Solidi A, 16 (1973) 515

[33] H.X. Jiang, and J.Y. Lin, Phys. Rev. Lett., 64 (1990) 2547

[34] H.X. Jiang and J.Y. Lin, Phys. Rev. B, 40 (1989) 10025

[35] A.F.S. Penna, J. Shah, T.Y. Chang and Burroughs, Solid State Commun., 52 (1984) 425

[36] P. Blood, A.D.C. Grassie, J. Appl. Phys., 56 (1984) 1866

[37] J.A. Kash, A. Ron and E. Cohen, Phys. Rev. B, 28 (1983) 6147

[38] D.V. Lang, R.A. Logan and M. Jaros, Phys. Rev. B, 19 (1979) 1015

[39] New Developments in Semiconductor Physics, J.M. Langer, edited by F. Beleznay, G. Ferenczi, and J. Giber (Springer-Verlag, 1980), p.123

[40] Deep Centres in Semiconductors, edited by Sokrates T. Pantelides, (Gordon and Breach Publications, 1992), p.591

[41] M. Baj, L. Dmowski, M. Konczykowski and S. Porowski, Phys. Stat. Sol. (a), 33 (1976) 421

[42] B.C. Burkey, R.P. Koshla, J.R. Fisher and D.L. Losee, J. Appl. Phys., 47 (1976) 1095

[43] R. Legros, Y. Marfaing and R.T. Triboulet, J. Phys. Chem. Solids, 39 (1978) 179

[44] J. Hubbard, Proc. Roy. Soc. London Ser. A, 276 (1963) 238

[45] S. Battacharyya, K.S.R. Koteswara Rao, S.V. Subramanyam and D. Kanjilal, Appl. Phys. Lett., 68 (1996) 2079

[46] J. Kakalios and H. Fritzsche, Phys. Rev. Lett., 53 (1984) 1602

[47] Advances in Solid State Physics: Festkorperprobleme, G.H. Dohler, edited by P. Grosse (Vieweg, Braunschweig, 1983) Vol. 23, p 207

[48] A. Vaseashta and L.C. Burton, Appl. Phys. Lett., 58 (1991) 1193

[49] J.M. Epp and J.G. Dillard, Chem. Mater., 1 (1989) 325

[50] Y. Yuba, T. Ishida, K. Gamo and S. Namba, J. Vac. Sci. Technol. B, 6 (1988) 253

[51] R. Kohlraush, Ann. Phys., (Leipzig) 12 (1847) 393

[52] K.L. Ngai, Comments solid Stae Phys., 9 (1980) 141

[53] R.G. Palmer, D.L. Stein. E. Abrahams, and P.W. Anderson, Phys. Rev. Lett., 53 (1984) 958

[54] D.L. Huber, Phys. Rev. B, 31 (1985) 6070

[55] J. Kakalios, R.A. Street and W.B. Jackson, Phys. Rev. Lett., 59 (1987) 1037

[56] Chris G. Van de Walle, Phys. Rev. B, 53 (1996) 11292

[57] H. Scher and E.W. Montroll, Phys. Rev. B, 12 (1975) 2455

CHAPTER 6

6 SUMMARY AND CONCLUSION

In the present thesis, the irradiation effects in CdS thin films were investigated by various techniques such as optical absorption spectrometry, Raman scattering spectroscopy, positron annihilation spectroscopy and X-ray diffraction. Photoconductivity studies were also carried out on the as-deposited and irradiated films. The important observations and conclusions are given in this chapter along with the future plan of the work in this area.

A detailed account of the preparation and characterisation of CdS thin films using vacuum evaporation and chemical bath deposition techniques was presented in the third chapter. The preparation procedure for obtaining good quality, adherent films of CdS was optimized by varying process parameters like molar concentration, dipping time and temperature of the bath. It was found that the best quality films of good adhesion and uniformity could be achieved with equimolar concentrations of cadmium and sulphur compounds at a bath temperature of about 333 K. The as-deposited thin films were found to be crystalline, containing both the cubic and hexagonal phases. The films were found to show high resistance, with the resistivity in the range of 10^5 to 10^7 ohm cm. On thermal annealing in flowing argon atmosphere, the structural transformation of the films from metastable cubic to the stable hexagona phase was observed. This was accompanied by substantial grain growth. Optical absorption measurements carried out on the as-deposited and annealed CBD films revealed a band gap reduction on thermal annealing. The observed shift in the band gap has been attributed to the change in the volume of the unit cell as a consequence of the phase transformation from the metastable cubic phase to stable hexagonal phase. Annealing of the films in air at 573 K resulted in the partial conversion of CdS to CdO and consequent decrease in resistivity.

The effect of argon ion implantation on chemical bath deposited CdS thin films was in-

vestigated by X-ray diffraction, Positron annihilation spectroscopy, Raman scattering and optical absorption techniques. The X-ray diffraction pattern of the as-deposited CdS thin films showed the presence of both sphalerite(cubic) and wurtzite(hexagonal) phases. Phase transition from the as-deposited mixed phase to the more stable hexagonal phase along with grain growth is observed on post implantation annealing. Depth profiling studies of defects in CdS thin films using a low energy positron beam are reported. Doppler broadening line-shape S-parameter in the as-grown and irradiated films have been monitored as a function of positron beam energy. It was found that the defect sensitive S-parameter in irradiated films shows a reduction as compared to that of as-deposited thin film. The observations are attributed to the formation cadmium clusters during irradiation. Isochronal annealing behaviour of the irradiated and as-grown films indicate the annealing out of irradiation induced Cd clusters and grain growth at high temperatures.

Optical absorption studies on Ar^+ irradiated CdS thin films showed a systematic reduction in the optical bandgap and the band edge sharpness with the irradiation dose. Similar results were also seen in samples implanted with nitrogen and oxygen ions. These effects are attributed to irradiation induced lattice disorder. Raman scattering studies on argon irradiated CdS films show a decrease in the intensity of the Raman peak of CdS A_1(LO) mode on implantation and on post implantation annealing, the intensity is found to increase. A drastic reduction in the FWHM value of the films subjected to post implantation annealing compared to that of the as-deposited or the implanted films suggests the removal of defects and strain during annealing. The peak position of the Raman mode of CdS remains more or less the same. The Raman scattering studies on vacuum evaporated thin films, showed increase in the peak height with irradiation dose. The effect is attributed to the enhanced Raman scattering caused by irradiation induced surface roughening.

The effect of nitrogen ion implantation in CdS thin films is discussed in the fifth chapter. The investigations of the as-deposited, implanted and subsequently annealed thin films of CdS are reported here. Nitrogen ion implantation induced changes in the electrical properties of the films and in particular the increase in the conductivity of the films with an increase in

the nitrogen fluence is reported and it is attributed to the formation of acceptor levels. On nitrogen irradiation, type conversion from n to p in CdS films was observed. Ion irradiation induced persistent photoconductivity phenomenon is thoroughly studied and the results reveal that the persistent photoconductivity increases with the irradiation dose and it is attributed to the random local potential fluctuations caused by compositional variations. The decay constants of the as-deposited films and the films irradiated to various doses of nitrogen ions were obtained. It was found that the decay constant of the films increases with the irradiation dose. Persistent photoconductivity measurements were carried out on the films at low temperature also and it was found that the decay constants increase with decrease in temperature. PPC is of technological importance because the films with large decay constant can be used as photo memory devices.

Raman scattering studies of the oxygen ion implanted CdS thin films prepared by vacuum evaporation method are presented in the thesis. The studies reveal that the peak position of the A_1(LO) mode of CdS thin film increases due to lighter oxygen ions replacing heavier sulphur ions in the CdS matrix. The area under the peak increased at low doses due to implantation induced surface roughness which resulted in Raman intensity enhancement. The observed decrease in peak area at higher doses is attributed to the ion implantation induced lattice damage.

To conclude, several aspects of irradiation effects in CdS have been investigated using a number of techniques. Some of the important observations include the conversion of n type CdS thin films to p type, systematic reduction of the optical bandgap and bandedge sharpness due to irradiation induced lattice disorder and persistent photoconductivity in N^+ implanted CdS thin films.

6.1 Future scope of the work

CdS thin films prepared by chemical bath deposition process will be the irradiated with nitrogen ions of different energies to various doses. P type CdS thin films will be formed

by nitrogen ion implantation and homojunction CdS solar cells will be fabricated. We have been working in the developmental activities of a 400 kV implanter which can be used for the implantation of the metal ions like aluminium, copper etc. Cu^+ ions will be implanted into CdS thin film and to form a p-type CdS layer. Formation of homojunction solar cells due to copper ion implantation will also be attempted.

PUBLICATIONS

[1] Chemical bath deposition of CdS thin films and its partial conversion to CdO on annealing
K. L. Narayanan, K. P. Vijayakumar, K. G. M. Nair and G. V. N. Rao
Bull. Mater. Sci., 20 (1997) 287

[2] Structural transformation of dip coated CdS thin films during annealing
K. L. Narayanan, K. P. Vijayakumar, K. G. M. Nair, N. S. Thampi and K. Krishan.
J. Mater. Sci., 32 (1997) 4837

[3] Raman scattering and optical absorption studies of Ar^+ implanted CdS thin films
K. L. Narayanan, K. P. Vijayakumar, K. G. M. Nair, B. Sundarakkannan, G. V. N. Rao and R. Kesavamoorthy,
Nucl. Instr. Meth. Phys. Res. B 132 (1997) 61

[4] Effect of irradiation induced disorder on the optical absorption spectra of CdS thin films
K. L. Narayanan, K. P. Vijayakumar, K. G. M. Nair and N. S. Thampi,
Physica B 240 (1997) 8

[5] Raman scattering studies of Ar^+ implanted CdS thin films prepared by vacuum evaporation
K. L. Narayanan, K. P. Vijayakumar, K. G. M. Nair and R. Kesavamoorthy,
Physica Status Solidi - A. (In press)

[6] Positron beam studies of argon irradiated CdS thin films
G. Amarendra, **K. L. Narayanan**, G. Venugopal Rao, B. Viswanathan, K. G. M. Nair and K. P. Vijayakumar,
Communicated to J. Appl. Phys.

[7] Irradiation induced persistent photoconductivity of CdS thin films prepared by chemical bath deposition

K.L. Narayanan, R. Rajaraman, M.C. Valsakumar, K. G. M. Nair and K. P. Vijayakumar. [Manuscript under preparation]

[8] Optical absorption studies of nitrogen irradiated CdS thin films prepared by chemical bath deposition method.
K.L. Narayanan, P. Magudapathy, K. Suresh, K. P. Vijayakumar and K. G. M. Nair, [Mansucript under preparation]

[9] Electrical characterization and type conversion in nitrogen irradiated CdS thin films
K.L. Narayanan, R. Rajaraman, M.C. Valsakumar, K. G. M. Nair and K. P. Vijayakumar [Manuscript under preparation]

[10] Raman scattering studies of oxygen irradiated CdS thin films prepared by vacuum evaporation
K. L. Narayanan, K. P. Vijayakumar, K. G. M. Nair, B. Sundarakkannan and R. Kesavamoorthy [Manuscript under preparation]

SEMINARS/CONFERENCES

[1] Characterisation of CdS thin films prepared by chemical bath deposition technique using SEM. **K. L. Narayanan**, K. P. Vijayakumar, K. G. M. Nair, N. S. Thampi and K. Krishan.
Paper presented in the National Seminar on Emerging trends in thin film technology and device fabrication, held at Cochin University of Science and Technology, Cochin during 27-29 1995

[2] Optical band gap shift in ion implanted CdS thin films **K. L. Narayanan**, K. P. Vijayakumar, K. G. M. Nair, N. S. Thampi and K. Krishan.

Paper presented in the Conf. on Frontiers in Materials modelling and Design, held at IGCAR, Kalpakkam during 20-23 August 1997

[3] Positron beam study of CdS thin films G. Venugopal Rao, G. Amarendra, B. Viswanathan, **K. L. Narayanan** and K. G. M. Nair
Solid State Physics (India), Vol.39C, (1996) 219

[4] Raman scattering studies of Ar^+ implanted CdS thin films **K. L. Narayanan**, K. P. Vijayakumar, K. G. M. Nair and R. Kesavamoorthy
Solid State Physics (India), Vol.39C, (1996) 159

[5] Raman scattering studies of O^+ implanted CdS films **K. L. Narayanan**, K. P. Vijayakumar, K. G. M. Nair, B. Sundarakkannan and R. Kesavamoorthy
Laser Applications in Materials Science and Industry, Eds R. Kesavamoorthy, C. Babu Rao, A.K. Arora and P. Kalyanasundaram, Allied Publishers Ltd., 1997

[6] Irradiation indueced Persistent photoconductivity in CdS thin films prepared by chemical bath deposition. **K.L. Narayanan**, R. Rajaraman, M.C. Valsakumar, K. G. M. Nair and K. P. Vijayakumar. Accepted in Solid State Physics Symposium, 1997